Metamaterial Structures for Wakefield Acceleration and High Power Microwave Generation

by

Xueying Lu

B. S. (Engineering Physics), Tsinghua University (2012)

Submitted to the Department of Physics
in partial fulfillment of the requirements for the degree of

Doctor of Philosophy

at the

MASSACHUSETTS INSTITUTE OF TECHNOLOGY

February 2019

Author .....
Department of Physics
November 16, 2018

Certified by .....
Richard J. Temkin
Senior Scientist, Department of Physics
Thesis Supervisor

Accepted by .....
Nergis Mavalvala
Associate Department Head

Metamaterial Structures for Wakefield Acceleration and High Power Microwave Generation

by

Xueying Lu

Submitted to the Department of Physics
on November 16, 2018, in partial fulfillment of the
requirements for the degree of
Doctor of Philosophy

Abstract

This thesis presents the theoretical and experimental investigation of the interaction of metamaterial structures with electron beams for two applications: wakefield acceleration and high power microwave generation.

Under the topic of wakefield acceleration, on the theoretical side, several metamaterial structures have been designed and simulated. The novel phenomenon of reversed Cherenkov radiation has been found to enhance the beam-wave interaction in metamaterials. A metallic wagon wheel metamaterial structure was designed and built for use in an experiment at the Argonne Wakefield Accelerator (AWA) Facility.

On the experimental side, this thesis presents the first demonstration of high-power, reversed Cherenkov wakefield radiation by short electron bunches passing through the wagon wheel structure at the AWA. Single 45 nC electron bunches of 65 MeV energy traversing the structure generated up to 25 MW in 2 ns pulses at 11.4 GHz, in excellent agreement with theory. Two bunches of 85 nC with appropriate temporal spacing generated up to 80 MW by coherent wakefield superposition. If this power were applied to a trailing witness bunch in a collinear wakefield accelerator, it would provide an accelerating gradient of 75 MV/m.

Under the topic of high power microwave generation, on the theoretical side, an analytical theory has been developed to predict the novel Cherenkov-cyclotron interaction in metamaterial-based microwave devices. An S-band metamaterial-loaded waveguide with reverse symmetry has been designed and built to work with the Cherenkov-cyclotron interaction.

On the experimental side, this thesis presents the experimental results of the metamaterial-loaded waveguide built at MIT. Power levels to 2.9 MW at 2.4 GHz in full 1 μs pulses were generated by an electron beam of up to 490 kV of voltage and 84 A of current. Frequency tuning measurements verified that pulses above 1 MW of output power were only seen in the Cherenkov-cyclotron mode.

With these results, this thesis demonstrates the unique features of metamaterial structures that are very attractive for high-gradient wakefield accelerators and high power microwave sources. Advantages include the high shunt impedance for intense

beam-wave interaction; the simple and rugged structure; and a large parameter space for various optimization goals.

Thesis Supervisor: Richard J. Temkin
Title: Senior Scientist, Department of Physics

Acknowledgments

This thesis is the product of the tremendous support and help I was fortunate to receive from many people, to whom I owe a debt of gratitude.

I would like to thank my thesis advisor, Dr. Richard Temkin, who has all the great things that an amazing advisor can have: knowledge, insight, patience, willingness to help, and many more. I thank Rick for bringing me to MIT and for making my PhD years enjoyable. It has been my great honor to work in the group.

I would like to thank Dr. Michael Shapiro, who also closely advised my research and contributed greatly to the completion of this thesis. A quick talk with Michael would often lead to solutions to some mysteries that troubled me for days or weeks.

I would like to thank Dr. Ivan Mastovsky, who always knows how to deal with misbehaving lab equipment. Ivan's experimental expertise helped me get over all the hurdles during my time in the lab.

I would like to thank my colleagues in the group past and present. I am so lucky to get to know and to work with these great people. I thank Dr. Jason Hummelt for showing me how to run the experiment in the West Cell. I thank Dr. Jacob Stephens and Dr. Guy Rosenzweig for their help and good conversations in the lab. I thank Dr. Jiexi Zhang for being a patient climbing buddy. I thank Dr. Alexander Soane for sending postcards from all over the world. I thank Dr. Sudheer Jawla, Julian Picard, Samuel Schaub and Haoran Xu for helpful discussions and comments on my work. I thank my previous officemates Dr. Sergey Arsenyev, Dr. Elizabeth Kowalski and Hannah Hoffmann for making the work environment happy.

I would like to thank our collaborators at the Argonne National Laboratory, Dr. John Power, Dr. Manoel Conde, Dr. Jiahang Shao, Dr. Eric Wisniewski, Scott Doran, Charles Whiteford and Dr. Chunguang Jing, for their great help. They made my experience in Argonne both rewarding and fun.

I would like to thank the MIT central machine shop, Andrew Gallant and Michael Abruzzese, for making almost all the parts for my experiments and for helping me to improve the mechanical drawings.

I would like to thank Dr. Miklos Porkolab and Dr. John Belcher for being on my thesis committee and my oral exam committee. Dr. Earl Marmar also served on my oral exam committee. From them I received comments and suggestions which helped greatly throughout the preparation and the review of this thesis.

I would like to thank my undergraduate professors at Tsinghua University, Dr. Wenhui Huang, Dr. Jianfei Hua, Dr. Chuanxiang Tang, Dr. Huaibi Chen and Dr. Yi-Kang Pu, for encouraging me to pursue my graduate study in physics.

I would like to thank all my friends, at MIT, in Boston, in the US, and in China, for sharing numerous good memories with me. I am most proud of the friends I have kept for over a decade long: Yan, Jessica Qijie, Yipeng, Zhao, Rui and Zong. During these years, we have grown separately, but we have never grown apart.

Last but not least, I would like to thank my parents. My father Chao Lu introduced me to classical Chinese literature when I was a kid, which has taught me the great values of kindness, integrity and courage. My mother Xiaoxia Xue provides me with a great example of an independent and strong woman. I thank you for your love and support, and this thesis is dedicated to you.

Xueying Lu

November 15, 2018

During first snow of the season

Cambridge, MA

Contents

List of Figures

List of Tables

Chapter 1

Introduction

This thesis studies the interaction of metamaterials with electron beams, with its two applications explored both theoretically and experimentally. The two applications are wakefield acceleration and high power microwave generation.

In this section, three topics will be introduced: metamaterials in Section 1.1, wakefield acceleration in Section 1.2 and high power microwave sources in Section 1.3. The thesis outline will be introduced in Section 1.4.

1.1 Metamaterials

Metamaterials refer to a category of periodic structures with the period much smaller than the operating wavelength, so it can be seen as an artificial medium with the effective ϵ and μ determined by the unit cell design.

Metamaterials are built out of natural materials, either metal or dielectric. By arranging the subwavelength periodic elements built by natural materials in carefully designed shapes and patterns, unusual properties can be found, such as a negative refractive index.

The physics of electromagnetic wave traveling in a medium with simultaneous negative ϵ and μ was first studied in 1968 in Ref. [1]. Realization of a metamaterial structure with a negative refractive index was first proposed in 2000 in Ref. [2], when the concept of split ring resonators was demonstrated as a building block for

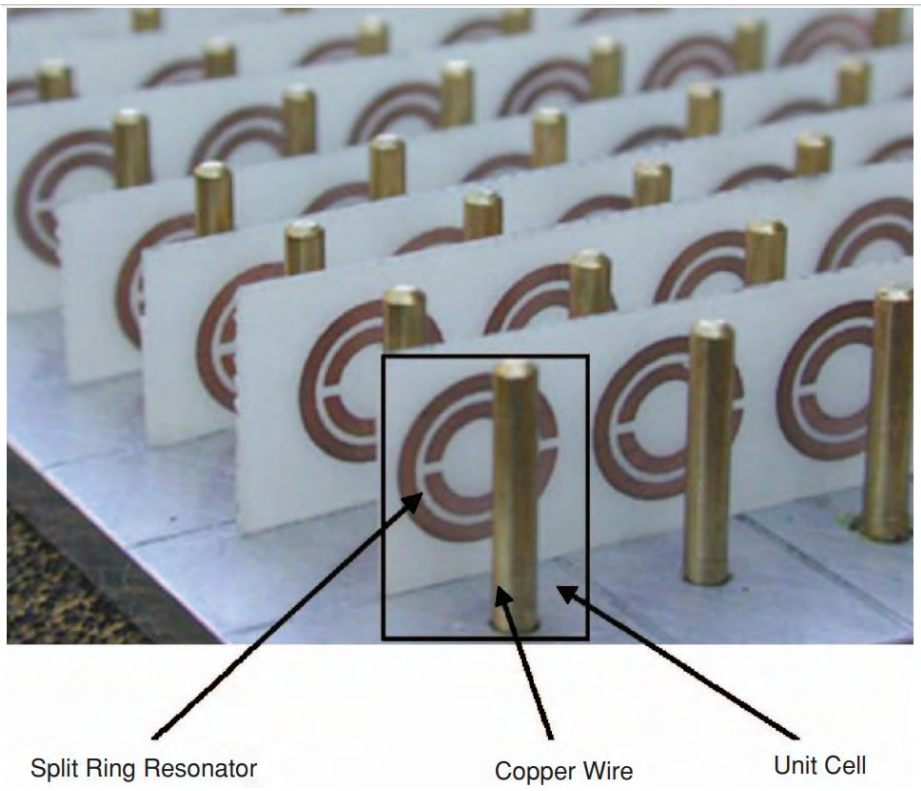

Figure 1-1: Example of a metamaterial structure as an array of the split ring resonators combined with copper wire arrays. The metamaterial structure is periodic, with the unit cell comprising of one split ring resonator and one copper wire. This figure is cited from Ref. [3].

metamaterials. An example of a metamaterial structure as an array of the split ring resonators combined with copper wire arrays is shown in Fig. 1-1. Since then, metamaterials have been intensively studied at microwave and optical frequencies. Metamaterials are promising to provide improved performance over traditional devices in the way that the unit cell design process allows more controllability and flexibility of electromagnetic characteristics, for example, dispersion [4, 5]. Then we can build devices with interesting features and better performance by engineering the unit cell.

In the area of passive microwave devices, metamaterials are applied to cloaking [6], perfect lens [7, 8], antenna design [9], etc. In this thesis, the focus is to study metamaterial-based active devices with electron beams involved.

In this section, I will first introduce the basic physics of a propagating wave in

metamaterials with a negative refractive index in Section 1.1.1. In section 1.1.2 I will introduce the negative refraction in metamaterials, which is widely applied in passive microwave devices. Then in Section 1.1.3 I will introduce the novel physics phenomenon when particle beams travel in metamaterials, the reversed Cherenkov radiation.

1.1.1 Basic Principles of Metamaterials

In this part, I will show how electromagnetic waves can propagate in a medium with double negative permittivity ϵ and permeability μ. The basic principles of metamaterials can be derived from the Maxwell's equations.

In a medium without external charge or current, the Maxwell's equations have the form of

$$\begin{aligned} \nabla \times \vec{E} &= -\mu \frac{\partial \vec{H}}{\partial t}, \\ \nabla \times \vec{H} &= \epsilon \frac{\partial \vec{E}}{\partial t}, \\ \nabla \cdot \vec{E} &= 0, \\ \nabla \cdot \vec{H} &= 0. \end{aligned} \tag{1.1}$$

We assume the permittivity ϵ and the permeability μ are both isotropic, so they follow the constitutive relations of

$$\begin{aligned} \vec{D} &= \epsilon \vec{E}, \\ \vec{B} &= \mu \vec{H}. \end{aligned} \tag{1.2}$$

For a plane wave with the space and time dependence as $\exp(i\vec{k} \cdot \vec{r} - i\omega t)$, i.e. $\vec{E} = \vec{E}_0 \exp(i\vec{k} \cdot \vec{r} - i\omega t)$ and $\vec{H} = \vec{H}_0 \exp(i\vec{k} \cdot \vec{r} - i\omega t)$, where $\vec{k}$ is the wave vector, and ω is the angular frequency, we can rewrite Eq. (1.1) as

$$\begin{aligned} \vec{k} \times \vec{E} &= \mu\omega \vec{H}, \\ \vec{k} \times \vec{H} &= -\epsilon\omega \vec{E}, \\ \vec{k} \cdot \vec{E} &= 0, \\ \vec{k} \cdot \vec{H} &= 0. \end{aligned} \tag{1.3}$$

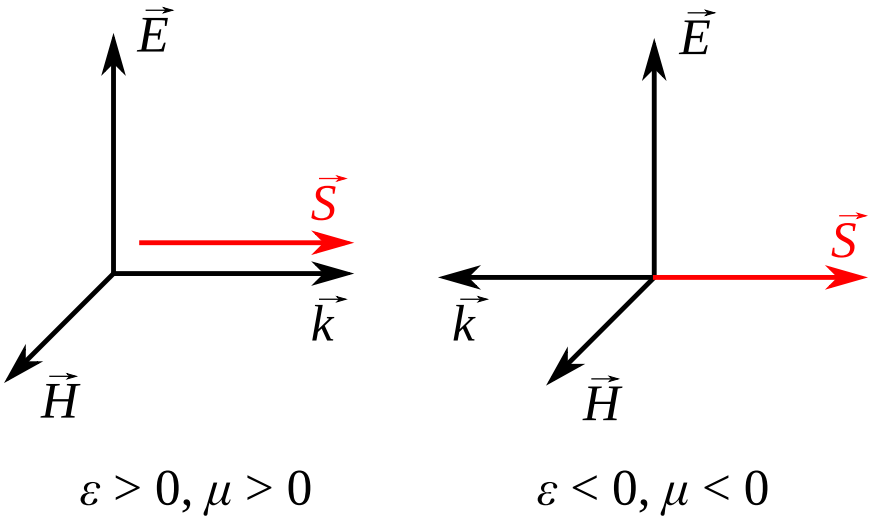

Figure 1-2: Comparison of the relations of the vectors $\vec{k}$, $\vec{E}$, and $\vec{H}$ as a right-handed triplet in normal materials in the left figure, and as a left-handed triplet in double-negative metamaterials in the right figure.

From Eq. (1.3), we can derive the dispersion relation as

$$k^2 = \epsilon\mu\omega^2. \tag{1.4}$$

For a propagating wave, k needs to be real. From Eq. (1.4), we can see that k has a real solution in two cases: (1) $\epsilon > 0$, $\mu > 0$; (2)$\epsilon < 0$, $\mu < 0$. Case (1) corresponds to natural materials, and Case (2) corresponds to double-negative metamaterials. So a propagating wave can live in a double-negative metamaterial.

Equation (1.3) also reveals an interesting feature of metamaterials, the left-handedness. In natural materials with $\epsilon > 0, \mu > 0$, the three vectors $\vec{k}$, $\vec{E}$, and $\vec{H}$ form a right-handed triplet. However, in metamaterials with $\epsilon < 0, \mu < 0$, then $\vec{k}$, $\vec{E}$, and $\vec{H}$ form a left-handed triplet. For this reason, double-negative metamaterials are also called left-handed materials. An illustration is presented in Fig. 1-2 to compare the right-handed triplet and the left-handed triplet.

The Poynting vector $\vec{S}$ is also shown in Fig. 1-2. The direction of the Poynting

vector is not changed by the signs of ϵ and μ, from its definition as

$$\vec{S} = \vec{E} \times \vec{H}. \tag{1.5}$$

Since $\vec{S}$ represents the direction of the wave energy flow, we can see from Fig. 1-2 that the energy flow and the wavefront (represented by $\vec{k}$) are anti-parallel to each other. This reveals the backward wave propagation phenomenon in double-negative metamaterials.

The backward wave propagation phenomenon can be derived in another way [4]. Now we look at the time-averaged electromagnetic field energy density U in a dispersive medium for a quasi-monochromatic wavepacket,

$$U = \frac{1}{4}\left[\frac{\partial(\omega\epsilon)}{\partial\omega}|\vec{E}|^2 + \frac{\partial(\omega\mu)}{\partial\omega}|\vec{H}|^2\right]. \tag{1.6}$$

In a physical system, the energy density must be positive, so from Eq. (1.6), we have

$$\frac{\partial(\omega\epsilon)}{\partial\omega} > 0, \ \frac{\partial(\omega\mu)}{\partial\omega} > 0 \tag{1.7}$$

Since $k^2 = \epsilon\mu\omega^2$ from Eq. (1.4), then

$$\frac{\partial k^2}{\partial\omega} = \omega\epsilon\frac{\partial(\omega\mu)}{\partial\omega} + \omega\mu\frac{\partial(\omega\epsilon)}{\partial\omega}. \tag{1.8}$$

Now combining Eq. (1.7) and Eq. (1.8), we have

$$\frac{\partial k^2}{\partial\omega} < 0. \tag{1.9}$$

with double-negative metamaterials. Then from the definitions of the phase velocity $v_p = \omega/k$, and the group velocity $v_g = \partial\omega/\partial k$,

$$\frac{\partial k^2}{\partial\omega} = \frac{2\omega}{v_p v_g}. \tag{1.10}$$

Therefore, from Eq. (1.9) and Eq. (1.10), we derive the signs of the phase velocity

and the group velocity in metamaterials, as

$$v_p v_g < 0. \tag{1.11}$$

This again proves that the energy flow and the wavefront are traveling in opposite directions in double-negative metamaterials.

1.1.2 Negative Refraction

Negative refraction in metamaterials is the phenomenon studied intensively in passive microwave devices. Here I will give a brief introduction.

Refraction happens at the interface of two different materials, with the refractive indices as n_1 and n_2. The incidence angle is θ_1, and the refractive angle is θ_2. From Snell's Law,

$$n_1 \sin\theta_1 = n_2 \sin\theta_2. \tag{1.12}$$

For the double-negative metamaterials, the refractive index is negative as

$$n = -c\sqrt{\epsilon\mu} < 0. \tag{1.13}$$

Note that Snell's Law can be derived from the minimized optical path, and it can be proven easily that on the interface of a natural material with $n_1 > 0$ and a metamaterial with $n_2 < 0$, Snell's Law still holds [1].

In the case of $n_1 > 0$, $n_2 < 0$, we have

$$\sin\theta_2 = n_1 \sin\theta_1 / n_2 < 0,$$

so θ_2 is negative. We measure the refractive angle from the normal line of the interface to the refractive ray, and define the angle to be positive in the refraction case with $n_1 > 0, n_2 > 0$. Therefore, having a negative θ_2 means that in the negative refraction case the refractive ray falls on the same side of the normal line as the incident ray. Figure 1-3 compares the normal refraction and the negative refraction. In the figure,

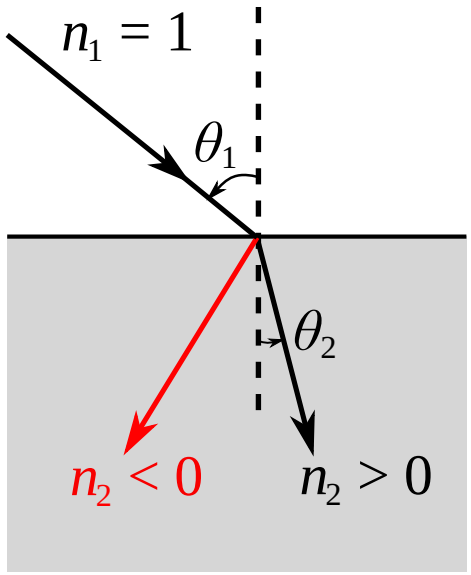

Figure 1-3: Illustration of refraction at the interface of the two media n_1 and n_2. Normal refraction: $n_2 > 0$, negative refraction: $n_2 < 0$.

when the incident ray comes from air or vacuum with $n_1 = 1$ to the interface of the two media n_1 and n_2, normal refraction happens if $n_2 > 0$, and negative refraction happens if $n_2 < 0$.

From the negative refraction phenomenon, the wave propagation direction can be controlled by designing the unit cell of the metamaterial structure for the desired effective refractive index. This feature has found its applications in passive microwave devices, such as cloaking.

Figure 1-4, taken from Ref. [6], is an example of a metamaterial cloak. Figure 1-4 (A) shows the ideal cloaking in simulation. A donut shaped metamaterial is placed outside of the copper cylinder in the center. Without the cloak, the wavefronts are distorted by the copper cylinder itself, as in Fig. 1-4 (C); but with the metamaterial cloak, the wavefronts can remain almost unchanged, as in Fig. 1-4 (A). So looking from the right side, the copper cylinder is close to invisible.

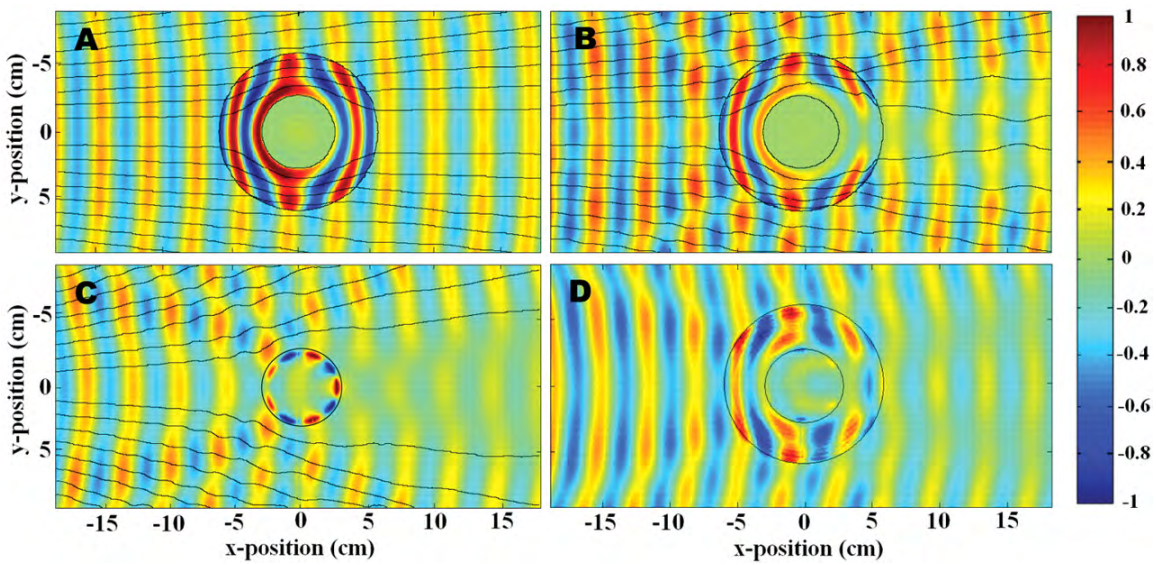

Figure 1-4: Example of a metamaterial cloak in Ref. [6]. The cloak is in the donut shape, and a copper cylinder is in the inner circle. The microwave travels from the left to the right. (A) Simulation of the ideal metamaterial cloak with no absorption loss. (B) Simulation of the real cloak properties with loss. (C) Experiment with only the copper cylinder. (D) Experiment of the cloaked copper cylinder. This figure is cited from Ref. [6].

1.1.3 Reversed Cherenkov Radiation

In the area of active microwave devices with electron beams involved, which is the focus of this thesis, metamaterials show great promise due to the novel phenomenon of the reversed Cherenkov radiation [1, 10–16].

Unlike the Cherenkov radiation in normal materials where the radiated waves travel forward with respect to the beam, in metamaterials with a negative group velocity, the radiated waves travel backward, so the reversed Cherenkov radiation is also called the backward Cherenkov radiation.

Figure 1-5 shows a comparison of the normal Cherenkov radiation in natural materials and the reversed Cherenkov radiation in metamaterials [17]. When the particle beam travels from the left to the right with the speed of v, which exceeds the phase velocity of light in the normal materials, the wave vector and the energy flow of the generated Cherenkov radiation are parallel to each other, and they are both in the forward direction with respect to the beam. However, in metamaterials

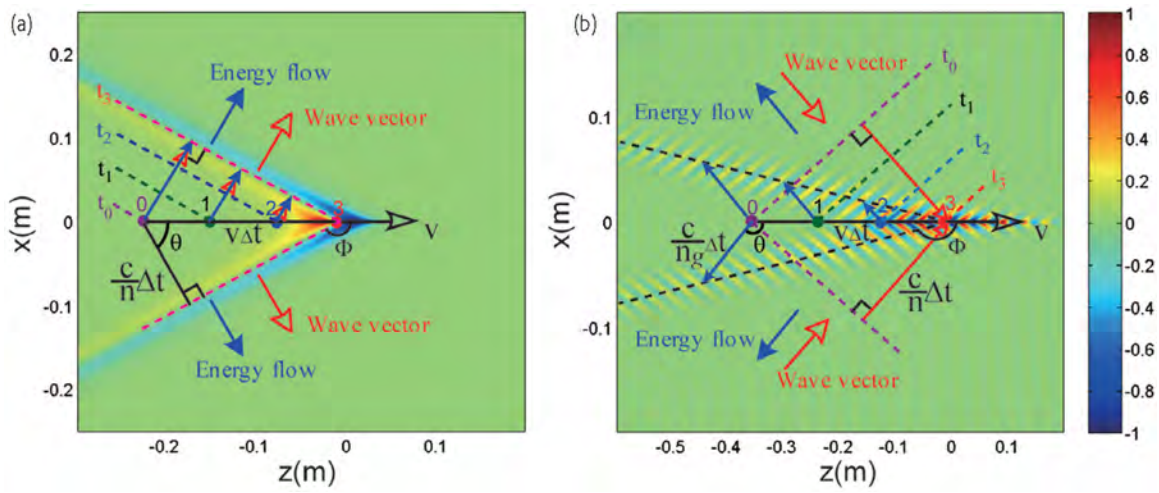

Figure 1-5: Comparison of the normal Cherenkov radiation in natural materials (left) and the reversed Cherenkov radiation in metamaterials (right). In both figures, the particle beam travels from the left to the right with the speed of v. This figure is cited from Ref. [17].

with a negative effective refractive index as shown in the right figure of Fig. 1-5, the wave vector and the energy flow are anti-parallel to each other. This stems from the opposite group velocity and phase velocity in the double-negative metamaterials, as in Eq. (1.11). So in the reversed Cherenkov radiation, the energy flow goes backward while the beam travels forward.

1.2 Wakefield Acceleration

The first topic of this thesis is to study metamaterial structures for wakefield acceleration, so here I will introduce the motivation for high gradient accelerator research in Section 1.2.1. There are two major types of wakefield acceleration, plasma-based acceleration, as will be introduced in Section 1.2.2, and structure-based wakefield acceleration, as will be introduced in Section 1.2.3. Finally, I will name some advantages of metamaterial structures for wakefield acceleration in Section 1.2.4.

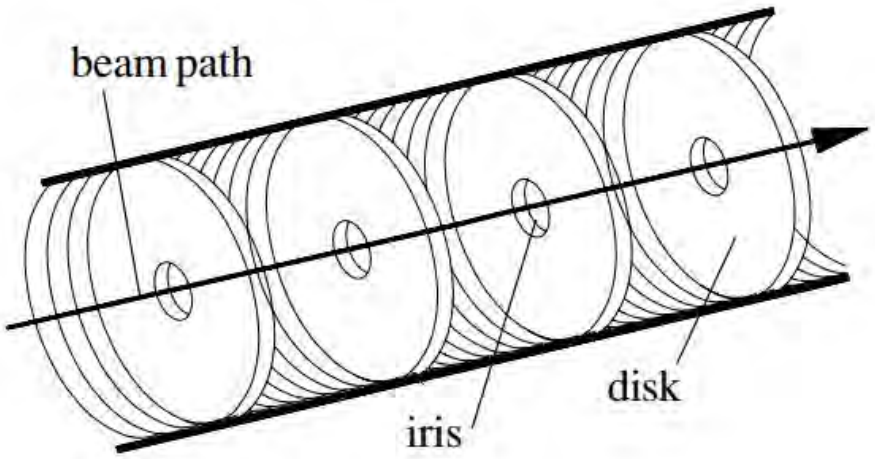

Figure 1-6: Illustration of the periodic disk-loaded waveguide in RF particle accelerators. This figure is cited from Ref. [18].

1.2.1 Motivation for High Gradient Accelerator Research

High energy particle accelerators are crucial to the next big discovery in particle physics. Particle accelerators on the tera-electron-volt (TeV) energy scale can reveal the answers to fundamental particle physics. The Large Hadron Collider (LHC), with a collision energy of 13 TeV in the center-of-mass frame, is the record holder for hadron colliders. The discovery of the Higgs boson is an exciting achievement for the huge machine with a circumference of 27 km, and higher energy beams are desired for the next big discovery.

There is also a pressing need for a TeV scale lepton collider for discovering new physics and complementing the findings of the LHC. Right now, the highest record of lepton energy is held by the Large Electron-Positron Collider at CERN with a collision energy of 209 GeV.

In particle accelerators, the beam energy is equal to the accelerating gradient times the effective accelerating structure length. Therefore, increasing the accelerating gradient is crucial to build the next high energy collider in a compact way.

Conventional high energy accelerators are built by radiofrequency (RF) accelerating cavities. Periodic disk-loaded waveguides are commonly used as accelerating

structures, with the illustration shown in Fig. 1-6.

X-band (with the frequency range of 8 GHz to 12 GHz) accelerator structures have been demonstrated to reach a gradient of 100 MV/m [21–23]. The limiting factor of increasing the accelerator gradient in RF accelerators is the phenomenon of RF breakdown. In an event of an RF breakdown, with the sudden rise of dark current, RF properties like frequency and stored energy are drastically changed [24].

Novel accelerator concepts have been proposed and demonstrated in recent years with the goal of identifying attractive designs for future TeV colliders at the high-energy physics frontier [25,26]. Among these novel concepts, wakefield acceleration is a very promising approach for achieving high accelerating gradient up to the GeV/m level [27–30, 32–41].

Unlike conventional RF accelerator structures, which are driven by high power microwave sources like klystrons, in wakefield acceleration, the energy sources are either particle beams or laser beams, which are called wakefield drivers. Different wakefield drivers, including laser pulses [27–29], electron beams [30–39], positron beams [40], and proton beams [41] have been studied. When the wakefield drivers travel into the acceleration medium, either plasmas or structures in vacuum, the energy is transferred from the drivers into the energy in the electromagnetic field after the drivers, called the 'wake'. Now if a trailing witness beam comes into the system, it can be accelerated by the electric field in the wake.

There are two major types of wakefield acceleration research, plasma-based wakefield acceleration and structure-base wakefield acceleration. The following sections will give an introduction on both types.

This thesis adopts the method of the structure-based wakefield acceleration, as it shows great promise, either in dielectric structures [28–31, 33–35, 37] or metallic structures [36, 38, 39] . Based on these findings, particle colliders up to the tens of TeV level [42–46] and advanced light sources [47, 48] have been proposed.

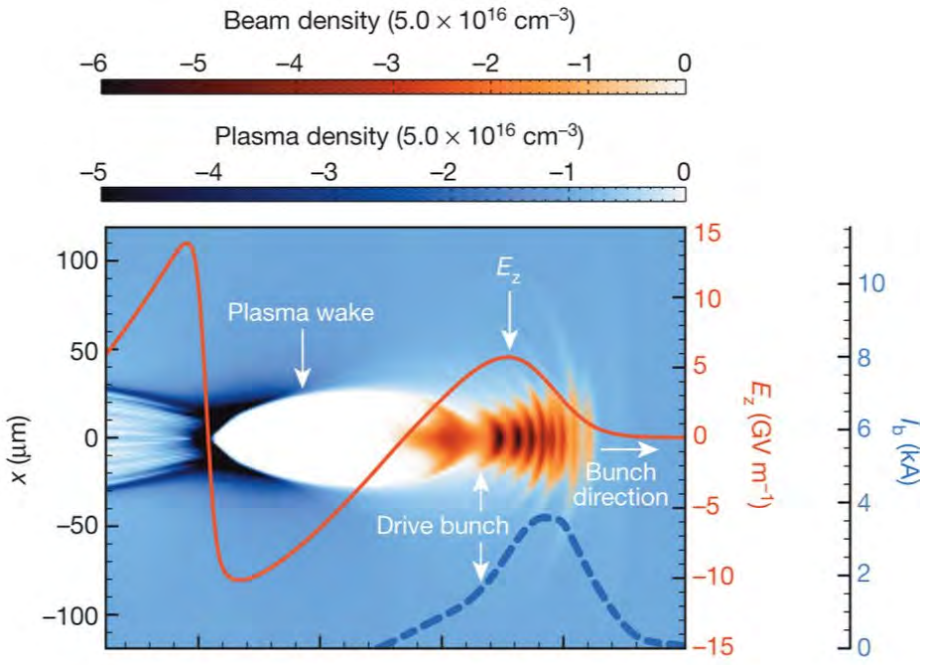

Figure 1-7: Simulation results of the beam-driven plasma wake. This figure is cited from Ref. [50].

1.2.2 Plasma Wakefield Acceleration

Here I will briefly introduce of the process of plasma wakefield acceleration for completeness, though this thesis is focused on structure-based wakefield acceleration.

Plasmas have the potential to sustain an ultra-high accelerating gradient, decided by the wave-breaking limit as [49]

$$E = \frac{m_e c \omega_p}{e}, \tag{1.14}$$

where m_e is the electron mass, $\omega_p = \sqrt{n_e e^2/(\epsilon_0 m_e)}$ is the plasma frequency, and n_e is the electron density in the plasma. From Eq. (1.14), to achieve a gradient of over 1 GeV/m, the plasma density needs to be greater than 10^{14} cm^{-3}.

To excite such a high field, high intensity laser pulses or particle beams are sent into the plasma. Figure 1-7 shows the process of the wakefield generation in the plasma excited by a particle beam. A short driver as the energy source 'blows out'

plasma electrons to create a 'bubble' with almost no plasma electrons inside. Then the displaced electrons rush back to create a region of dense plasma electrons behind the bubble. A high accelerating wakefield (to a trailing electron beam) is thus formed in the latter half of the bubble.

The plasma wakefield acceleration has been demonstrated to be an effective and promising approach to achieve high accelerating gradient beyond GeV/m. There are also some challenges at present, including a large energy spread and a short accelerating distance.

1.2.3 Structure-Based Wakefield Acceleration

The structure-based wakefield acceleration happens in a structure placed in vacuum. The structure can be driven by laser pulses and particle beams. Here we discuss the beam-driven structure-based wakefield acceleration.

In beam-driven, structure-based wakefield acceleration, a high-charge drive beam travels through a structure in vacuum and transfers its energy as a wakefield into a high power radiofrequency (RF) pulse. The extracted RF pulse can be used to accelerate a low-charge witness bunch, either in the same structure (collinear wakefield acceleration regime), or in a different structure (two-beam acceleration regime) [25, 26].

Compared to RF linear accelerators often driven by klystrons [21–23], structure-based wakefield acceleration can have a much shorter RF pulse length to achieve a high accelerating gradient. The reason is that one limiting factor in raising the gradient is the phenomenon of RF breakdown. The physics of RF breakdown has not been thoroughly understood, but an experimental scaling law has been summarized on the influence of accelerating gradient E_a and the RF pulse length t_p on breakdown rate (BDR) as [51]

$$\frac{E_a^{30} \cdot t_p^5}{\mathrm{BDR}} = \text{constant} \tag{1.15}$$

The breakdown rate is the probability of a breakdown event during an RF pulse and often in the unit of breakdowns per pulse per meter. From the scaling law in

Eq. (1.15), we know that at a given BDR, the gradient scales with the RF pulse length as

$$E_a \propto t_p^{-1/6} \tag{1.16}$$

This indicates that operating at short RF pulses can help increase the accelerating gradient, so the structure-based wakefield acceleration is promising to achieve higher gradient.

Now I'll introduce collinear wakefield acceleration and two-beam acceleration.

Collinear Wakefield Acceleration

In the structure-based collinear wakefield acceleration, the drive beam and the witness beam travel in the same wakefield structure. An illustration is shown in Fig. 1-8.

When the drive beam enters the structure, it radiates into the wakefield of the structure and gets decelerated. Then a trailing witness beam enters, and if the timing is correct, the witness beam can be synchronized to the accelerating spot in the generated wakefield and experience a high accelerating gradient.

The advantages of the collinear regime include: (1) Only one wakefield structure is needed; (2) The RF power can be transferred directly from the drive beam to the witness beam without RF couplers. The RF coupling at high frequencies is challenging, so in THz frequencies, the collinear regime is always used.

Two-beam Acceleration

In the structure-based two-beam acceleration, the drive beam and the witness beam travel in two different structures. An illustration is shown in Fig. 1-9. The extracted wakefield power from the drive beam is coupled to the separate witness beam line through RF couplers.

The advantages of the two-beam acceleration include: (1) The power extractor structure on the drive beam line and the accelerator structure on the witness beam line can be optimized independently. The power extractor structure often has a relatively large beam aperture to transmit a high charge drive beam for a high extracted power,

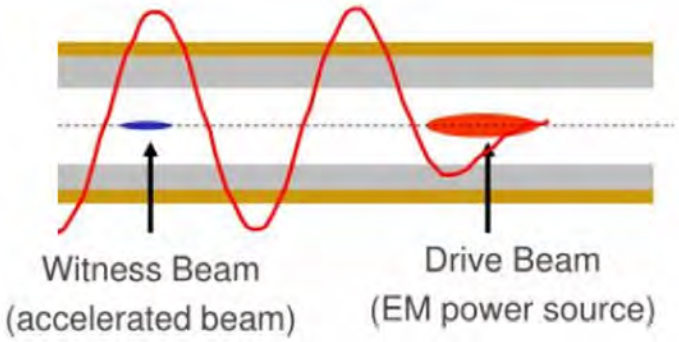

Figure 1-8: Illustration of the structure-based collinear wakefield acceleration. The drive beam and the witness beam travel in the same wakefield structure. Figure credit: Argonne Wakefield Accelerator Facility website [52].

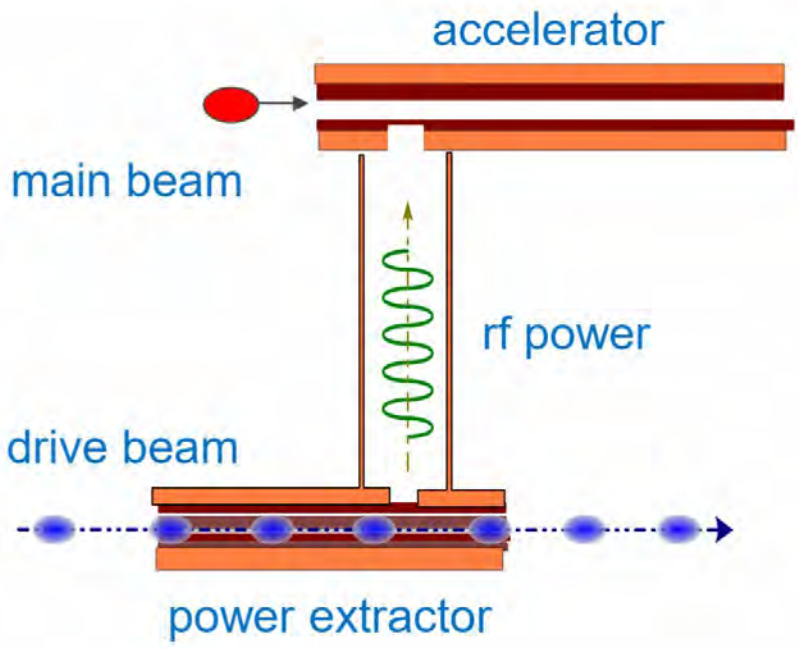

Figure 1-9: Illustration of the structure-based two-beam acceleration. The drive beam and the witness beam travel in two separate wakefield structures. Figure credit: Argonne Wakefield Accelerator Facility website [52].

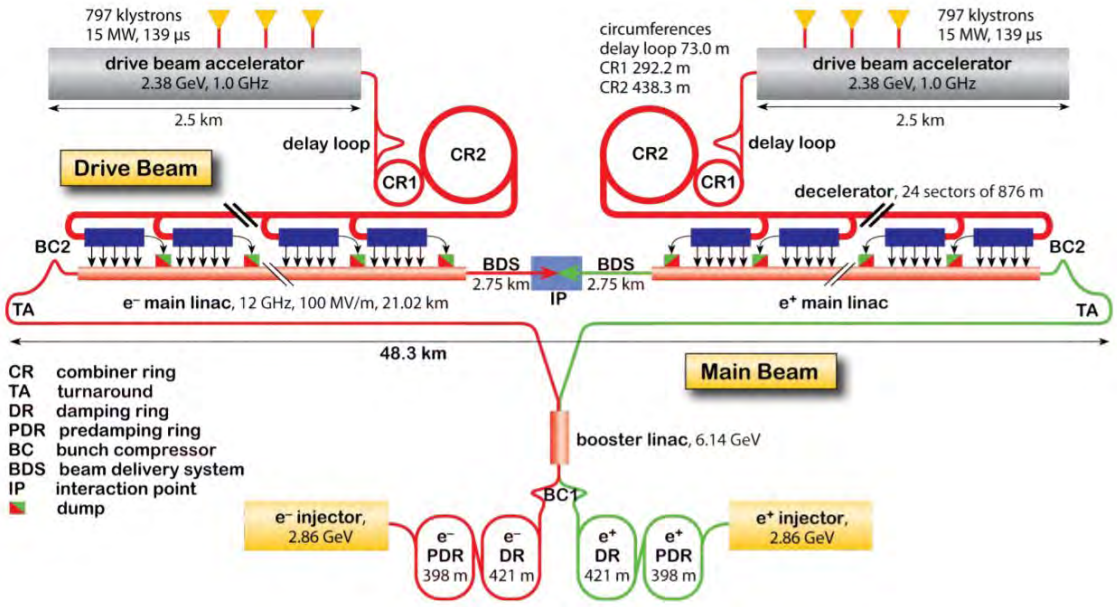

Figure 1-10: Layout of the CLIC 3 TeV collider design based on two-beam acceleration. This figure is cited from the CLIC design report [46].

while the accelerator structure often has a small beam aperture to achieve a high accelerating gradient. (2) The beam optics can be designed independently for the drive beam and the witness beam. It could be challenging in the collinear regime to use the same set of beamline components for the drive beam and the witness beam with very different charge. (3) The two-beam setup allows for staging [36], which refers to the use of sequential accelerator modules on the witness beamline.

The Compact Linear Collider (CLIC) at CERN is a proposed electron-position collider based on two-beam acceleration working at X-band (12 GHz). Figure 1-10 shows the layout of the CLIC conceptual design. The design goal is a 3 TeV collision energy.

In the CLIC design, there are 24 sectors of decelerator structures, which are fed with drive bunch trains. The drive beam is generated in a 1 GHz RF accelerator with an energy of 2.38 GeV. Power is extracted from the drive bunch trains by power extraction and transfer structures (PETS) to the main beamline. The pulse length is limited to 150 ns to lower the breakdown rate. The main beam line has a design

frequency of 12 GHz, with a nominal accelerating gradient of 100 MV/m. This gradient has already been demonstrated to work well in metallic disk-loaded structures at CERN with a low breakdown rate of 10^{-7}/pulse/m.

In the US, the major facility that devotes to structure-based wakefield acceleration is the Argonne Wakefield Accelerator (AWA) at the Argonne National Laboratory. The AWA group also has a two-beam accelerator design with dielectric structures at 26 GHz, and the targeted gradient is 350 MV/m due to the short pulse length of 20 ns [53].

The experiment in this thesis on metamaterial structures for wakefield acceleration was carried out at the AWA facility. The details of the experimental facilities will be presented later in Chapter 3.

1.2.4 Advantages of Metamaterial Structures for Wakefield Acceleration

A metamaterial structure has numerous potential advantages for particle-beam driven, structure-based wakefield acceleration.

First, the metamaterial structure is inherently a subwavelength interaction space so that the shunt impedance is increased and the generated fields are highly concentrated at the witness bunch.

Second, the metallic metamaterial structure is simple and rugged.

Third, the metamaterial structure with a large parameter space presents a new direction of engineered structures, opening the path to more precise control of the electromagnetic properties. The accelerating performance of a metamaterial structure can be optimized in various ways such as increasing the group velocity to shorten the pulse length for reduction of RF breakdowns; increasing the shunt impedance to improve the energy efficiency; and suppressing the harmful higher order modes.

As a first step to demonstrate the potential of metamaterial structures for wakefield acceleration, I will present in this thesis the first results on high power microwave wakefield generation by a drive bunch in a simple, rugged metamaterial structure,

named the 'wagon wheel' structure, with 80 MW of peak power achieved at 11.4 GHz from a pair of drive bunches.

1.3 High Power Microwave Generation

High power microwave sources [54] are active devices where energy is transferred from a DC electron beam to the microwave energy inside vacuum tubes. Based on whether there is an input microwave signal, the high power microwave devices can be divided into oscillators, when there is no input signal, and amplifiers, where there is an input signal which can be amplified by the use of the electron beams.

In Section 1.3.1 I will introduce the metamaterial-based microwave sources, and in Section 1.3.2 I will present the physics of the stimulated Cherenkov radiation as the theoretical basis for high power microwave generation.

1.3.1 Metamaterial-Based Microwave Sources

This thesis studies the application of metamaterial structures in the oscillator type of devices. The illustration of such a device is shown in Fig. 1-11. A DC electron beam is emitted from the cathode of an electron gun and then goes into the interaction region with a metamaterial circuit. There are solenoid magnets to guide the electron beam with a DC longitudinal magnetic field for focusing. Since the metamaterial structure has a negative group velocity with the generated waves traveling backwards, the output power is coupled out from the electron gun end. It is also possible to reflect the backward waves at the electron gun end so that they propagate to the collector end, where it is sometimes more convenient to couple out the generated power. This is the approach used in our research.

In the microwave sources operating with a traveling wave mode, like traveling wave tubes and backward wave oscillators (including the device shown in Fig. 1-11), the high power microwaves are generated by the mechanism of stimulated Cherenkov radiation [55] of the electron beam. The physics of this phenomenon will be introduced in the following section.

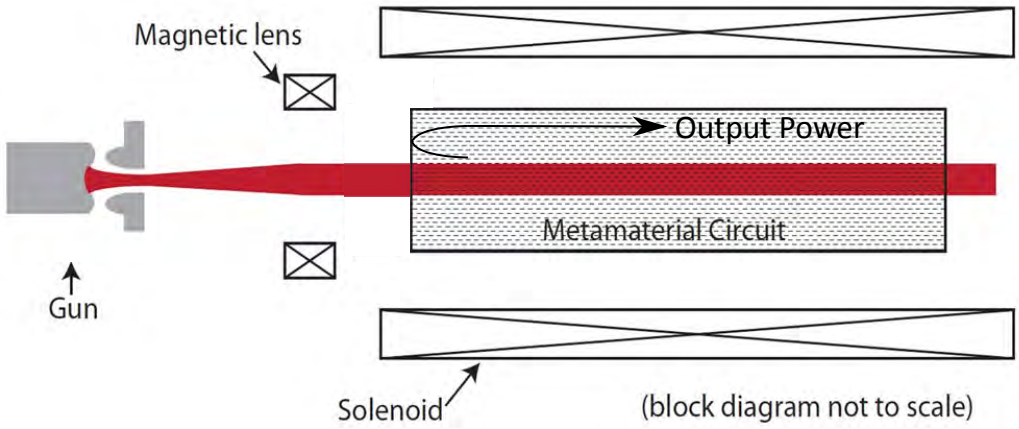

Figure 1-11: Illustration of a metamaterial-based backward wave oscillator. This figure is cited from Ref. [19].

1.3.2 Stimulated Cherenkov Radiation

Cherenkov radiation, as the radiation by a charged particle moving faster than light in a medium, has been discussed briefly in Section 1.1.3 earlier in this chapter. The spontaneous radiation from each individual moving particle is incoherent, as in the case of a single particle traveling fast enough in water.

Now if the electron beam is sent in a slow-wave structure, such as a dielectric tube, which supports an electromagnetic wave whose phase velocity is synchronized to the beam velocity, the DC electron beam can get bunched and radiate power by the stimulated Cherenkov radiation coherently.

Here we look at how the Cherenkov radiation of a magnetized electron beam in a medium with a relative permittivity ϵ_r can lead to a Cherenkov gain in a plane wave [55].

The electron beam propagates at a speed of v_0 in the z direction along the magnetic axis of a strong DC magnetic field $\vec{B}_0$. We assume the current and velocity modulation happens only in the z direction from the strong focusing magnetic field. Suppose the plane wave again has a temporal and spatial dependence of $\exp(ikz - i\omega t)$, where k is the longitudinal wavenumber. We consider the wave propagating at angle to the beam, with a transverse wavenumber p. So the uncoupled dispersion relation in the

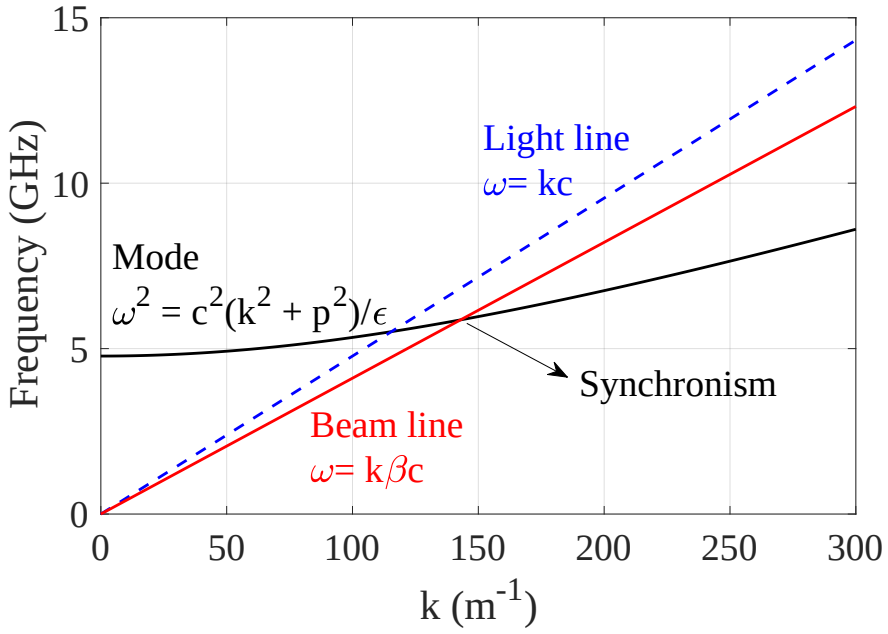

Figure 1-12: Dispersion diagram showing the synchronism of the uncoupled dispersion with the beam dispersion. The vertical axis plots the frequency as $\omega/2\pi$, and the horizontal axis plots the longitudinal wavenumber k. Here the transverse wavenumber p is set as constant and $p = 200$ m^{-1}, the permittivity is set as $\epsilon = 2$.

system is

$$\omega^2 = (k^2 + p^2)c^2/\epsilon. \tag{1.17}$$

This dispersion relation can intersect with the electron beam line of $\omega = k\beta c$, so the synchronism condition between the wave and the beam can be found.

Figure 1-12 illustrates the synchronism of the uncoupled dispersion with the beam line, where the transverse wavenumber p is set as constant and $p = 200$ m^{-1}, and the permittivity is set as $\epsilon = 2$. Such a diagram plotting the frequency $\omega/2\pi$ vs. the longitudinal wavenumber k is called a dispersion diagram. Dispersion diagrams will be used frequently later in this thesis for analyzing the interaction of electron beams with slow wave structures.

Now we calculate the modulation as a small perturbation in the system. The first order velocity modulation v_{z1}, electron density modulation n_1, and the current density modulation J_{z1} can be calculated from the continuity condition $\partial n/\partial t + \nabla \cdot (n\boldsymbol{v}) = 0$

and the equation of motion $dp_z/dt = -eE_z$. The results of the modulation terms are:

$$\begin{aligned} v_{z1} &= -(ie/m\gamma^3)E_z/(\omega - kv_0), \\ n_1 &= \frac{n_0 k v_{z1}}{\omega - kv_0} \\ &= -\frac{ien_0}{m\gamma^3}\frac{kE_z}{(\omega - kv_0)^2}, \\ J_{z1} &= -n_0 e v_1 - n_1 e v_0 \\ &= \frac{i\epsilon_0\omega_p^2}{\gamma^3}\frac{\omega E_z}{(\omega - kv_0)^2}, \end{aligned} \tag{1.18}$$

where n_0 is the unperturbed electron density in the beam, γ is the Lorentz factor of the electron beam traveling at the unperturbed velocity v_0, and $\omega_p = \sqrt{n_0 e^2/\epsilon_0 m}$ is the plasma frequency.

If we combine Eq. (1.18) with the Maxwell's equations, we derive the dispersion relation as

$$\frac{\omega^2\epsilon}{c^2} - k^2 - p^2 - \frac{\omega_p^2}{\epsilon\gamma^3}\frac{(\omega^2\epsilon/c^2 - k^2)}{(\omega - kv_0)^2} = 0 \tag{1.19}$$

This is the coupled dispersion, with the presence of the electron beam taken into consideration.

Next we look at the Cherenkov gain. By plugging the uncoupled dispersion relation Eq. (1.17) into Eq. (1.19), we have

$$(\omega - kv_0)^3(\omega + kv_0) = \frac{\omega_p^2}{\epsilon\gamma^3}\omega^2\left(1 - \frac{1}{\beta^2\epsilon}\right) \tag{1.20}$$

Near the synchronism condition of $\omega \approx kv_0$, there is

$$(\omega - kv_0)^3 = \frac{\omega_p^2}{2\epsilon\gamma^3}\omega\left(1 - \frac{1}{\beta^2\epsilon}\right) \tag{1.21}$$

From the dependence of $\exp(ikz - i\omega t)$, the Cherenkov gain can be found when the imaginary part of k is nonzero. Equation (1.21) can have such solutions of k under the condition of

$$\beta > \sqrt{\frac{1}{\epsilon}}. \tag{1.22}$$

The one real roots and two complex roots are as follows:

$$\begin{aligned} \omega - kv_0 &= \left[\frac{\omega_p^2}{2\epsilon\gamma^3}\omega\left(1-\frac{1}{\beta^2\epsilon}\right)\right]^{1/3} \\ \omega - kv_0 &= \left[\frac{\omega_p^2}{2\epsilon\gamma^3}\omega\left(1-\frac{1}{\beta^2\epsilon}\right)\right]^{1/3}\frac{1\pm i\sqrt{3}}{2} \end{aligned} \tag{1.23}$$

We define the spatial growth rate *alpha* from the imaginary part of k as $\alpha = \mathrm{Im}(k)$, and from Eq. (1.23) α can be expressed as

$$\alpha = \frac{\sqrt{3}}{2}\left(\frac{\omega_p^2\omega}{2\epsilon\gamma^3}\right)^{1/3}\frac{(1-1/\beta^2\epsilon)^{1/3}}{c\beta} \tag{1.24}$$

From here, it is shown that the stimulated Cherenkov radiation can be applied to the generation of high power microwaves in a slow wave structure with a dispersion curve which can intersect with the electron beam line under the Cherenkov radiation condition of Eq. (1.22).

1.4 Thesis Outline

In this thesis, I will discuss two topics: metamaterial structures for wakefield acceleration and metamaterial structures for high power microwave sources. Under both topics, theoretical and experimental studies will be presented.

Chapter 2 will present theoretical studies on metamaterial structures for wakefield acceleration, with the following metamaterial structures studied: the subwavelength circular deep corrugation structure, the 'wagon wheel' structure, the volumetric 3D metamaterial structure, and the elliptical deep corrugation structure. Among them, the 'wagon wheel' structure design has led to the experiment at AWA.

Chapter 3 will present experimental studies on the 'wagon wheel' structure for wakefield acceleration. The experimental facilities at AWA, the structure fabrication and assembly, and the experimental results will be presented in Chapter 3. The major achievement in this experiment is the generation of 80 MW of X-band microwave power in a 2 ns pulse when the 'wagon wheel' structure is excited by a pair of 65 MeV

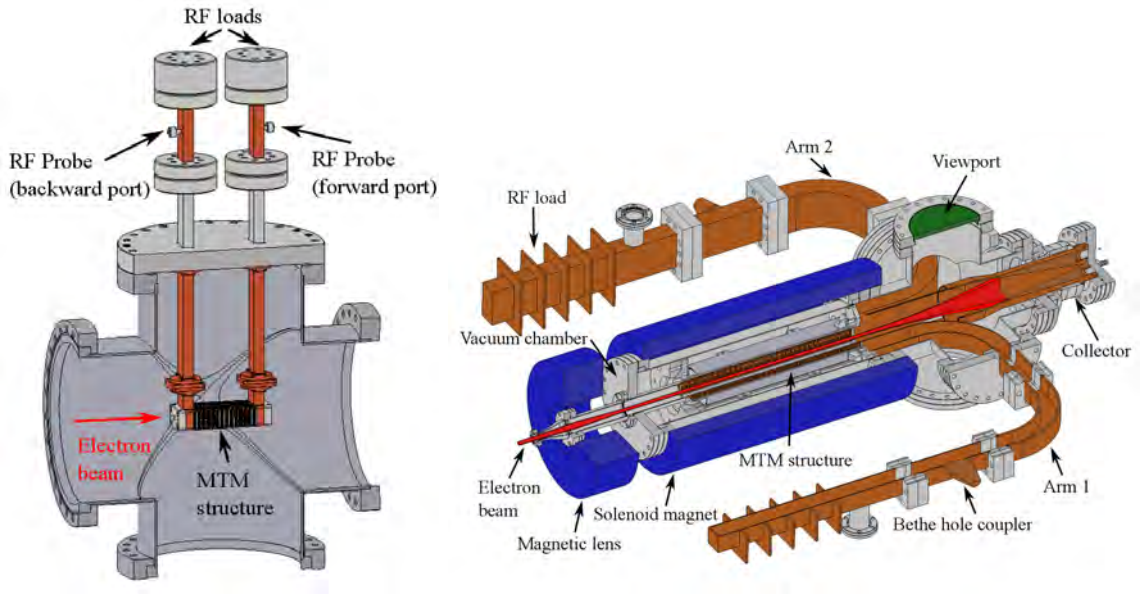

(a) (b)

Figure 1-13: Snapshots of the two major experiments in this thesis. (a) Experimental setup of a metamaterial structure for wakefield acceleration at AWA. (b) Experimental setup of a metamaterial-based high power microwave source at MIT.

drive bunches with a total charge of 85 nC. A snapshot of this experiment is shown in Fig. 1-13a.

Chapter 4 will present theoretical studies on metamaterial structures for high power microwaves, including an analytical study on the Cherenkov-cyclotron instability in a metamaterial-loaded waveguide, and a design by simulation on a metamaterial-based high power microwave source working with a 490 kV, 84 A electron beam.

Chapter 5 will present the experimental studies on metamaterial structures for high power microwave generation. The experiment was built in-house at MIT. The major achievement in this experiment is the generation of 2.9 MW of S-band microwave power in a 1μs pulse when the metamaterial-loaded waveguide with reverse symmetry is excited by a 1 μs electron beam of up to 490 kV and 84 A. A snapshot of this experiment is shown in Fig. 1-13b.

Chapter 6 will summarize the achievements in this thesis, and propose future plans to continue the work.

Chapter 2

Theory of Metamaterial Structures for Wakefield Acceleration

This chapter presents the theory of several metamaterial structures designed for wakefield acceleration, including: (1) theory of a circular deep corrugation structure; (2) theory of a wagon wheel metamaterial structure, which leads to an experiment as will be described in Chapter 3; (3) theory of a volumetric 3D metamaterial structure; (4) theory of an elliptical deep corrugation structure.

2.1 Motivation

Structure-based wakefield acceleration operating at a short microwave pulse length is promising for achieving high accelerating gradient [28–30, 33–37, 39]. Dielectric structures [28–30,33,35,37] are easy to fabricate and can make a compact accelerator, but they are susceptible to beam damage when beam collision happens. A metallic structure in vacuum for wakefield acceleration may be attractive because it is stable and less susceptible to beam damage. Metallic metamaterial structures not only have the advantage of being simple and rugged from the all-metal design, but also show great possibilities to optimize in the huge parameter space of the unit cell design.

In the later sections, we explore the theory and design of several metallic metamaterial structures for wakefield acceleration.

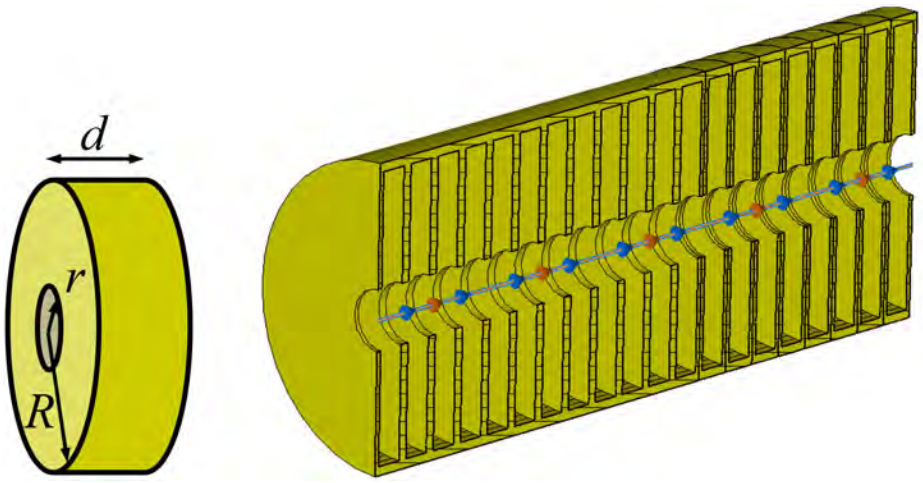

Figure 2-1: Illustration of a subwavelength circular deep corrugation structure. Left: a single cavity. Right: full multi-cell structure.

2.2 Theory of Circular Deep Corrugation Structure

2.2.1 Design of the Circular Deep Corrugation Structure

The deep corrugation structure is an array of metallic subwavelength cylindrical cavities, as in Fig. 2-1. It is different from the conventional corrugated waveguide structure in the way that the corrugation depth is larger than the iris radius, and the period is much smaller than the wavelength. With the deep corrugation design, the iris part is generally below the cut-off frequencies of the cavity modes. The cell-to-cell coupling through the beam holes is not allowed in the deep corrugation structure.

Two methods of analysis are adopted to study the wakefield in such a structure excited by a short electron bunch. The first one is the analytical method to calculate the wakefield in a single cavity, and the second one is the numerical method to simulate the wakefield in a multi-cell structure with the numerical codes in the CST Particle Studio [56].

2.2.2 Analytical Theory

The circular deep corrugation structure is a single cylindrical cavity with a radius R and a length d. We are interested in the case where d is much smaller than the microwave wavelength. In the simplified case, we assume the beam aperture r is much smaller than the cavity radius R, and the iris thickness is also ignored.

The electron beam used for wakefield excitation in the circular deep corrugation structure is a Gaussian bunch with a charge Q (the minus sign for electrons included) and an rms length of σ_z moving at a constant speed of v_0 along the axis in the z direction with $x = y = 0$.

We first consider calculate the wakefield excited by a single point charge with a charge Q, so the current distribution in the z direction is

$$J_z(\vec{r}, t) = \frac{Qv_0}{2\pi r}\delta(r)\delta(z - v_0 t). \tag{2.1}$$

The longitudinal component of the magnetic vector potential $A_z(\vec{r}, t)$ satisfies

$$\left[\frac{1}{r}\frac{\partial}{\partial r}r\frac{1}{\partial r} + \frac{\partial^2}{\partial z^2} - \frac{1}{c^2}\frac{\partial^2}{\partial t^2}\right] A_z(r, z, t) = -\mu_0 J_z(r, z, t). \tag{2.2}$$

At the same time, the boundary condition in the cavity gives

$$A_z(r, z, t) = \sum_{s=1,n=0}^{\infty} A_{s,n}(t) J_0\left(p_s \frac{r}{R}\right) \cos\left(\frac{\pi n}{d} z\right) \tag{2.3}$$

where p_s is the sth zero of the J_0 Bessel function.

We can plug Eq. 2.3 into 2.2 to calculate $A_{s,n}(t)$. Note that $A_{s,n}(t)$ needs to be calculated under three different circumstances: before the bunch enters the cavity, when the bunch is still in the cavity, and when the bunch leaves the cavity with a length d. If we assume the bunch enters the cavity at the time of $t = 0$, and the

velocity change of the bunch is neglected, then we have the expressions for $A_{s,n}(t)$ as:

$$A_{s,n}(t<0)=0, \tag{2.4}$$

$$A_{s,n}(0<t<\frac{d}{v_0})=\alpha_{s,n}\left[\cos(\omega_n t)-\cos(\Omega_{s,n}t)\right], \tag{2.5}$$

$$A_{s,n}(t>\frac{d}{v_0})=\alpha_{s,n}\left[(-1)^n-\cos\left(\Omega_{s,n}\frac{d}{v_0}\right)\right]\cos\left[\Omega_{s,n}\left(t-\frac{d}{v_0}\right)\right]$$
$$+\alpha_{s,n}\sin\left(\Omega_{s,n}\frac{d}{v_0}\right)\sin\left[\Omega_{s,n}\left(t-\frac{d}{v_0}\right)\right], \tag{2.6}$$

where

$$\omega_n=\frac{\pi n}{d}v_0,$$

$$\Omega_{s,n}=c\sqrt{\left(\frac{p_s}{R}\right)^2+\left(\frac{\pi n}{d}\right)^2},$$

$$\alpha_{s,n}=\frac{Qv_0}{\pi\epsilon_0 g_n d}\frac{1}{R^2J_1^2(p_s)}\frac{1}{\Omega_{s,n}^2-\omega_n^2},$$

and

$$g_n=\begin{cases}1, \text{ for } n=0\\ 0.5, \text{otherwise.}\end{cases}$$

Here ω_n is the wave-beam interaction frequency, and $\Omega_{s,n}$ is the eigenfrequency of the cavity TM_{0sn} mode.

Then the longitudinal electric field E_z can be derived from the relation

$$E_z(\vec{r},t)=-c^2\int dt\frac{1}{r}\frac{\partial}{\partial r}r\frac{\partial}{\partial r}A_z(\vec{r},t), \tag{2.7}$$

and the expressions for E_z when the bunch is still in the cavity and when the bunch

leaves the cavity are as follows:

$$E_z(r,z,0<t<\frac{d}{v_0}) = \sum_{s=1,n=0}^{\infty} \alpha_{s,n}\left(\frac{cp_s}{R}\right)^2 J_0\left(p_s\frac{r}{R}\right)\cos\left(\frac{\pi n}{d}z\right) \cdot\left[\frac{\sin(\omega_n t)}{\omega_n}-\frac{\sin(\Omega_{s,n}t)}{\Omega_{s,n}}\right] \tag{2.8}$$

$$E_z(r,z,t>\frac{d}{v_0}) = \sum_{s=1,n=0}^{\infty} \alpha_{s,n}\left(\frac{cp_s}{R}\right)^2 J_0\left(p_s\frac{r}{R}\right)\cos\left(\frac{\pi n}{d}z\right) \cdot\left[(-1)^n\frac{\sin\left[\Omega_{s,n}\left(t-\frac{d}{v_0}\right)\right]}{\Omega_{s,n}}-\frac{\sin(\Omega_{s,n}t)}{\Omega_{s,n}}\right] \tag{2.9}$$

The energy loss W of the point charge is calculated as the time integral of E_z at the charge location, and the result is

$$W = \frac{Q^2v_0^2}{4\pi\epsilon_0c^2d}\sum_{s=1,n=1}^{\infty}\left[\frac{2p_s}{J_1(p_s)}\right]^2\frac{1}{g_n\left[p_s^2+(\pi nR/\gamma d)^2\right]^2} \cdot\left[1-(-1)^n\cos\left(\frac{\Omega_{s,n}}{v_0}d\right)\right] \tag{2.10}$$

Next we consider a Gaussian bunch with the rms length of σ_z. The wakefield calculated for the point charge above can be used as the Green's function.

We introduce the form factor as a function of ω_n and σ_z,

$$F(\omega_n,\sigma_z) = \exp\left(-\frac{\omega_n^2\sigma_z^2}{2c^2}\right) \tag{2.11}$$

When the beam is in the cavity, both the cavity eigenfrequency $\Omega_{s,n}$ and the wave-beam interaction frequency ω_n are excited, so the spectrum is more complicated; but when the beam is out of the cavity, only the cavity eigenfrequency $\Omega_{s,n}$ stays. So we can rewrite the field when $t > d/v_0$ in Eq. (2.9) as a summation of contributions from frequencies $\Omega_{s,n}$, as follows

$$E_z(r,z,t) = \sum_{s=1,n=1}^{\infty} E_{s,n}(r,z,t,\Omega_{s,n}) \tag{2.12}$$

Then a simple relation holds between the wakefield excited by a point charge E_z and by a Gaussian bunch $E_{z,g}$,

$$E_{z,g}(r,z,t>\frac{d}{v_0}) = \sum_{s=1,n=1}^{\infty} E_{s,n}(r,z,t,\Omega_{s,n})F(\Omega_{s,n},\sigma_z) \tag{2.13}$$

We will later use the analytical expression in Eq. (2.13) to calculate the wakefield to benchmark with numerical simulations, as will be presented in the following section.

2.2.3 Numerical Simulation of a Multi-Cell Structure

The CST Particle Studio Wakefield Solver is used to simulate the wakefield in the multi-cell circular deep corrugation structure when it is excited by a short relativistic electron bunch.

Figure 2-2 shows the longitudinal electric field on the middle cutting plane with a bouncing field pattern observed. The pattern is formed when the drive bunch initially excites a decelerating wake (in red) after it. The decelerating wake travels outward and bounces at the metal wall with a 180-degree phase shift, transforming into an accelerating wake (in blue). The accelerating wake then travels inward and is focused at the beam axis. A following witness bunch can be placed at the refocusing location in blue to be accelerated.

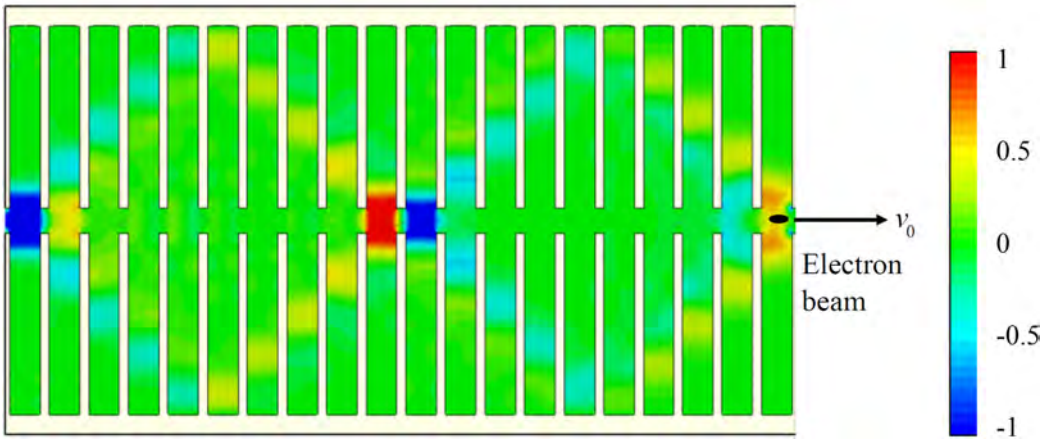

Figure 2-2: Longitudinal electric field E_z plot on the linear scale in the circular deep corrugation structure driven by an electron beam. Red: decelerating for a trailing electron beam, blue: accelerating for a trailing electron beam.

Table 2.1: Nominal design of the circular deep corrugation structure.

Cavity radius R (mm)	Cavity length d (mm)	Beam hole radius r (mm)
8	2	0.1

Bunch length σ_z (mm)	Energy (MeV)	Charge (nC)
1	70	10

2.2.4 Benchmarking

In order to benchmark the analytical theory with the numerical simulation, a single cavity with a radius of $R = 8$ mm and a cavity length of $d = 2$ mm is simulated in the CST Wakefield Solver. A valid CST run must have a finite-size beam hole to allow the beam to pass through, so a small beam hole with a radius of $r = 0.1$ mm is added in the CST runs.

In both the analytical theory and the CST simulation, a 70 MeV Gaussian bunch with a total charge of 10 nC and an rms length $\sigma_z = 1$ mm is used to excite the structure. See a summary of the structure and beam parameters in Table 2.1.

Figure 2-3 shows the comparison of the longitudinal wakefield results by the analytical theory and the CST simulations. The agreement is very good. Note that here $E_z > 0$ corresponds to the decelerating zone for a witness electron bunch, and $E_z < 0$ corresponds to the accelerating zone.

The highest accelerating gradient for the analytical calculation and the CST simulation are 132.7 MV/m (or 13.27 MV/m/nC) and 129.0 MV/m (or 12.90 MV/m/nC), respectively. One reason for the slight difference is that the structure in the CST simulation has a 0.1 mm beam hole, while the beam hole is infinitely small in the analytical theory. Another reason is that in the CST run a frequency range must be defined from the meshing process. The upper frequency limit is defined as 120 GHz, so the CST simulation might miss some amount of microwave power in the frequency range

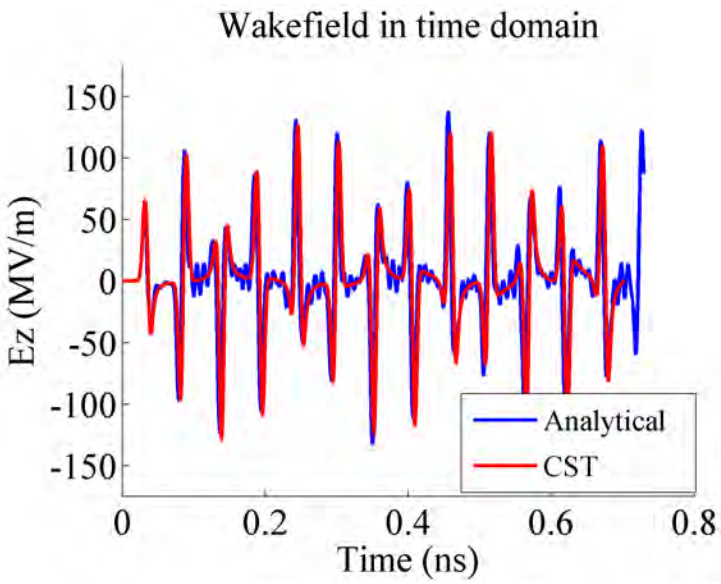

Figure 2-3: Longitudinal wakefield in the time domain when the circular deep corrugation structure is excited by a 70 MeV Gaussian bunch with a total charge of 10 nC and an rms length $\sigma_z = 1$ mm. The analytical theory is benchmared with the CST simulation.

beyond 120 GHz.

The comparison of the frequency domain wake spectrum is shown in Fig. 2-4, with a good agreement. The CST definition of wake impedance is different from the 'standard' definition, as in Eq. 2.14 and Eq. 2.15 respectively.

$$Z_z(\omega)|_{\text{CST}} = \frac{\int_{-\infty}^{\infty} V_z(s) \exp(-i\omega s) ds}{\int_{-\infty}^{\infty} \lambda(s) \exp(-i\omega s) ds} \tag{2.14}$$

$$Z_z(\omega)|_{\text{standard}} = \int_{-\infty}^{\infty} V_z(s) \exp(-i\omega s) ds \tag{2.15}$$

where Z_z stands for the longitudinal wake impedance, V_z for the longitudinal wake potential, $\lambda(s)$ for the charge distribution function.

The difference means that the CST wake impedance is evaluating the field strength at a given frequency assuming that this field is excited by a point charge. It is a quantity characterizing only the structure. However, in the standard definition, we take into account the bunch distribution spectrum in the frequency domain.

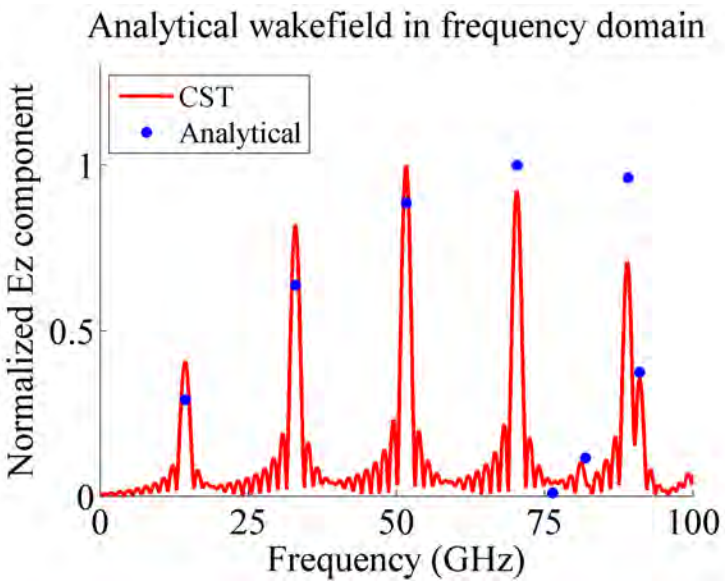

Figure 2-4: Longitudinal wakefield in the frequency domain when the circular deep corrugation structure is excited by a 70 MeV Gaussian bunch with a total charge of 10 nC and an rms length $\sigma_z = 1$ mm. The analytical theory is benchmared with the CST simulation.

The results in Fig. 2-4 are presented by the CST definition. In the following section, we will go back to the standard definition when a wake spectrum is shown.

2.2.5 Scaling Study

This section will present the scaling study of the structure gradient with various structure and beam parameters, including the cavity radius R, the cavity length d, the beam hole radius r, the Gaussian bunch rms length σ_z, the bunch energy E_0 and the bunch charge Q.

In the scaling study, when one of these parameters is varied, all the other parameters are kept fixed as the default values, as listed in the nominal design parameters in Table 2.1.

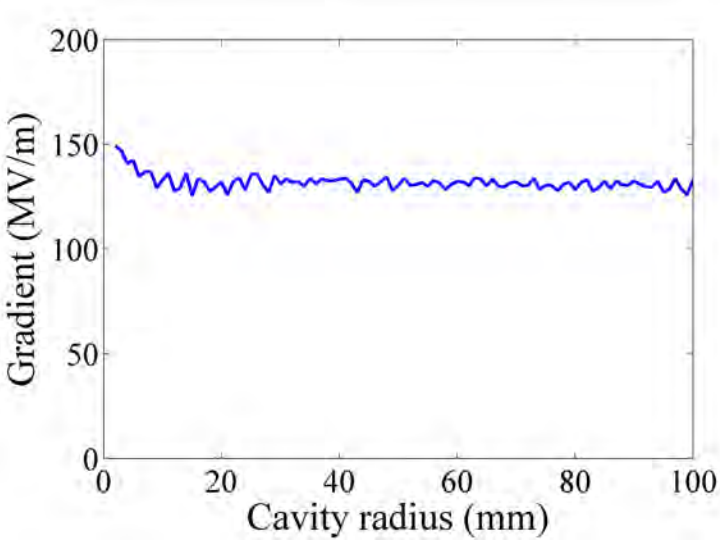

Figure 2-5: Scaling of the gradient in the circular deep corrugation structure with the cavity radius R.

Cavity Radius R

An interesting conclusion is that the cavity radius R does not affect the accelerating gradient, as is shown in Fig. 2-5. The pictorial explanation is that when the radius R is changed, from the bouncing wakefield pattern, the interval between two accelerating or decelerating peaks is changed, but the wakefield still gets focused right on the beam axis to maintain the same total gradient.

To explain the difference of the small radius R case with the large radius R case, here I present two examples with $R = 2$ mm and $R = 20$ mm, respectively, as in Fig. 2-6 for the $R = 2$ mm case and in Fig. 2-7 for the $R = 20$ mm case.

When R is very small as 2 mm, from the frequency spectrum in Fig.2-6b, we can see that the cavity eigenmodes have high frequencies. With a moderate bunch length of $\sigma_z = 1$ mm, the frequency spectrum from the current Gaussian distribution can merely just excite the TM_{010} mode. So the structure with $R = 2$ mm operates almost in the single-frequency regime.

When R gets larger as 20 mm, from the frequency spectrum in Fig.2-7b, we can see that the cavity eigenmodes have lower frequencies. So the structure now turns to

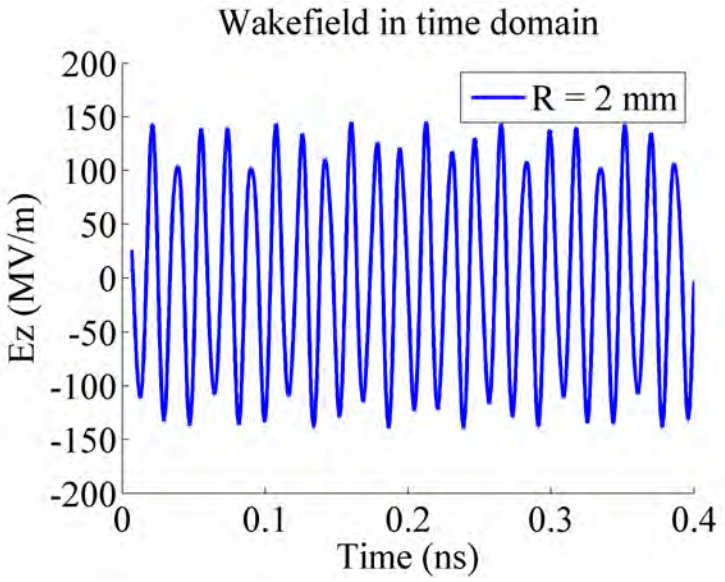

(a)

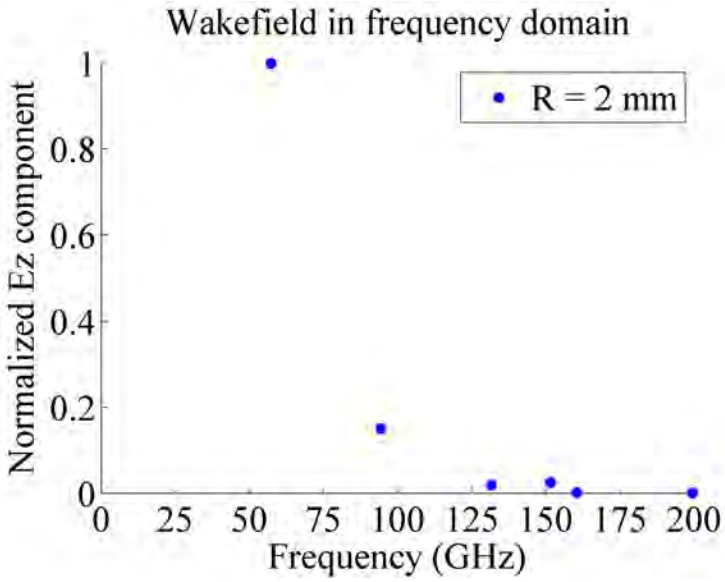

(b)

Figure 2-6: Longitudinal wakefield in (a) the time domain, and (b) the frequency domain when the cavity radius $R = 2$ mm, and all the other parameters are fixed as in the nominal design. In this case, the structure operates almost in the single-frequency regime.

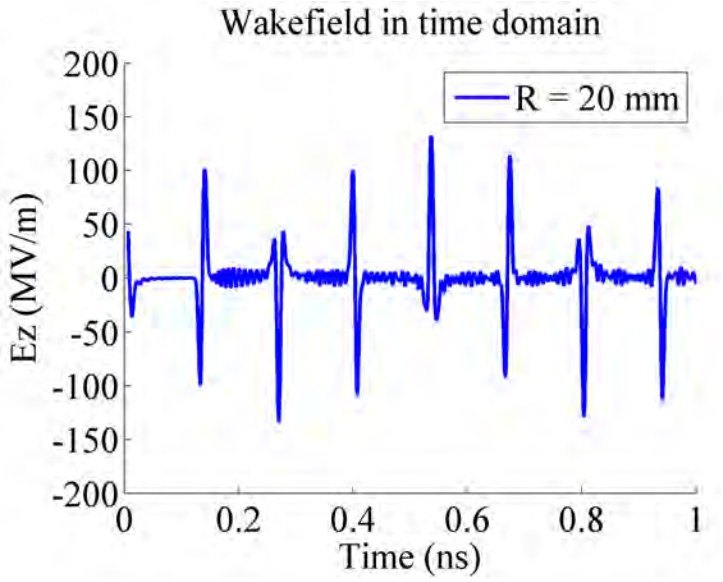

(a)

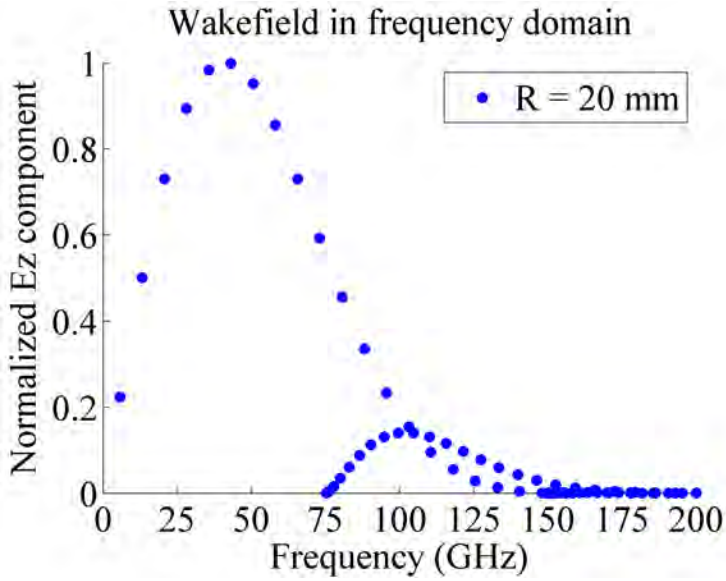

(b)

Figure 2-7: Longitudinal wakefield in the (a) time domain, and (b) frequency domain when the cavity radius $R = 20$ mm, and all the other parameters are fixed as in the nominal design. In this case, the structure operates in the multiple-frequency regime. In (b), the upper group of data points corresponds to the TM_{0s0} modes, and the lower group corresponds to the TM_{0s1} modes.

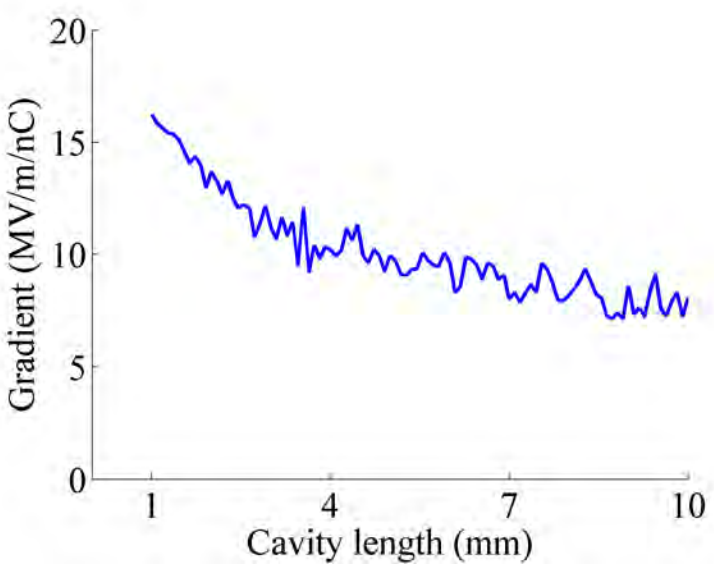

Figure 2-8: Scaling of the gradient in the circular deep corrugation structure with the cavity length d.

the multiple-frequency regime, since there are multiple modes to be excited by the bunch frequency spectrum. The switch between the single-frequency regime and the multiple-frequency regime is also dependent on the bunch length σ_z.

In the time domain figures, Fig. 2-6a and Fig. 2-7a, the full width at half maximum (FWHM) of a single accelerating peak is the same (6 ps) for both the $R = 2$ mm case and the $R = 20$ mm case. The time interval between two peaks is different, since the interval between peaks is caused by the wakefield traveling radially outward and then getting reflected inward to the focus.

Cavity Length d

Figure 2-8 shows the change of the gradient with the cavity length. The shorter the cavity length is, the higher gradient can be achieved.

Beam Hole Radius r

The gradient scaling study with the beam hole radius r is done with the CST Wakefield Solver, since the analytical model assumes an infinitely small the beam hole

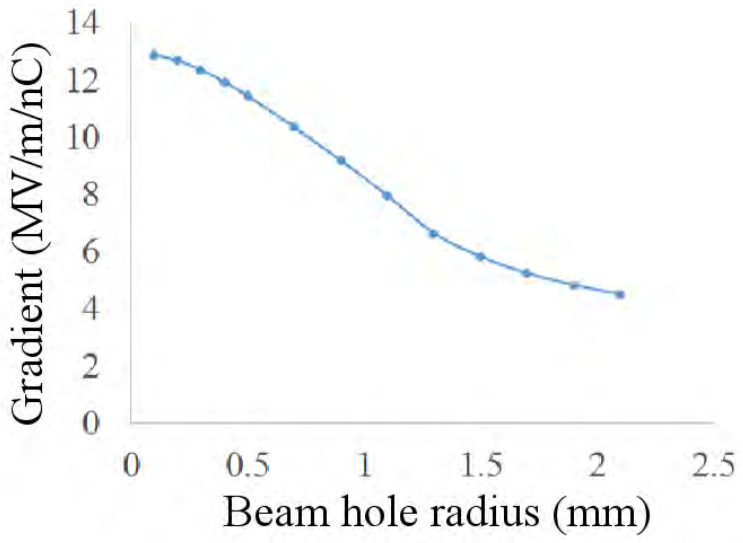

Figure 2-9: Scaling of the gradient in the circular deep corrugation structure with the beam hole radius r. The result is from the CST Wakefield Solver.

size.

The scaling result is shown in Fig. 2-9. With all the other parameters fixed, a higher accelerating gradient can be achieved with a smaller beam hole size.

The beam hole radius is a critical parameter, since the scaling of the gradient with the beam hole radius is more sensitive compared to that with other structure parameters. In a feasible structure design, the beam hole size needs to be optimized based on the total structure length and the beam parameters, such as bunch charge and energy, to ensure a good beam transmission.

Bunch Length σ_z

The bunch rms length σ_z is another critical parameter, as shown in Fig. 2-10. The shorter the bunch length is, the more eigenmodes of the structure with higher frequencies can be excited, and thus the total gradient is higher.

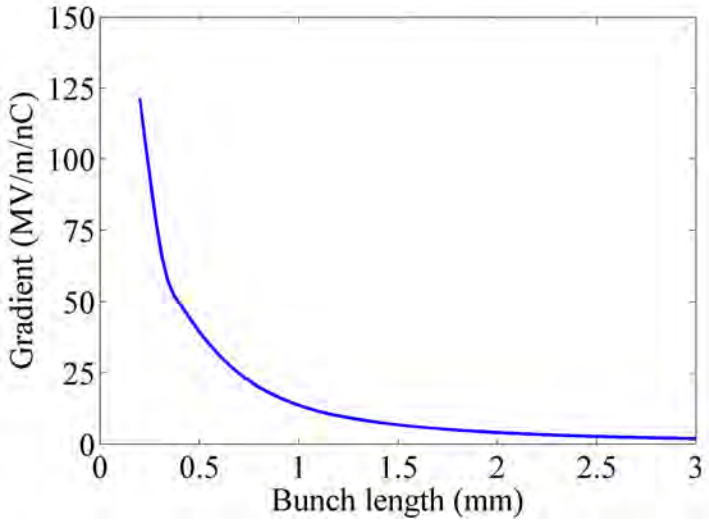

Figure 2-10: Scaling of the gradient in the circular deep corrugation structure with the bunch rms length σ_z.

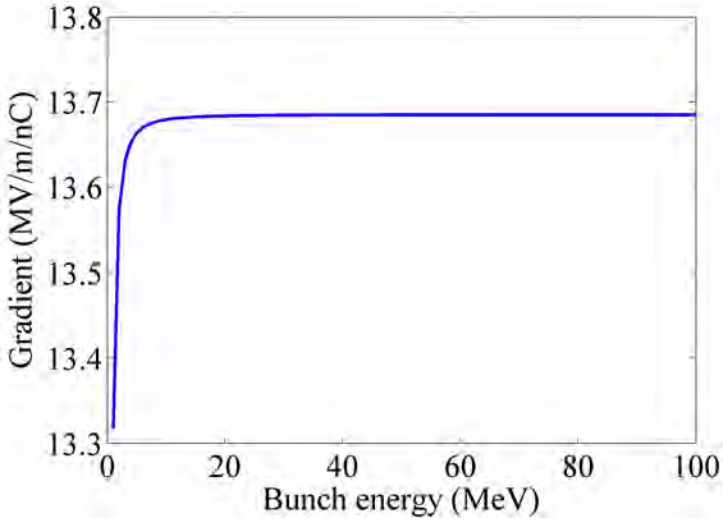

Figure 2-11: Scaling of the gradient in the circular deep corrugation structure with the beam energy E_0.

Table 2.2: Summary of the scaling law of the gradient with the structure and beam parameters in the circular deep corrugation structure.

Cavity Radius R	Cavity Length d	Beam Hole Radius r
No effect	Smaller	Smaller

Bunch Length σ_z	Energy	Charge
Smaller	No effect	Proportional

Beam Energh E_0

Figure 2-11 shows the scaling of the gradient with the beam energy E_0. In the figure, when the beam energy E_0 is above 10 MeV, the gradient does not grow further with an increasing energy.

However, operating at a higher beam energy helps to decrease the bunch size in both the longitudinal and the transverse directions, so a higher gradient can possibly be achieved from a smaller beam hole size and a smaller σ_z.

Bunch Charge Q

The trivial conclusion is that the total gradient is proportional to the bunch charge Q.

Summary of Scaling

In summary, the preferred choices of the structure and beam parameters to achieve a high accelerating gradient are listed in Table 2.2.

2.2.6 Nominal Design

A nominal design based on the Argonne Wakefield Accelerator (AWA) 70 MeV beam parameters is shown in Table 2.3. The rep rate of the AWA bunch train is 1.3 GHz, so the fundamental frequency of the nominal design is set as a harmonic frequency of

Table 2.3: A nominal design with the AWA parameters.

Charge	σ_z	Energy	R	Hole radius
10 nC	0.6 mm	70 MeV	9.8 mm	0.5 mm

d	Iris thickness	r_s	Gradient
1.5 mm	0.5 mm	37 MΩ/m	200 MV/m

1.3 GHz, since the fundamental mode content is generally strong. We choose the 9^{th} harmonic in the X-band, 11.7 GHz.

2.2.7 Conclusions

The circular deep corrugation structure is a good candidate for collinear wakefield acceleration. An analytical theory has been developed and benchmarked with the CST particle simulations. With the analytical theory, a thorough scaling study has been done to investigate the influence of vaious structure and beam parameters on the accelerating gradient, without running lengthy numerical simulations. A nominal structure is designed for the AWA 70 MeV beam, based on the rules summarized from the scaling study.

In the circular deep corrugation structure, cell-to-cell coupling is not allowed due to the below cut-off beam hole size. Therefore, this structure cannot serve as a traveling wave device in the two-beam acceleration regime.

Another design of a metamaterial structure for wakefield acceleration, named the 'wagon wheel' structure, will be presented in the following sections. The structure is named the wagon wheel structure for the similarity in the geometry, which will be explained later. The wagon wheel metamaterial structure can be used both in the collinear wakefield acceleration regime and the two-beam acceleration regime.

Section 2.3 will present the electromagnetic design of the wagon wheel metamaterial structure, Section 2.4 will present the analytical theory of the generated wakefield,

and Section 2.5 will present the numerical simulation results.

2.3 Design of Wagon Wheel Structure

The wagon wheel structure was designed and built by MIT, and tested at the Argonne Wakefield Accelerator. In this work, the highly innovative concept of a wakefield electron accelerator using a metamaterial structure is proposed and experimentally studied. The achieved output power and effective accelerator gradient exceed results achieved in prior work and are promising for much greater extension.

2.3.1 Motivation

There are mainly two motives for the wagon wheel metamaterial structure experiment.

The first motive is to verify the reversed Cherenkov radiation [1, 10, 11, 15, 16, 19, 57, 58] experimentally. There are some indirect experimental findings related to the reversed Cherenkov radiation in metamaterials, for example, the experiment in Ref. [16] used phased antennas to mock a moving particle beam. A previous experiment [10, 57] carried out at AWA studied the interaction of a metamaterial structure with short electron bunches by measuring the frequency spectrum of the generated radiation, but no direct evidence of the reverse Cherenkov radiation was provided. Our wagon wheel experiment is designed to examine experimentally the reversed Cherenkov radiation in a direct way.

The second motive is to extract high power microwaves from an intense drive electron beam for future wakefield acceleration applications in either the collinear regime or the two-beam acceleration regime. This experiment is the first successful high power microwave extraction experiment from short electron bunches based on a metamaterial structure, and it marks the highest RF power that metamaterial structures ever experienced without damage.

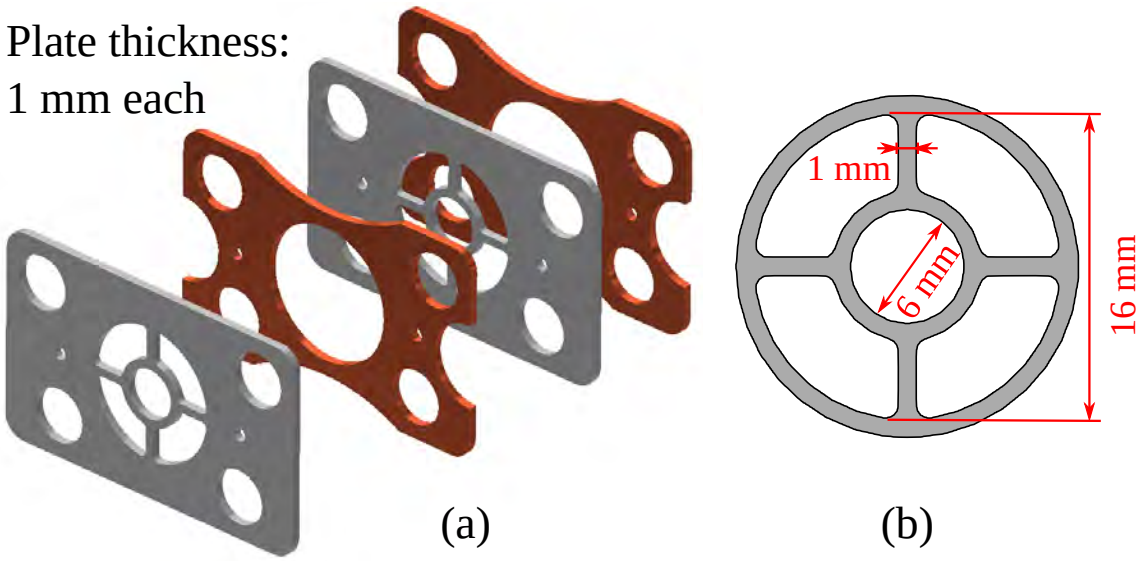

Figure 2-12: Wagon wheel metamaterial structure unit cell design. (a) Alternating wagon wheel plates and spacer plates. Each period has one SST plate of 1 mm thick and one copper plate of 1 mm. 40 plates of each type are clamped together to form an 8 cm long structure. (b) Wagon wheel plate geometry.

2.3.2 Unit Cell Design

The metamaterial wagon wheel structure is a periodic structure with the unit cell shown in Fig. 2-12. The design frequency is 11.42 GHz. The structure contains two materials, copper and stainless steel (SST). The wagon wheel patterns are in SST for ease of machining the small features. Each period has one SST plate and one copper plate, and the whole structure is a stack of the alternating plates clamped together, as shown in Fig. 2-12a.

Figure 2-12b shows the geometry of the wagon wheel design. Some key parameters include: beam aperture as 6 mm, thickness of each plate as 1 mm, diameter of the outer waveguide as 16 mm, thickness of spokes as 1 mm. An electron bunch will be sent through the central 6 mm diameter hole (perpendicular to the plates) to radiate its energy into the electromagnetic field energy in the metamaterial structure.

The wagon wheel structure has the features of a metamaterial structure, a negative group velocity in the fundamental mode. The dispersion (ω vs. k_z) of the fundamental

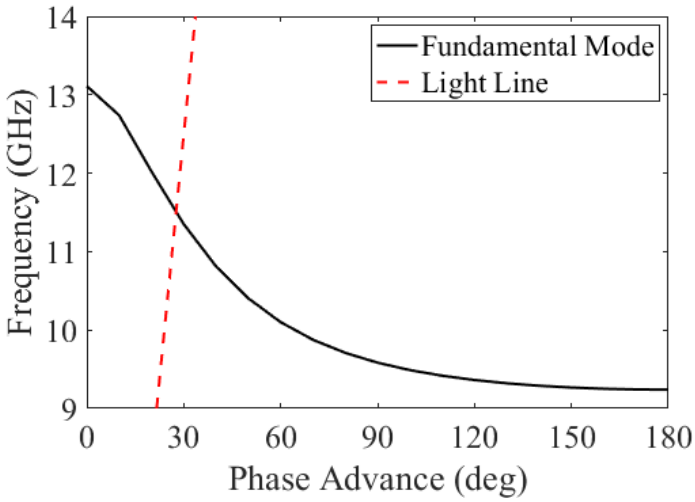

Figure 2-13: Dispersion curve of the fundamental TM mode in the wagon wheel structure. The horizontal axis plots the phase advance in one unit cell as $k_z p$, where $p = 2$ mm is the structure period.

mode is shown in Fig. 2-13, which was calculated using the Eigenmode Solver of the CST Microwave Studio. In the dispersion plot, the horizontal axis means the phase advance in one unit cell as $k_z p$, where $p = 2$ mm is the structure period. The light line is also shown, and the intersection point of the light line with the TM mode dispersion curve is where the beam-wave interaction happens.

The fundamental mode is a TM-like mode, which has a longitudinal electric field (parallel to the beam propagation direction). The longitudinal electric field component can interact with the 65 MeV beam at 11.42 GHz, and the group velocity there is -0.158 c.

The field pattern of the fundamental mode in a single period of 2 mm length is shown on a linear scale in Fig. 2-14. Figure 2-14a shows the longitudinal electric field E_z on the cross section at $z = 0$. The field is only plotted in the vacuum region of the cross section. The field is excluded, shown as white, in the wagon wheel metallic structure. Figure 2-14b shows the vector electric field on the middle cutting plane. The electric field in the z direction interacts with the electron beam. Figure 2-14c shows the tangential H field H_{perp} on the cross section, where H_{perp} is strongest around

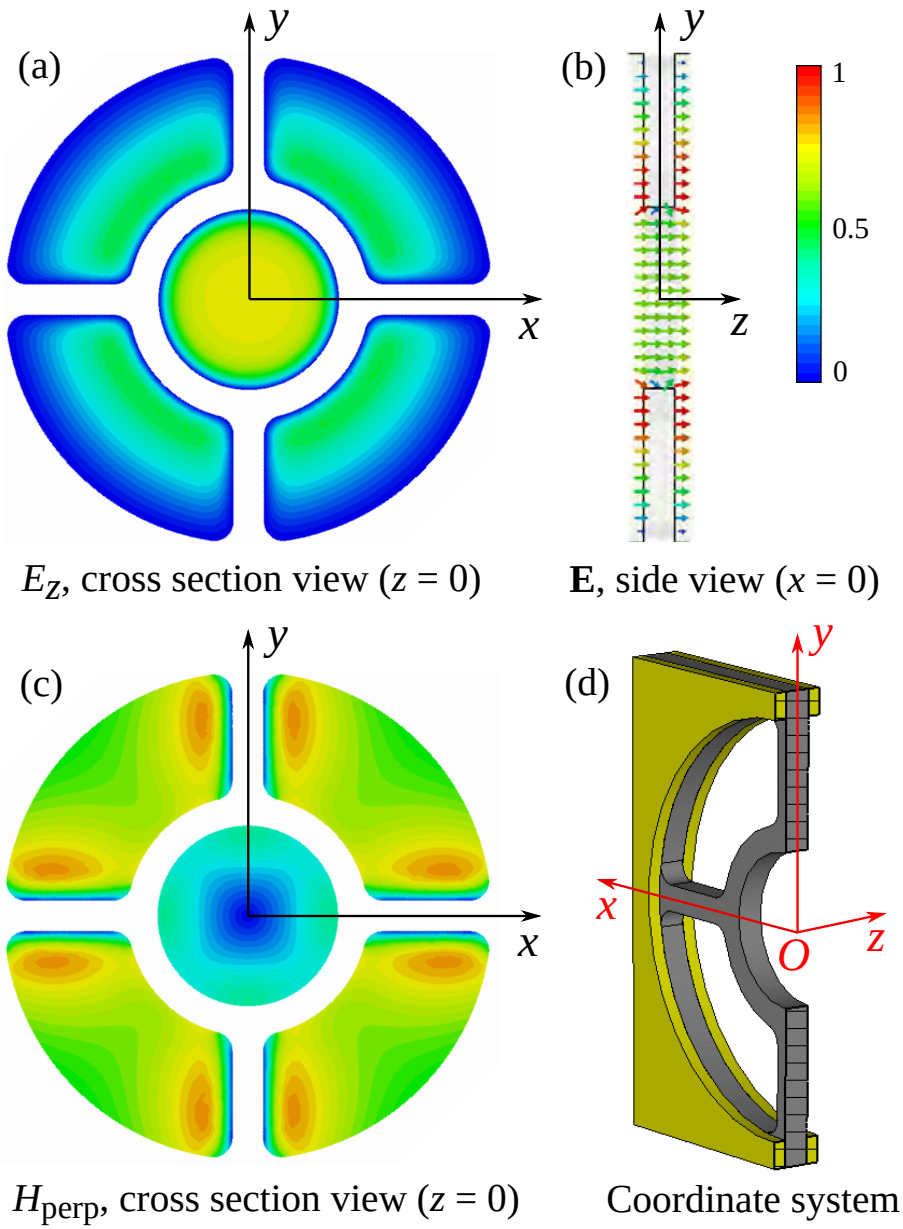

Figure 2-14: Electromagnetic field pattern of the fundamental metamaterial mode plotted on a linear scale. (a) E_z on the cross section $z = 0$. The z direction is the beam propagation direction. (b) Vector electric field on the middle plane of $x = 0$. (c) Amplitude of the tangential H field, H_{perp}, on the cross section $z = 0$. (d) CAD drawing of a single 2 mm long period of the metamaterial structure with the coordinate system defined. The wagon wheel plate of stainless steel (gray) is 1 mm thick, centered between 0.5 mm thick copper spacer plates (yellow) on both sides. The origin is in the center of the wagon wheel.

the rods. Figure 2-14d presents the definition of the coordinate system.

The unit cell has been optimized for the design goal of high power microwave generation. There are some trade-offs in the design process.

For example, a smaller beam aperture leads to an increased output power from a given electron beam charge, but it also limits the maximum charge Q that can be transmitted through the structure. The reason is that the electron beam expands due to the space charge effect, so more charge in a bunch leads to a larger transverse size. As the total power scales as Q^2 (the detailed math will be presented in Section 2.4), the beam aperture cannot be too large or too small to achieve the maximum output power. The present design is optimized for a beam energy near 65 MeV. At much higher beam energies, on the GeV scale, the available charge can be compressed to a smaller radius leading to a different optimization and potentially much higher microwave power generation.

Another example of the design trade-off is the plate thickness. A thinner plate helps improve the beam-wave interaction which leads to a high output microwave power, but it also causes trouble in the structure manufacturing and leads to a lower structure mechanical strength. So a structure with thinner plates is more likely to suffer from damage in the beam test. With the goal of achieving a stable high power operation of the metamaterial structure, the optimized plate thickness is decided to be 1 mm.

2.3.3 Double Negative Permittivity and Permeability

Insight into the properties of the metamaterial mode may be made by reference to effective medium theory. For a propagating wave with a negative group velocity, the effective refractive index is negative, requiring both the effective permittivity ϵ and the effective permeability μ to be negative. Here we show the double negative feature of the wagon wheel metamaterial structure.

In the design of the wagon wheel structure, a circular waveguide with the same outer dimension as the wagon wheel structure, being 8.1 mm, has a cutoff frequency for the TM_{01} mode of 14.2 GHz. So the fundamental mode frequency is below the

cutoff frequency of the outer waveguide if it were constructed without the wagon wheel structures. The waveguide operating below the cutoff frequency provides a negative μ as

$$\mu = 1 - \frac{\omega_{cr}^2}{\omega^2} < 0 \quad \text{when } \omega < \omega_{cr}, \tag{2.16}$$

where ω is the operating angular frequency, and ω_{cr} is the cutoff angular frequency which equals $2\pi \times 14.2$ GHz.

The effective permittivity ϵ is also negative for the wagon wheel design, and it can be modeled by [60]

$$\epsilon = 1 - \frac{\omega_p^2}{\omega^2 - \omega_0^2}, \tag{2.17}$$

where $\omega_0 = 2\pi \times 9.24$ GHz is the resonant angular frequency, and $\omega_p = 2\pi \times 11.0$ GHz is the plasma frequency of the effective medium. These parameters are obtained by fitting the calculated dispersion, as shown in Fig. 2-13.

Figure 2-15a shows the effective parameters ϵ and μ which are both negative around the operating frequency of 11.4 GHz, and Fig. 2-15b compares the dispersion curve calculated by CST Microwave Studio using the exact structure dimensions with the curve calculated from the effective medium model of Eqs. (2.16) and (2.17). There is very good agreement between the two.

We use Eqs. (2.16) and (2.17) to show the characteristic double-negative feature of the metamaterial structure and to provide insight into the wave propagation below the cutoff frequency. We did not use the effective medium model to design the structure or to analyze the experimental results. For these tasks, we use full-wave simulations based on the electromagnetic mode of the wagon wheel structure as shown in Fig. 2-14. These simulations are more accurate.

2.3.4 Enhanced Beam-Wave Interaction

The metamaterial structure has enhanced beam-wave interaction from the subwavelength feature, and this enhancement is represented by the increased r/Q, where r is the shunt impedance per unit length, and Q is the quality factor. r/Q is a frequently used figure of merit to describe the intensity of beam-wave interaction in accelerator

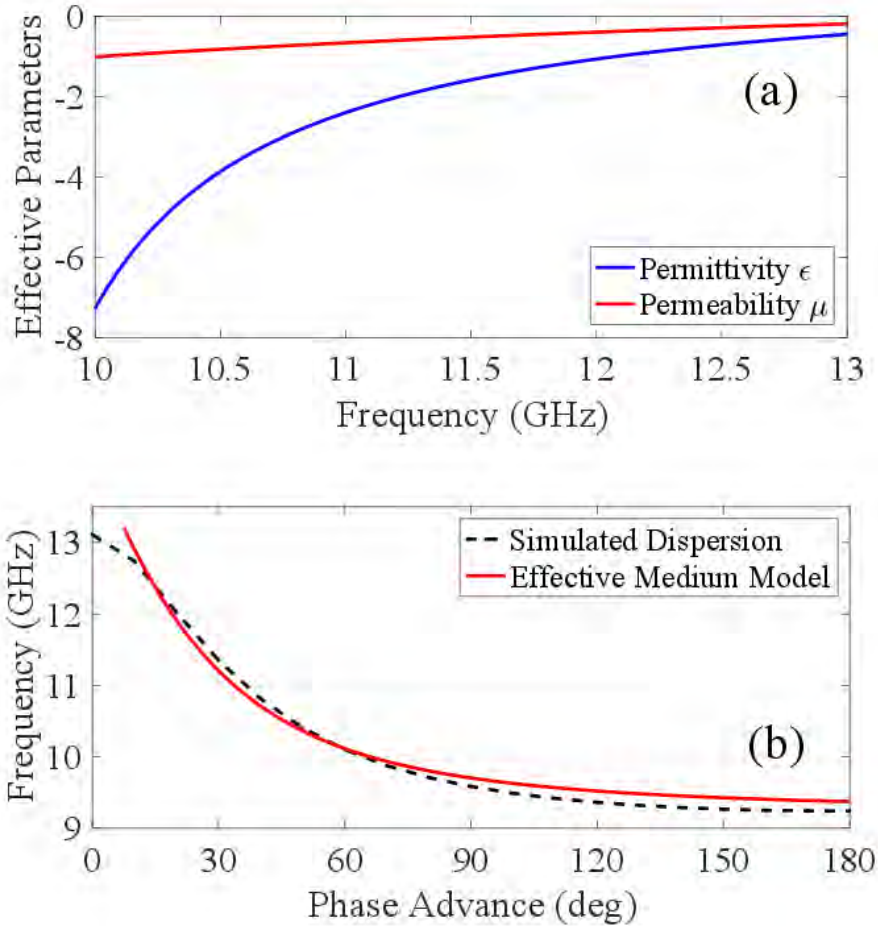

Figure 2-15: Double negative permittivity ϵ and permeability μ. (a) Effective medium theory of ϵ and μ around the interaction frequency. (b) Comparison of the simulated dispersion and the calculated one from the effective medium model. The phase advance as the horizontal axis is calculated for a single 2 mm long period.

physics [23], with a larger value indicating a stronger interaction.

r/Q can be calculated as

$$r/Q = \frac{E_a^2}{\omega U} \tag{2.18}$$

where E_a is the longitudinal electric field for beam acceleration, ω is the angular frequency of the operating mode, U is the total energy stored per unit length. The r/Q factor is an inherent feature of the structure geometry under a certain operating mode. The r/Q factor has the unit of Ω/m, and there is another quantity not normalized with the structure length, the R/Q factor, defined as

$$R/Q = \frac{V_a^2}{\omega U}, \tag{2.19}$$

where V_a is the effective acceleration voltage in the total structure length L. The R/Q factor has the unit of Ohm (Ω). R/Q does not change when the structure geometry is scaled uniformly to other frequencies.

The quality factor, or Q factor, is another commonly used parameter describing the resonance feature. It is a dimensionless quantity defined as

$$Q = \frac{\omega U}{P_l}, \tag{2.20}$$

where U is the stored energy, and P_l is the dissipated power. So the Q factor is a measure of the number of cycles for the stored power to be dissipated in the cavity.

These quantities characterizing the beam-wave interaction were calculated in CST Microwave Studio, and the results are in Table 2.4.

Table 2.5 compares the metamaterialstructure with the X-band metallic disk-loaded and the dielectric-loaded structures. The metamaterial design has a higher r/Q than some other structures at the same design frequency as a result of the creation of negative group velocity in the fundamental mode.

The advantage of the metamaterial structure is that it has a high group velocity and a high r/Q value at the same time. Normally in a metallic disk-loaded structure or in a dielectric structure, one can have either a high group velocity with a large

Table 2.4: Beam-wave interaction parameters of the wagon wheel structure.

r/Q	21 kΩ/m
Q	1050
r	22 MΩ/m
Group Velocity	-0.158 c

Table 2.5: Comparison of the metamaterial structure with the metallic disk-loaded structures and dielectric-loaded structure.

Structure	Beam aperture (mm)	Frequency (GHz)	Group velocity	r/Q (kΩ/m)
Wagon wheel	6	11.4	-0.158 c	21
Alumina-loaded tube	6	11.7	0.106 c	10
Metallic disk-loaded [61]	6	11.7	0.016 c	16.5
Metallic disk-loaded [61]	17.6	11.7	0.22 c	3.9

beam aperture or a high r/Q with a small beam aperture. In order to achieve high power in the wakefield, both a high group velocity and a high r/Q are required. This makes the metamaterial structure an advantageous design.

2.3.5 Output Ports Design

Based on the unit cell design presented in Section 2.3.3, a complete structure is designed as a clamped structure of 40 unit cells, with a total length L of 8 cm. An output port design is now needed to couple the generated wakefield radiation out.

For this goal, two output ports are placed at the two ends of the structure, as the backward port at the beam entrance, and the forward port at the beam exit. Each output coupler consists of a coupling cell and a taper section on the side. An illustration of the coupler design is shown in Fig 2-16.

The waveguide size in the coupling cell (9.4 mm radius) is slightly larger than the waveguide size in the wagon wheel structure (8.1 mm radius). The design has been optimized for the minimal conversion loss in the output coupler. A small slot with a

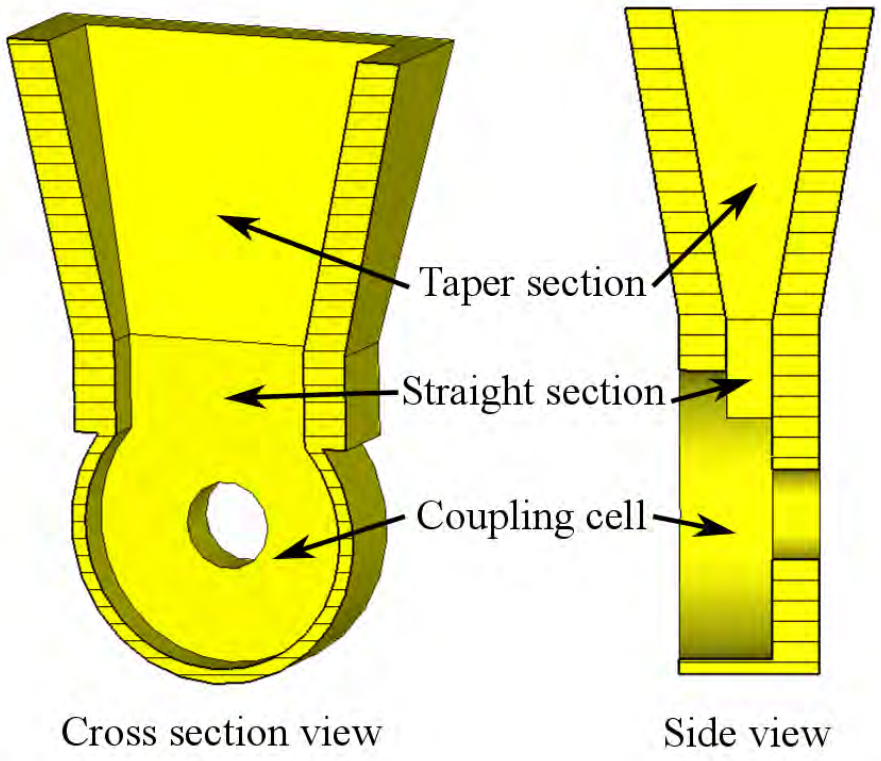

Figure 2-16: Output coupler design. A taper section connects a small slot on the side to the WR90 waveguide, so the TM-like mode in the coupling cell can be transformed to the TE_{10} fundamental mode of the WR90 waveguide.

width of 3 mm is cut on the waveguide wall. The geometry of the slot has also been optimized. Then the taper section transforms adiabatically from the slot shape to the WR90 waveguide cross section. With the taper design, the TM-like mode in the wagon wheel structure can be transformed into the fundamental TE_{10} mode of the WR90 waveguide.

The two output ports are set up for verification of the reversed Cherenkov radiation. When the structure is excited by a drive electron bunch, the amplitudes of the RF signals can be compared at the two ports. If the backward port measures much higher power than then forward port, then it means that the RF power is generated by the reversed Cherenkov regime, with the microwaves traveling in the backward direction as the beam travels forward.

2.4 Theory of Wagon Wheel Metamaterial Structure

This section will present the analytical calculation of the pulse length and the output power in the complete 40-cell wagon wheel structure from the wakefield theory.

2.4.1 Pulse Length

The fundamental TM-like mode in the metamaterial wagon wheel structure has a negative group velocity $v_g = -0.158c$. When a short electron bunch travels through, the excited RF pulse length in the $L = 8$ cm long metamaterial structure can be calculated as

$$t_p = L/|v_g| + L/c = 1.96 \text{ ns} \approx 2 \text{ ns}. \tag{2.21}$$

The pulse excitation process is explained in Fig. 2-17.

In the metamaterial structure, the RF power is extracted from the backward port at the beam entrance side. The pulse at the backward port starts when the bunch enters the structure, defined as the time $t = 0$. At $t = L/c$, the relativistic bunch (almost traveling at the speed of light) reaches the other end of the structure. With a backward traveling wave, the latest RF signal is generated at $t = L/c$ at the position of $z = L$, and this signal arrives at the backward port at $t = L/c + L/|v_g|$ after a traveling time of $L/|v_g|$ in the structure.

In comparison, in forward wave structures with a positive group velocity $v_g > 0$, such as disk-loaded waveguides and dielectric tubes, the pulse length is [31]

$$t_p = L/v_g - L/c. \tag{2.22}$$

The evolution of the RF pulse and the electron bunch in a forward wave structure is presented in Fig. 2-18 [31]. With a forward propagating wave, the RF pulse can be measured at the forward port at the beam exit side from $t = L/c$ to $t = L/v_g$.

From the comparison in Fig. 2-17 and Fig. 2-18, we can see that the metamaterial structure with a negative group velocity, when driven by a short relativistic electron bunch, can generate a longer RF pulse length than a conventional structure with a

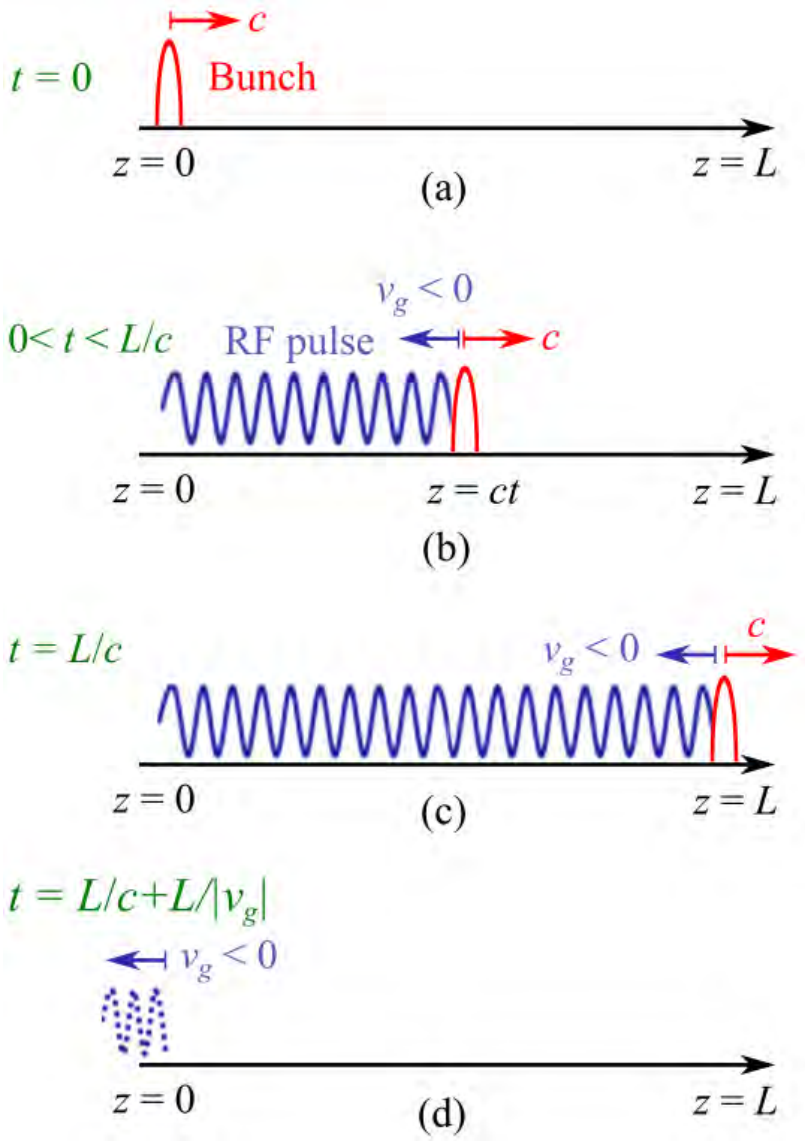

Figure 2-17: Illustration of the RF pulse from a single drive bunch in the metamaterial structure with a negative group velocity. The backward port is at $z = 0$, and the forward port is at $z = L$, where L is the structure length. (a) $t = 0$, bunch enters the structure. The RF pulse starts at the backward port. (b) $0 < t < L/c$, bunch in the structure. The radiated RF pulse propagates backward to the backward port. (c) $t = L/c$, bunch exits the structure. The RF pulse keeps propagating backward. (d) $t = L/c + L/|v_g|$, the tail of the RF pulse exits from the backward port. The RF pulse ends.

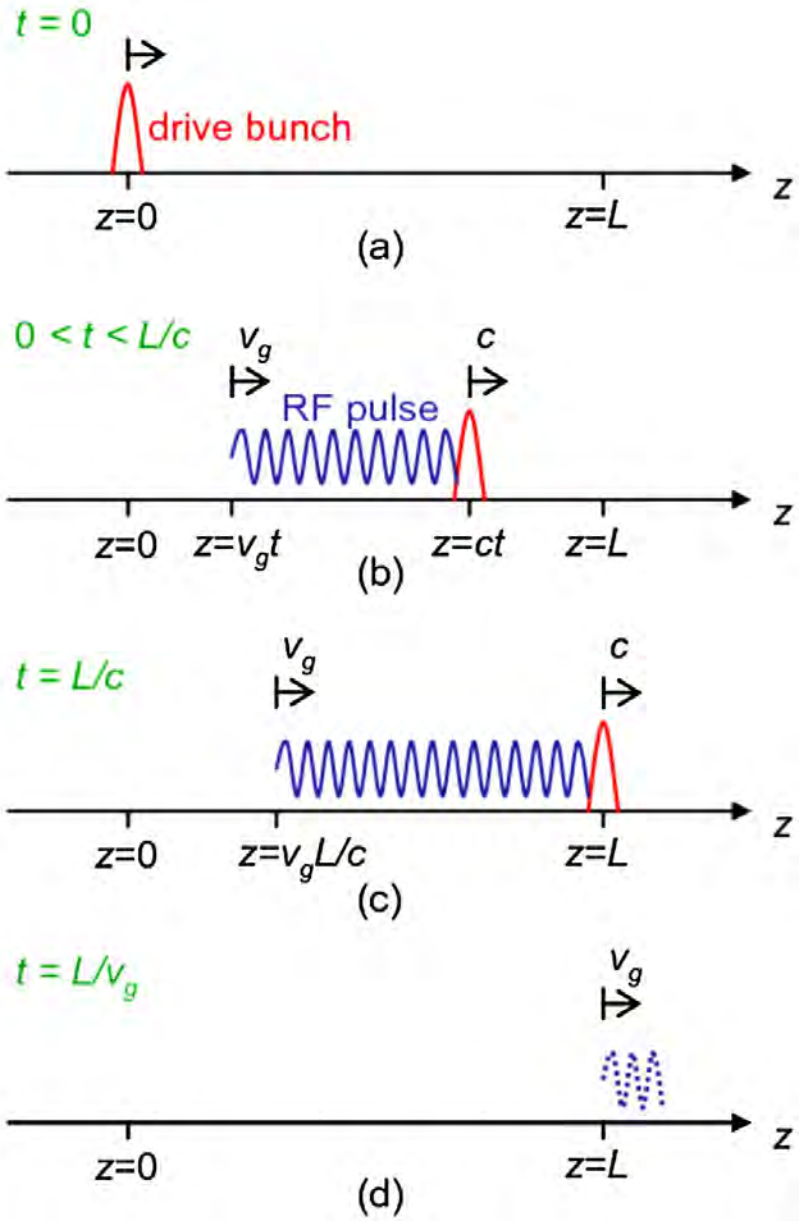

Figure 2-18: Illustration of the RF pulse from a single drive bunch in a structure with a positive group velocity. The output port is at $z = L$, where L is the structure length. (a) $t = 0$, bunch enters the structure. (b) $0 < t < L/c$, bunch in the structure. The radiated RF pulse propagates forward to the forward port. (c) $t = L/c$, bunch exits the structure. The RF pulse starts at the forward port. (d) $t = L/v_g$, the tail of the RF pulse exits from the forward port, then the RF pulse ends. This figure is cited from Ref. [31].

positive group velocity of the same absolute value $|v_g|$.

2.4.2 Output Power from a Single Bunch

The output RF power P from a short relativistic bunch with a charge q and a longitudinal (z direction) Gaussian distribution of σ_z is given by [31]

$$P = q^2 k_L |v_g| \left(\frac{1}{1 - v_g/c}\right)^2 \Phi^2. \tag{2.23}$$

where $k_L = (\omega/4) \cdot (r/Q)$ is the loss factor, and $\Phi = \exp[-(k_z\sigma_z)^2/2]$ is the form factor for a Gaussian bunch.

For example, when a single bunch with a charge $q = 45$ nC and a Gaussian distribution $\sigma_z = 1.2$ mm travels through the wagon wheel structure with the $r/Q = 21$ kΩ/m, the output power is 25 MW, and the power is expected at the backward port from the reversed Cherenkov radiation. For an arbitrary charge number q, the extracted RF power (in MW) can be calculated as 1.25 (q/ 10 nC)^2.

From Eq. (2.23), we can see the effect of the beam aperture on the output power more clearly. A smaller beam aperture leads to a higher shunt impedance, but also results in a reduction in the transmitted charge q and the group velocity $|v_g|$. Since the output power increases with r/Q and the group velocity, and also scales with the charge q in a bunch as q^2, a beam aperture too large or too small will not yield high microwave power. The beam aperture here is chosen as 6 mm to allow for up to 45 nC of charge in a single bunch to go through the structure.

2.4.3 Output Power from a Bunch Train

Since the extracted RF power from the reversed Cherenkov radiation is coherent, a train of N bunches in phase with each other can build up the microwave power as N^2 times the power from a single bunch. To make the coherent adding from N bunches happen, there are two requirements.

The first requirement is that the radiated wakefield frequency in the structure is

a harmonic of the electron beam repetition rate. The electron gun and the linac are both at 1.3 GHz at the AWA beamline, and the laser photocathode can generate two or more bunches separated at around the frequency of 1.3 GHz with laser splitters which provide precise control and tuning of the spacing between bunches. So the wagon wheel structure with a design frequency of 11.42 GHz, the 9th harmonic of an 1.27 GHz bunch train, can generate coherent wakefield superposition.

The second requirement is that the structure is long enough, so that the RF pulse length from a single bunch is long enough for the RF pulses from all the N bunches to overlap with each other. If the number $N+1$ bunch arrives after the RF pulse from the first bunch ends, while the number N bunch arrives before, then the RF power from the first to the number N bunch can add up together to create a peak power of N^2 times of the single bunch power, but the number $N+1$ bunch cannot add up on top of the RF pulse from the first bunch. In this case, we say the output power from a train of bunches saturates on N bunches. As a result, the number of electron bunches N whose RF pulses can add up together before saturation happens is

$$N = \text{ceiling}(t_p/T_b), \tag{2.24}$$

where t_p is RF pulse length from a single bunch, and T_b is the spacing in time between two neighboring bunches.

For the wagon wheel structure, the single bunch pulse length $t_p = 1.96$ ns, and the bunch spacing is $T_b = 0.79$ ns, so the saturating bunch number is $N = 3$. A longer structure can increase the RF pulse length, thus increasing the saturating bunch number. The structure length has to be reasonable though, for the bunch train to pass through without problems in beam transmission.

2.5 Simulations of Wagon Wheel Metamaterial Structure

Microwave and particle simulations were performed with the CST numerical codes for the complete wagon wheel structure. The full structure simulated in the CST code is shown in Fig. 2-19. The metamaterial structure consists of 40 periods of the alternating copper and SST plates, and in the two ends are the two output ports, labeled as Port 1 and Port 2.

2.5.1 Microwave Simulations

Microwave simulations were carried out in the CST Microwave Studio. There is no electron beam in the microwave simulations, and the goal is to verify the frequency response of the wagon wheel structure, and to minimize the microwave transmission loss.

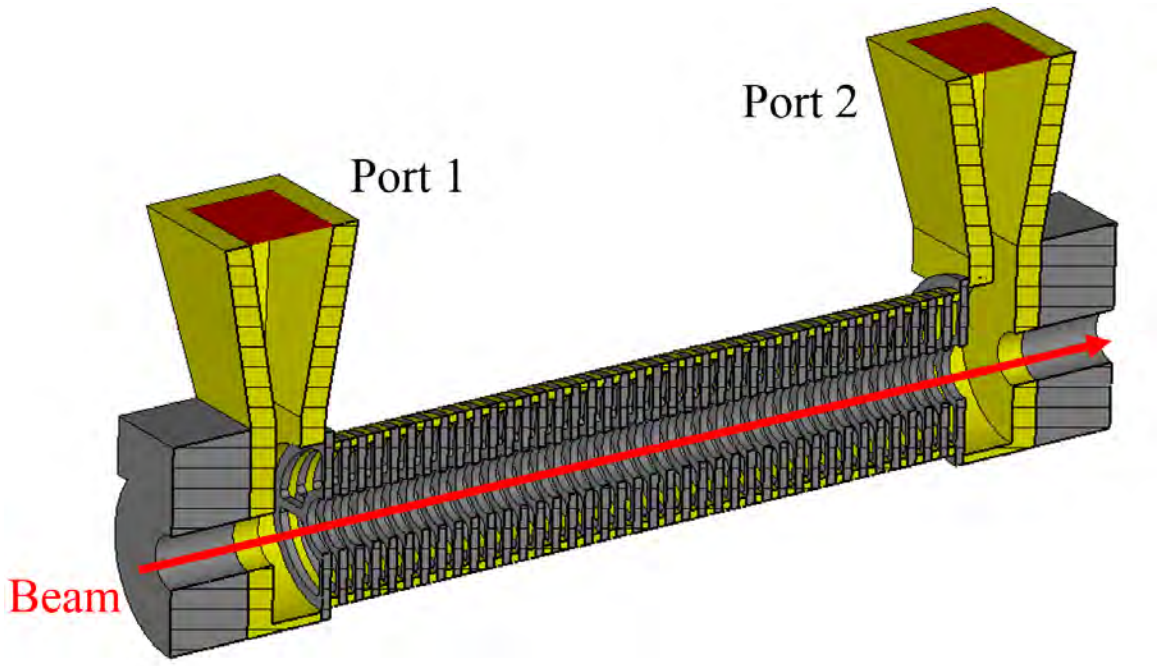

Figure 2-19: Simulation model of the complete 40-cell wagon wheel structure in the CST simulations.

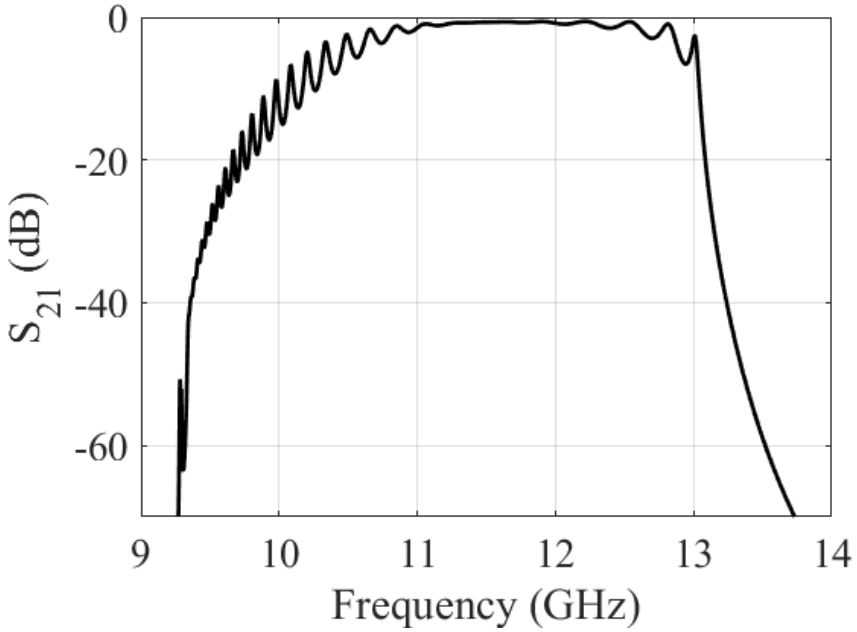

Figure 2-20: CST Microwave Studio simulation of the amplitude of S_{21} as the transmission coefficient between the two output ports.

In the CST Frequency Domain Solver, the transmission, between the two ports, Port 1 and Port 2, is calculated in a frequency range around the design frequency.

In microwave theory, the S parameters are used to characterize a two-port system. Suppose Port 1 is the input port, then an input signal with a voltage amplitude of V_1 is launched from Port 1. Then at Port 2 as the receiving port , or output port, a voltage amplitude of V_2 is measured. Then we define an S_{21} parameter to describe the transmission from Port 1 to Port 2, whose amplitude is $|S_{21}| = V_2/V_1$. Similarly, we define the S_{11} parameter to describe the reflection as the ratio of reflected voltage at Port 1 to the input voltage at Port 1. The amplitudes of the S parameters are often presented in the unit of dB.

These S parameters, simulated by the CST Frequency Domain Solver, are potted in Fig. 2-20 and Fig. 2-21.

In the S_{21} amplitude plot, there is a wide passband around the design frequency of 11.4 GHz. The transmission loss, being $-|S_{21}|$, is about 0.7 dB. In the frequency band

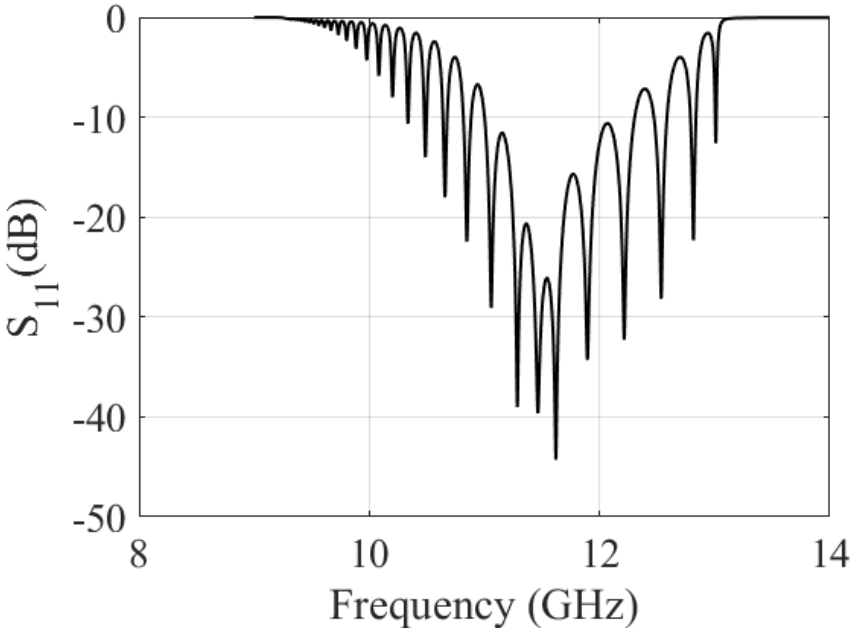

Figure 2-21: CST Microwave Studio simulation of the amplitude of S_{11} as the reflection coefficient at Port 1.

from 10.5 GHz to 12.8 GHz, the transmission loss is below 3 dB. The wide passband is designed so that if there is a frequency shift due to factors like fabrication errors, the microwaves in the structure still do not suffer from noticeable ohmic loss.

2.5.2 Beam Simulations

Simulations with the electron beams involved were done in the CST Particle Studio. In these simulations, the beam travels through the beam hole, and the output power is recorded at the two output ports. The power traces are shown in Fig. 2-22. The simulation result in Fig. 2-22 agrees with the analytical wakefield theory of Eq. (2.23). A single 45 nC bunch generated 26 MW of radiation in the backward port, while the analytical theory number is 25 MW. In the two output ports, the backward port (Port 1 in Fig. 2-19) has much higher power than the forward port (Port 2 in Fig. 2-19), indicating that the radiated microwaves travel in the backward direction as a result of the reversed Cherenkov radiation.

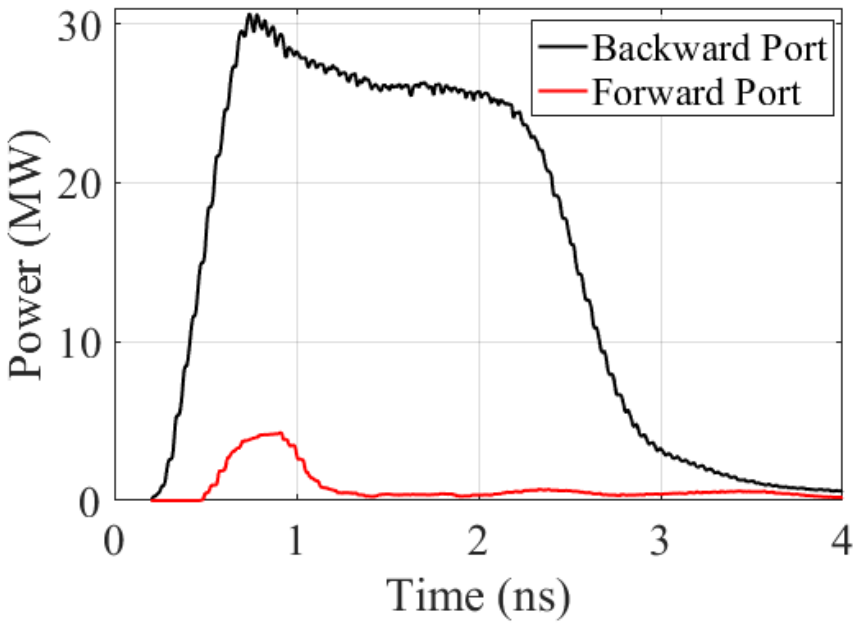

Figure 2-22: CST simulation of output power at the two ports from a single 45 nC bunch.

Figure 2-23 is a plot of the longitudinal electric field E_z on the middle plane. The beam travels in the $+z$ direction, and leaves the reversed Cherenkov radiation pattern after it. The field pattern has a similar bouncing feature as that in a dielectric tube, so the metamaterial structure is acting as an artificial dielectric tube with all the parts made of metal. The dielectric structure might be susceptible to electron beam damage and discharge, so the performance of the dielectric structure may degrade with more pulses. The wagon wheel structure, as an all-metal structure, is more rugged and reliable.

The wagon wheel structure can be seen as a 1D metamaterial structure, with only the longitudinal period being subwavelength. In the next section, I will present the theory of a volumetric 3D metamaterial structure with a cubic unit cell.

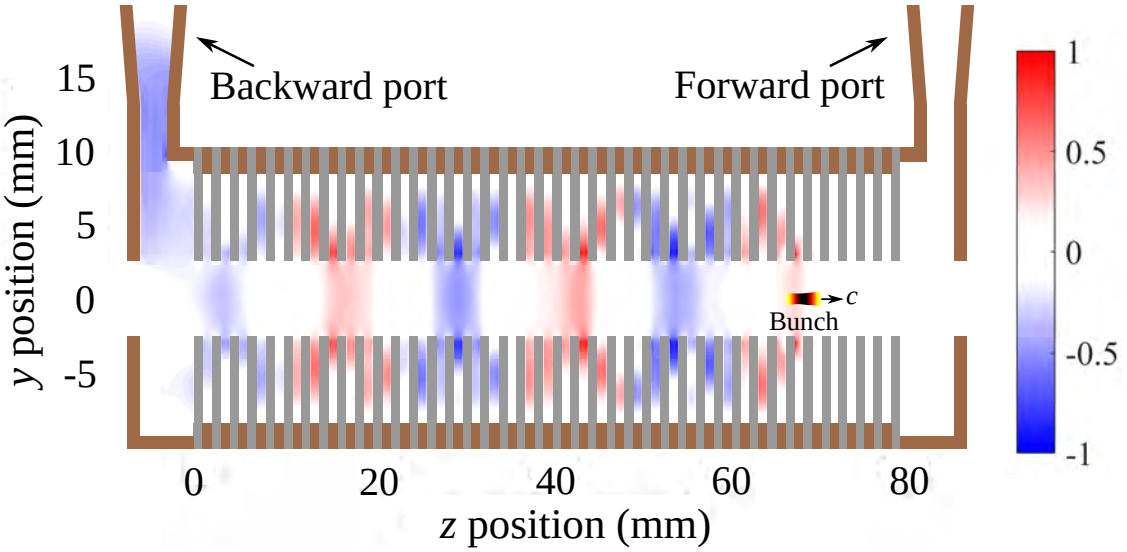

Figure 2-23: Plot of the normalized longitudinal electric field on the middle plane in the linear scale. For a single 45 nC bunch, the peak surface field is 70 MV/m. The metamaterial structure is represented in grey.

2.6 Theory of Volumetric 3D Metamaterial Structure

In this section, a theoretical study will be presented on the beam-wave interaction in a volumetric metallic metamaterial structure. The wagon wheel structure described in Section 2.3 to Section 2.5 is an one-dimensional (1D) metamaterial structure. The subwavelength feature is only in the longitudinal direction, but not in the transverse direction. As a result, the negative group velocity also only appears in the longitudinal direction. In contrast, the volumetric metamaterial structure to be explained in this section is a three-dimensional (3D) metamaterial structure. The subwavelength and the negative group velocity feature happen in all the three dimensions. The volumetric 3D metamaterial structure is designed for the demonstration of the reversed Cherenkov radiation and its application in the beam-driven wakefield acceleration.

2.6.1 Motivation

Research on high power microwave sources and particle accelerators can benefit from introducing metamaterials [10, 57, 62]. The challenge of applying metamaterials to active devices is that a design with planar unit cells naturally has the electromagnetic fields concentrated on the planar plates, so at the beam location, which must be at a distance away from the plates, field intensities are low. This might limit the achievable coupling impedance in metamaterial structures with planar unit cells.

The work described in this section is new and different in the way that a real volumetric metallic 3D metamaterial structure is designed from a cubic unit cell which can fill the full space automatically. Although volumetric metamaterial designs based on dielectric materials have been extensively studied, dielectric materials are less attractive for applications where electron beams propagate in vacuum through the metamaterial structure, such as in vacuum electron devices or particle accelerators. We can study the interaction of an electron beam with the 3D metallic metamaterial directly without a substrate supporting the metamaterial structure or other supporting parts.

Characterization of metamaterials has aroused a lot of interest. Different methods have been developed to find the effective dielectric and magnetic parameters, such as the scattering parameter extraction method and the field averaging method [63–66]. These parameters are often scalar functions depending only on frequency, i.e. $\epsilon(\omega)$ and $\mu(\omega)$. However, this model is not a good approximation outside the low frequency range, since multipoles besides dipoles become important [67,68]. A parallel approach is to use a set of fields of $\vec{E}$, $\vec{D}$, and $\vec{B}$ with $\vec{D} = \epsilon\vec{B}$, where ϵ is a tensor and depends on the frequency and the wave vector, $\epsilon = \epsilon(\omega, k)$. In this section, we will use the latter approach. Demetriadou and Pendry [69] realized the role of spatial dispersion in longitudinal waves in 3D wires, though their goal was trying to minimize the dispersion. A successful modeling of surface waves on the interface of a wire array and vacuum using the spatial dispersion approach is presented by Shapiro et al [70], and a discussion on the importance of spatial dispersion on polaritons with negative

group velocity has been carried out by Agranovich and Gartstein [71].

Novel dispersion relations of the metamaterials may give rise to unusual radiated waves from the electron beams. In conventional materials, when particles travel faster than the speed of light in the medium, Cherenkov radiation occurs. It is widely used in particle counters and position monitors [72]. In the research area of metamaterials, planar metamaterial structures aimed at generating reversed Cherenkov radiation were developed [73] first in 2002. Both theoretical and experimental work [74–77] has verified the reversed Cherenkov radiation using a phased antenna array to mimic a traveling current. The first experiment with a real electron beam was performed by Antipov et al [10]. A waveguide loaded with SRRs and a wire array was built, and the measured frequency response of the incoming electron beam was in the negative-index band. Vorobev et al [78] calculated the Cherenkov radiation generated by an electron bunch traveling perpendicular to a 2D wire array and found that the radiation appears with an arbitrary charge velocity. The radiated field profile changes with different bunch lengths, thus their discovery indicates a possible application of measuring beam bunch length and velocity using Cherenkov radiation in metamaterials.

In Section 2.6.2, I will present the design of a cubic unit cell with 3D negative group velocity. Section 2.6.3 presents the effective medium theory with spatial dispersion as an analytical model. Section 2.6.4 presents the beam-wave interaction using the effective medium theory. Section 2.6.5 discusses the radiation pattern calculated using the CST code. Application of the structure as a wakefield accelerating structure is discussed in Section 2.6.6 and conclusions are presented in the end.

2.6.2 Unit Cell Design

For the design of the metallic, volumetric metamaterial, we chose the unit cell to be a cube. We further chose to have an empty unit cell, with metallic capacitive and inductive elements arranged on the faces of the cube. Each face of the cube is identical to make the structure quasi-isotropic. To allow transmission of an electron beam, each face has a beam aperture in the center. To allow propagation of electromagnetic waves, each face has a set of four coupling slots, each about one tenth of a wavelength,

arranged symmetrically around the beam aperture. The detailed structure is shown in Figure 2-24. The dimensions are chosen to put the operating frequency at around 17 GHz.

An eigenmode solver needs to be used to study the dispersion characteristics, and we chose the HFSS [79] Eigenmode Solver to calculate the dispersion in the first Brillouin zone, as shown in Figure 2-25a. One unit cell is simulated, with master and slave boundaries exerted. The boundaries force a given phase difference between the opposing boundary walls, and the eigenmode frequencies are calculated for each of the phase difference combinations, so that the dispersion relation between ω and k is calculated. In (k_x, k_y, k_z) space, the coordinates of the high symmetry points for a cubic lattice are $\Gamma(0,0,0), X(\pi/p,0,0), M(\pi/p,\pi/p,0), R(\pi/p,\pi/p,\pi/p)$, where p is the period of the unit cells.

We chose the specific parameters in Figure 2-24 to make the structure balanced, i.e., all the modes have the same cut-off frequency at the Γ point. In this way, we can have dispersion curves with a greater slope; otherwise the slope at the Γ point must be zero due to periodicity. Negative group velocity of the proposed unit cell is an inherent feature and is not critically dependent on a certain set of geometry parameters. For example, if we vary the size of the central square beam hole with the rest of the parameters unchanged, the fundamental mode (Mode 1 in Figure 2-25) will always have a negative group velocity in the $\Gamma - X$ region.

In the $\Gamma - X$ region, there are four modes, as in Figure 2-25b; among them, Mode 1 and Mode 3 are longitudinal. We are primarily interested in the longitudinal modes, which will strongly couple to an electron beam. Mode 2 and Mode 4 are transverse modes that do not couple to the electron beam. Mode 4 is doubly degenerate with fields polarized in the y and z directions, respectively. In the $X - M$ and $\Gamma - M$ regions, when the symmetry of the y and z directions is broken, Mode 4 splits into two modes.

The electric field patterns of the longitudinal modes in the $\Gamma - X$ regions are shown in Figure 2-26. In the eigenmode simulation, there is no electron beam, but finally we will put a relativistic beam into an array of the unit cells, where the beam

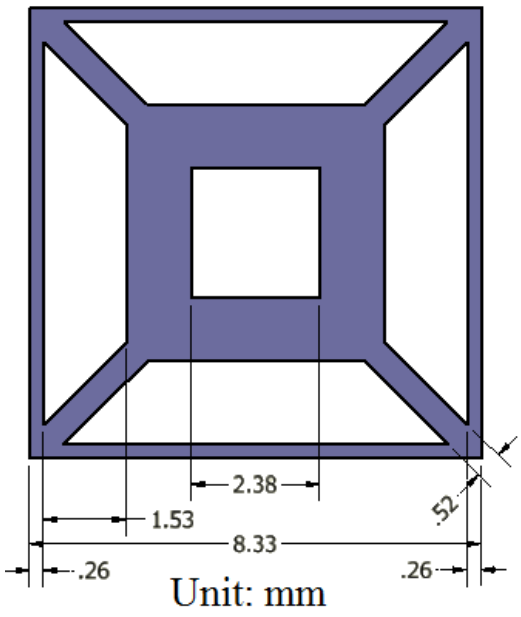

(a)

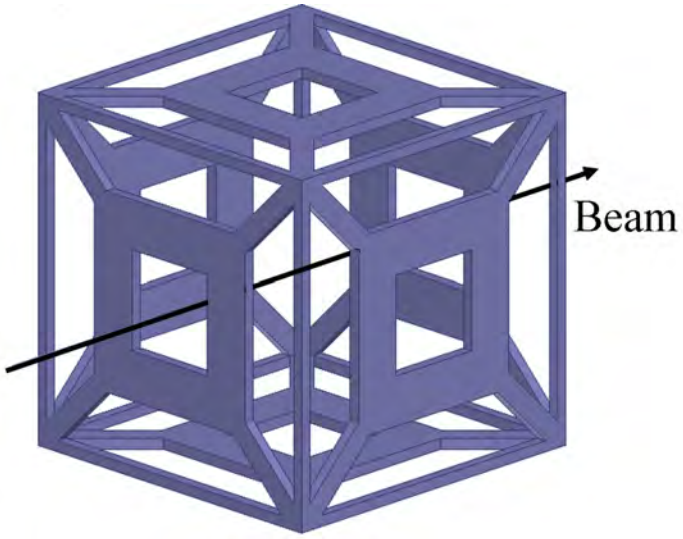

(b)

Figure 2-24: Unit cell design of the volumetric 3D metamaterial structure. (a) Face view. The thickness of each face is 0.26 mm. (b) 3D view. In later sections the electron beam will be introduced which goes through the center of the beam holes of the cells lying on the beam line.

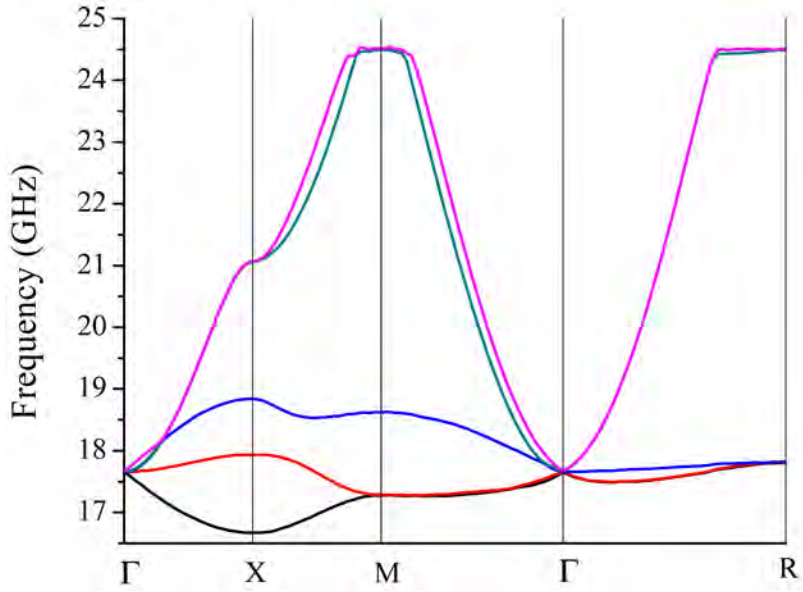

(a)

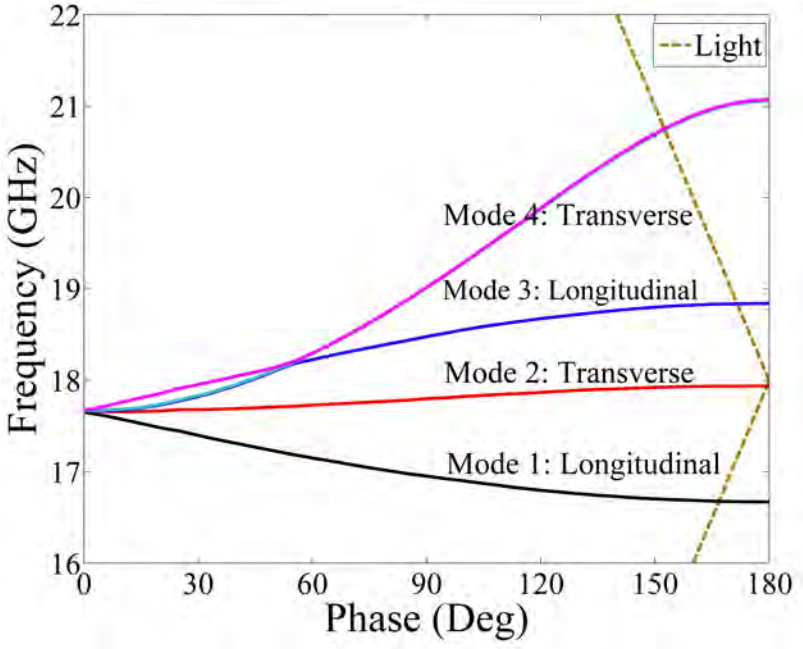

(b)

Figure 2-25: Brillouin diagram of a unit cell. (a) Different regions in the first Brillouin zone. (b) $\Gamma - X$ region dispersion showing intersection with the light line.

Table 2.6: Comparison of wave-beam interaction frequencies (unit: GHz).

	HFSS Eigenmode Solver	Effective Medium Theory	CST Wakefield Solver
Mode 1	16.7	16.6	16.6
Mode 3	18.8	19.1	18.7

lies on the axial line of the beam holes of the central-region unit cells, as denoted by the black arrows in Figure 2-26a, Figure 2-26b. With the electron beam traveling at near the speed of light, the synchronized points of the beam and the longitudinal modes are 16.7 GHz and 18.8 GHz. These are the points in Figure 2-25b where the light line intersects Modes 1 and 3, respectively. We will compare these frequencies calculated using the HFSS code with the frequencies calculated using the effective medium theory and the CST code later in this section, as shown in Table 2.6 below.

The quantitative axial electric fields at these synchronized points are shown in Figure 2-26d where Mode 1 has a field in the same direction within the same unit cell, while Mode 3 has the opposite direction.

2.6.3 Effective Medium Theory with Spatial Dispersion

One goal of this study is to investigate the interaction of an electron beam with the metamaterial medium. To get an analytical solution, we need to replace the actual structure of Figure 2-24 with an effective medium. The effective medium model must agree well with the HFSS model for the dispersion characteristics. Effective medium theory aims to model sub-wavelength periodic structures with a continuous medium. It is a method of geometry simplification under the principle of keeping equivalent electromagnetic characteristics.

We will use the set of fields of $\vec{E}$, $\vec{D}$, and $\vec{B}$ with spatial dispersion. The tensor $\epsilon_{ij}(\omega, \vec{k})$ includes both electric and magnetic responses, since $\vec{E}$ and $\vec{B}$ are related by $\nabla \times \vec{E} = -(\partial \vec{B}/\partial t)/c$. The dependence of $\vec{D}$ on $\vec{B}$ can be equivalently treated

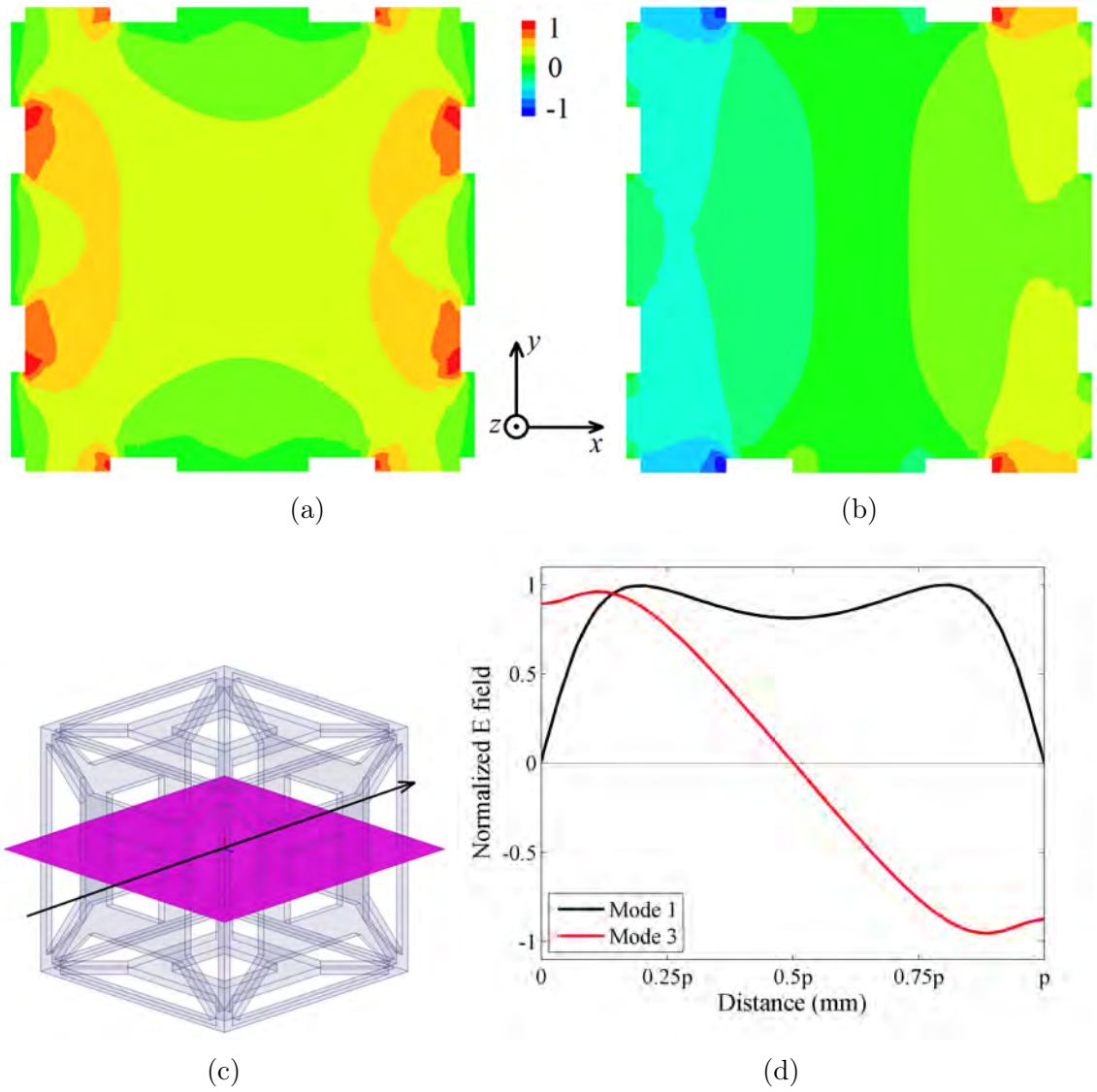

Figure 2-26: Field patterns of the longitudinal eigenmodes in the $\Gamma - X$ region. The cutting plane is the middle plane going through the center of the beam hole. Black arrows denote possible beam paths for the purpose of later sections. Waves propagate to the right. The fields are shown on a linear scale. (a) Mode 1 (the negative index mode), y and z directions are symmetric. (b) Mode 3 (the positive index mode). (c) Cutting plane and future beam position. (d) Axial field patterns at the synchronized points with a relativistic beam at the speed of light.

as a dependence of $\vec{D}$ on the spatial derivative of $\vec{E}$, i.e. a permittivity with spatial dispersion takes good care of both fields. Thus, it does not lose generality to set $\mu_{ij}(\omega) = \delta_{ij}$ [67].

In the simple case, permittivity and permeability only depend on frequency, since we assume that the local electric polarization at a point is decided only by the field at that point. From the Fourier transform

$$E_i(\omega, \vec{k}) = \frac{1}{(2\pi)^4} \int dt \int d\vec{r} \exp[-i(\vec{k} \cdot \vec{r} - \omega t)], \tag{2.25}$$

and the constitutive relation

$$D_i(\omega, \vec{k}) = \epsilon_{ij}(\omega, \vec{k}) E_j(\omega, \vec{k}), \tag{2.26}$$

we can see that when the field is not strictly local, the dependence of the field on $\vec{r}$ corresponds to the dependence of permittivity on $\vec{k}$ in the frequency domain. The inclusion of the spatial dispersion is also a natural requirement to study longitudinal waves, since otherwise the group velocity of the longitudinal waves goes to zero [67].

The general form of the dielectric tensor in optical crystals with spatial dispersion [68] is written as

$$\epsilon_{ij}(\omega, \vec{k}) = \epsilon_{ij}(\omega) + \alpha_{ijlm}(\omega) k_l k_m, \tag{2.27}$$

which comes as a Taylor expansion with the correction of the spatial terms, and the first non-zero terms are to the second order of $\vec{k}$. The zeroth order term $\epsilon_{ij}(\omega)$ is substituted with the plasma permittivity

$$\epsilon_p(\omega) = 1 - \omega_p^2/\omega^2, \tag{2.28}$$

since a 3D wire array is shown to be plasma-like in the GHz range [4]. ω_p is evaluated as the cut-off angular frequency (the corresponding frequency $f_p = 17.7$ GHz). Note that in this section, all the equations are in Gaussian units, and the Einstein summation notation is used.

We propose a trial solution of the permittivity tensor

$$\epsilon_{ij}(\omega,\vec{k}) = \begin{cases} \epsilon_p(\omega) + \dfrac{\alpha_1 k_i^2 c^2 + \sum\limits_{l\neq i} \alpha_2 k_l^2 c^2}{\omega^2 - \omega_p^2}, (j=i) \\ \dfrac{2\alpha_3 k_l k_j c^2}{\omega^2-\omega_p^2}, (j\neq i) \end{cases} \tag{2.29}$$

to use in the Maxwell equations in Gaussian units describing electromagnetic fields in a medium

$$\begin{aligned} &\nabla\cdot\vec{B} = 0, \\ &\nabla\cdot\vec{D} = 4\pi\rho_0, \\ &\nabla\times\vec{E} = -\frac{1}{c}\partial\vec{B}/\partial t, \\ &\nabla\times\vec{B} = \frac{1}{c}\partial\vec{D}/\partial t + \frac{4\pi}{c}\vec{j}_0. \end{aligned} \tag{2.30}$$

The pole we put in the α_{ijlm} terms is similar to that of the quadrupole transition of an exciton between two states [68]. Near a dipole transition, we have

$$\epsilon(\omega) = \epsilon_0 - \frac{\Omega_0^2}{\omega^2-\omega_{0s}^2}, \tag{2.31}$$

where $\omega_{0s} = \omega_s - \omega_0$ is the frequency difference between the two states, and Ω_0 is defined from $\Omega_0^2 = \text{constant}\cdot\left|\int \psi_s^*\vec{r}\psi_0 d\vec{r}\right|^2$, where ψ represents the wave functions of the two states. For a quadrupole mode, the Ω_0^2 changes to $\Omega_0^2 = \text{constant}\cdot\left|\int \psi_s^*\vec{r}(\vec{k}\cdot\vec{r})\psi_0 d\vec{r}\right|^2$, so near the quadrupole line, the permittivity has the form of

$$\epsilon(\omega,\vec{k}) = \epsilon_0 - \frac{\text{constant}\cdot k^2}{\omega^2-\omega_{0s}^2}, \tag{2.32}$$

Then we decide the remaining parameters α_1, α_2 and α_3 from fitting the dispersion curves calculated with the following wave equation derived from Equation (2.30) in the special case of no free charge or current

$$\det\left(\frac{\omega^2}{c^2}\epsilon_{ij} - k^2\delta_{ij} + k_i k_j\right) = 0. \tag{2.33}$$

Figure 2-27 shows the fitting results and the best fit of α_1, α_2 and α_3. In the $\Gamma - X$ region, the modes of interest (Mode 1 and Mode 3) are modeled well, and they are nearly straight lines with slopes proportional to $\pm\sqrt{-\alpha_1}$ with $|\alpha_1| \ll 1$. For the dispersion in the $\Gamma - X$ region of Mode 4, the assumption of treating the structure as a homogeneous medium is not as good as for the lower modes due to a smaller wavelength. However, Modes 1 and 3 are important to the interaction of an electron beam with the wave, so the quality of this fit, which is very good, is important. The same number of modes and similar changing patterns with frequency are not easily achieved by establishing an analytical model without the introduction of spatial dispersion. Spatial dispersion is not a slight correction here, but makes qualitative differences. This can happen when a pole exists, since the dispersion relation is modified most drastically in the vicinity of the pole, as even a small $\vec{k}$ can change the permittivity significantly, and additional roots of the dispersion equation may appear [68].

2.6.4 Wave-Beam Interaction Using Effective Medium Theory

Next we study the interaction of the volumetric metamaterial structure with a relativistic beam. Theoretically we can use the effective medium theory to predict the energy loss of the beam due to radiation.

Suppose a point charge moves in the x direction at $\vec{v} = v\vec{e}_x$ into the effective homogeneous medium. Charge and current densities are $\rho_0(\vec{r}, t) = q\delta(\vec{r} - \vec{v}t)$, $\vec{j}_0(\vec{r}, t) = qv\delta(\vec{r} - \vec{v}t)\vec{e}_x$. From the Maxwell equations as Equation (2.30), the equation for $E_i(\omega, \vec{k})$ is

$$E_i(\omega, \vec{k}) = i\frac{4\pi\omega}{c^2} A_{ij}^{-1} j_{0j}(\omega, \vec{k}), \tag{2.34}$$

where A is a matrix whose element A_{ij} is

$$A_{ij} = k^2\delta_{ij} - k_i k_j - \frac{\omega^2}{c^2}\epsilon_{ij}. \tag{2.35}$$

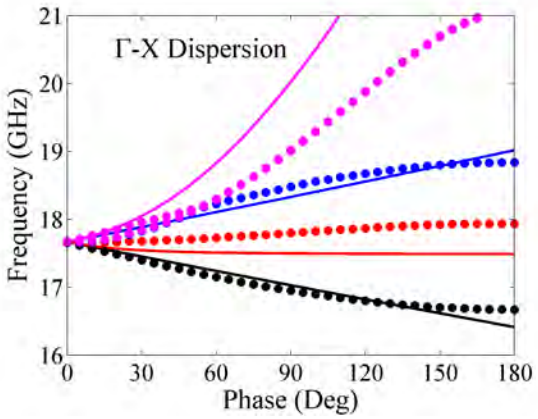

(a)

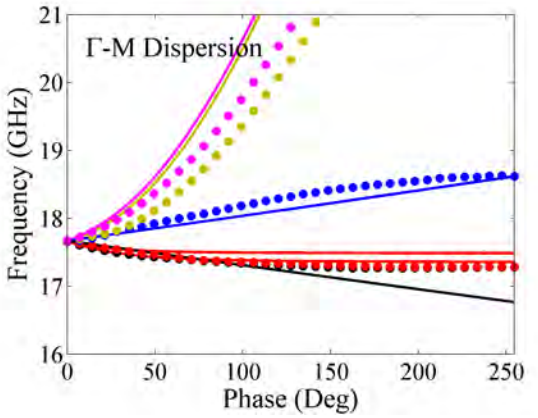

(b)

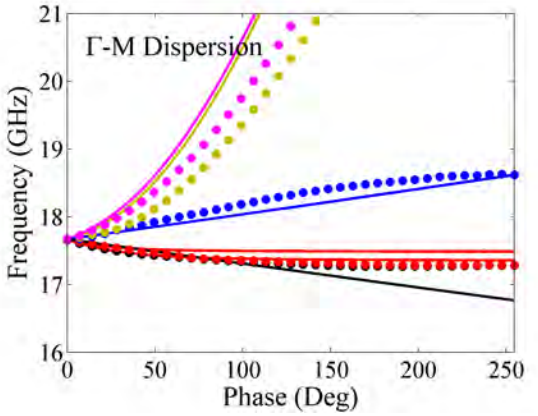

(c)

Figure 2-27: Fitting results of the dispersion curves. HFSS results are in dotted lines, and the fitting curves are in solid lines. The optimized parameters are $\alpha_1 = -0.0209$, $\alpha_2 = -0.0209$, $\alpha_3 = 0.0156$. (a) $\Gamma - X$. (b) $\Gamma - M$. (c) $\Gamma - R$. Modes 1, 2, 3, 4 are denoted with black, red, blue and magenta, respectively. In the $\Gamma - M$ region, Mode 4 splits into two modes.

The current of the point charge in the frequency domain is

$$j_{0j}(\omega,\vec{k}) = \frac{qv_j}{(2\pi)^4}\int dt\int d\vec{r}\delta(\vec{r}-\vec{v}t)\exp[-i(\vec{k}\cdot\vec{r}-\omega t)] \tag{2.36}$$

$$= \frac{qv_j}{(2\pi)^3}\delta(\omega-\vec{k}\cdot\vec{v}). \tag{2.37}$$

Note that only v_x is nonzero, so

$$E_x(\omega,\vec{k}) = \frac{iq\omega v}{2\pi^2c^2}A_{xx}^{-1}\delta(\omega-k_xv). \tag{2.38}$$

Then we inverse transform the $\vec{k}$ space back to the $\vec{r}$ space. The frequency spectrum $E_x(\omega,\vec{r})$ on the beam trajectory with $y=z=0$ is

$$E_x(\omega,\vec{r})|_{y=z=0} = -\frac{q\omega}{2\pi^2c^2}\iint dk_ydk_z\ \mathrm{Im}\left[\exp\left(i\frac{\omega x}{v}\right)A_{xx}^{-1}\right]\Big|_{k_x=\omega/v}. \tag{2.39}$$

The integrands become peaked when $|A_{xx}^{-1}|$ has a resonance, and the peaks mean that electromagnetic waves are excited by the moving charge [80]. We consider the loss in the effective medium model by changing the denominators in the spatial dispersion terms from $\omega^2-\omega_p^2$ to $\omega^2-\omega_p^2+i\gamma_l\omega$, where the $i\gamma_l\omega$ term represents a small ohmic loss, and $\gamma_l \ll \omega_p$.

We calculate $E_x(\omega,\vec{r})|_{y=z=0}$ numerically and find two peaks at 16.6 GHz and 19.1 GHz when v is close to c. These frequencies agree well with the frequencies calculated using the HFSS eigenmode solver, as shown in Table 2.6. Since the energy loss of the charge in the medium per unit path length is decided by $W = q\left(\vec{v}\cdot\vec{E}\right)/v$ at $\vec{r}=\vec{v}t$, these frequencies are also where the beam loses energy most intensively to the radiated field. This energy loss is caused by longitudinal modes (plasmons) only, and there is no velocity threshold in this case unlike the condition for normal Cherenkov radiation.

To test the above result, we use the CST Wakefield Solver in the Particle Studio to simulate fields radiated by a passing beam. The beam in the Wakefield Solver is represented with a line current with longitudinally Gaussian shaped charge. The

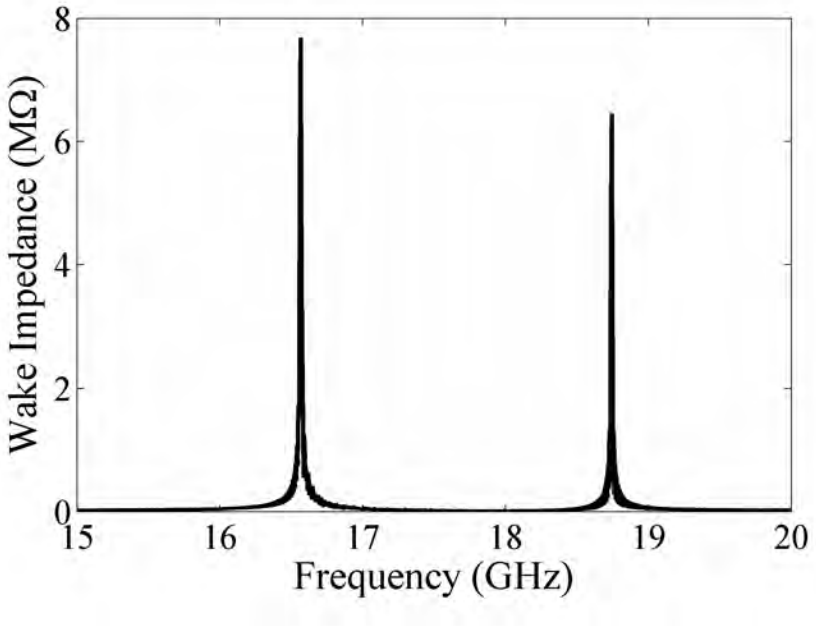

Figure 2-28: Longitudinal wake impedance spectrum. Peaks are located at 16.6 GHz and 18.7 GHz, corresponding to eigenmode 1 and 3.

model is set up with periodic boundaries on the side walls and 36 cells in the beam propagating direction. So the actual structure is an array of the unit cells infinite in the transverse directions resembling a homogeneous medium.

The wake potentials generated by a bunch with charge q at a distance of s behind it can be expressed as [23]

$$\vec{W}(y,z,s) = \frac{1}{q}\int_{-\infty}^{\infty}\left[\vec{E}\left(x,y,z,t=\frac{s+x}{v}\right) + \frac{\vec{v}}{c}\times\vec{B}\left(x,y,z,t=\frac{s+x}{v}\right)\right]dx, \tag{2.40}$$

and the longitudinal wake impedance is defined by

$$Z_x(\omega) = \frac{1}{c}\int_{-\infty}^{\infty} W_x(s)\exp\left(-i\omega s/c\right)ds. \tag{2.41}$$

We can simulate the wake impedance with the CST code, and Figure 2-28 shows the simulated spectrum of the structure with an infinite array of cells in the transverse

direction. For this simulation, we have used a 1 pC charge bunch traveling at the speed of light with a FWHM length of 2 mm. The peak interaction frequency points agree very well with the results of the effective medium theory, as shown in Table 2.6. Thus, the effective medium model successfully locates the interaction frequencies.

2.6.5 Radiation Pattern in a Volumetric Array of Metamaterial Unit Cells

In reality, we need a finite-size structure, so the simulation in CST is then performed by simulating the transmission of a relativistic beam through an array of the unit cells. The radiation pattern is naturally complicated by two additional effects. Firstly, the microstructure of the unit cells prevents the whole structure from acting strictly as a homogeneous medium, so when the beam passes through the inhomogeneous regions, transition radiation happens in addition to the Cherenkov radiation. Secondly, the structure is metallic, so it will deform the radiated field by imposing boundary conditions at metal walls.

We group the unit cells into an array as shown in Figure 2-29a. Cell numbers in the x, y, z directions are 10, 7 and 7, respectively. The beam travels through the central line along the $+x$ direction. Perfect absorbing boundaries are imposed at a distance of 7 cells away from the structure in the x, y and z directions. This setup enables us to study the radiation pattern in the bulk structure in an unbounded state.

Figure 2-29b shows the pattern of radiated longitudinal electric field E_x in the middle cutting plane ($y = 0$ plane). As a comparison, we show the radiation pattern in a volume of the same shape but built with a dielectric of $\epsilon = 1.5$ in Figure 2-29c. In the metamaterial case, electromagnetic energy goes backward, until the waves exit the structure at the same end where the beam enters. However, in the case of radiation in the dielectric medium, as in Figure 2-29c, electromagnetic energy travels forward, as is expected in conventional Cherenkov radiation.

Since the unit cell has the feature of 3D negative group velocity, we can observe backward radiation in directions different from the coordinate axes. Figure 2-30a

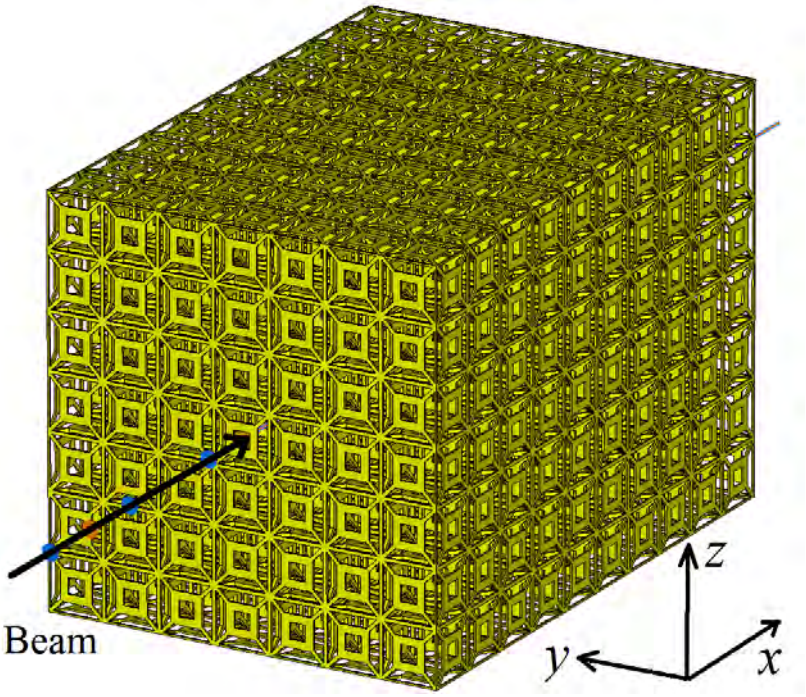

(a)

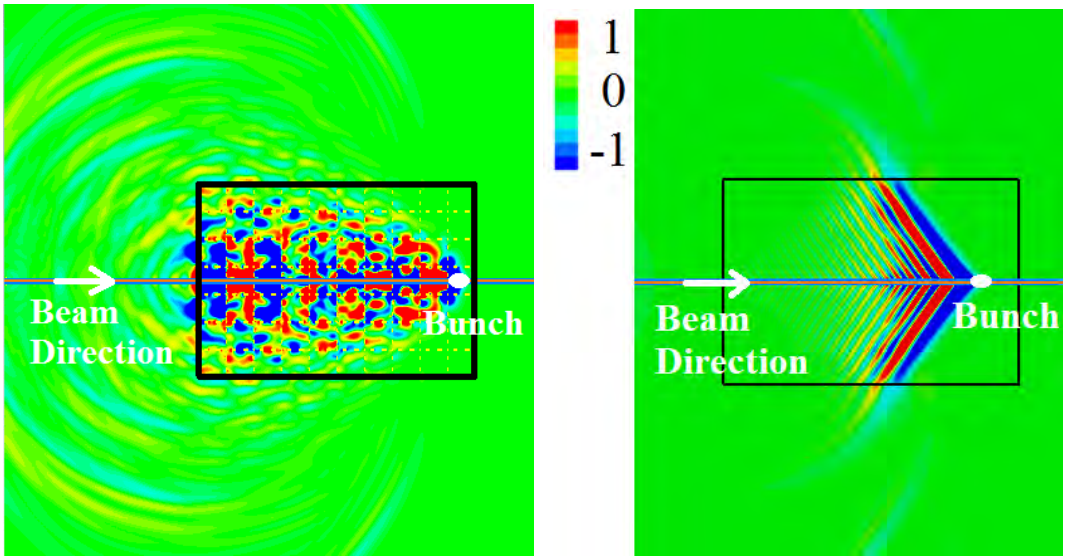

(b) (c)

Figure 2-29: Radiation pattern with a relativistic beam. (a) Illustration of the bulk structure. The beam passes through the line of $y = z = 0$. (b) Longitudinal E field (E_x) on $y = 0$ middle cutting plane for the metamaterial structure. The metamaterial region is enclosed in the black rectangles. (c) The same result for the volume mode of a dielectric with $\epsilon = 1.5$.

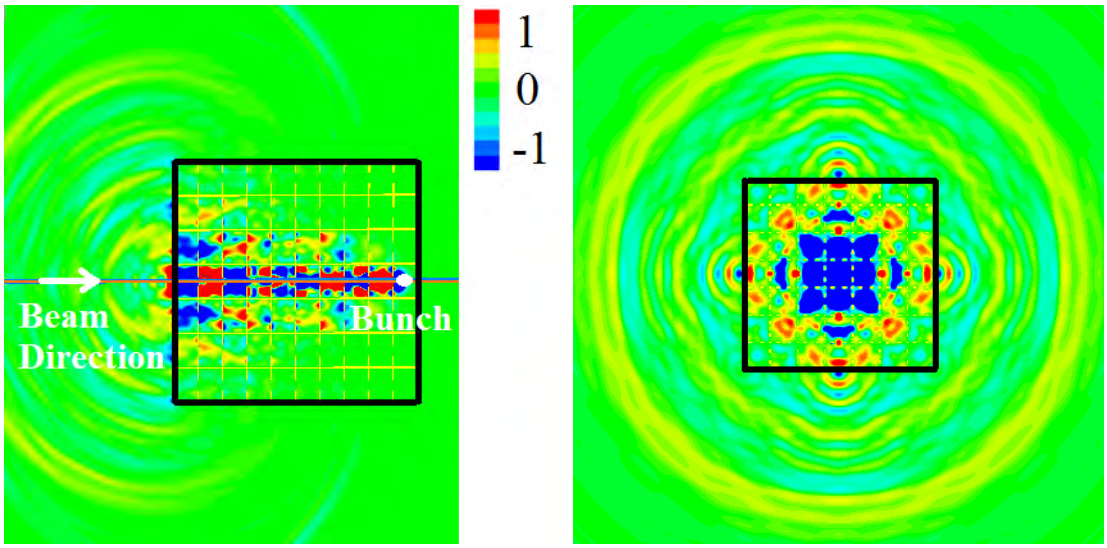

(a) (b)

Figure 2-30: 3D radiation properties. (a) Radiated E_x field on an oblique cutting plane rotated 45 degrees around the x axis starting from the $y = 0$ plane. (b) Radiation pattern on the cutting plane of x = constant, i.e. the cutting plane is perpendicular to the longitudinal direction.

shows the field on the cutting plane which is rotated 45 degrees from the $y = 0$ plane around the beam axis. This plane and the $y = 0$ plane are not symmetric geometrically, but a similar pattern of backward radiation is observed. Figure 2-30b shows the E_x pattern on a cutting plane perpendicular to the x direction. The metamaterial structure itself is not isotropic, but the waves grow as isotropic, nearly spherical wave fronts when they enter the vacuum region. So when the beam goes through the volumetric structure, a cone is formed behind it in the vacuum region where wave fronts are spherical-like and propagate backward.

2.6.6 Application of the Volumetric Metamaterial for Wakefield Acceleration

When a bunch travels through the structure, wakefields are generated by the Cherenkov radiation mechanism, and this leads to the possible application of wakefield acceleration. The scheme of wakefield acceleration is that an intense electron drive bunch

excites wakefields which can be used to accelerate a following witness bunch with a smaller charge [81], and the system is generally a dielectric-lined waveguide [82–84]. The metamaterial structure can operate in a manner similar to the dielectric wakefield acceleration regime but with only metal. This has the potential advantage of producing a more rugged structure and a structure that does not suffer from dielectric breakdown effects.

To fit the structure in a waveguide, we modify the unit cell from the 6-face cubic to two faces supported by four rods, as shown in Figure 2-31. 12 unit cells are aligned in a single row inside a waveguide. The coupling slots lock the frequency below the cut-off frequency of the waveguide. The eigenmode simulation shows that the cut-off frequency of the metamaterial structure shown in Figure 2-31 is 17.5 GHz.

The electron beams consist of a drive bunch and a witness bunch going through the central line in the $+x$ direction. The drive bunch is a Gaussian bunch of FWHM length 2 mm carrying a charge of 40 nC, and the witness bunch carries 1 pC and is 0.4 mm long. The spacing of the witness bunch behind the drive bunch is optimized to 25 mm to achieve the maximum average accelerating gradient. The drive bunch has an initial energy of 6 MeV, and the witness bunch 1 MeV.

Figure 2-32 shows the evolution of the two bunches in phase space. The drive bunch keeps losing energy to electromagnetic waves in the structure until it exits the structure, and the witness bunch is accelerated from 1 MeV to 3.1 MeV. This corresponds to an average accelerating gradient of 21 MV/m on the witness bunch path.

2.6.7 Conclusions

In this section, we present the design of a metallic metamaterial unit cell that can be used to fill all of space. The cell size is scaled to work for 17 GHz, and can be easily scaled to other frequencies. Of all the eigenmodes of the unit cell, the mode with negative group velocity is the lowest order mode and shows a longitudinal electric field pattern. Theoretically we have proved that a homogeneity approximation with spatial dispersion accurately describes the dispersion characteristics. Spatial

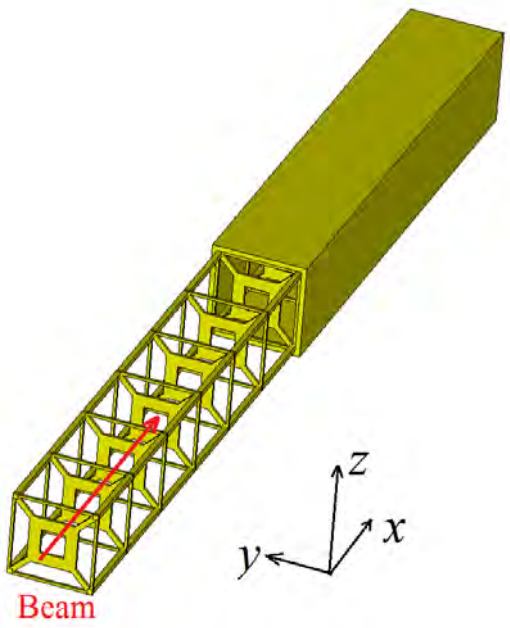

Figure 2-31: Structure for wakefield acceleration demonstration. Part of the waveguide is removed to show the inside structure.

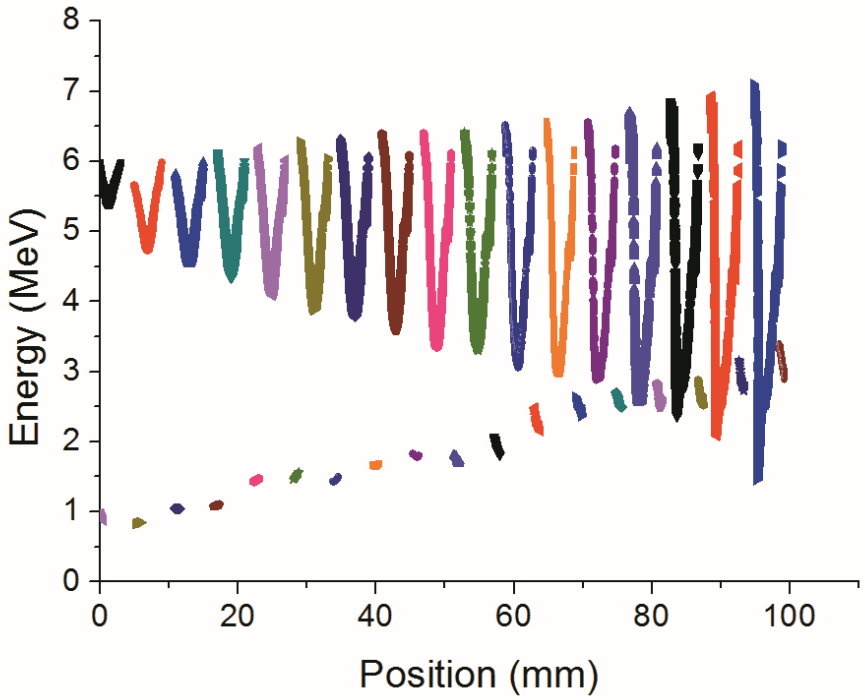

Figure 2-32: Phase space evolution in the x direction of the drive bunch (the top group) and the witness bunch (the bottom group) in the wakefield acceleration process. The time interval between every two snapshots is 0.02 ns. The plots of the two bunches at the same time are represented with the same color. The witness bunch is injected into the structure 25 mm after the drive bunch.

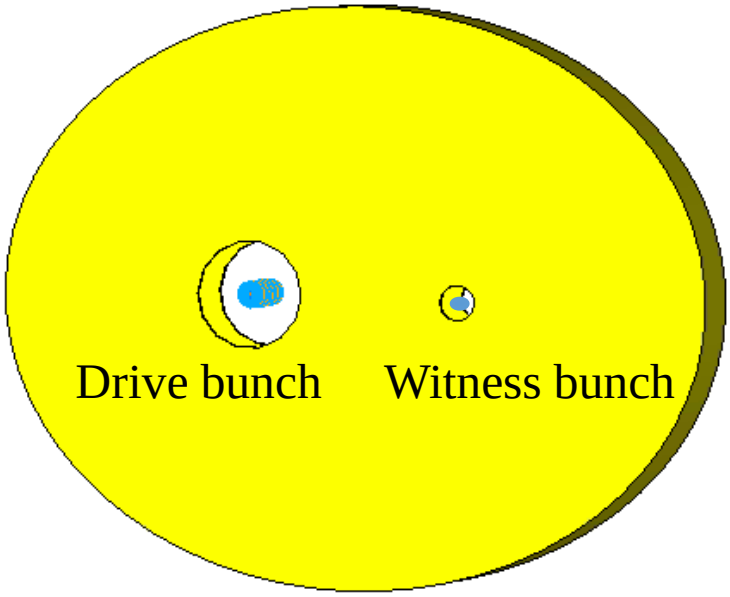

Figure 2-33: Elliptical corrugated structure illustration for the application of two-beam acceleration. The drive beam and the witness beam travel through the two focal points of the elliptical cavity.

dispersion yields a strong modification to the dispersion curves instead of a small modification, as additional modes appear. When interacting with relativistic electron beams, the metamaterial structure shows a backward radiation pattern. The wakefield generated by a drive bunch can be used to accelerate a following witness bunch.

2.7 Theory of Elliptical Deep Corrugation Structure

The bouncing field pattern of the circular deep corrugation structure in Fig. 2-2 inspires the idea of the elliptical subwavelength waveguide for two-beam acceleration. The structure is shown in Fig. 2-33. The drive and the witness bunch pass through two focal points of the ellipse.

Figure 2-34 plots the longitudinal electric field when the elliptical structure is excited by a drive beam. The decelerating wake of the drive bunch at one focal point first expands (Fig. 2-34a), and then it is reflected at the elliptical wall and changed

to the accelerating wake. It keeps propagating towards the other focal point where the witness bunch passes through (Fig. 2-34b).

For a 10 nC, 70 MeV drive bunch, an accelerating gradient of 100 MV/m is estimated at the witness bunch location with both the beam hole radii being 0.5 mm.

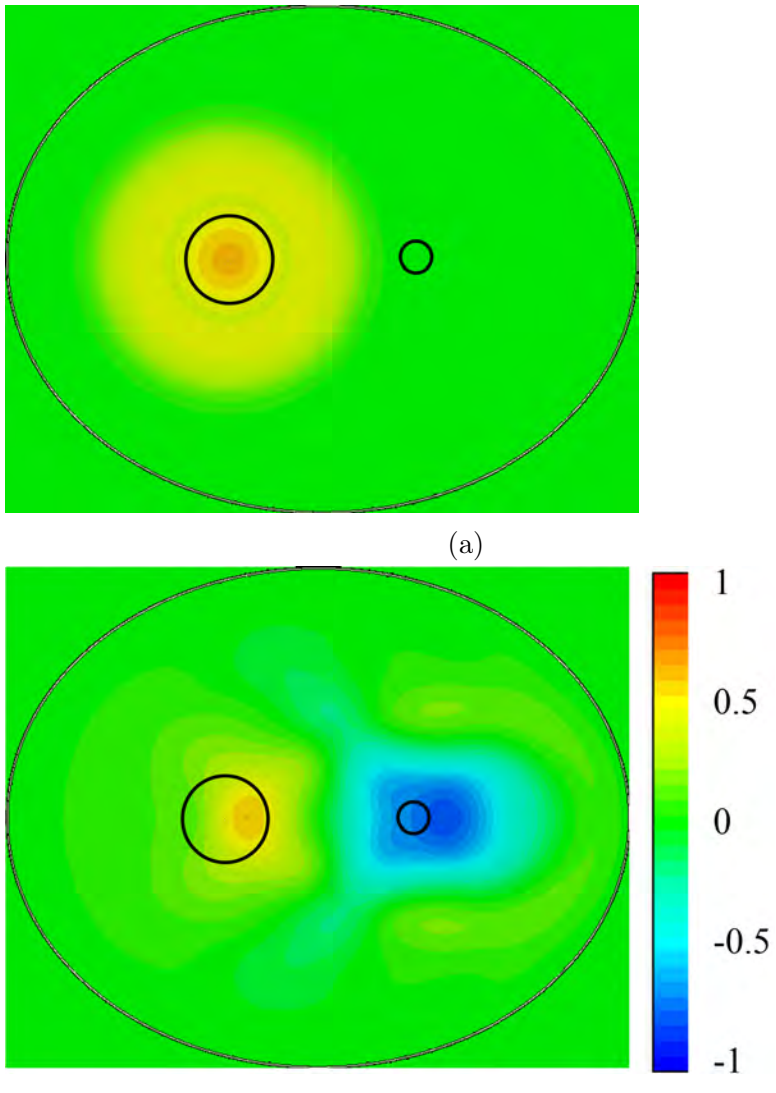

(a)

(b)

Figure 2-34: Longitudinal electric field when the elliptical corrugated structure is excited by a drive bunch traveling through the focal point on the left. (a) Expanding of decelerating wake (red). (b) Focusing of accelerating wake (blue).

Chapter 3

Experiment of Metamaterial Structures for Wakefield Acceleration

In this chapter, I will introduce the experimental study on the metamaterial wagon wheel structure. The corresponding theory is presented in Sections 2.3 to 2.5 in Chapter 2. The metamaterial wagon wheel structure was installed and tested at the Argonne Wakefield Accelerator (AWA) 65 MeV beam line in the Argonne National Laboratory.

Section 3.1 will introduce the experimental facilities at the AWA laboratory, Section 3.2 will introduce the fabrication of the metamaterial structure, Section 3.3 will present the cold test method and results, and Section 3.4 will present the beam test results. Finally, conclusions will be in Section 3.5.

3.1 Experimental Facilities

The Argonne Wakefield Accelerator (AWA) [52] at the Argonne National Laboratory is an electron accelerator with a research focus on wakefield acceleration. The AWA facility is known for the high bunch charge operation, and this feature greatly benefits the electron beam driven wakefield acceleration experiments in both the structure-based experiments and the plasma-based experiments [30, 34, 36, 38, 53, 61, 85–88].

There are two beam lines at the AWA facility, a drive beam line and a witness

Figure 3-1: Overall layout of the AWA facility, with the 65 MeV drive electron beam line, and the 15 MeV witness electron beam line.

beam line. An overall layout of the facility is shown in Fig. 3-1.

The drive beam line can generate 65 MeV electron bunches. The electron source is a Cesium Telluride photocathode lighted by a laser pulse or a pulse train. The electron gun operates at 1.3 GHz in the L-band. A photo of the photocathode electron gun in the magnet is shown in Fig. 3-2.

The electron beam can be generated as a single bunch or as a train of bunches, when the photocathode is excited by a train of laser pulses. There are laser splitters to double the number of bunches, so there can be 1, 2, 4, 8, 16 and 32 electron bunches in a train. At a rep rate of 1.3 GHz for the electron gun, the nominal spacing between two bunches is 230.8 mm. Movable stages are available in the beam splitting system, so the spacing between neighboring bunches in a train can be tuned within a small range around the nominal spacing of 230.8 mm.

The drive beam line at the AWA facility can generate the world's highest charge in short electron bunches devoted to wakefield acceleration research [52]. The maximum charge in a single electron bunch can reach 100 nC, and the maximum charge in a bunch train can reach 600 nC in total.

The electron beam then goes through six linac sections operating at 1.3 GHz and gets accelerated to a final energy of 65 MeV. A photo of the linac sections is shown in Fig. 3-3. The 65 MeV beam then travels to the experimental area. A section of

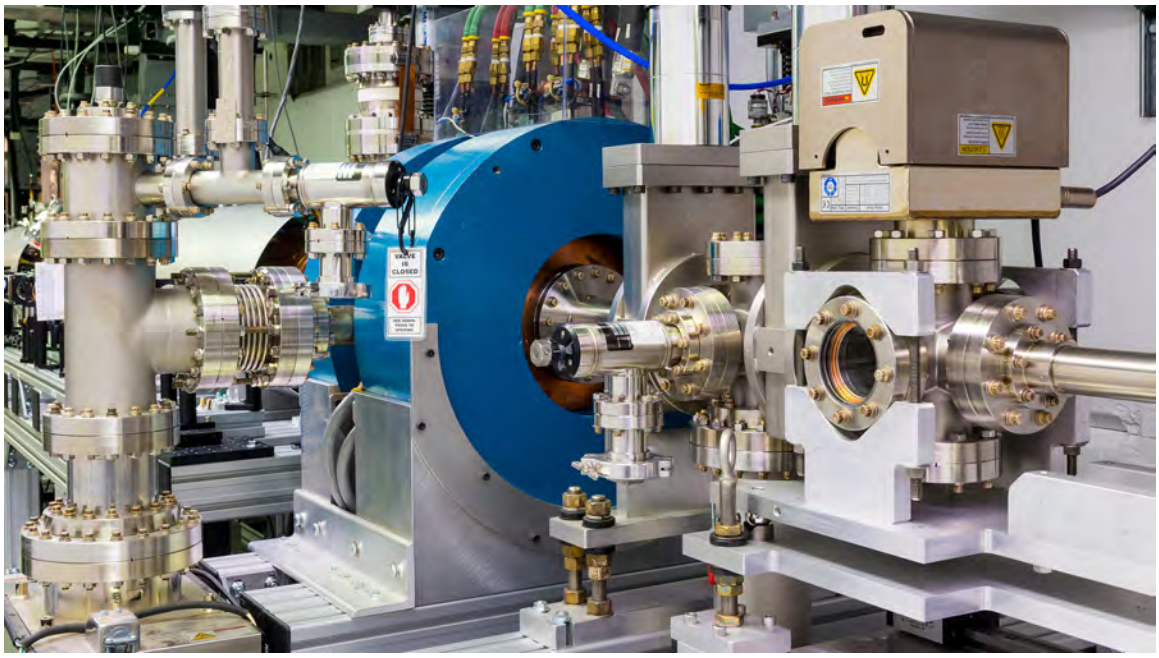

Figure 3-2: Photo of the photocathode electron gun of the 65 MeV drive electron beam line. Photo credit: AWA group.

the beam line in the experimental area is shown in Fig. 3-4.

Besides the 65 MeV drive beam line, there is also a separate 15 MeV witness beam line. The witness beam line can generate single electron bunches with a bunch charge ranging from 50 pC to 60 nC. As can be seen in Fig. 3-1, the witness beam travels in the opposite direction as the drive beam, and there is a U-turn to guide the witness beam into the experimental area for the two-beam acceleration experiments.

The purpose of the witness beam line is to demonstrate acceleration by sending in a small witness bunch as a probe after the drive beam in the two-beam acceleration regime. In our experiment of the wagon wheel structure, we use only the 65 MeV drive beam line, with the goal of measuring the extracted wakefield power from the drive beam. The illustration of the wagon wheel structure experimental setup is shown in Fig. 3-5. The vacuum chamber with the wagon wheel structure sitting inside is installed on the 65 MeV drive beam line. Details about installation of the wagon wheel structure into the chamber will be discussed in the Section 3.2.

There are various beam line components for beam manipulation and diagnostics

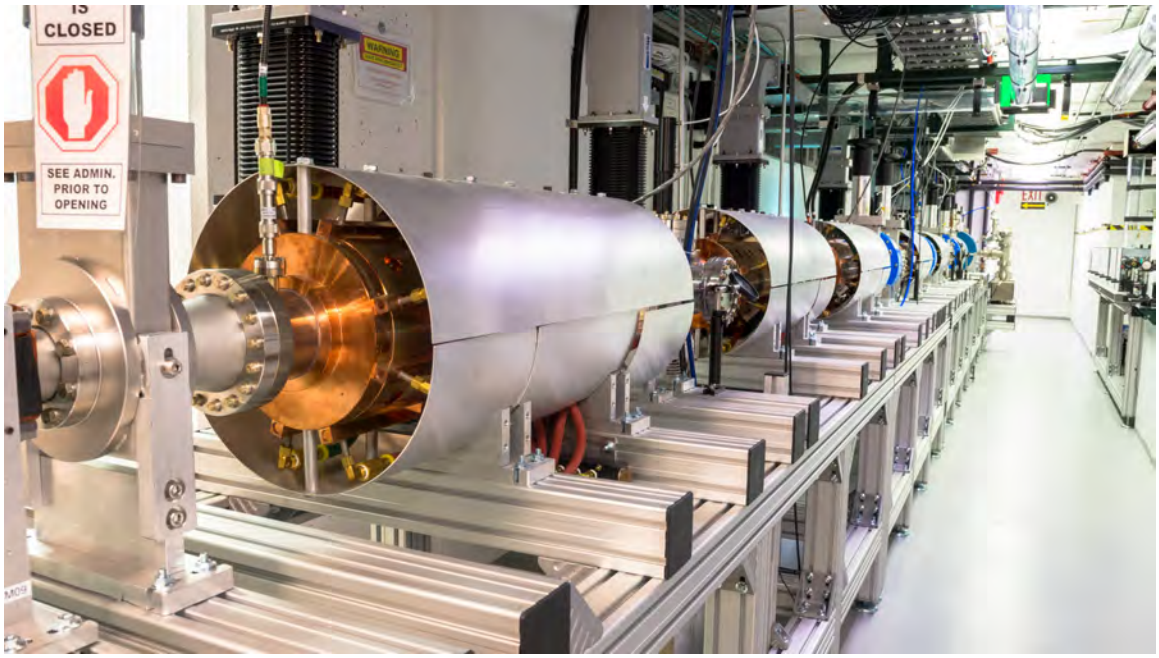

Figure 3-3: L-band 1.3 GHz linac sections. There are six linac sections to accelerate the drive beam to a final energy of 65 MeV. Photo credit: the AWA group.

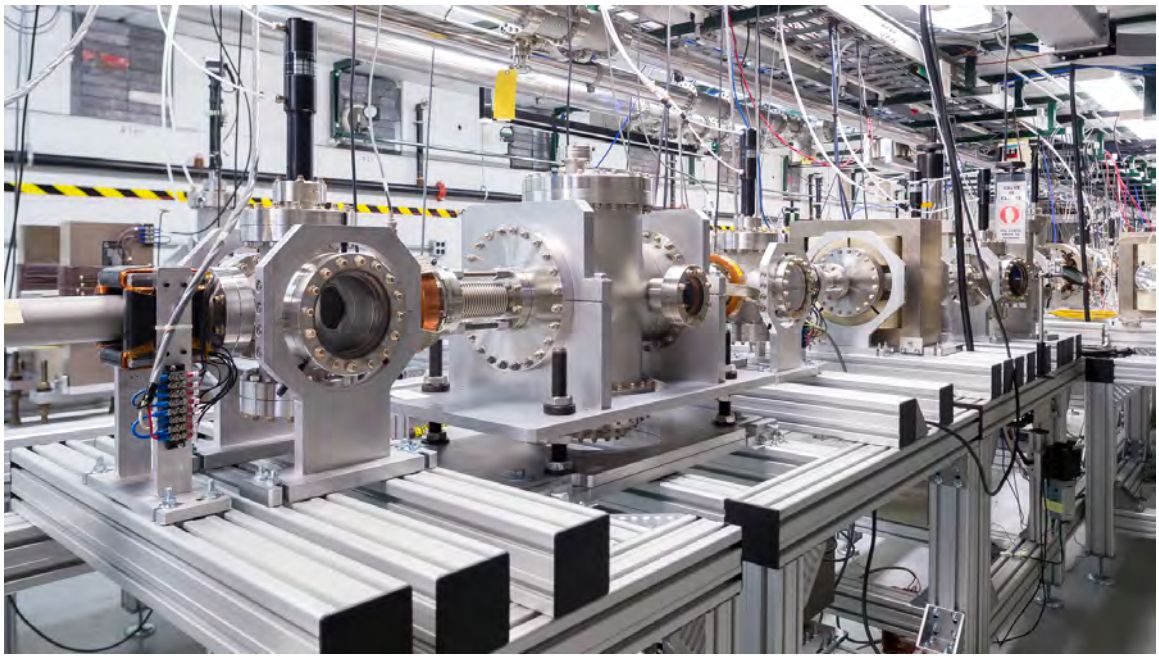

Figure 3-4: Beam line photo of the experimental area at AWA. Photo credit: the AWA group.

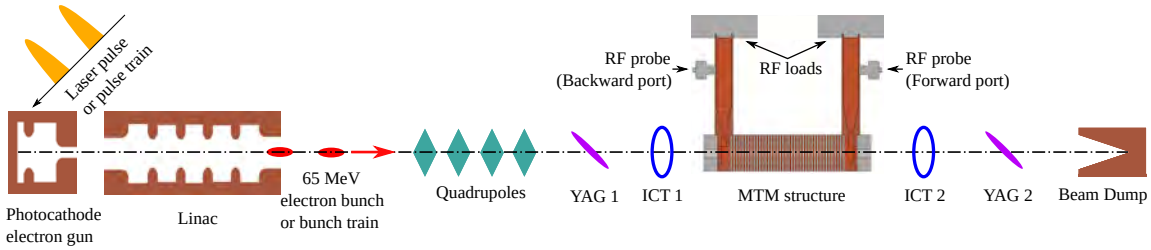

Figure 3-5: Schematic drawing of the overall experimental setup.

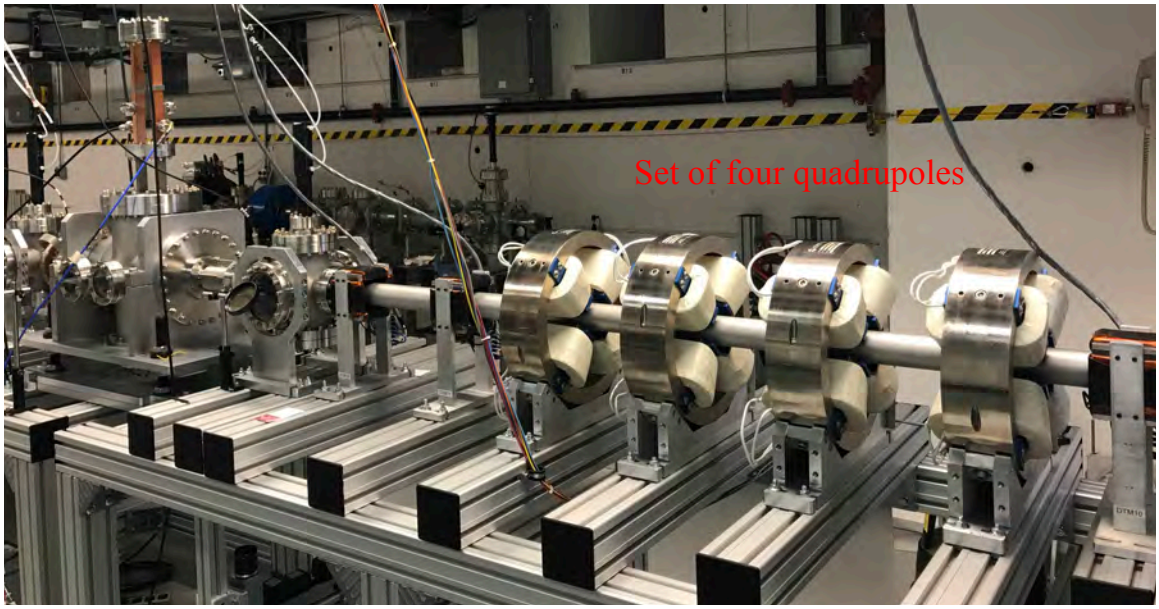

Figure 3-6: Photo of the set of four quadrupoles for beam steering between the accelerator section and the test vacuum chamber.

purposes.

For the beam confinement purpose, quadrupoles are used for minimizing the transverse beam size. There is one set of quadrupoles between the linac section and the experimental area. Figure 3-6 is a photo of the set of four quadrupoles, with the beam coming in from the right side, and going into the experimental area on the left of the photo.

To measure the transverse beam profile, there are removable yttrium aluminum garnet (YAG) screens at different locations of the beam line: one before and one after the metamaterial structure to measure the transverse beam size at the two locations.

To measure the charge sent to the structure location and the charge transmitted

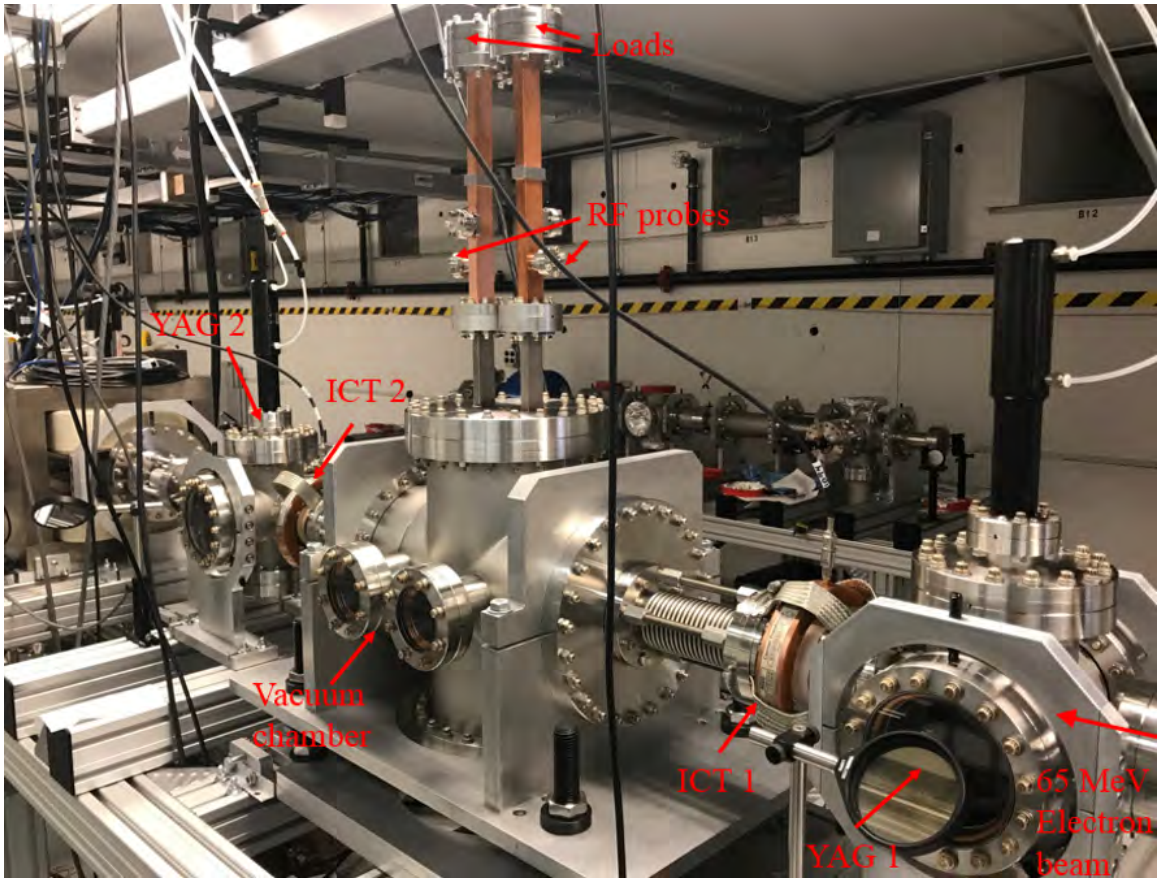

Figure 3-7: Beam line photo with the YAG screens, the integrating current transformers (ICTs), the vacuum chamber, and the RF pick-up system.

through the structure, two integrating current transformers (ICTs) were installed, one before and one after the metamaterial structure. A photo with the YAG screens, the ICTs, and the vacuum chamber holding the wagon wheel structure is shown in Fig. 3-7. There is also one ICT monitor close to the electron gun to measure the total emitted current.

The sample traces of the ICT signals are shown in Fig. 3-8. ICT1 is closest to the gun for the total charge, ICT2 is right before the structure, and ICT3 is right after the structure. The ICT can integrate the measured current signal in a short time window to measure the total current in the short electron bunches with good accuracy. The bunch length varies with charge but is generally around rms length of 1 mm. For example, the bunch length (in z direction) for 45 nC is σ_z =1.2 mm in

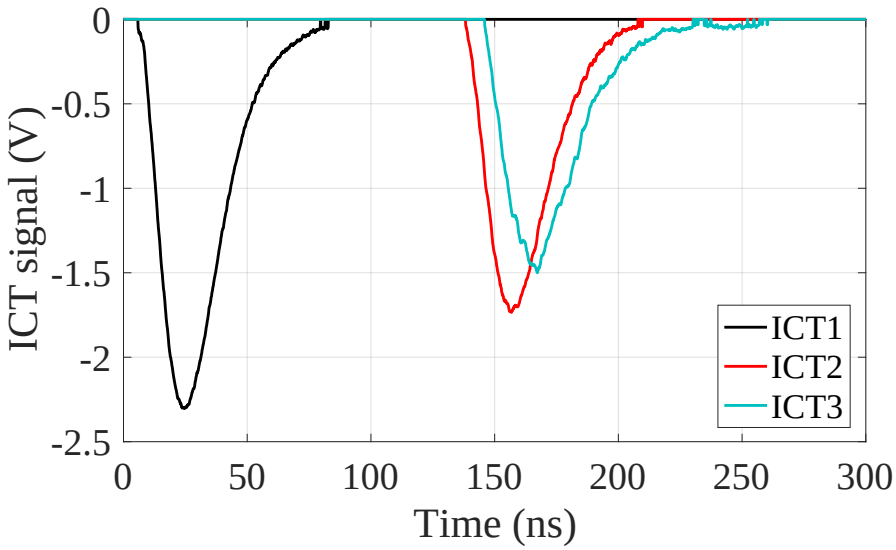

Figure 3-8: Sample traces of the ICT signals for a single 45 nC bunch passing by. ICT1 is closest to the gun for the total charge, ICT2 is right before the structure, and ICT3 is right after the structure. Integration of each ICT signal trace gives the transmitted charge at each location.

a Gaussian distribution. The current pulse on the ICT from such electron bunches is a few tens of nanoseconds long, while the bunch spacing at 1.3 GHz is only 0.77 ns. So when a train of electron bunches travel through, we cannot tell the individual current peaks corresponding to each individual bunch in the train, but integration of the current trace will give the total charge transmitted in the train.

With this setup, electron bunches of up to 45 nC per bunch were sent through the 6 mm diameter beam hole of the wagon wheel structure with almost 100% transmission from the ICT measurement. The transmission is calculated as the ratio of the integration of ICT3 signal to the integration of ICT2 signal.

The generated output power is then guided into two X-band WR90 waveguides, and the power is measured from the calibrated RF probes, as shown in Fig. 3-7. The signals at the RF probes are measured with a fast oscilloscope.

There are two output ports, the backward port close to the beam entrance and the forward port close to the beam exit. In this setup, the reversed Cherenkov radiation phenomenon can be directly verified by comparing the power in the two ports. The

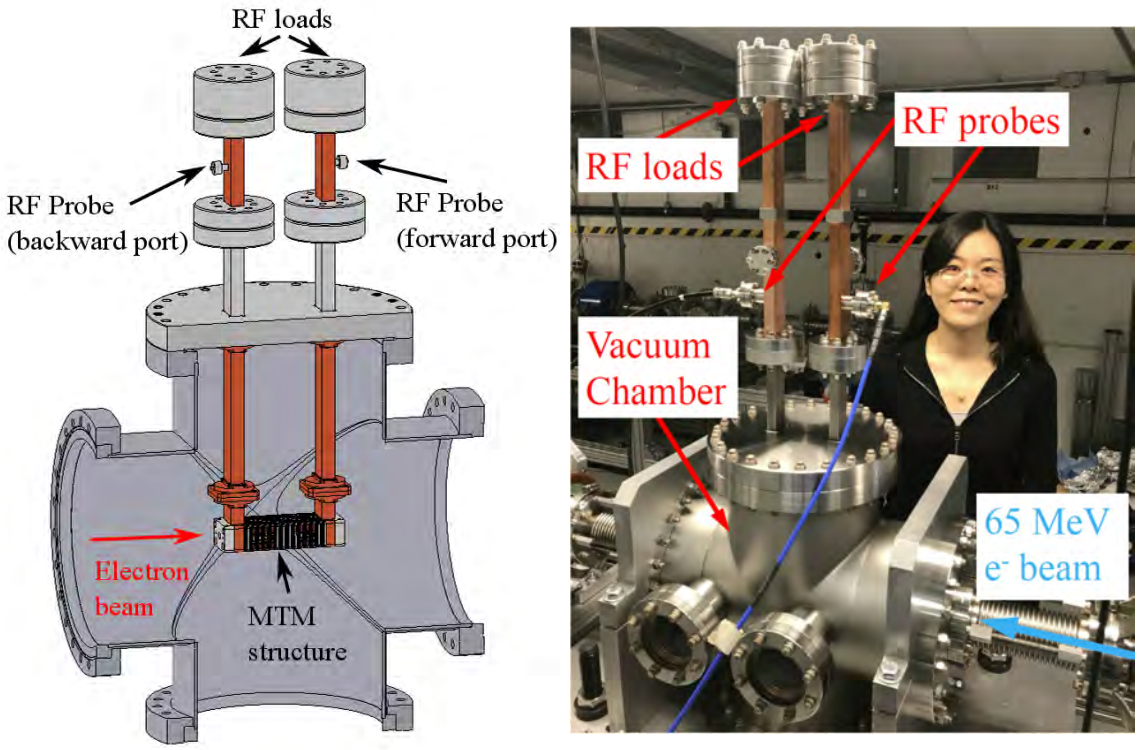

(a) (b)

Figure 3-9: CAD drawing and lab photo of the test chamber holding the wagon wheel structure. (a) CAD drawing. The wagon wheel structure hangs on the two WR90 waveguides inside a 10-in vacuum chamber. The 65 MeV electron bunch goes through the center of the 40-cell wagon wheel test structure. (b) Lab photo of the test chamber inserted on the beam line.

backward port is expected to get most of the power from a radiated wakefield traveling backwards. Finally the microwaves are guided into the RF loads and the used electron beam is dumped.

The CAD drawing and the lab photo of the test chamber are presented in Fig. 3-9. In the next section, fabrication of the structure will be introduced.

3.2 Structure Fabrication

3.2.1 Full Assembly

The full assembly of the metamaterial structure built at MIT is shown in Fig. 3-10. The test structure is hanging on the top flange of the test vacuum chamber by the

two X-band WR90 waveguides. Two rectangular holes with the same dimension as the WR90 waveguides were drilled on the top flange to let the microwaves through. The 10-in top flange goes on top of the 10-in test vacuum chamber together with the structure and the waveguides as shown in Fig. 3-9 on the beam line.

In the bottom of the photo is the clamped metamaterial structure. Fabrication of the metamaterial structure will be introduced in the following Section 3.2.2. Fabrication of the waveguides, the copper and the stainless steel (SST) ones, will be introduced in Section 3.2.3.

3.2.2 Metamaterial Structure Part

The metamaterial structure part comprises of wagon wheel plates in SST and spacer plates in copper, forming a 40-cell period structure in an alternating pattern. At the two ends are the copper output couplers and the end plates in SST for better compressing the clamped structure. Figure 3-11 shows a photo of the clamped metamaterial structure with the two output couplers. The effective interaction part is 8 cm long, excluding the output ports and the SST end pieces.

A photo of the wagon wheel plate and the copper spacer plate is shown in Fig. 3-12. Each plate is 1 mm thick, so one period, containing one SST plate and one copper plate, is 2 mm long. The fabrication method we chose for the plates is wire electrical discharge machining (EDM). In this way, multiple plates can be machined in a stack at the same time.

On the wagon wheel plate, the wagon wheel feature is in the central area, while the outside holes are for clamping (the four bigger ones) and alignment (the two smaller ones). The material for the wagon wheel plates is SST for good material strength and ease of cutting. Though the ohmic loss of SST is higher than copper, the SST material is still tolerable in the structure. The transmission loss from one output port to the other is around 2 dB, which will be explained in further details in Section 3.3.

For the spacer plates, the material is copper to reduce the ohmic loss. The central hole on the spacer plate has the same dimension as the outer radius of the wagon wheel plate. The additional cuts on the four edges of the copper plate are designed

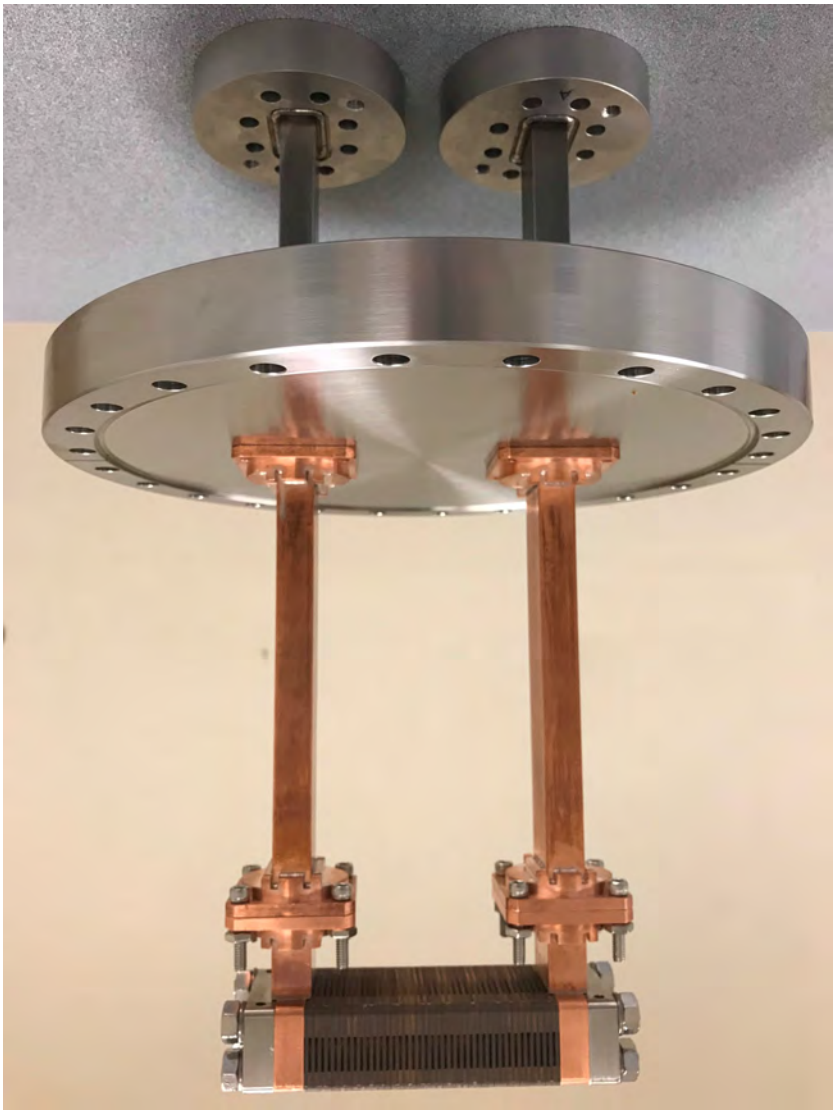

Figure 3-10: Photo of the metamaterial structure hanging on the two waveguides from the top flange. The two flanges on the top are later connected to RF probes for power measurement, which are not shown.

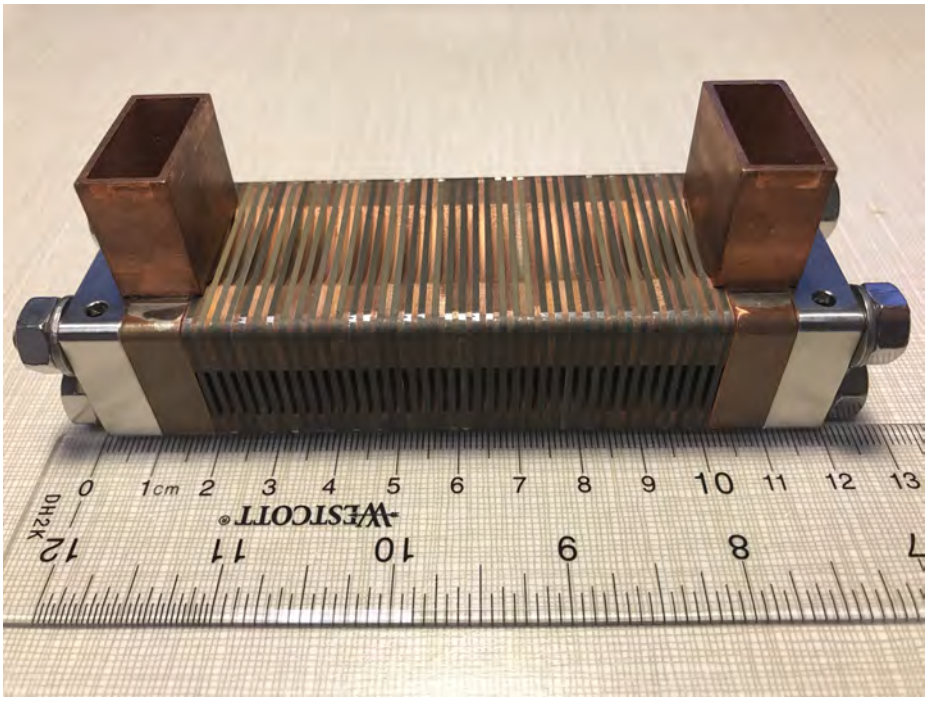

Figure 3-11: Photo of the clamped metamaterial structure part with output couplers on the two ends.

to reduce the surface area in contact with the neighboring plates in order to reduce the air trapped between the plates. This can help with the pumping speed in the vacuum chamber.

A drawing of the output coupler is shown in Fig. 3-13a, with the front cross section view on the left and the side cross section view on the right. The top part of the coupler is a taper piece done by wire EDM, which transforms almost adiabatically from a small slot cut on the side wall of the structure to the WR90 waveguide. The bottom part of the coupler is a coupling cell with a slightly larger radius than the outer radius of the wagon wheel structure to minimize the coupling loss.

The photo of the output coupler part after brazing is shown on the left of Fig. 3-13b. The brazing was done by the CuSil alloy of 72% silver and 28% copper.

On the right of Fig. 3-13b is the SST end pieces with a thickness of 0.375 inches. They are designed to help clamp the whole structure on the two ends. On the SST end pieces, there are beam holes of the same dimension as the beam aperture of the

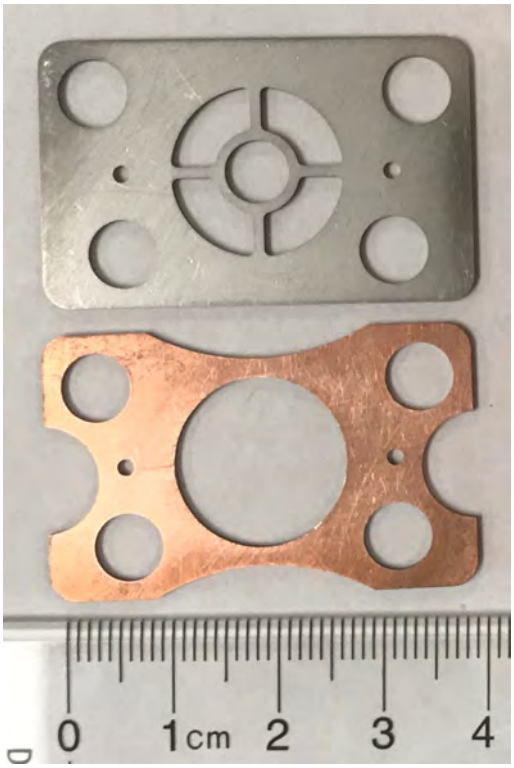

Figure 3-12: Photo of the wagon wheel plate in stainless steel (top) and the spacer plate in copper (bottom)

wagon wheel plates. With this design, if the electron beam injects at a large angle with respect to the central axis mistakenly, the electrons will collide with the SST end pieces instead of with the wagon wheel plates. So the SST end pieces can help reduce beam damage on the structure. The two slots cut from top to bottom are designed for the venting purpose.

3.2.3 Waveguides

On the top part of Fig. 3-9, there are two X-band SLAC flanges, which are later connected to the two calibrated RF probes (not shown). The two flanges were welded to the stainless steel waveguides. The SST waveguides were chosen for better support of the RF probes and loads standing on the top. The other ends of the SST waveguides were welded to the 10-in top flange. A photo of the welded SST waveguides is shown in Fig 3-14.

Under the 10-in flange, two copper WR90 flanges were bolted into the bigger flange

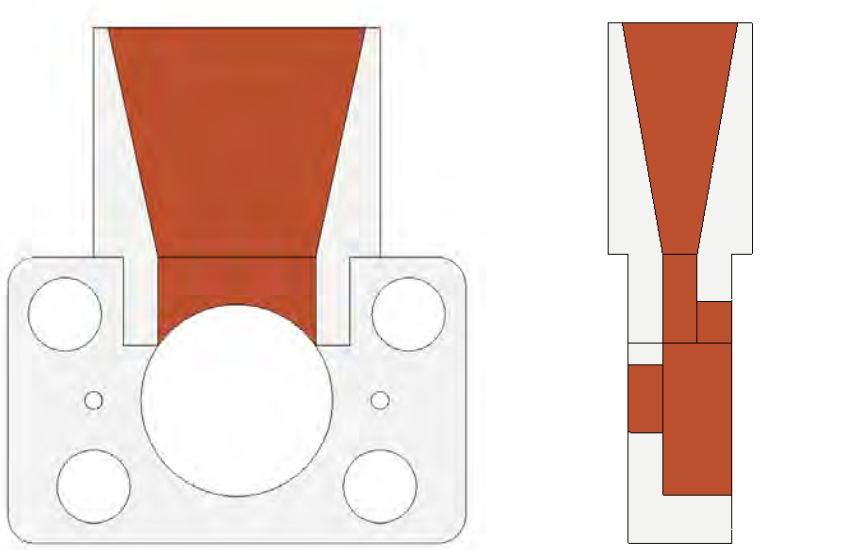

(a)

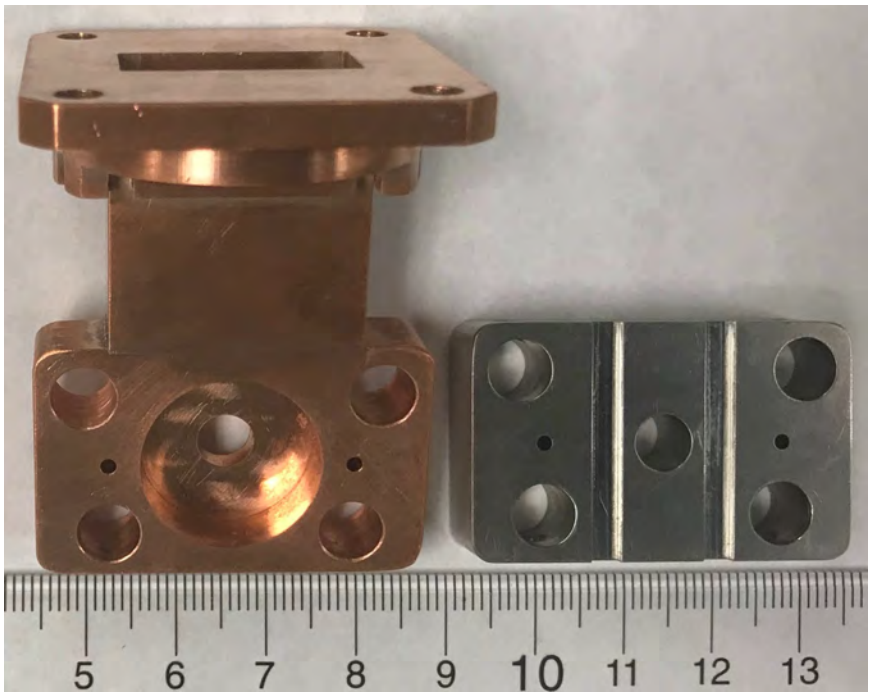

(b)

Figure 3-13: Output couplers and end piece. (a) Drawings of the output coupler design in the front cross section view (left), and the side cross section view (right). (b) Photo of the output coupler after brazing on the left, and the stainless steel end piece for clamping on the right.

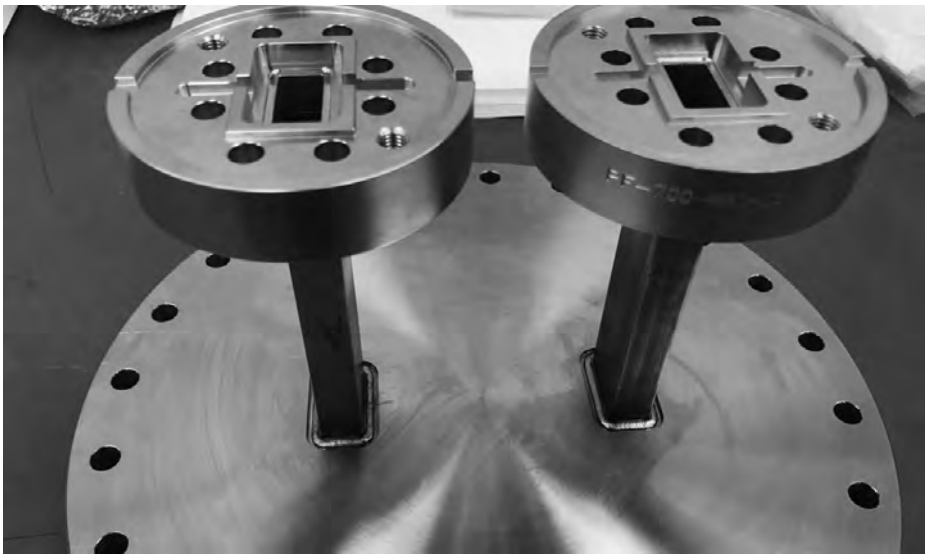

Figure 3-14: Photo of the welded SST waveguides onto the 10-inch top flange.

from the bottom. Then the copper waveguides were brazed to the WR90 flanges on the two ends with the CuSil brazing alloy. The brazing material was picked to avoid unwanted elements which can poison the photocathode.

3.3 Cold Test

Cold test is an RF measurement performed on a vector network analyzer (VNA) at a low microwave power level. From the cold test, we can benchmark the RF characteristics of the structure with the simulation to get prepared for the beam test. The same structure was used for the cold test as for the beam test.

In the cold test of the wagon wheel structure, there are two measurements, the transmission measurement from a two-port cold test as discussed in Section 3.3.1, and the electric field distribution measurement from a bead pull test as discussed in Section 3.3.2.

3.3.1 Transmission Measurement

The transmission measurement gives the loss in the process of transmitting the RF power from one port of the structure to the other. In the two-port system, transmission loss in dB is equal to $-S_{21}$. We have aimed for a small transmission loss around the operating frequency in the structure design.

The VNA measurement setup is shown in Fig. 3-15. Two ports of the VNA were connected to the two output ports on the 40-cell wagon wheel structure, respectively. The VNA cable has an SMA type of connector on the structure side, so there were two SMA to waveguide adapters to convert the power from the VNA into the fundamental TE_{10} mode of the waveguide.

The result of the transmission measurement is presented in Fig. 3-16. It shows the amplitude of the S_{21} parameter between the two ports from three ways, the simulation, the cold test before cleaning, and the cold test after cleaning. The difference between 'before cleaning' and 'after cleaning' is that we performed the cold test before and after sending the structure to the vacuum shop for vacuum-compatible cleaning.

From Fig. 3-16, we can see that the S_{21} from the cold test is slightly lower than in simulation. This might be caused by slight fabrication errors. Another observation is that the S_{21} is improved by the cleaning procedure. The transmission loss is about 2 dB at the design frequency 11.4 GHz, while the simulation results is 0.7 dB. The measured transmission is still good in the range of 11 GHz to 12 GHz with less than 3 dB of loss.

3.3.2 Beadpull Measurement

The beadpull measurement was also done with the VNA in the cold test lab to verify the dispersion curve of the traveling wave structure. In the beadpull measurement, we moved a small bead along on the central axis of the structure, while the two ports of the structure were connected to the VNA. The signals from the VNA can be transferred into the fundamental mode at the X-band in the metamaterial structure.

The bead is made with a thin piece of silver foil wrapped into a cylinder shape

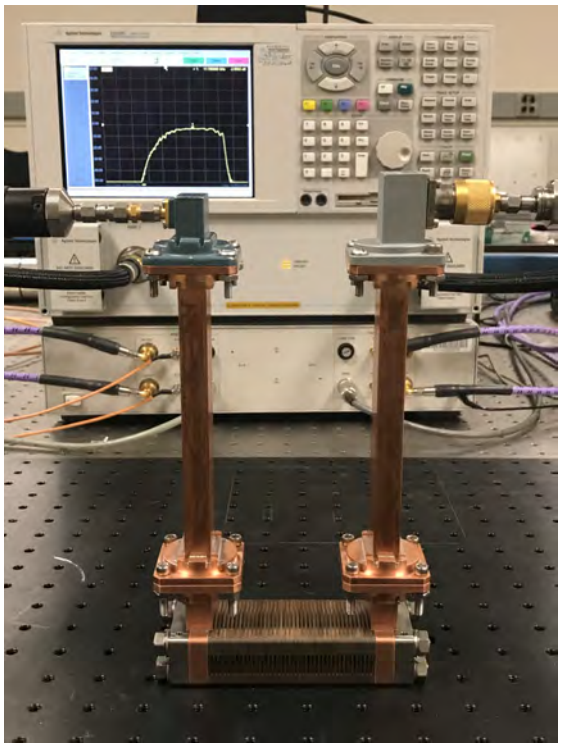

Figure 3-15: Photo of the 40-cell structure under cold test with the VNA at MIT.

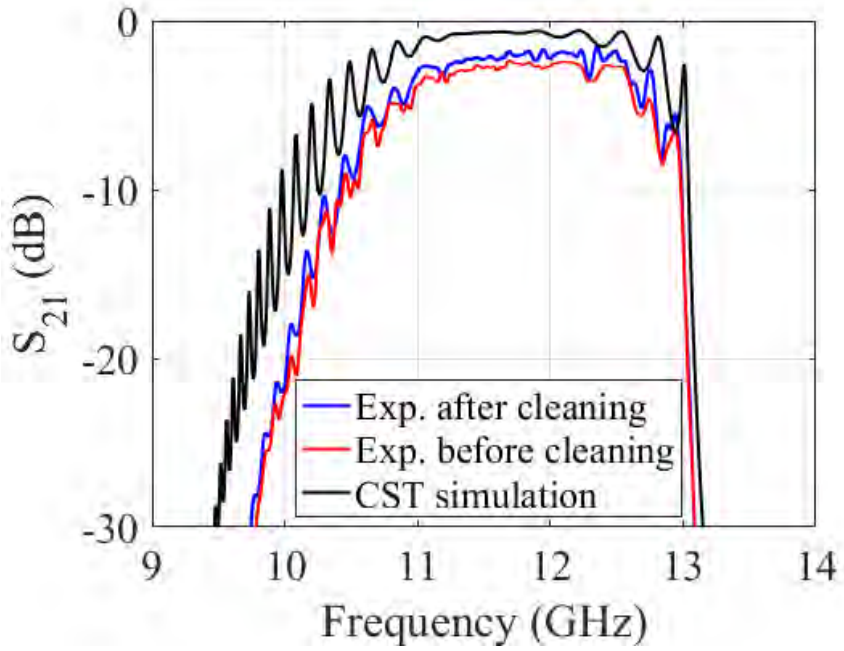

Figure 3-16: Transmission S_{21} of the 40-cell structure benchmarked with the CST simulation. The black curve is the simulation result from the CST Microwave Studio, and the red and the blue curves are the experimental measurement before and after structure cleaning.

around a thin wire. The small bead can exert a perturbation to the electromagnetic field in the structure, and when the bead is pulled through the structure, we can calculate the properties of the electromagnetic field from measuring the response of the bead perturbation on the VNA.

A photo for the setup of the beadpull measurement is presented in Fig. 3-17. The bead was attached to a wire driven by a step motor. The motor step size is 1 mm. The S parameters were measured for each step.

The beadpull measurement can reveal the amplitude and phase of the on-axis electric field, and the principle is described in [89] based on a nonresonant perturbation theory. The theory works for a single-moded structure, and a small perturbing object whose influence on the electromagnetic field can be treated as a dipole. The theory relates the change in the S_{11} parameter to the electric field by the following equation,

$$\Delta S_{11}(z) = A|E(z)|^2 e^{-2j\theta(z)}, \tag{3.1}$$

where $E(z) = |E(z)|e^{-j\theta(z)}$, and A is a constant.

The vector network analyzer can measure the amplitude of S_{11}, which is related to the amplitude of the electric field, and the phase of S_{11}, which is related to the phase of the electric field. At each fixed frequency, the bead is pulled through the whole length of the structure with 1 mm step size, and the amplitude and phase of the electric field are derived for this fixed frequency. From several frequency data points, we can plot the dispersion curve ω vs. k for the excited mode.

Figure 3-18 shows the measurement results at 11.4 GHz. Figure 3-18a presents the amplitude of the perturbed ΔS_{11} along the z axis (longitudinal direction). The decrease in the amplitude of ΔS_{11} is a result of the ohmic loss in the round trip for the microwave signal. When z gets larger, the S_{11} signal experiences more ohmic loss from the longer round trip, so accordingly $|\Delta S_{11}|$ gets smaller. Figure 3-18b presents the phase evolution of the perturbed ΔS_{11}. Two adjacent data points are from measurement at two locations with an 1 mm distance. The vertical axis plots the imaginary part of ΔS_{11}, and the horizontal axis plots the real part of ΔS_{11}. When

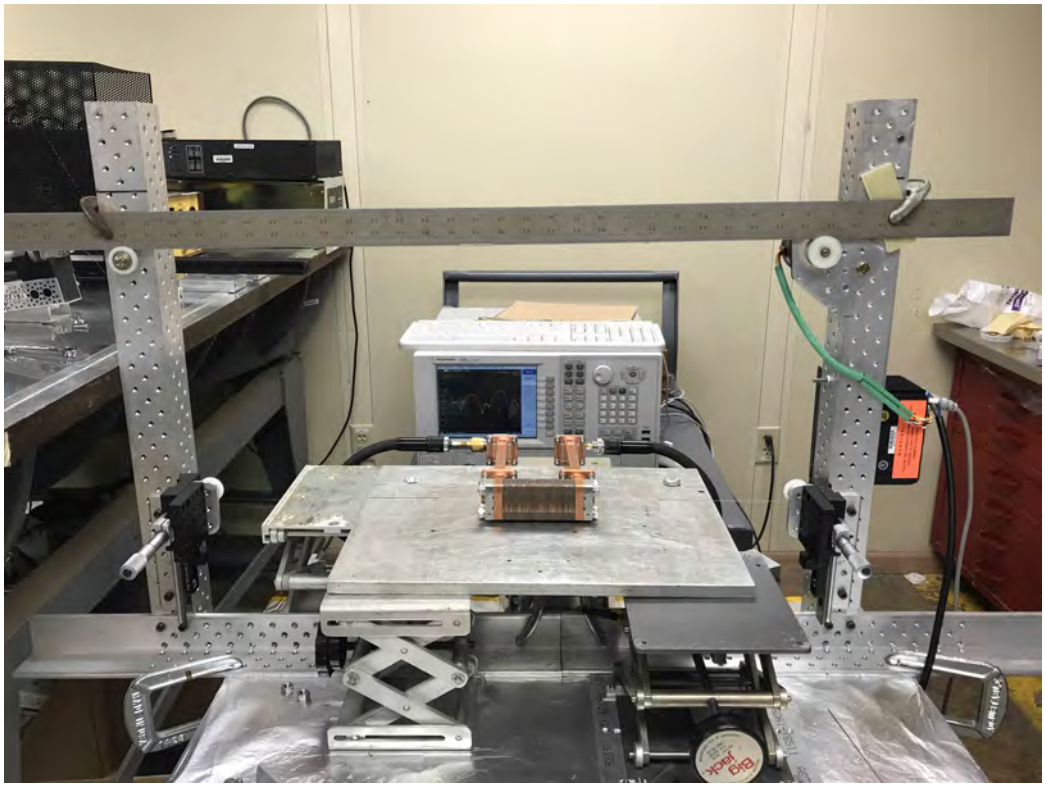

Figure 3-17: Experimental setup for the bead pull test. The two ports on the wagon wheel structures are attached to the two ports of the VNA. A small bead is attached to a thin string which goes through the center of the beam aperture. The string is driven by a step motor to make 1 mm move at each step.

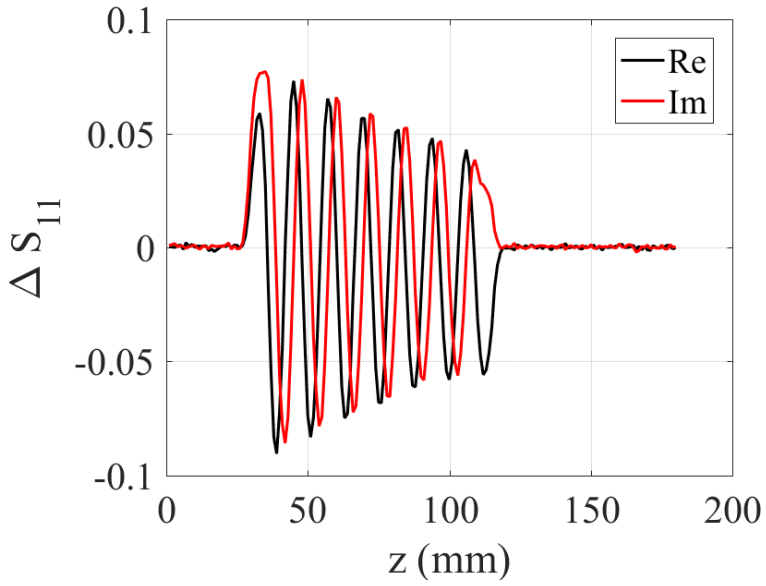

(a)

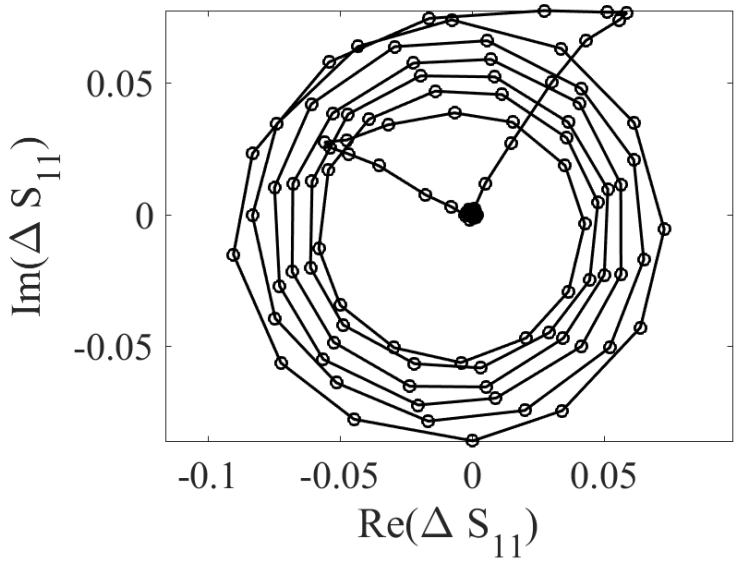

(b)

Figure 3-18: S_{11} measurement results from the beadpull measurement at the design frequency of 11.4 GHz. The z axis is in the longitudinal direction, and the bead travels on the central axis of the 6 mm beam aperture. (a) Amplitude of the perturbed ΔS_{11} along the z axis. (b) Phase of the perturbed ΔS_{11}. The vertical axis plots the imaginary part of ΔS_{11}, and the horizontal axis plots the real part of ΔS_{11}.

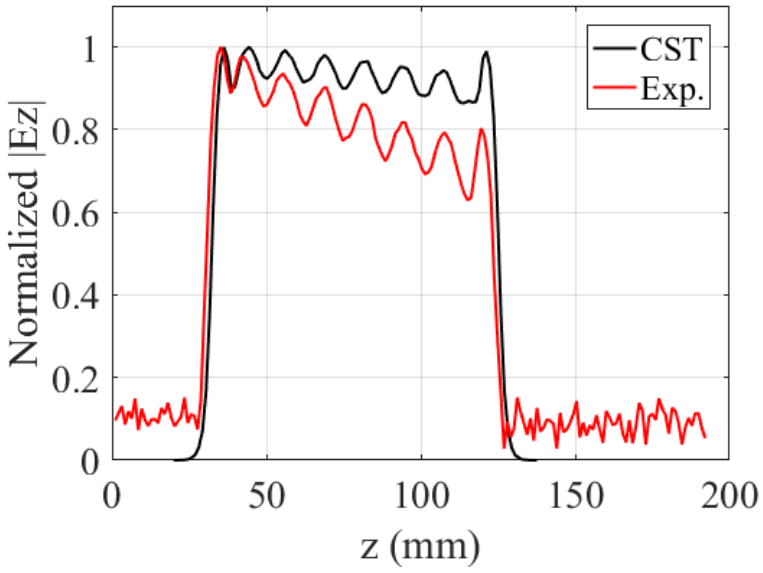

(a)

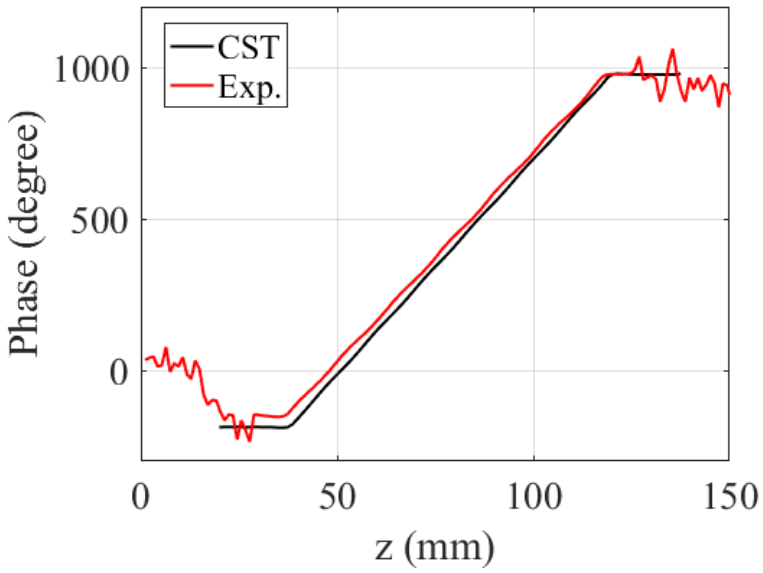

(b)

Figure 3-19: Amplitude and phase of the longitudinal electric field E_z on the beam axis from the bead pull measurement and the CST Microwave Studio Simulation. (a) Amplitude of E_z. (b) Phase of E_z.

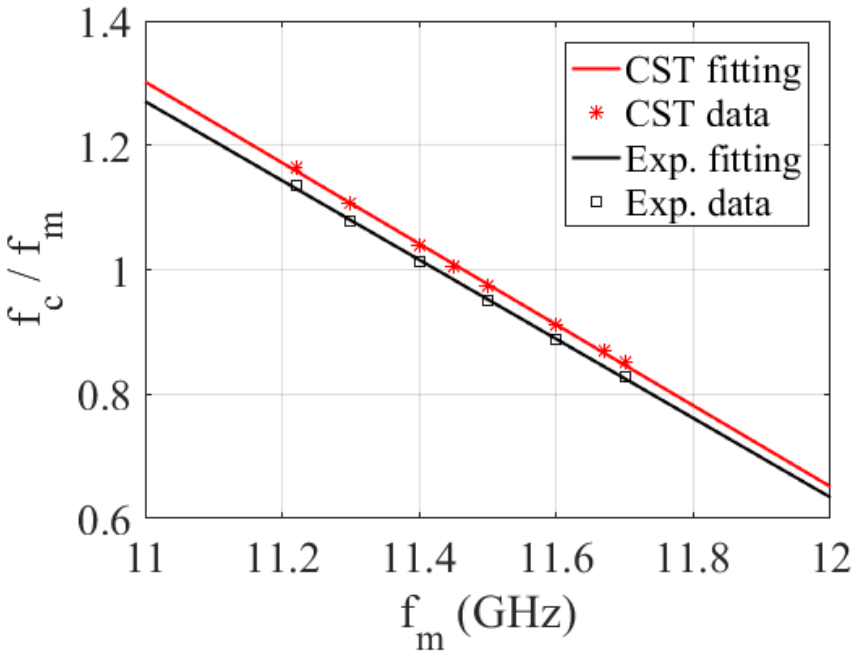

Figure 3-20: Benchmark of the dispersion relation measured from the beadpull test with the simulation result from the CST Microwave Studio.

z gets larger, the data points rotate anticlockwise inward, and the phase evolution follows a good circular pattern. This indicates a constant phase velocity everywhere in the metamaterial structure.

Figure 3-19 shows the processed results at 11.4 GHz from the data acquired in Fig. 3-18. Figure 3-19a shows the amplitude of the longitudinal electric field E_z along the central axis from the beadpull test, together with the benchmark from the CST Microwave Studio simulation. The oscillations in the field amplitude correspond to the design frequency of 11.4 GHz, and this proves the 40-cell metamaterial structure to be a subwavelength structure. The fall in the amplitude on the right side is from the ohmic loss again, and the difference between the experiment and the CST simulation indicates a bigger ohmic loss in experiment. The difference between the experiment and the simulation is 1.3 dB, and this result is in agreement with the transmission measurement as described in Section 3.3.1.

Figure 3-19b shows the phase of the longitudinal electric field E_z at 11.4 GHz.

The bead pull measurement result agrees perfectly with the CST simulation, which means that the angular wavenumber k at 11.4 GHz has a perfect agreement between simulation and measurement. Another feature is that the phase has almost a linear dependence on the axial position, so the phase velocity is constant from the subwavelength design. This is a different feature from conventional corrugated waveguide structures.

With the bead pull test repeated at several other frequency points, we can calculate the angular wavenumber corresponding to each frequency, and then plot the dispersion relation as ω vs. k. The result is shown in Fig. 3-20, with great agreement between experiment and simulation.

The conclusion of the bead pull measurement is that the interaction frequency of the traveling wave with the beam is 11.42 GHz and it agrees well with the design frequency. The same structure used for the bead pull test was cleaned and then went into the vacuum chamber on the AWA beam line for the beam test.

3.4 Beam Test Results

The 40-cell wagon wheel structure was tested with the 65 MeV electron beam at the Argonne Wakefield Accelerator. We sent in both single bunches and bunch trains with two bunches, and the experimental results will be described in the following sections, respectively.

3.4.1 Single Bunch Experiment

During the experiment, we sent in single electron bunches with varied charge. Smaller charge bunches from 3 nC to 15 nC were generated by the laser with the excimer amplifier turned off. The laser pulse in this case was only 1.5 ps long. With the excimer laser turned on, higher intensity laser pulses can be achieved to generate intense electron bunches. The highest charge successfully sent through the structure was 45 nC. When the excimer amplifier was on, the laser pulse length was 6 ps long.

The laser intensity was increased bit by the bit to the highest case, and thousands

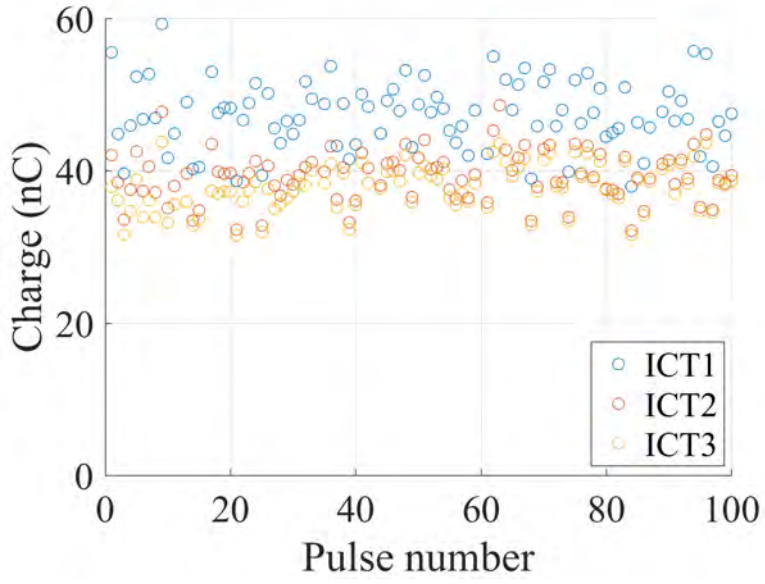

(a)

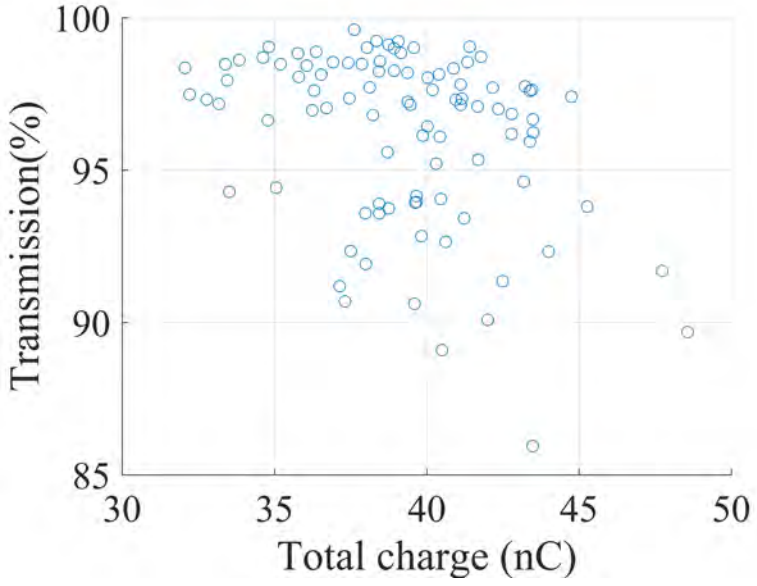

(b)

Figure 3-21: Charge transmission for the highest charge case. (a) ICT signals at different locations on the beam line. ICT1: closest to the electron gun; ICT2: right before the structure; ICT3: right after the structure. Results for 100 shots are shown. (b) Charge transmission calculated as the ratio of charge after the wagon wheel structure (ICT3) to the charge right before the wagon wheel structure (ICT2). The horizontal axis shows the charge measured by ICT2.

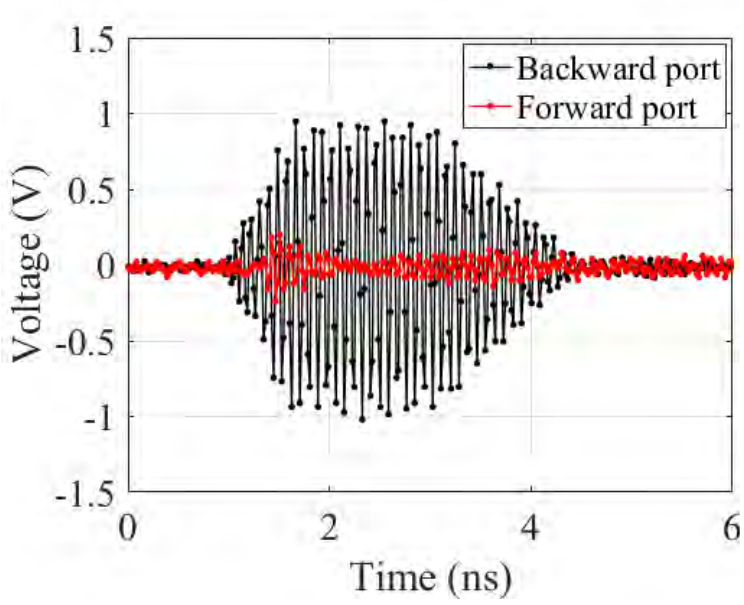

Figure 3-22: Voltage signals of the extracted microwave from a single bunch. The voltage signal from the RF probes was directly measured on the oscilloscope.

of pulses were fired at each setup. An example of the charge transmission with the highest charge we tried in the single bunch experiment is shown in Fig. 3-21. 100 shots were included in the figure to show the statistical performance of the experiment. Again, ICT1 measures the charge emitted from the photocathode, ICT2 measures the charge delivered to the experiment chamber location and before the structure, and ICT3 measures the charge transmitted through the structure. The transmission is close to 100%.

With each pulse, the output power traces from the two output ports were measured by the Tektronix MSO71604C oscilloscope with a bandwidth of 16 GHz and a maximum sampling rate 100 GSa/s. A sample set of traces directly measured from the two ports is presented in Fig. 3-22. The voltage measured on the scope is later transformed into the actual microwave power from the cable and probe calibration.

The highest microwave power measured from a single electron bunch is presented in Fig. 3-23, and the transmitted charge is 45 nC with an rms bunch length of 1.2 mm. Figure 3-23(a) shows that 25 MW of power was generated in the backward port,

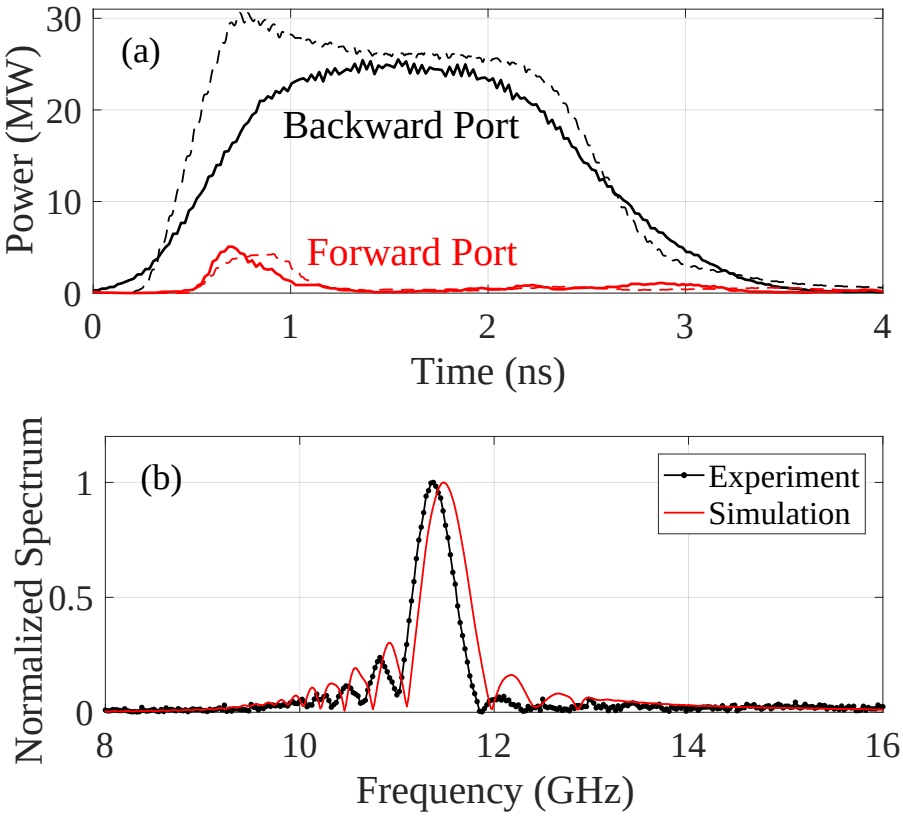

Figure 3-23: High power microwave extraction from a single bunch. (a) Output microwave power in the two ports from a single 45 nC bunch. Solid lines: experiment, dashed lines: CST simulations. (b) Frequency spectrum.

in good agreement with the CST particle-in-cell (PIC) simulation and the analytical calculation described in Chapter 2, which is also 25 MW.

Between the two output ports, the backward port has much higher power than the forward port, indicating that the radiated microwaves indeed travel in the backward direction. Therefore, this experiment provides a clear proof of the reversed Cherenkov radiation generation in a metamaterial structure with a negative group velocity.

Figure 3-23 (b) shows good agreement between the measured frequency spectrum and the PIC simulation, with a central frequency of 11.4 GHz and a bandwidth BW $= 1/t_p = 0.5$ GHz. The small frequency difference between the measurement and the simulation is due to possible small errors in the parts fabrication.

A scaling study of the extracted microwave power with the charge q was carried out and is shown in Fig. 3-24. The good agreement with the analytical theory indicates

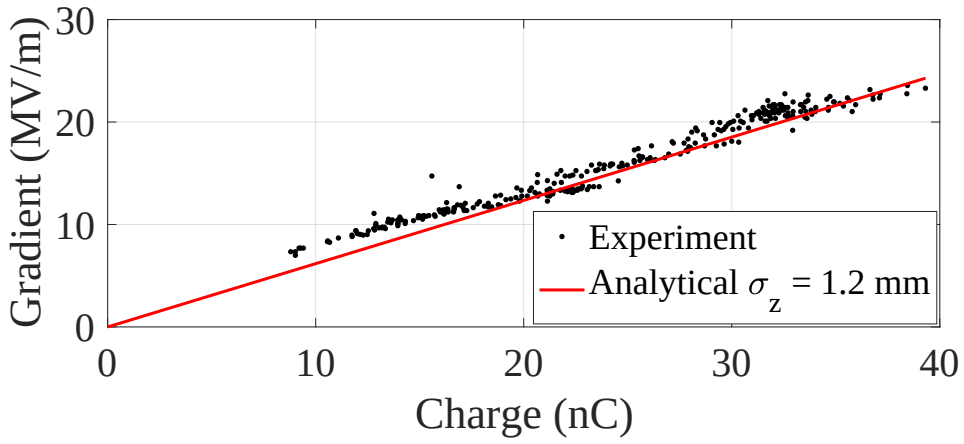

(a)

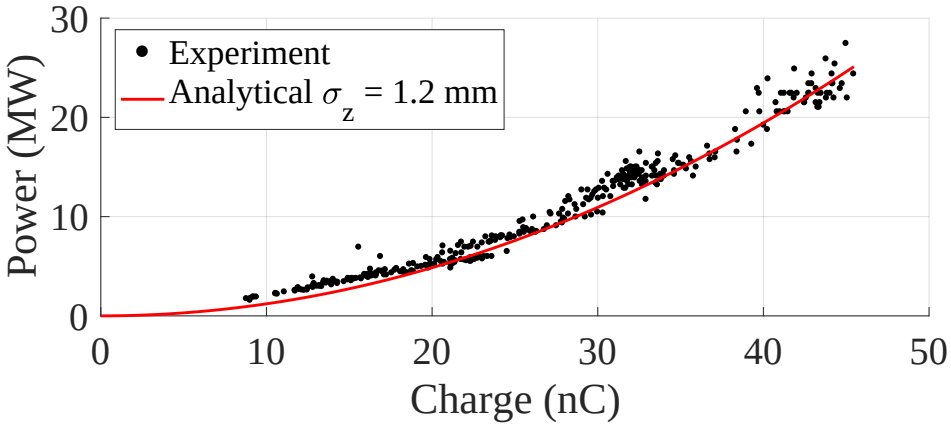

(b)

Figure 3-24: Comparison of experiment and analytical theory of the extracted microwave power as a function of the transmitted charge. The bunch rms length is 1.2 mm in a Gaussian distribution. (a) Scaling of decelerating gradient vs. transmitted charge. (b) Extracted microwave power in the backward port vs. transmitted charge.

that the structure operation is very reliable, without evidence of the beam break-up instability [90].

3.4.2 Two-Bunch Experiment

The laser photocathode can generate two or more bunches separated at the 1.3 GHz frequency with laser beam splitters. The frequency is tunable from a series of splitting mirrors with tunable spacing. The structure frequency of 11.4 GHz is close to the 9^{th} harmonic of the electron gun frequency, so two electron bunches separated in time by

$1/(1.3\text{ GHz}) = 0.77$ ns can contribute to the wakefield coherently.

The splitting mirrors are on moving stages controlled by the Thorlabs APT program which provides precise control. The spacing between bunches can be adjusted by the moving stages. In the two-bunch train, by adding a different delay, the second bunch can be emitted at a different phase from the L-band photocathode. The electron gun frequency of 1.3 GHz corresponds to a bunch spacing of 230.8 mm, so 10 degrees at 1.3 GHz corresponds to a distance of 6.4 mm. With the laser splitters, when one stage is moved by a distance Δx, the path length changes by $2\Delta x$, so 10 degrees phase variation at 1.3 GHz corresponds to 3.2 mm of stage moving distance with the splitting mirror.

Two bunches with a varied phase difference ϕ were sent through. The phase difference ϕ here is in terms of the X-band structure frequency $\omega/2\pi = 11.4$ GHz, rather than the electron gun frequency of 1.3 GHz. In the time slot when the RF pulses from the two bunches overlap, coherent adding or canceling happens.

Suppose the RF voltage signal generated by Bunch 1 has an amplitude of V_1, and the signal by Bunch 2 has an amplitude of V_2, then with the coherent radiation, the temporal voltage signal from the train of both Bunch 1 and Bunch 2, $V_{\text{train}}(t)$, is

$$V_{\text{train}}(t) = V_1 \sin(\omega t) + V_2 \sin(\omega t + \phi), \tag{3.2}$$

The amplitude, or the peak value of the voltage signal from the train V_{train} is

$$\begin{aligned} V_{\text{train}} &= \max |V_1 \sin(\omega t) + V_2 \sin(\omega t + \phi)| \\ &= \sqrt{|V_1^2 + V_2^2 + 2V_1 V_2 \cos\phi|}, \end{aligned} \tag{3.3}$$

So the maximum of the bunch train voltage signal is

$$\max(V_{\text{train}}) = V_1 + V_2, \text{ when } \phi = 0^\circ, \tag{3.4}$$

and the minimum is

$$\min(V_{\text{train}}) = |V_1 - V_2|, \text{ when } \phi = 180^\circ. \tag{3.5}$$

When the two bunches have exactly the same amount of charge, the RF signals they can generate are equal, as $V_1 = V_2 = V$. In this case, the bunch train signal V_{train} varies between 0 and $2V$. The RF power from two bunches with equal charge, scaled as the square of the voltage signal, can reach a maximum of four times of that from a single bunch.

In the experiment, for each specific phase difference between the two bunches, we measured the voltage signal on the oscilloscope for Bunch 1 only, Bunch 2 only, and both bunches together, respectively. The charge applied for this task is about 4 nC in each bunch.

Figure 3-25 compares the voltage signal generated by a single bunch and that generated by a train of two bunches. Figure 3-25 (a), (b) and (c) present the output voltage signal from a single bunch, two bunches with the same phase, and two bunches with the opposite phase, respectively. The in-phase and out-of-phase here are again for the X-band structure frequency of 11.4 GHz. The cancellation is not complete because the charge in the two bunches is not exactly the same.

Figure 3-26 shows the voltage signals in the two-bunch measurement, from Bunch 1 only, Bunch 2 only and the two bunches together in a train. Each measured shot is represented by a data point in the figures. Figure 3-26a shows the case with the two bunches in phase with each other ($\phi = 0^\circ$), and Fig. 3-26b shows the case with the two bunches out of phase with each other ($\phi = 180.3^\circ$).

Similar figures as Fig. 3-25 and Fig. 3-26 are generated for each value of the phase difference ϕ, and the data were taken at an interval of about 30°.

To characterize the superposition, an R factor is defined as

$$R = \frac{2V_{\text{train}}/Q_{\text{train}}}{V_1/Q_1 + V_2/Q_2}, \tag{3.6}$$

where $Q_{\text{train}} = Q_1 + Q_2$. V_1, V_2 and V_{train} are the amplitudes of the voltage signals from

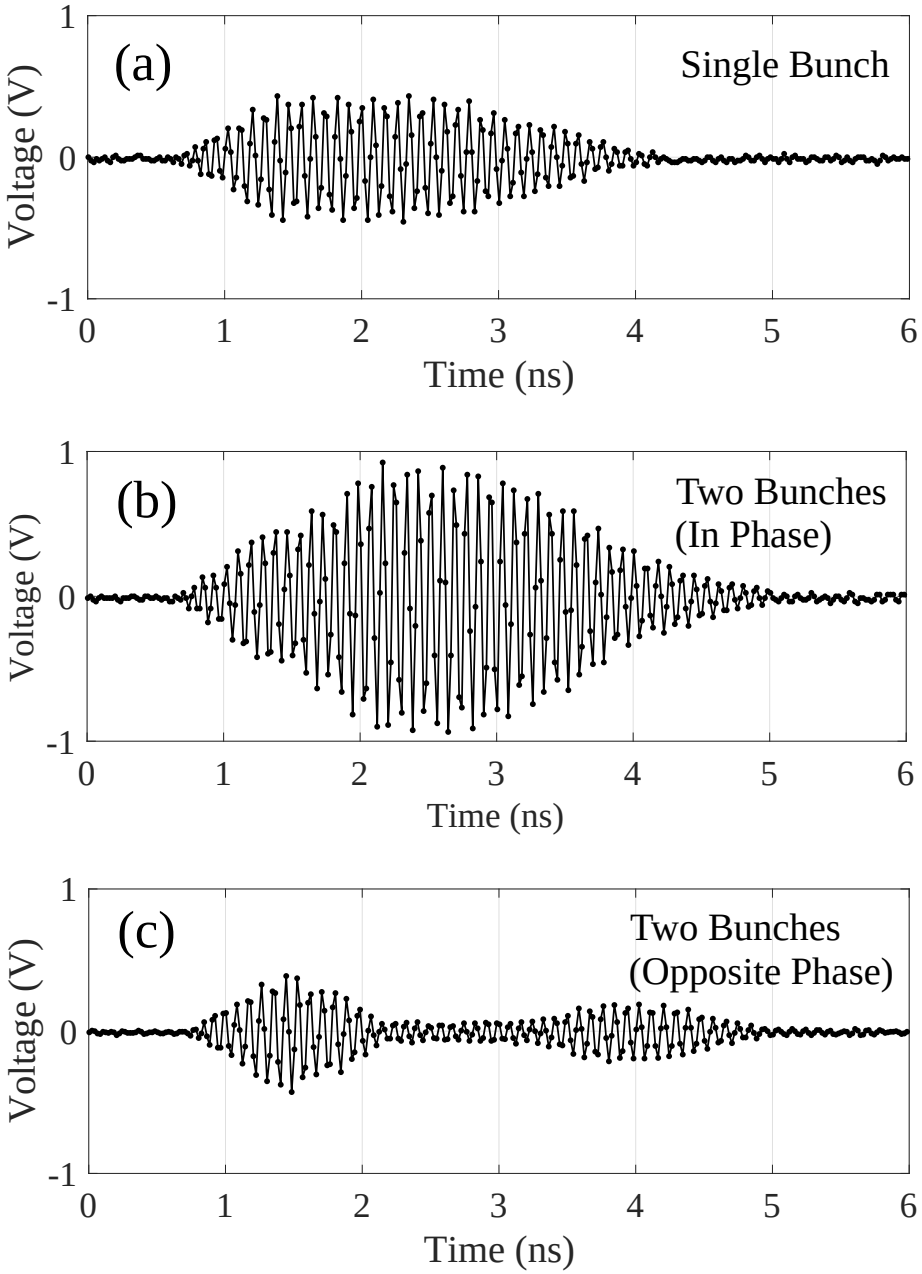

Figure 3-25: Experimental measurements of backward power with two bunches. Voltage signal from (a) a single bunch, (b) two bunches with 0 deg phase difference, (c) two bunches with 180 deg phase difference. The phase here means the X-band phase at 11.4 GHz.

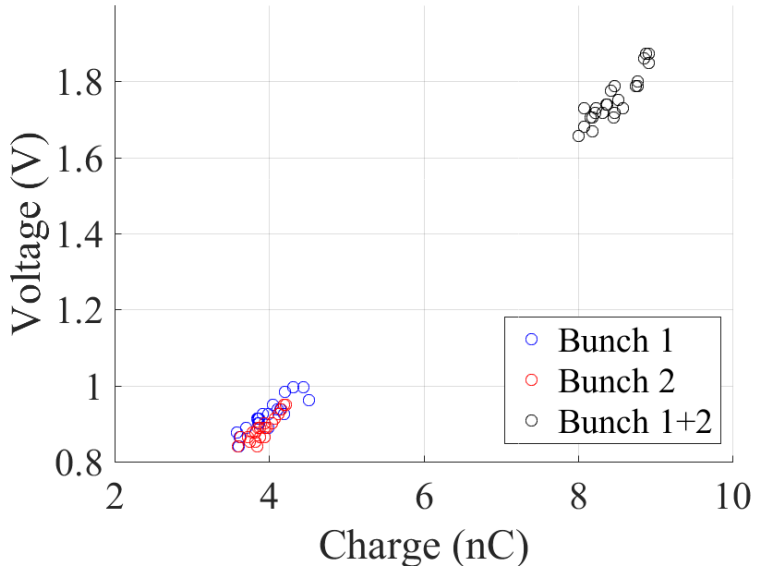

(a)

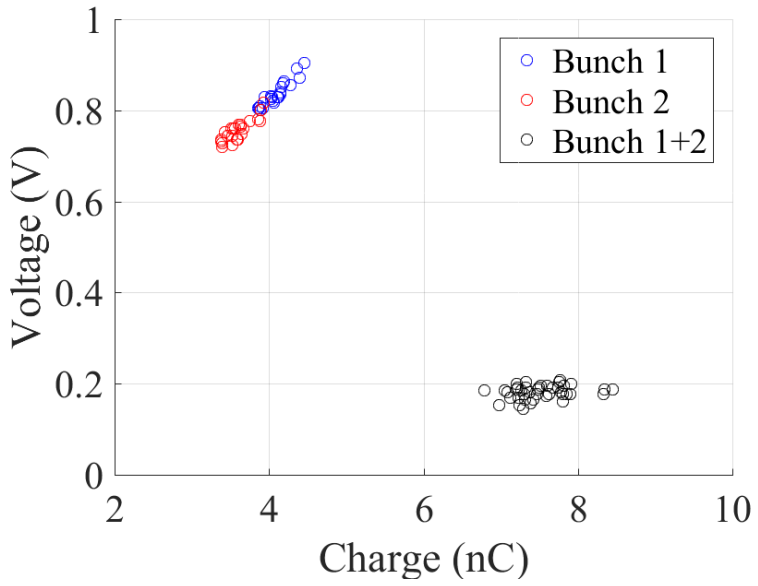

(b)

Figure 3-26: The voltage signals vs. charge from Bunch 1 only, Bunch 2 only and the two bunches together in a train. Each dot represents an experimental shot. (a) Two bunches in phase with each other, 0° phase difference. (b) Two bunches out of phase with each other, 180° phase difference. The vertical axes show the voltage values measured on the oscilloscope. The comparison of the single bunch voltage and the two-bunch voltage is the effective information here, rather than the absolute values of the voltage.

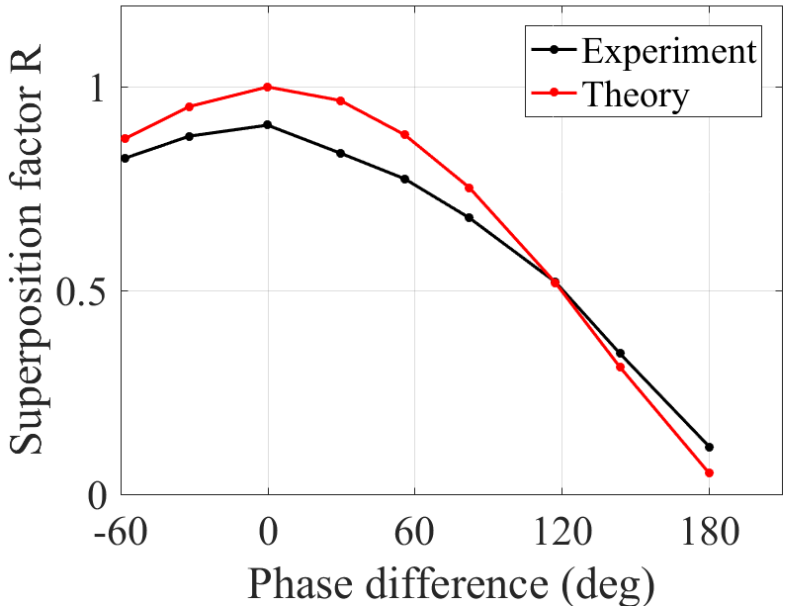

Figure 3-27: Variation of superposition factor R, as defined in Eq. (3.6) with phase difference between the two bunches in a train.

Bunch 1 only, Bunch 2 only, and the bunch train, respectively. V_{train} is calculated as the envelope voltage of the RF pulse only in the region where Bunch 1 and Bunch 2 overlap.

The R factor is a general form to describe the two-bunch superposition by normalizing the voltage signal with the charge, so it is a good indicator of the phase difference when the two bunches in a train do not have the same amount of charge.

In the special case when $Q_1 = Q_2$, R ranges between 0 and 1. $R = 0$ means full cancellation and $R = 1$ means complete adding. In the general case of $Q_1 \neq Q_2$, when R approaches 1 to its maximum value, the two bunches are adding up completely; when R goes down to almost 0, it means that the two bunches are canceling each other.

Figure 3-27 is from the measurement results of a train of two 4 nC bunches, and it shows the variation of the defined superposition factor R with the phase difference between the two bunches, with the comparison of experiment and theory. In the figure, the experimental R factor is calculated using Eq. (3.6) with all the voltage

and charge from the measurement, as

$$R_{\text{experiment}} = \frac{2V_{\text{train}}/Q_{\text{train}}}{V_1/Q_1 + V_2/Q_2} \tag{3.7}$$

The theoretical R factor uses the measured single bunch values (V_1, V_2, Q_1, Q_2) and Eq. (3.3) to calculate V_{train}, as follows:

$$R_{\text{theory}} = \frac{2\sqrt{|V_1^2 + V_2^2 + 2V_1V_2\cos\phi|}/(Q_1 + Q_2)}{V_1/Q_1 + V_2/Q_2} \tag{3.8}$$

The experiment agrees very well with the theory, indicating that the phase can be controlled very precisely in the bunch train experiment.

The highest power achieved in the experiment with the wagon wheel structure was from two bunches radiating in phase with a total charge of 85 nC transmitted. Charge transmission is still good in this case, as shown in Fig. 3-28. The charge emitted by the photocathode can exceed 100 nC.

The measured RF power in the backward port is shown in Fig. 3-29. The experimental result agrees perfectly with the CST PIC simulation. The peak power reached 80 MW, and this is the highest RF power up to date observed with a metamaterial structure. This amount of power corresponds to a decelerating gradient of 50 MV/m on the second electron bunch. The peak surface electric field was estimated as 130 MV/m from CST simulations.

In the present experiment, this power was extracted and it thus represents the power that would be available in a two beam accelerator configuration. Alternatively, if this power were applied to a trailing witness bunch in a collinear wakefield accelerator, it would provide an accelerating gradient of 75 MV/m.

A visual inspection and a cold test of the structure after completion of the high power tests showed no evidence of damage.

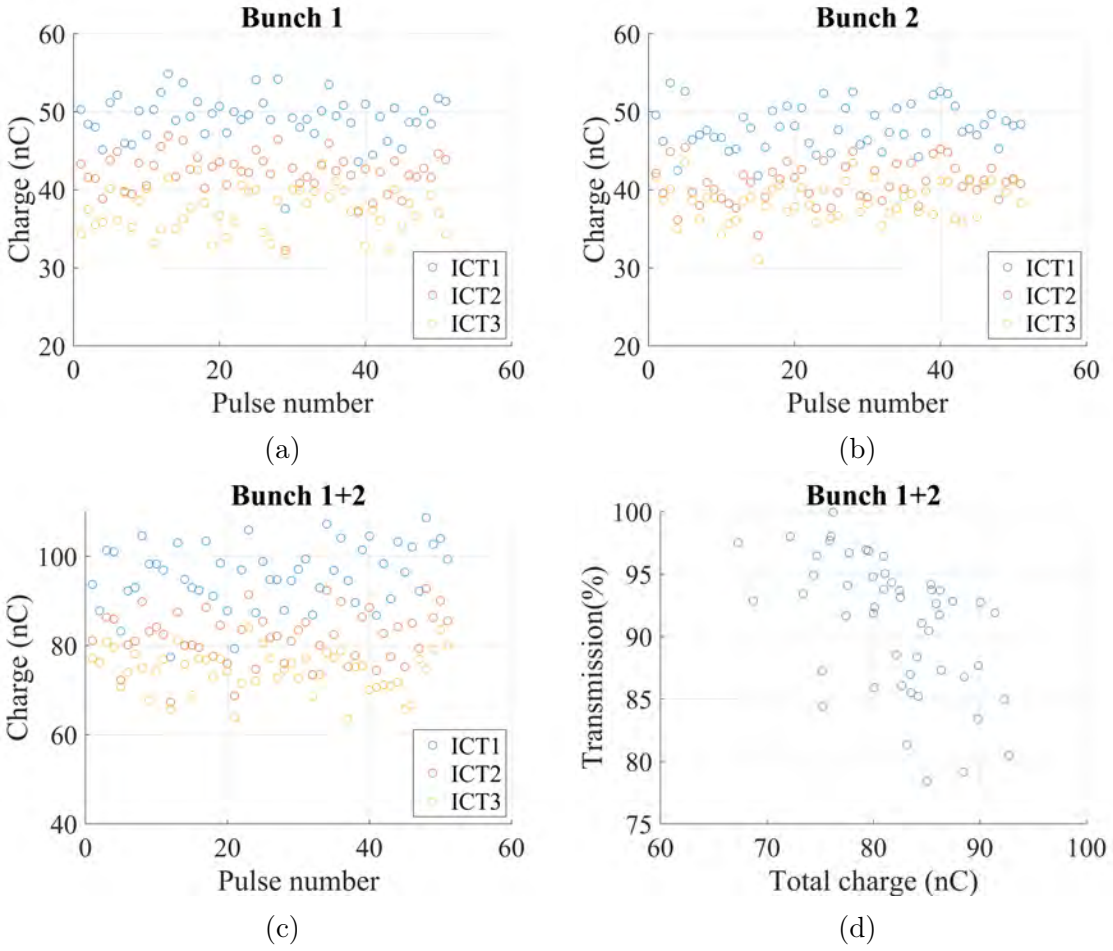

Figure 3-28: Charge transmission for the highest charge case in the two-bunch train experiment. (a) ICT signals at different locations on the beam line for Bunch 1. (b) ICT signals at different locations on the beam line for Bunch 2. (c) ICT signals at different locations on the beam line for Bunch 1 and Bunch 2. ICT1: closest to the electron gun; ICT2: right before the structure; ICT3: right after the structure. Results for 50 shots are shown. (d) Charge transmission for both Bunch 1 and Bunch 2 together in a train, calculated as the ratio of charge after the wagon wheel structure (ICT3) to the charge right before the wagon wheel structure (ICT2). The horizontal axis shows the charge measured by ICT2.

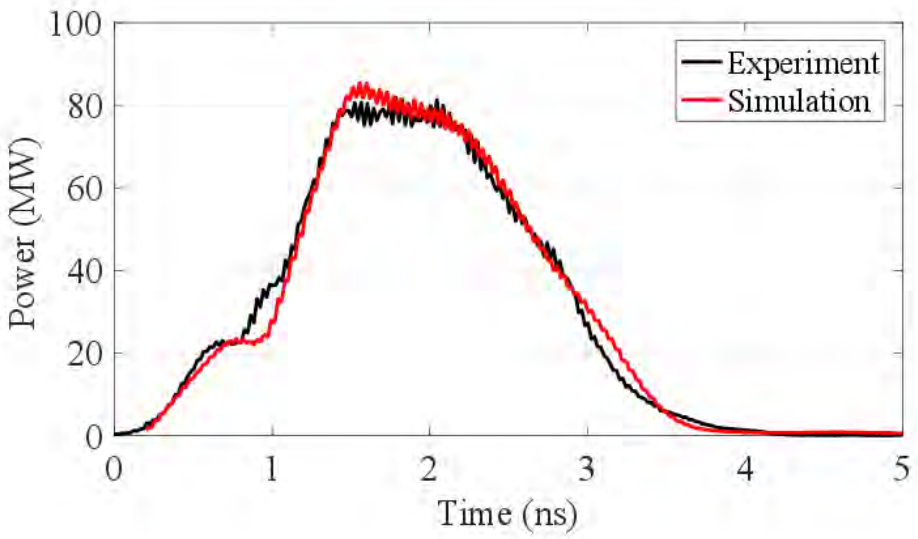

Figure 3-29: Highest power shot from two bunches with a total charge of 85 nC transmitted. Output power in the backward port.

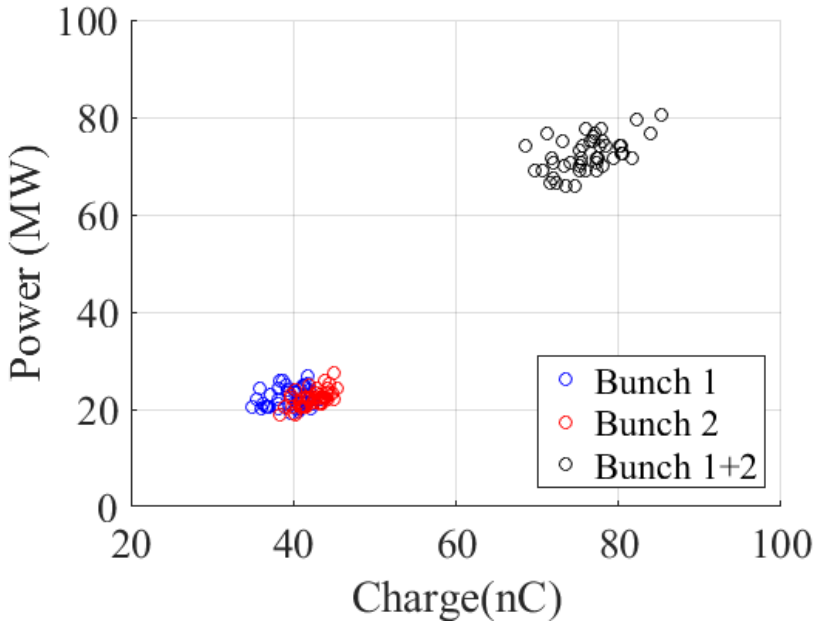

Figure 3-30: Power over charge plot for Bunch 1, Bunch 2, and two bunches together at the same phase in the highest charge two-bunch run. Each date point represents a shot in the experiment.

3.5 Conclusions

In conclusion, the experimental results of the X-band wagon wheel metamaterial structure are presented in this paper. The experiment provides direct evidence of the reversed Cherenkov radiation from a short and relativistic electron bunch in a metamaterial structure. We have also demonstrated that the metamaterial structure is a promising power extractor design for wakefield acceleration with good reliability and simple fabrication. From a single bunch with a charge of 45 nC and a length of $\sigma_z = 1.2$ mm, 25 MW of microwave power at 11.4 GHz has been extracted with a pulse length of 2 ns. The experimental results agree very well with the analytical calculation and CST simulations. The highest power from two bunches with a total charge of 85 nC reached 80 MW. The available gradient for a witness bunch was 75 MV/m, making a strong candidate for structure-based wakefield acceleration.

Chapter 4

Theory of Metamaterial Structures for High Power Microwave Generation

In Chapter 2 and Chapter 3, I discussed the metamaterial structures designed and built for wakefield acceleration. In Chapter 4 and Chapter 5, I will discuss the application of metamaterial structures for high power microwave sources.

The two applications of metamaterial structures in this thesis, wakefield acceleration and high power microwave sources, share the same focus of interaction of metamaterial structures with electron beams; but they have different design strategies given the different goals. So in the high power microwave studies, complete different metamaterial structures have been developed to work with an electron beam source at MIT.

This chapter is organized as follows.

In Section 4.1 I will give a review of the previous metamaterial experiment at MIT, named as the Stage I experiment. Stage I experiment was completed in 2016 by Jason Hummelt [19].

In Section 4.2, I will move on to my theoretical work on metamaterial structures for high power microwaves and introduce an analytical theory to describe the Cherenkov-cyclotron instability in metamaterial structures.

In Section 4.3, I will describe the simulation and design of the Stage II metamaterial experiment. The design work for the Stage II experiment led to an in-house

experiment at MIT, which will be presented in Chapter 5 of this thesis.

4.1 Review of Previous Metamaterial-Based High Power Microwave Research at MIT

The research effort on metamaterials at the MIT group can be dated back to 2006 as in Ref. [70], where the effect of spatial dispersion in negative permittivity metamaterials was studied. The idea of active metamaterials, i.e. the interaction of metamaterial structures with electron beams, was first explored theoretically in 2012 in Ref. [62], where complementary split ring resonators were proposed to serve as the interaction circuit with an electron beam.

Based on these theoretical research findings, the design work towards the Stage I metamaterial experiment was started [91], and later the experiment was built in-house at MIT.

In the Stage I metamaterial-based high power microwave experiment at MIT [19, 20, 92], we built a multi-megawatt microwave source at 2.4 GHz based on a metamaterial structure. An electron gun was used to generate a 490 kV, 84 A, 1 μs electron beam. In the Stage I experiment, it was demonstrated that MW level coherent Cherenkov-cyclotron radiation can be generated in a waveguide loaded with two identical metamaterial plates.

Before this experiment, several active metamaterial-based structures with an electron beam for high power microwave generation had been studied theoretically [11, 62, 66, 95–100]. However, very few experiments had been carried out to actually generate high power microwaves with an electron beam passing through a metamaterial structure [10, 101–103].

The Stage I metamaterial structure has two metamaterial plates loaded in a waveguide with dimensions below the cut-off of the lowest TM mode of the rectangular waveguide, the TM_{11} mode. The CAD drawing and a photo of the structure are shown in Fig. 4-1. The implementation we chose is the complementary split ring

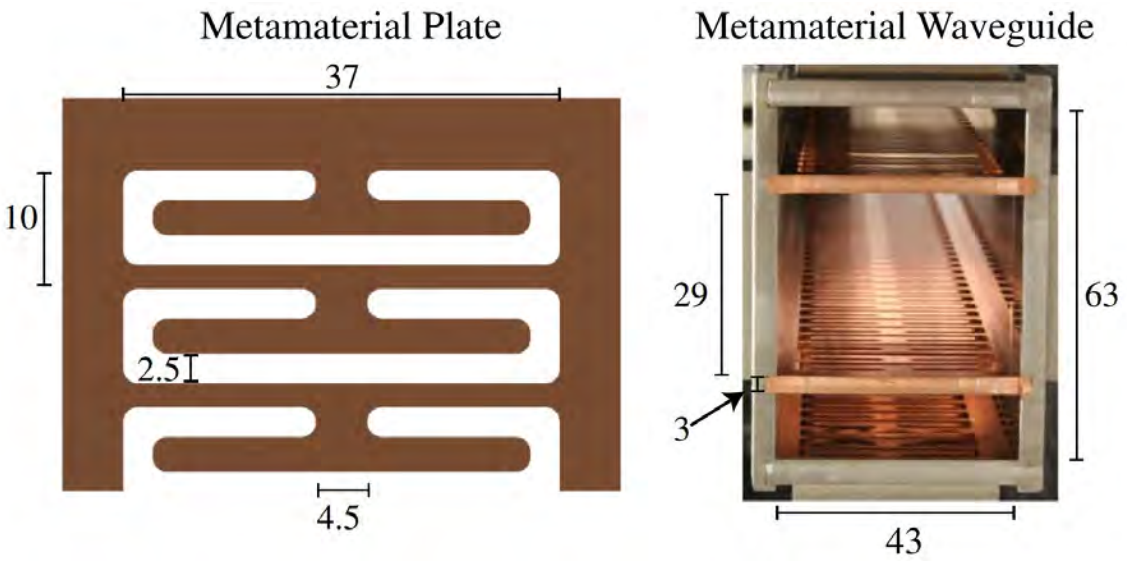

Figure 4-1: A CAD rendering of the Stage I metamaterial structure built at MIT. Left: one of the metamaterial plates. Right: a photograph of the fully assembled structure. Dimensions are in mm. This figure is cited from Ref. [20].

resonators (CSRRs) [60]. The C-shaped cuts in Fig. 4-1a are the designed CSRRs.

The CSRRs enable us to design an all-metal structure compatible with the vacuum condition and the high power requirements. The CSRRs are responsible for a negative permittivity ϵ. The TM_{11} mode provides the axial electric field necessary for interaction with the electron beam.

According to Ref. [104], if we would use the ϵ and μ model of a plane wave in an open medium to describe the TM mode bounded in the waveguide, we can introduce the permeability μ to represent the axial electric field. Then in the ϵ and μ model, only the transverse electric and magnetic fields remain to form a plane wave. The permeability μ is expressed using the axial electric field component of the waveguide TM mode on the axis and transverse magnetic field averaged over the cross-section. The permeability μ is negative when the waveguide TM mode is below cutoff. Therefore, since both the permittivity ϵ and the permeability μ are negative, microwaves can propagate in the structure with a negative group velocity, as explained in Chapter 1.

In our previous design, the two metamaterial plates are identical and they are

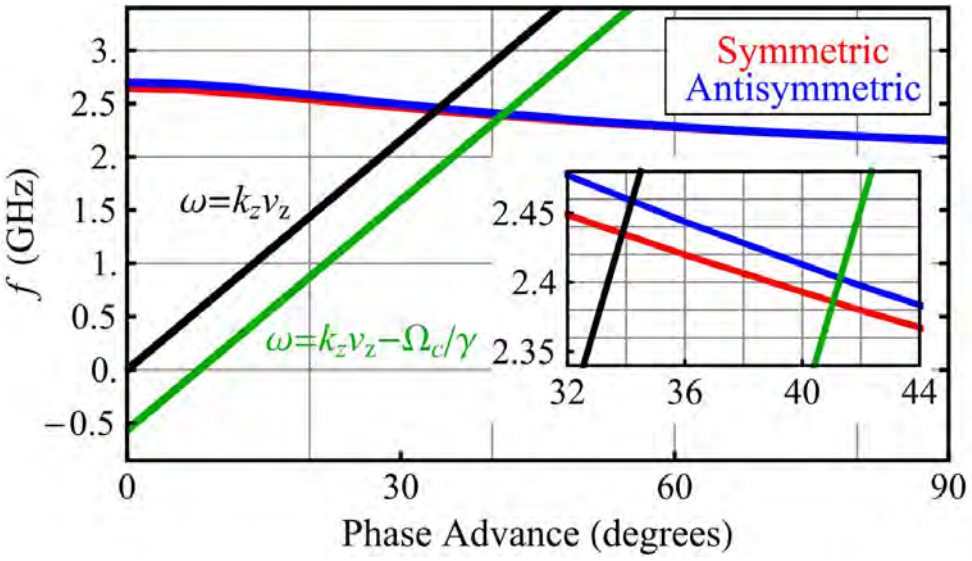

Figure 4-2: Dispersion relation for the symmetric (red) and antisymmetric (blue) modes of the metamaterial structure with the Cherenkov (black) and Cherenkov-cyclotron (green) beam lines. The phase advance is $k_z p$ and $p = 10$ mm. The beam energy is 490 keV and the magnetic field 400 G for the Cherenkov-cyclotron mode. This figure is cited from Ref. [20].

arranged in a symmetric way. In this setup, there are two types of eigenmodes in the structure, a symmetric mode and an antisymmetric mode. The dispersion relation, i.e. ω vs. k of the two modes, is shown in Fig. 4-2, where the phase advance in the horizontal axis is calculated for a single period and equals $k_z p$. Here $p = 10$ mm is the period of the CSRRs.

The names 'symmetric' and 'antisymmetric' are defined as the electric field symmetry across the middle plane between the two copper plates with CSRRs. Figure 4-3 shows the electric field plots of the symmetric mode in Fig. 4-3a, and the antisymmetric mode in Fig. 4-3b. Assume the electron beam is propagating in the $+z$ direction. The symmetric mode has a longitudinal electric field E_z on the central beam axis, with the electric field parallel with the metamaterial plates. The antisymmetric mode has a transverse electric field E_y on the central beam axis, with the electric field perpendicular to the metamaterial plates. In this case, the field vector has to point towards one plate or the other, thus breaking the symmetry between the metamaterial plates.

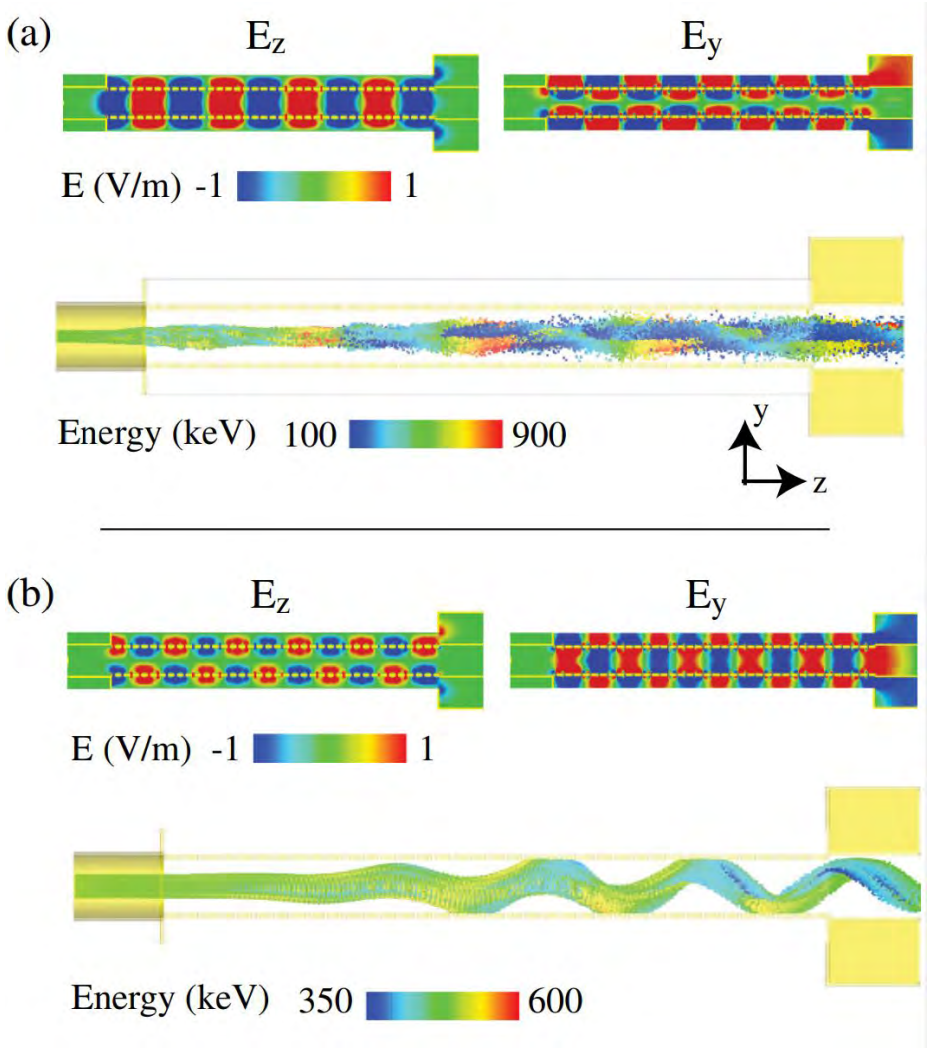

Figure 4-3: PIC simulation of the metamaterial structure with a 490 keV 84 A electron beam showing the E_z and E_y field components and the particle orbits when the (a) symmetric mode is excited at 1500 G and the (b) antisymmetric mode is excited at 700 G. This figure is cited from Ref. [20].

In Fig. 4-2, there are four possible beam-wave interaction points, where the two eigenmode dispersion curves intersect with the two electron beam lines. The two beam lines represents two types of beam-wave interaction, the Cherenkov interaction $\omega = k_z v_z$ and the Cherenkov-cyclotron interaction $\omega = k_z v_z - \Omega_c/\gamma$, where $\Omega_c = eB/m$ is the angular cyclotron frequency, B is the longitudinal DC magnetic field, and γ is the Lorentz factor of the electron beam. The Cherenkov-cyclotron mode is also called the anomalous Doppler mode [105–107].

With the cyclotron frequency involved, in the Cherenkov-cyclotron interaction, the electron beam performs the cyclotron motion. Figure 4-3 also compares the different beam profiles with the Cherenkov and the Cherenkov-cyclotron interaction from the CST particle-in-cell simulation results. Beam cyclotron motion is present at low magnetic field in the Cherenkov-cyclotron interaction type.

In the experiment, megawatt power level pulses were generated in the antisymmetric mode in the Cherenkov-cyclotron type of interaction at a low magnetic field. Surprisingly, high power was only found in the Cherenkov-cyclotron mode and was not found in the expected Cherenkov mode.

Sample traces of the measured microwave power are shown in Fig. 4-4. Figure 4-4a shows 60 watts of microwave power in the Cherenkov mode at a high magnetic field of 1500 G, and Fig. 4-4 (b) shows the peak power of 2.7 MW in the Cherenkov-cyclotron mode at a low magnetic field of 375 G.

The solenoidal magnetic field pointed along the electron beam axis is necessary to transport the beam in a microwave source. During the experiments the magnetic field was scanned, and the generated frequency was tuned by the magnetic field. Figure 4-5 shows the measurement results. The Cherenkov-cyclotron type tunes with the magnetic field by showing the negative slope, while the Cherenkov type is not supposed to tune.

To conclude, in the Stage I experiment, a high power microwave source using a 490 kV, 84 A, 1 μs electron beam interacting with a metamaterial loaded waveguide has been designed [91] and experimentally demonstrated [19, 20, 92]. The metamaterial was built as complementary split-ring resonators (CSRRs) [60] machined on metallic

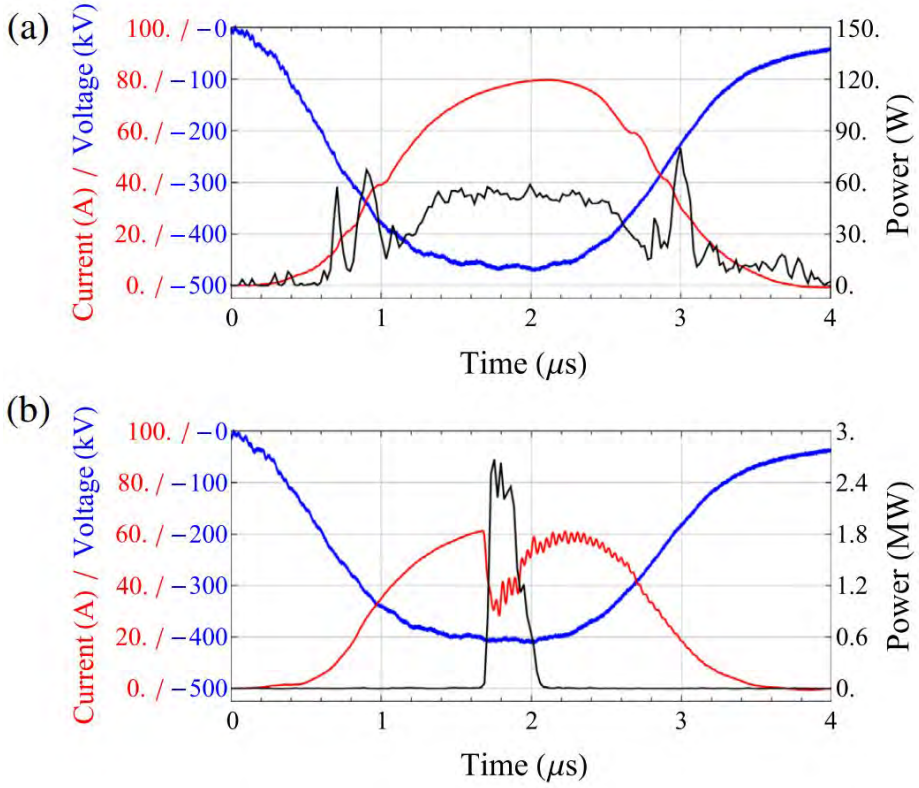

Figure 4-4: Microwave power (black), electron gun voltage (blue), and measured collector current (red) in the Stage I experiment for an applied magnetic field of (a) 1500 G and (b) 375 G. This figure is cited from Ref. [20].

plates oriented along the waveguide propagation axis [62, 108]. The MW power level, microsecond long pulses at around 2.4 GHz were observed in these experiments [19,92]. We know from the experiment that the Cherenkov-cyclotron instability causes the coherent high power microwave generation. Besides, the antisymmetric mode that has a transverse electric field on the beam axis was excited at low magnetic fields by the gyrating electron beam whereas a symmetric mode with the maximum longitudinal field on the axis was excited at higher magnetic fields though at low power. The experimental results were in agreement with the CST simulations [19].

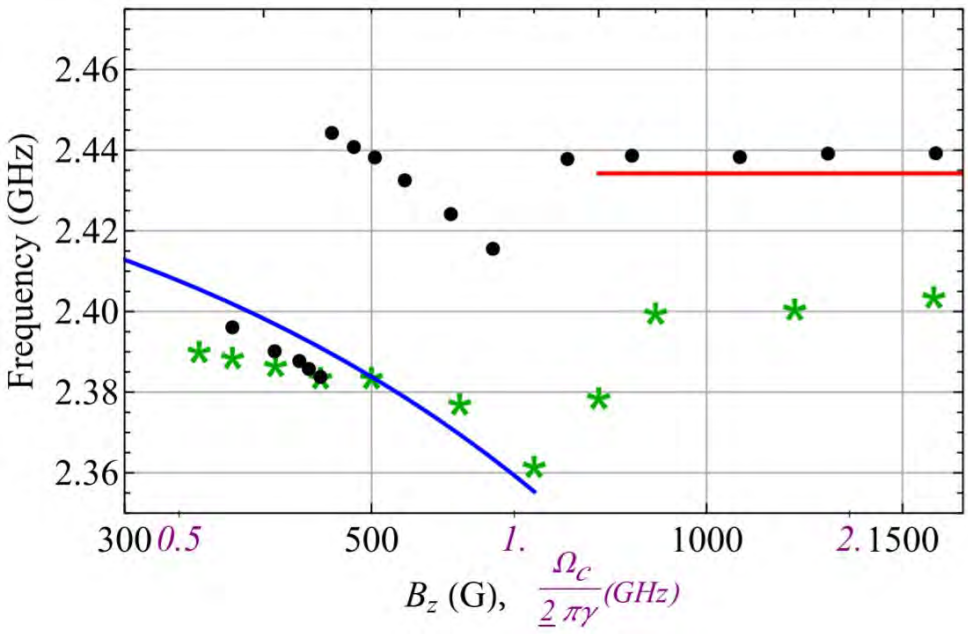

Figure 4-5: Measured (black) and simulated (green) frequency tuning with the solenoid magnetic field. In addition, the red line is the symmetric mode Cherenkov instability ($\omega = k_z v_z$), and the blue line is the antisymmetric mode Cherenkov-cyclotron instability ($\omega - k_z v_z = -\Omega_c/\gamma$).

Although multi-megawatt power level pulses were obtained with the symmetric structure, the microwave pulses had a short pulse length. With a continuous electron beam 1 μs long, microwave pulses of only 100 ns to 400 ns long were observed. This leads to the design of the Stage II experiment [58, 93, 94], which will be presented in Section 4.3. The design goal of Stage II is to achieve full 1 μs long, multi-megawatt microwave pulses.

4.2 Theory of Cherenkov-Cyclotron Instability in a Metamaterial Waveguide

4.2.1 Motivation

This section will present an analytical model of the Cherenkov-cyclotron instability of an electron beam in a metamaterial loaded waveguide in a finite longitudinal magnetic field. The interaction with the antisymmetric mode is analyzed. This analytical model is a useful addition to the CST simulations for designing metamaterial-based microwave sources.

Let us review the previous theoretical work on the Cherenkov-cyclotron instability in conventional waveguides and media. The cyclotron instability is used in the gyrotron type vacuum electron devices [105]. The operating modes of these devices are the TE modes of a cylindrical cavity or waveguide. In a gyro-type traveling wave tube, the interaction occurs at the normal Doppler synchronism of the waveguide mode with the electron beam $\omega - hv_z = \Omega_c/\gamma$, where ω is the frequency, h is the axial wavenumber, v_z is the axial beam velocity, $\Omega_c = eB_0/m$ is the cyclotron frequency, e and m are the electron charge and mass, B_0 is the axial magnetic field, γ is the Lorentz factor. The anomalous Doppler synchronism $\omega - hv_z = -\Omega_c/\gamma$ is possible as well, and it has the interesting feature that the cyclotron instability starts without an initial transverse velocity of the electron beam [105, 107]. Given this feature, no transverse kicker is required for the instability to happen in a device. The theory of microwave oscillator based on the anomalous Doppler synchronism has been developed for a simple interaction circuit like a dielectric waveguide [107, 109, 110].

The theory in this section will focus on the Cherenkov-cyclotron instability in a metamaterial waveguide, with a sample geometry shown in Fig. 4-6. Figure 4-6a shows the waveguide loaded by the metallic metamaterial plates, which is the design for the Stage I experiment, as described in Section 4.1. The metamaterial loaded waveguide mode has a negative refraction index, i.e. a dispersion different to that of a dielectric waveguide. Therefore, the beam-wave interaction at the anomalous

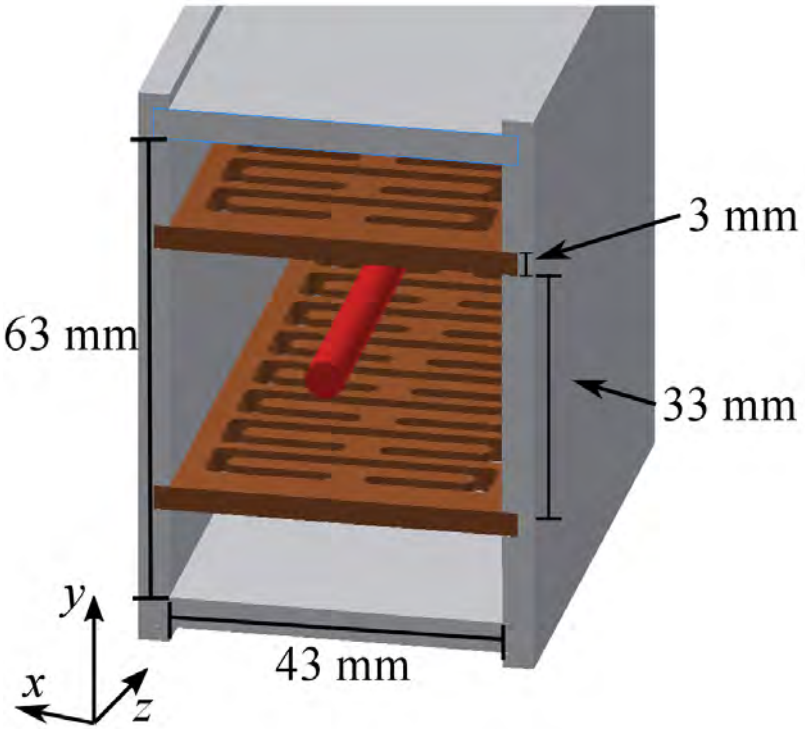

(a)

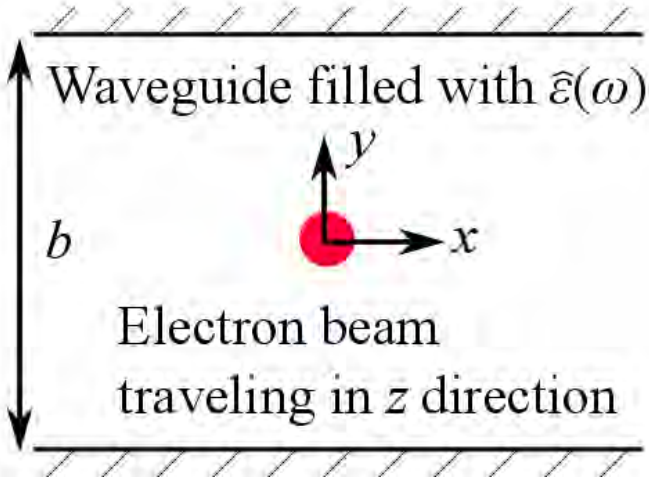

(b)

Figure 4-6: Model of the metamaterial-loaded waveguide. (a) Waveguide loaded with two copper metamaterial plates. This is the exact model used in CST simulations. The metamaterial plates have the design of the CSRRs as the C-shapes. (b) Waveguide filled with the artificial medium, the effective field model used for analytical analysis.

Doppler synchronism has to be analyzed specifically for the metamaterial waveguide. The metamaterial mode has a longitudinal electric field in the CSRRs. Therefore, the metamaterial waveguide mode is a TM mode.

Ref. [111] analyzed the competition between the Cherenkov mode and the Cherenkov-cyclotron mode in a backward wave oscillator (BWO). In this section, we use the method of Ref. [111] to formulate the equations of electron motion and the equation for the complex amplitude of the metamaterial mode with a negative refractive index. We restrict ourselves by a linear analysis valid for the starting operation conditions of the microwave device. We solve this system of linear equations with the boundary conditions and calculate the starting current of the instability.

4.2.2 Metamaterial Loaded Waveguide Mode

In this analysis, we substitute the metamaterial structure as in Fig. 4-6a with a uniform effective medium, whose electromagnetic properties are a good approximation to those of the actual structure. Figure 4-6b shows the planar waveguide filled with the effective medium. The longitudinal direction is the z direction, and in the transverse direction, the dimension in the y direction is b.

From the Maxwell's equations for the electric $\boldsymbol{E}$ and magnetic $\boldsymbol{H}$ fields, we have

$$\nabla \times \boldsymbol{E} = i\omega\mu_0 \boldsymbol{H},\ \nabla \times \boldsymbol{H} = -i\omega\epsilon_0 \hat{\epsilon} \cdot \boldsymbol{E}, \tag{4.1}$$

where ϵ_0 and μ_0 are the permittivity and permeability of vacuum. We first assume a time dependence of $e^{-i\omega t}$. We also assume a diagonal permittivity tensor $\hat{\epsilon}$ in Eq. (4.1) with the components of

$$\epsilon_{xx} = 1, \epsilon_{zz} = 1, \epsilon_{yy} = (1-F)\frac{\omega^2 - \omega_0^2/(1-F)}{\omega^2 - \omega_0^2} \tag{4.2}$$

The permittivity ϵ_{yy} given in Eq. (4.2) is negative in the region $\omega_0 < \omega < \omega_0/\sqrt{1-F}$. $F < 1$ is a constant that can be fitted from the known dispersion relation corresponding to the actual structure in Fig. 4-6a, and the negative ϵ_{yy} comes from the CSRR

design [60].

Suppose the propagation constant in the z direction is h, and the waveguide dimension is $a \times b$ ($a > b$). The mode being analyzed is a TM mode with the only nonzero field terms being E_y, E_z and H_x. The antisymmetric mode field components are represented as

$$\begin{aligned} E_y^{(a)} &= E_y^0 \cos\left(\frac{2\pi}{b}y\right) e^{ihz}, \\ H_x^{(a)} &= -\frac{\omega}{h}\epsilon_0\epsilon_{yy}E_y^0 \cos\left(\frac{2\pi}{b}y\right) e^{ihz}, \\ E_z^{(a)} &= -i\frac{\epsilon_{yy}}{h}\frac{2\pi}{b}E_y^0 \sin\left(\frac{2\pi}{b}y\right) e^{ihz} \end{aligned} \tag{4.3}$$

The superscript (a) stands for an antisymmetric mode. The 'antisymmetric' here means that the longitudinal electric field E_z is antisymmetric in the y direction from the sine distribution in the region of $y > 0$ and the region of $y < 0$.

This mode has the field distribution similar to that of the actual metamaterial structure, and the comparison is shown in Fig. 4-7a for the transverse electric field and Fig. 4-7b for the longitudinal electric field. The field distribution of the actual metamaterial structure is distorted by the presence of the two copper plates, marked with the dashed lines in the figures. The field is evanescent in the y-direction near the metamaterial plates in the actual structure, so the metamaterial design allows mode propagation even below the cutoff frequency. In our model, the effective medium to describe the metamaterial structure is homogenized, i.e. occupies the entire volume of the waveguide. The field is no longer evanescent in the transverse direction, it is sinusoidal. The analytic model that is being developed here is not meant to be an exact replica of the field structure of the actual metamaterial loaded waveguide. It is only intended to capture the relevant physics. In this respect, the agreement shown in Fig. 4-7 is believed to be a good basis for the following analytic analysis.

The dispersion relation from Eq. (4.3) is

$$h = \frac{\omega}{c}\sqrt{\epsilon_{yy}(1 - K^2)} \tag{4.4}$$

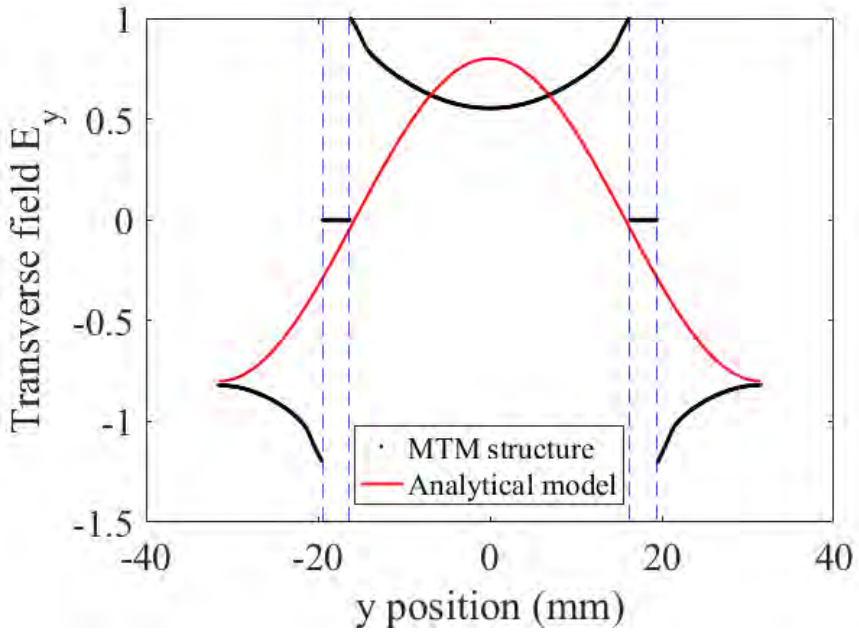

(a)

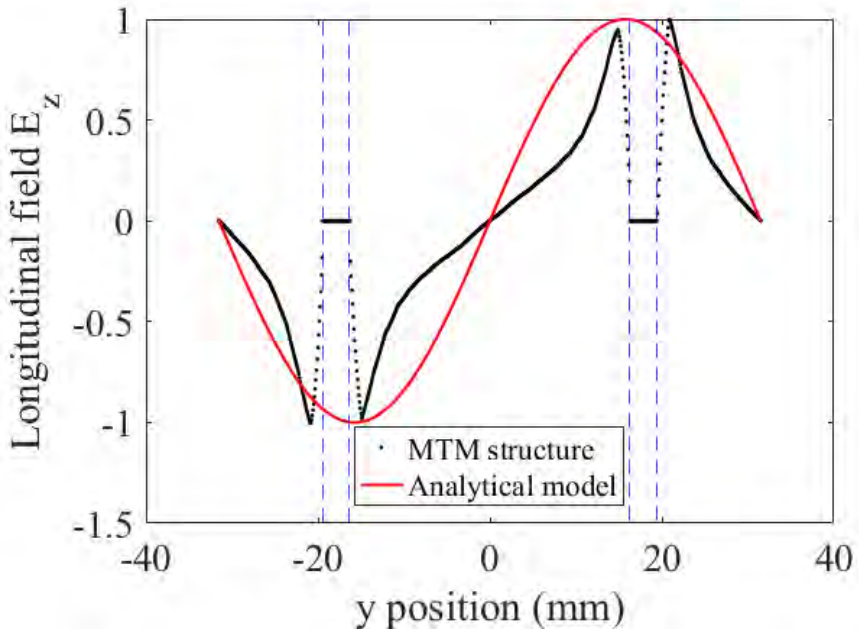

(b)

Figure 4-7: Comparison of the electric field calculated for the metamaterial structure used in the Stage I experiments vs. the field calculated for the analytical effective medium theory. (a) Transverse field E_y. (b) Longitudinal field E_z. In the figures, the position of the two plates in the real metamaterial structure are shown with the dashed lines.

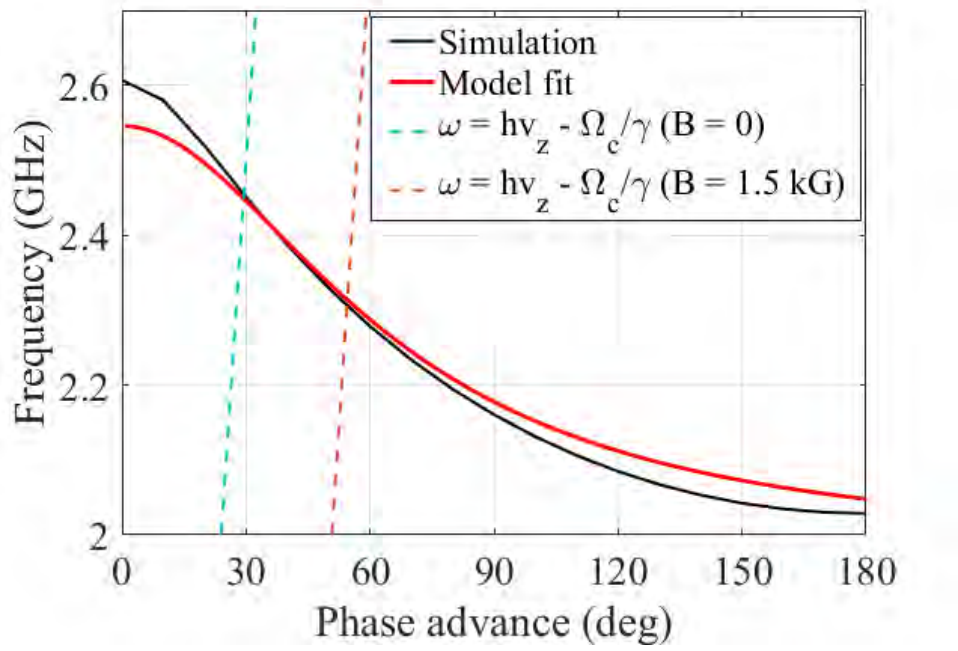

Figure 4-8: Comparison of the dispersion curves calculated from Eq. (4.2) with the simulation of the dispersion of the structure shown in Fig. 4-6 (a). The electron beam lines are drawn for a beam energy of 450 kV and a magnetic field of 1.5 kG.

where $K = \omega_{\rm cr}/\omega$, and $\omega_{\rm cr}$ is the cut-off (critical) angular frequency for an empty waveguide without filling as $\omega_{\rm cr} = 2\pi c/b$, where c is the speed of light. In the frequency range where $\epsilon_{yy} < 0$, the propagating wave frequency has to be below the cut-off frequency of the empty waveguide. So there is a requirement on the parameters as

$$2\pi c/b > \omega_0/\sqrt{1-F}. \tag{4.5}$$

The fitting results of the two parameters ω_0 and F from the dispersion of the metamaterial structure are shown in Fig. 4-8 with $\omega_0 = 2\pi \cdot 1.98$ GHz and F = 0.393. The phase advance is for one axial period d of the metamaterial structure with $d =$ 10 mm. The best fit, as shown in Fig. 4-8, is found in the area between the electron beam synchronism lines which correspond to the Cherenkov synchronism $\omega = hv_z$ and the anomalous Doppler synchronism $\omega - hv_z = -\Omega_c/\gamma$ for the maximum magnetic field B_0 of 1.5 kG, and an electron beam energy of 450 kV.

The metamaterial loaded waveguide has some novel electromagnetic properties, such as a negative energy flow. The Poynting flux

$$\begin{aligned} P^{(a)} =& \frac{1}{2}\int_{-b/2}^{b/2}(\boldsymbol{E}\times\boldsymbol{H}^{*})\cdot\hat{\boldsymbol{z}}dyL_x \\ =& -\frac{c\epsilon_0 bL_x}{4}|E_y^0|^2\sqrt{\frac{\epsilon_{yy}}{1-K^2}}, \end{aligned} \tag{4.6}$$

is negative in the longitudinal direction, so the field energy flows backward in the metamaterial loaded waveguide.

Even when the Poynting flux is negative in the metamaterial medium, the relation between the Poynting flux and the stored energy still holds as

$$P^{(a)} = v_g W\frac{1}{L_z}. \tag{4.7}$$

We verify the above relation by calculating the stored energy in a waveguide region of $b\times L_x\times L_z$ as follows. The electric energy is

$$\begin{aligned} W_E &= \frac{\epsilon_0}{4}L_xL_z\int_{-b/2}^{b/2}\left(|E_y|^2\frac{\partial(\omega\epsilon_{yy})}{\partial\omega}+|E_z|^2\right)dy \\ &= \frac{\epsilon_0}{8}bL_xL_z|E_y^0|^2\left(\frac{\epsilon_{yy}}{1-K^2}+\omega\frac{\partial\epsilon_{yy}}{\partial\omega}\right), \end{aligned} \tag{4.8}$$

and the magnetic energy is

$$W_H = \frac{\epsilon_0}{8}bL_xL_z|E_y^0|^2\frac{\epsilon_{yy}}{1-K^2}, \tag{4.9}$$

so then the total energy is

$$W = \frac{\epsilon_0}{8}bL_xL_z|E_y^0|^2\left(\frac{2\epsilon_{yy}}{1-K^2}+\omega\frac{\partial\epsilon_{yy}}{\partial\omega}\right). \tag{4.10}$$

The group velocity $v_g = \partial\omega/\partial h$ is

$$\frac{1}{v_g} = -\frac{1}{c}\sqrt{\frac{\epsilon_{yy}}{1-K^2}}-\frac{1}{2c}\sqrt{\frac{1-K^2}{\epsilon_{yy}}}\omega\frac{\partial\epsilon_{yy}}{\omega}<0. \tag{4.11}$$

From Eq. (4.6, 4.10, 4.11), we verify the relation in Eq. (4.7). These novel electromagnetic features illustrate how the metamaterial medium acts differently with an electron beam from normal circuits.

4.2.3 Electron Beam Interaction with the Antisymmetric Metamaterial Waveguide Mode: Cherenkov-Cyclotron Instability

We send in a continuous electron beam at the velocity $\boldsymbol{v} = v\hat{z}$ into the metamaterial medium traveling in the z direction under a DC magnetic field of B_0 to study their interaction. The full terms of the field component of the antisymmetric mode can be expanded from the eigenmode field terms as

$$\boldsymbol{E} = \mathbb{R}\{C(z)\boldsymbol{E}^{(a)}e^{-i\omega t}\},$$
$$\boldsymbol{H} = \mathbb{R}\{C(z)\boldsymbol{H}^{(a)}e^{-i\omega t}\}.$$

where $C(z)$ is the complex amplitude. The electron beam with a momentum $\boldsymbol{p} = \gamma m\boldsymbol{v}$ gyrate in the magnetic field by the particle motion equation

$$\frac{d\boldsymbol{p}}{dt} = -e\left(E_y + \mu_0 v_z H_x\right)\hat{\boldsymbol{y}} - e\left(E_z - \mu_0 v_y H_x\right)\hat{\boldsymbol{z}} - e\boldsymbol{v} \times B_0\hat{\boldsymbol{z}}. \tag{4.12}$$

In the cylindrical system,

$$p_x = -p_\perp \sin\phi, p_y = p_\perp \cos\phi.$$

and the Larmor radius is

$$a_c = \frac{p_\perp}{eB_0} = \frac{p_\perp}{p_z h_c},$$

where $h_c = eB_0/p_z$.

We then transform the equation of motion to the guiding center coordinates

(X, Y), where

$$\begin{cases} x = X + a_c \cos\phi, \\ y = Y + a_c \sin\phi, \text{ where } Y = 0 \end{cases} \tag{4.13}$$

Here we make the assumption that the Larmor radius is small, $\omega_{\rm cr} a_c/c \ll 1$, and rewrite Eq. (4.12) keeping only the terms with $\exp(ihz - i\omega t - i\phi)$ corresponding to the Cherenkov-cyclotron (or anomalous Doppler) synchronism condition of $\omega = hv_z - h_c v_z$. Under this assumption, the theory only applies to finite B_0, since otherwise a_c is not defined at zero magnetic field. The transformed equations of motion in the guiding center coordinates are:

$$\frac{dp_\perp}{dz} = -\frac{e}{2v_z}\mathbb{R}\left\{C(z)E_y^0\left(1+\beta_z\sqrt{\frac{\epsilon_{yy}}{1-K^2}}\right)e^{-i\chi}\right\}, \tag{4.14}$$

$$p_\perp\frac{d\phi}{dz} = p_\perp h_c + \frac{e}{2v_z}\mathbb{R}\left\{iC(z)E_y^0\left(1+\beta_z\sqrt{\frac{\epsilon_{yy}}{1-K^2}}\right)e^{-i\chi}\right\}, \tag{4.15}$$

$$\frac{dp_z}{dz} = \frac{e}{2v_z}\mathbb{R}\left\{C(z)E_y^0\sqrt{\frac{\epsilon_{yy}}{1-K^2}}\left(Ka_c\frac{\omega_{\rm cr}}{c}+\frac{p_\perp}{\gamma mc}\right)e^{-i\chi}\right\}. \tag{4.16}$$

where $\chi = \omega t - hz + \phi$, and $\beta_z = v_z/c$.

Next the growth rate of the electron energy can be calculated from Eqs. (4.14, 4.16) using the relation $\gamma^2 = 1 + (p_\perp^2 + p_z^2)/(m^2c^2)$, as

$$\frac{d\gamma}{dz} = -\frac{ep_\perp}{2\gamma m^2c^2v_z}\mathbb{R}\left\{C(z)E_y^0\left(1-\sqrt{\frac{\epsilon_{yy}}{1-K^2}}\frac{\omega_{\rm cr}^2}{\omega c h_c}\right)e^{-i\chi}\right\}. \tag{4.17}$$

Combining Eqs. (4.14, 4.17), we have

$$\frac{dp_\perp^2}{d\gamma} = 2\gamma m^2c^2\left(1+\beta_z\sqrt{\frac{\epsilon_{yy}}{1-K^2}}\right)\left(1-\sqrt{\frac{\epsilon_{yy}}{1-K^2}}\frac{\omega_{\rm cr}^2}{\omega c h_c}\right)^{-1}. \tag{4.18}$$

The Cherenkov-cyclotron instability happens when the beam starts gyrating from a zero initial transverse velocity, and gains perpendicular momentum as the beam loses energy from the beam-wave interaction. So the condition for the Cherenkov-cyclotron instability is

$$dp_\perp^2/d\gamma < 0, \tag{4.19}$$

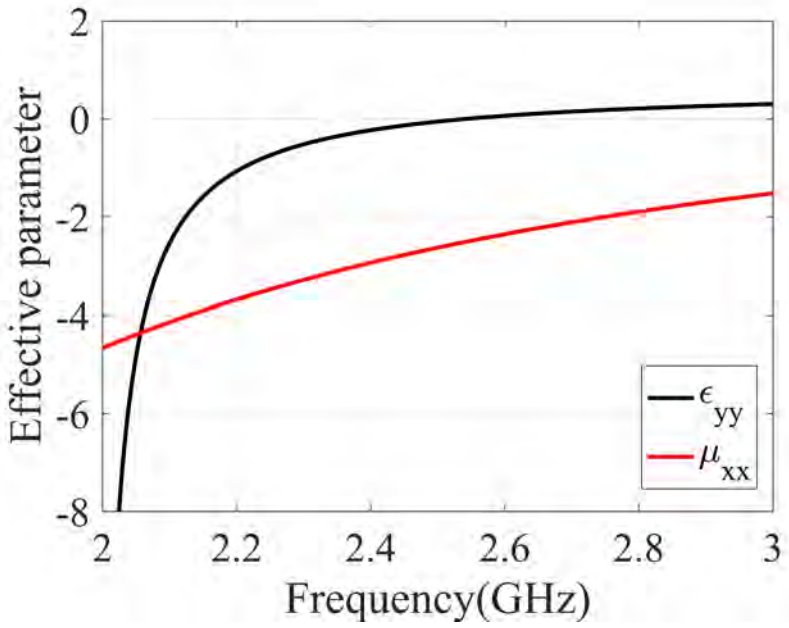

Figure 4-9: Effective parameters ϵ_{yy} and μ_{xx} for the analytical model. Both parameters are negative in the operating frequency range.

which gives

$$1 - \sqrt{\frac{\epsilon_{yy}}{1-K^2}} \frac{\omega_{\rm cr}^2}{\omega c h_c} < 0. \tag{4.20}$$

The condition only holds when the external DC magnetic field is low enough, such that

$$\frac{eB_0}{m} < \gamma v_z \sqrt{\frac{\epsilon_{yy}}{1-K^2}} \frac{\omega_{\rm cr}^2}{\omega c}. \tag{4.21}$$

The Cherenkov-cyclotron instability described here is a unique property of the double negative metamaterial, since according to Eq. (4.20), the frequency of the propagating wave has to be below the cut-off of the TM mode of the empty waveguide, i.e. $\omega < \omega_{\rm cr}$, where $\omega_{\rm cr} = 2\pi c/b = 2\pi \cdot 4.76$ GHz. This feature is equivalent to a negative permeability as [104]

$$\mu_{xx} = 1 - \frac{\omega_{\rm cr}^2}{\omega^2}. \tag{4.22}$$

Therefore, both ϵ_{yy} and μ_{xx} are negative in the operating frequency range, as shown in Fig. 4-9.

Next we calculate the starting current for the Cherenkov-cyclotron instability.

The waveguide excitation equation by a current density $\boldsymbol{j}$ is

$$\frac{dC}{dz} = \frac{1}{4P^{(a)}} \int \boldsymbol{j} \cdot \boldsymbol{E}^{(a)*} e^{i\omega t} dS_\perp \tag{4.23}$$

where $P^{(a)} < 0$ is the Poynting vector for the antisymmetric mode of Eq. (4.3). The integration is done over the beam cross section $S_\perp$. The current density of an electron beam with a number density of n_b can be represented as

$$\boldsymbol{j} = e n_b \left(\frac{p_\perp}{\gamma m} \sin\phi \ \hat{\boldsymbol{x}} - \frac{p_\perp}{\gamma m} \cos\phi \ \hat{\boldsymbol{y}} - v_z \hat{\boldsymbol{z}} \right) S_b \ \delta\left(x - X - a_c \cos\phi, y - a_c \sin\phi\right) \tag{4.24}$$

where S_b is the beam cross-section area. The gyrating electron beam trajectory is included as the arguments of the delta-function. Using Eqs. (4.13, 4.24) in Eq. (4.23) under the assumption of a small gyro-radius a_c and keeping gyro-radius terms to the first order, we have

$$\frac{dC}{dz} = \frac{I_b}{8P^{(a)}} \frac{p_\perp}{\gamma m v_z} E_y^{0*} \left(1 - \frac{\sqrt{-\epsilon_{yy}}}{\sqrt{\omega_{\rm cr}^2/\omega^2 - 1}} \frac{\omega_{\rm cr}^2}{\omega c h_c} \right) e^{-ihz + i\omega t + i\phi} \tag{4.25}$$

where $I_b = e n_b v_z S_b$ is the beam current.

Next we introduce the normalized parameters,

$$\begin{aligned} &\rho = \frac{p_\perp}{mc}, \ Z = kz, \\ &A = \frac{eCE_y^0}{mc^2 k}, \\ &I = -\frac{I_b |E_y^0|^2}{2k^2 P^{(a)}} \frac{e}{mc^2}, \end{aligned} \tag{4.26}$$

where $k = \omega/c$. Then we have

$$\frac{dA}{dZ} = -\frac{\rho I}{4\gamma\beta_z}\left(1 - \frac{\sqrt{-\epsilon_{yy}}}{\sqrt{-\mu_{xx}}}\frac{\omega_{\rm cr}^2}{\omega c h_c}\right)e^{i\chi}, \tag{4.27}$$

$$\frac{d\gamma}{dZ} = -\frac{\rho}{2\gamma\beta_z}\mathbb{R}\left[A\left(1 - \frac{\sqrt{-\epsilon_{yy}}}{\sqrt{-\mu_{xx}}}\frac{\omega_{\rm cr}^2}{\omega c h_c}\right)e^{-i\chi}\right], \tag{4.28}$$

$$\frac{d\rho}{dZ} = -\frac{1}{2\beta_z}\mathbb{R}\left[A\left(1 + \beta_z\frac{\sqrt{-\epsilon_{yy}}}{\sqrt{-\mu_{xx}}}\right)e^{-i\chi}\right], \tag{4.29}$$

$$\frac{d\chi}{dZ} = \frac{1}{\beta_z} - \sqrt{(-\epsilon_{yy})\,(-\mu_{xx})} + \frac{h_c}{k} + \frac{1}{2\beta_z\rho}\mathbb{R}\left[iA\left(1 + \beta_z\frac{\sqrt{-\epsilon_{yy}}}{\sqrt{-\mu_{xx}}}\right)e^{-i\chi}\right] \tag{4.30}$$

where β_z can be expressed as

$$\beta_z = \sqrt{1 - \gamma^{-2} - \rho^2\gamma^{-2}}.$$

The integral of Eqs. (4.27, 4.28) is

$$|A(z)|^2 - |A(0)|^2 = I(\gamma(z) - \gamma(0)) \tag{4.31}$$

Equations (4.20, 4.31) are the instability conditions: the current $I > 0$ because of $P^{(a)} < 0$ as in Eq. (4.26), the electrons lose energy $\gamma(z) < \gamma(0)$, gain transverse momentum $p_\perp$, and the field amplitude is the highest at the entrance $|A(0)| > |A(z)|$ from the backward wave.

We now introduce the linear current represented as

$$J = -i\rho e^{i\chi}, \tag{4.32}$$

Then from Eqs. (4.29, 4.30), we have

$$\frac{dJ}{dZ} = i\delta_c J + i\frac{A}{2\beta_z}\left(1 + \beta_z\frac{\sqrt{-\epsilon_{yy}}}{\sqrt{-\mu_{xx}}}\right), \tag{4.33}$$

where

$$\delta_c = \frac{1}{\beta_z} + \frac{h_c}{k} - \sqrt{(-\epsilon_{yy})(-\mu_{xx})}. \tag{4.34}$$

The condition of $\delta_c = 0$ corresponds to the cyclotron synchronism $\omega = hv_z - \Omega_c/\gamma$.

Equation (4.25) can be rewritten as

$$\frac{dA}{dZ} = -i\frac{IJ}{4\gamma\beta_z}\left(1 - \frac{\sqrt{-\epsilon_{yy}}}{\sqrt{-\mu_{xx}}}\frac{\omega_{\rm cr}^2}{\omega c h_c}\right). \tag{4.35}$$

Here we assume that

$$A, J \propto e^{\Gamma Z}, \tag{4.36}$$

then we can solve for Γ from Eqs. (4.33) and (4.35), and the result is

$$\Gamma_{1,2} = \frac{i\delta_c}{2} \pm i\sqrt{\frac{\delta_c^2}{4} + q^2}, \tag{4.37}$$

where

$$q = \sqrt{-\frac{I}{8\gamma_0\beta_{z0}^2}\left(1 + \beta_{z0}\frac{\sqrt{-\epsilon_{yy}}}{\sqrt{-\mu_{xx}}}\right)\left(1 - \frac{\sqrt{-\epsilon_{yy}}}{\sqrt{-\mu_{xx}}}\frac{\omega_{\rm cr}^2}{\omega c h_c}\right)}, \tag{4.38}$$

and $\beta_{z0} \cdot c$ is the initial electron velocity.

Representing the field as a superposition

$$A = A_1 e^{\Gamma_1 Z} + A_2 e^{\Gamma_2 Z}, \tag{4.39}$$

with arbitrary constants $A_{1,2}$, we solve for q from the boundary conditions

$$\begin{aligned} &J(Z=0) = 0,\ \gamma(Z=0) = \gamma_0, \\ &A(Z = Z_0 \equiv kL_z) = 0,\ \frac{dA}{dZ}(Z=0) = 0. \end{aligned} \tag{4.40}$$

These boundary conditions are typical for backward-wave interaction: no transverse velocity of the beam at the entrance $Z = 0$; the zero field derivative at the entrance means no initial modulation on the beam; the field is zero, therefore it is matched, at the end of the structure $Z = Z_0$. Substituting A in the boundary conditions with Eq. (4.39), we have

$$i\delta_c \sin\left(\sqrt{q^2 + \frac{\delta_c^2}{4}}Z_0\right) - 2\sqrt{q^2 + \frac{\delta_c^2}{4}}\cos\left(\sqrt{q^2 + \frac{\delta_c^2}{4}}Z_0\right) = 0 \tag{4.41}$$

The solution is possible at the cyclotron synchronism condition of $\delta_c = 0$, under the condition of

$$q = \left(\frac{\pi}{2} + n\pi\right) \frac{1}{Z_0}, \tag{4.42}$$

where n is an integer. Then combining the equations for q as Eqs. (4.38, 4.42), we have the minimum starting current I_{st} when $n = 0$ as

$$I_{\text{b st}}^{(a)} = -\frac{\pi b L_x}{4L_z^2} \left(\frac{4\pi\epsilon_0 mc^3}{e}\right) \gamma_0 \beta_{z0}^2 \left(\beta_{z0} + \sqrt{\frac{-\mu_{xx}}{-\epsilon_{yy}}}\right)^{-1} \left(1 - \frac{\sqrt{-\epsilon_{yy}}}{\sqrt{-\mu_{xx}}} \frac{\omega_{\text{cr}}^2}{\omega c h_c}\right)^{-1}. \tag{4.43}$$

A numerical calculation of the starting current from Eq. (4.43) is presented in Fig. 4-10, where is the starting current is calculated as a function of the magnetic field for the beam voltage of 420 kV. The effective ϵ_{yy} and μ_{xx} are extracted from the dispersion curves from the eigenmode simulation. The frequency is determined by the dispersion curve and beam line intersection in Fig. 4-8. The waveguide dimensions are L_z = 370 mm, L_x = 43 mm, and b=63 mm.

Figure 4-10 shows that the starting current drops with a lower magnetic field. This indicates that the Cherenkov-cyclotron instability happens more likely at low magnetic fields.

4.2.4 Electron Beam Interaction with the Symmetric Metamaterial Waveguide Mode: Cherenkov Instability

An important question concerns the competition between the Cherenkov-cyclotron regime operating in the antisymmetric mode and the Cherenkov regime of operating in the symmetric mode. The symmetric mode (superscript (s)) with a longitudinal

E_z field on the axis has the nonzero field components as

$$
\begin{aligned}
E_z^{(s)} &= E_z^0 \cos\left(\frac{2\pi}{b}y\right) e^{ihz}, \\
E_y^{(s)} &= i\frac{\omega b}{2\pi c}\sqrt{\frac{-\mu_{xx}}{-\epsilon_{yy}}} E_z^0 \sin\left(\frac{2\pi}{b}y\right) e^{ihz}, \\
H_x^{(s)} &= i\frac{\omega\epsilon_0 b}{2\pi} E_z^0 \sin\left(\frac{2\pi}{b}y\right) e^{ihz},
\end{aligned}
\tag{4.44}
$$

and the Poynting flux is

$$
P^{(s)} = -\frac{c\epsilon_0 b L_x}{4}\left(\frac{\omega b}{2\pi c}\right)^2 |E_z^0|^2 \sqrt{\frac{-\mu_{xx}}{-\epsilon_{yy}}}.
$$

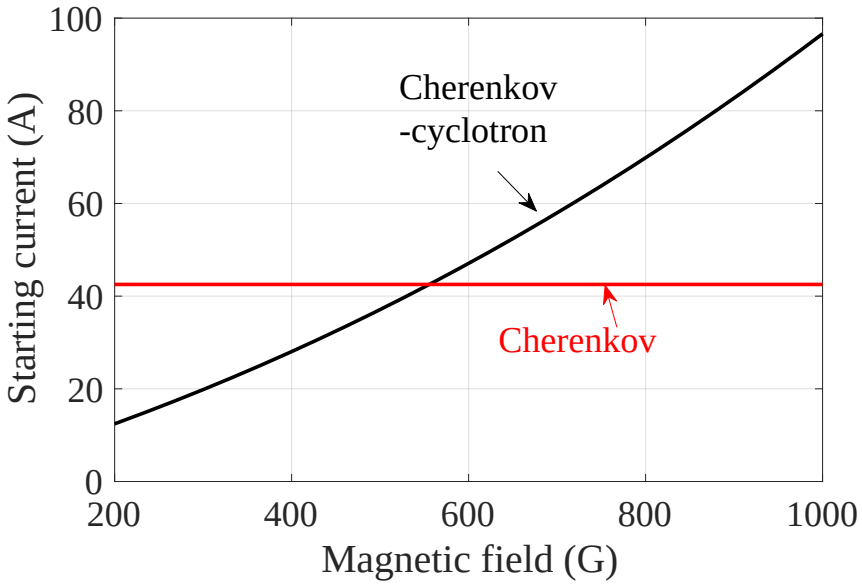

Figure 4-10: Variation of the starting current with the magnetic field for the Cherenkov-cyclotron instability and the Cherenkov instability. The beam voltage is 420 kV.

For simplicity, we present only an abbreviated derivation of the starting current of Cherenkov oscillator regime operation. The starting current can be calculated using the usual theory for a Backward Wave Oscillator (BWO) [54]. The dispersion

equation of wave-beam interaction is of the third order as

$$\left(\Gamma'\right)^2\left(\Gamma' - 1 + \frac{hv_{z0}}{\omega}\right) = -C_P^3 \tag{4.45}$$

where Γ' determines the z-dependence of the field and the current as $\exp(-i\Gamma'\omega z/v_{z0})$, and C_P is the Pierce parameter:

$$C_P = \left(-I_b\frac{|E_z^0|^2}{4P^{(s)}}\frac{e}{mc^2}\frac{c^2}{\omega^2\gamma_0^3}\right)^{1/3} \tag{4.46}$$

From the standard BWO boundary conditions including the field matching at the end of the structure at $z = L_z$ and absence of beam modulation at the entrance $z = 0$, the starting value of the Pierce parameter is determined as $C_P N_z$=0.314 where $N_z = \omega L_z/(2\pi v_{z0})$ is the number of axial wavelengths in the length of the waveguide. Using Eq. (4.46), the starting beam current for the symmetric mode $I_{\text{b st}}^{(s)}$ can be calculated as follows:

$$I_{\text{b st}}^{(s)} = 0.0155\left(\frac{4\pi\epsilon_0 mc^3}{e}\right)\frac{b^3 L_x}{L_z^3}\frac{\omega\gamma_0^3\beta_{z0}^3}{c}\sqrt{\frac{-\mu_{xx}}{-\epsilon_{yy}}} \tag{4.47}$$

This calculation uses the same effective medium parameters ϵ_{yy} and μ_{xx} as for the antisymmetric mode.

The numerical calculation of the starting current of the symmetric mode is shown in Fig. 4-10 together with that of the antisymmetric mode. The beam voltage is 420 kV for both cases. The starting current of the Cherenkov mode, therefore, is higher than for the Cherenkov-cyclotron mode for the magnetic fields $B < 550$ G for the 420 kV beam.

This calculation has been done at other beam voltage values, and the same trend holds. The Cherenkov mode is harder to start when the magnetic field $B < 630$ G for a 450 kV beam, and $B < 740$ G for a 490 kV beam.

If we compare Eq. (4.43) and Eq. (4.47), we have the ratio of the starting current

for the Cherenkov-cyclotron instability $I_{\mathrm{b\ st}}^{(a)}$ to that for the Cherenkov instability $I_{\mathrm{b\ st}}^{(\mathrm{s})}$:

$$\frac{I_{\mathrm{b\ st}}^{(a)}}{I_{\mathrm{b\ st}}^{(\mathrm{s})}} = \frac{50.67 L_z}{\gamma_0^2 b^2} \left(\beta + \sqrt{\frac{-\mu_{xx}}{-\epsilon_{yy}}} \right)^{-1} \left(\frac{\omega_{\mathrm{cr}}^2}{c^2 h_c} - \frac{\omega}{c} \sqrt{\frac{-\mu_{xx}}{-\epsilon_{yy}}} \right)^{-1} . \tag{4.48}$$

The Cherenkov-cyclotron instability is favored when the starting current of the antisymmetric mode with the Cherenkov-cyclotron type is lower than that of the symmetric mode with the Cherenkov type, i.e. $I_{\mathrm{b\ st}}^{(a)}/I_{\mathrm{b\ st}}^{(\mathrm{s})} < 1$. The ratio $I_{\mathrm{b\ st}}^{(a)}/I_{\mathrm{b\ st}}^{(\mathrm{s})}$ gets lower with a lower magnetic field B, so the Cherenkov-cyclotron mode dominates at low magnetic field. This important result of dominance of the Cherenkov-cyclotron mode at lower magnetic field was verified in the Stage I experiment [19, 20, 92] and the Stage II experiment [58, 93, 94], which is to be described in Chapter 5. The ratio gets higher with a longer structure length L_z, so the Cherenkov-cyclotron mode is predicted to be hard to find in a longer structure.

4.2.5 Discussions and Conclusions

The backward-wave oscillator (BWO) based on the instability of the electron beam in a metamaterial loaded waveguide has been experimentally demonstrated in [19,20,92]. High microwave power above 1 MW can be generated in this device only at low axial magnetic fields. The mode excited in the metamaterial loaded waveguide is an antisymmetric mode deflecting the electron beam off the axis. The simulations have shown the spiraling electron beam. It was proposed that the Cherenkov-cyclotron instability causes high power microwave generation in the device. The Cherenkov-cyclotron synchronism between the metamaterial waveguide mode and the electron beam in a finite magnetic field was experimentally proved using the frequency tuning by the magnetic field.

In this section, the analytical theory of the Cherenkov-cyclotron instability of an electron beam in a metamaterial loaded waveguide has been presented. The starting current, i.e. the threshold of the instability, is derived using the effective permittivity tensor of the medium filling the waveguide. The permittivity was determined using

the best fit to the dispersion curve of the real metamaterial structure. In agreement with the experiment, the Cherenkov-cyclotron instability can only start when the magnetic field is low enough, and the starting condition predicted by the analytical theory agrees well with our experimental observations.

Here we have also developed the linear, stationary (with a time dependence of $\exp(-i\omega t)$) theory of the Cherenkov-cyclotron instability in a metamaterial loaded waveguide, and transient processes are not included. The outcome of this theory is the starting current of the oscillator. The theory is simple and allows us to design the oscillator without running intense numerical simulations. Furthermore, it can be extended to model nonlinear and nonstationary regimes and calculate the efficiency of interaction. The metamaterial waveguide can be profiled along the z direction and optimized to obtain higher efficiency.

4.3 Design of a Metamaterial Waveguide with Reverse Symmetry

In this section, I will present the design work for the Stage II metamaterial experiment at MIT. The main focus is to improve the pulse length of the multi-MW microwave pulses from the Stage I experiment [19, 20, 92]. The design work leads to a new structure built and tested at MIT. The experimental setup and results will be explained in Chapter 5.

4.3.1 Motivation

The idea of a metamaterial structure with reverse symmetry comes from our experience with the Stage I experiment with the symmetric structure. In that structure, the electron beam favors the antisymmetric mode with a transverse electric field on the beam axis, and the symmetric mode with a longitudinal electric field on axis does not help to generate high power.

So in the new design, we have reversed one of the metamaterial plates to create

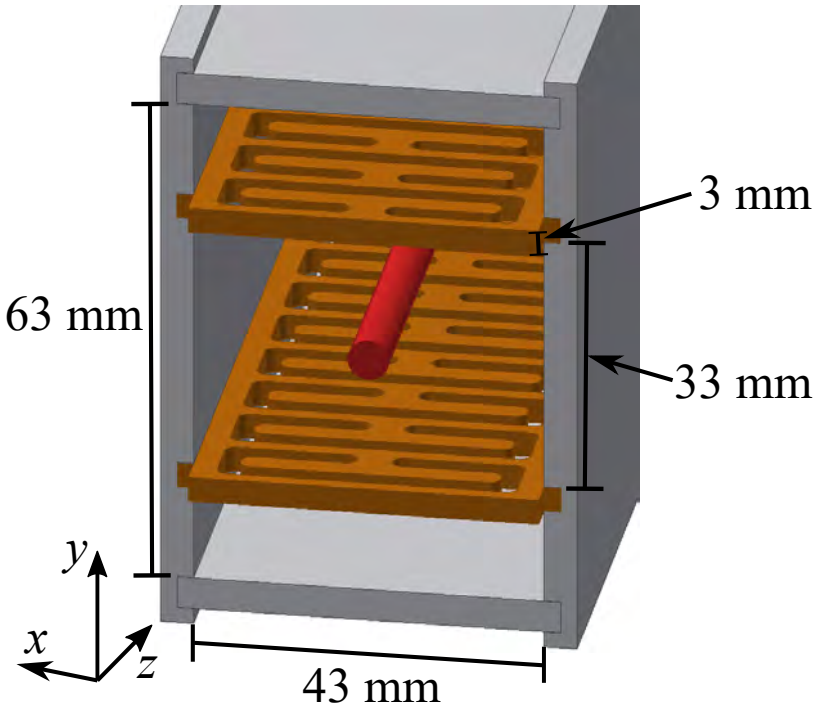

Figure 4-11: MTM-R circuit design. Two copper plates with the C-shapes aligned in opposite directions are placed in a rectangular waveguide. The period of the metamaterial plates is 10 mm. The red cylinder represents the electron beam traveling between the two plates along the central axis in the $+z$ direction. The origin of the coordinate system is placed in the center of waveguide, and $z = 0$ is at the edge of the metamaterial plates.

asymmetry. This new structure is named the reverse metamaterial structure, or the MTM-R structure. In this way, the symmetric mode with a longitudinal electric field on the beam axis becomes a hybrid mode with both a longitudinal and a transverse, deflecting electric field on the axis. Similarly, the antisymmetric mode of the metamaterial structure becomes a hybrid mode in the MTM-R structure. Therefore, any mode of the MTM-R structure has a transverse electric field on the axis which will deflect the electron beam but may improve high power operation of the device.

4.3.2 Circuit Design of the Metamaterial Structure with Reverse Symmetry

The MTM-R structure is shown in Fig. 4-11. It is a stainless steel waveguide with two copper metamaterial plates brazed onto it. The C-shaped cuts on the two metamaterial plates are aligned in opposite directions; that is, one plate is 'reversed' from the other, as can be seen in Fig. 4-11. The period of the metamaterial plate, containing one C-shaped cut, is 10 mm, and there are 37 periods in the 370 mm long structure. The length of one period is much smaller than the wavelength in S-band, and this is the general feature of a metamaterial structure. The two plates are 3 mm thick, and separated by 33 mm. The electron beam travels in the $+z$ direction, along the central line of the waveguide.

Fig 4-12 shows the dispersion relation between the eigenmode frequency and the phase advance per period of the metamaterial structure. The dispersion curves of the lowest two modes are plotted, labeled as Mode 1 and Mode 2.

In terms of the interaction with an electron beam, similar to the Stage I experiment, there are also two types of possible mechanisms, the Cherenkov type interaction with a dispersion relation of $\omega = k_z v_z$, and the Cherenkov-cyclotron type with a dispersion of $\omega = k_z v_z - n\Omega_c/\gamma$, where again $\Omega_c = eB_z/m$ is the cyclotron angular frequency, B_z is the DC magnetic field, n is an integer and $\gamma = (1 - v^2/c^2)^{-1/2}$ is the Lorentz factor. The case of $n = 1$ is the anomalous Doppler resonance. The $n = 1$ Cherenkov-cyclotron beam line $\omega = k_z v_z - \Omega_c/\gamma$ with a magnetic field of 400 G is shown in Fig. 4-12, along with the Cherenkov beam line as $\omega = k_z v_z$ for a 490 kV electron beam.

The electric field distribution for the two modes is shown in Fig. 4-13a, and the field is plotted on the middle cutting plane $x = 0$ in one period containing one pair of C-shaped cuts. Both Mode 1 and Mode 2 are hybrid. Figure 4-13b shows the phase of the transverse electric field E_y, and Mode 1 and Mode 2 have different relative phases. The waves generated in the upper and lower parts of the waveguides are guided into two S-band waveguide bends, Arm 1 and Arm 2, with Arm 1 on the bottom and Arm

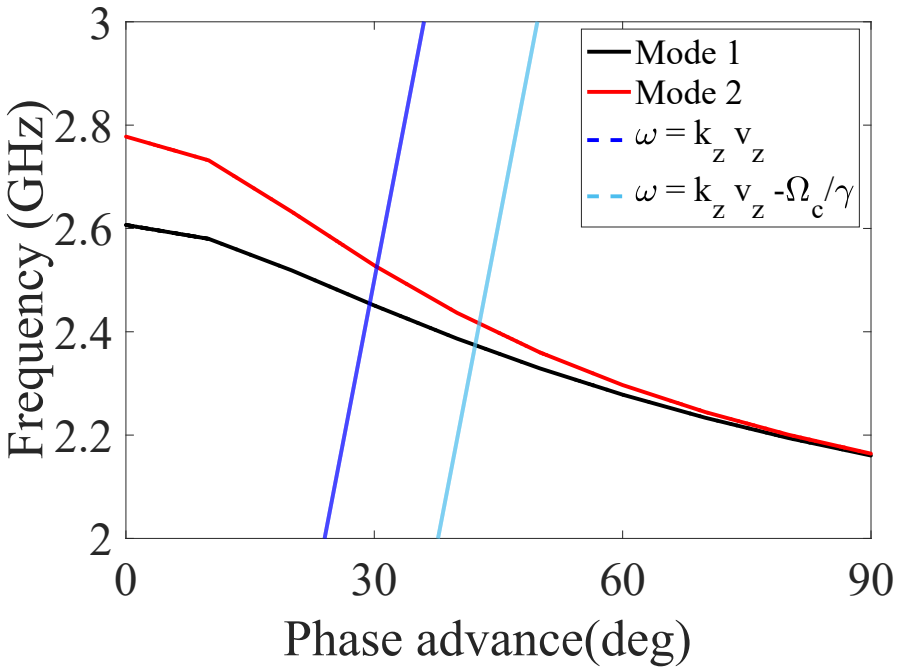

Figure 4-12: Dispersion curves from CST eigenmode simulation for a period of the metamaterial structure. The Cherenkov and the Cherenkov-cyclotron beamlines are calculated for a 490 kV electron beam in a constant magnetic field of 400 G.

2 on the top according to Fig. 4-11.

4.3.3 Particle-in-Cell Simulation of MTM-R Structure

The particle-in-cell (PIC) solver of the CST Particle Studio code is used to simulate the microwave excitation in the structure by a 490 kV, 84 A electron beam.

The electron beam starts straight, and goes through the metamaterial structure as illustrated in Fig. 4-14a. A longitudinal DC solenoid field is applied for beam confinement, but it also provides the possibility for the beam to perform cyclotron motion. In the simulation, the beam trajectory is helical, indicating the presence of the Cherenkov-cyclotron type interaction. The cyclotron motion starts from zero transverse velocity, therefore it is a result of the Cherenkov-cyclotron instability.

An example of the simulated power in the two output couplers is presented in

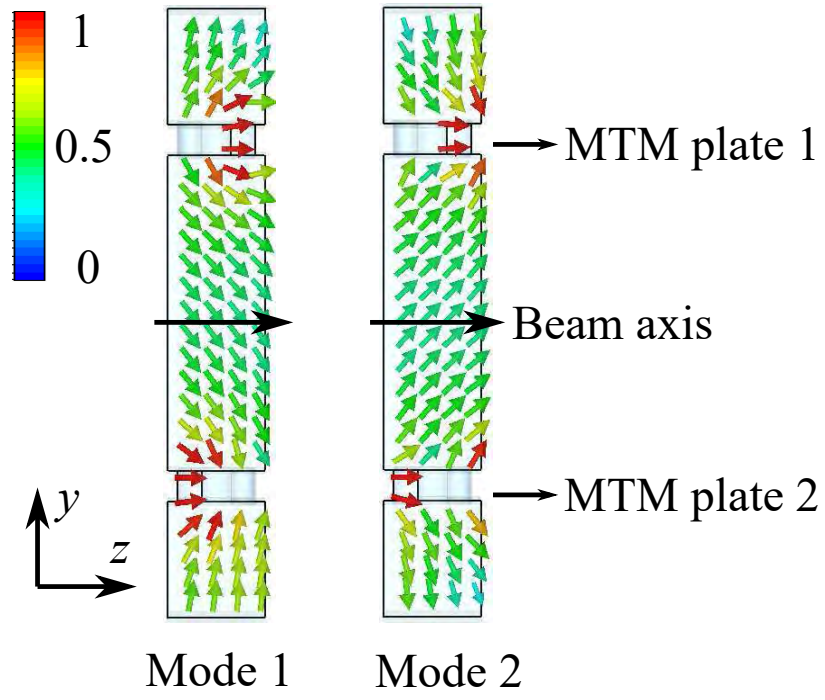

(a)

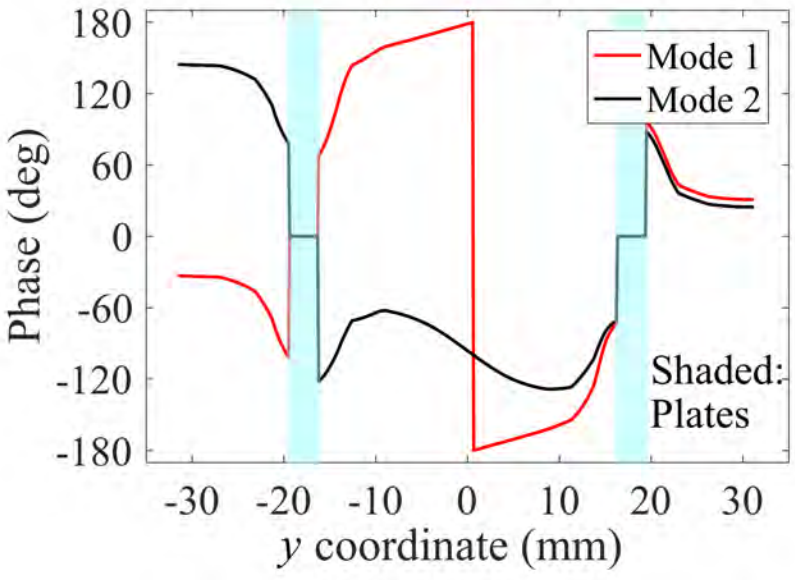

(b)

Figure 4-13: Electric field distribution of Mode 1 and Mode 2. (a) Electric field on the middle cutting plane of $x = 0$ for one period of the structure. (b) Phase of the E_y field for Mode 1 and Mode 2. The shaded blocks denote the positions of the two metamaterial plates.

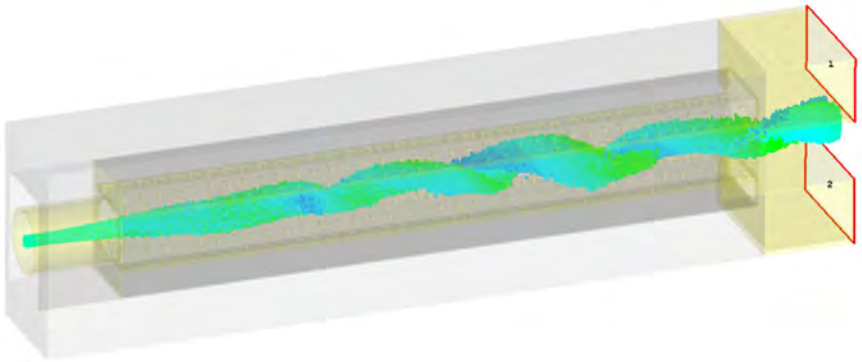

(a)

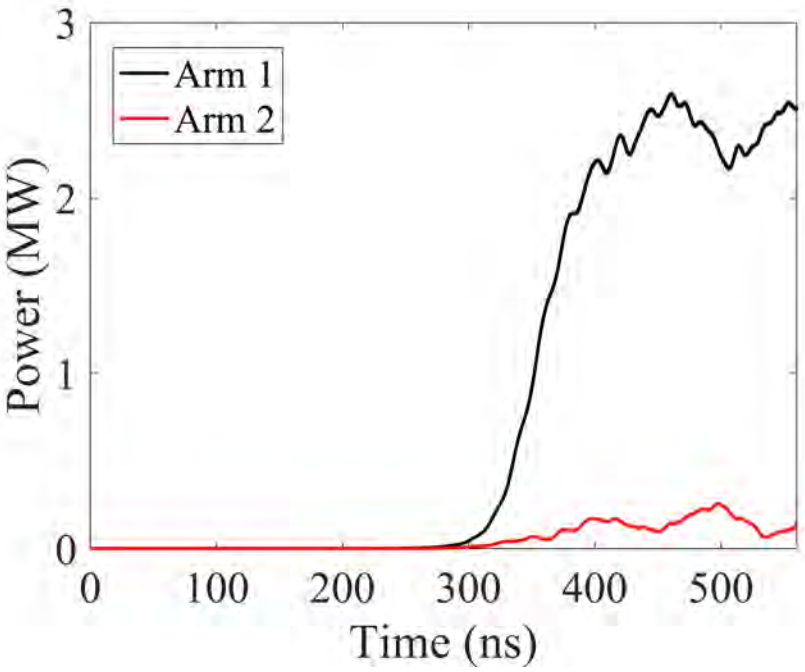

(b)

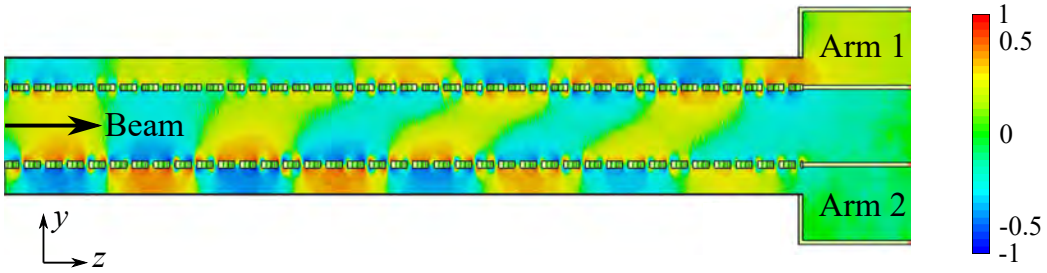

(c)

Figure 4-14: CST Particle Studio Particle-in-cell simulation results. (a) CST model and the helical beam trajectory with a magnetic field of 800 G. (b) Power in the two output ports labeled as Arm 1 and Arm 2. Arm 1 is on the side of the bottom plate as in Fig. 4-11. (c) Plot of E_y on the middle cutting plane $x = 0$. The field amplitude is in log scale.

Fig. 4-14b. With a solenoidal magnetic field of 800 G, the output microwave power reaches 2.5 MW.

Note that in Fig. 4-14b the power levels in the two output ports are uneven in the MTM-R design. This is different from the symmetric metamaterial structure in the Stage I experiment, with the symmetry between the two arms broken in this experiment.

The phenomenon of uneven power levels is caused by the fact that the longitudinal locations of peak electric field are alternating between the two plates as the beam spirals. So with a finite length of the metamaterial waveguide, one arm can receive the majority of the generated microwave power. A plot of the transverse electric field on the middle cutting plane $x = 0$ is shown in Fig. 4-14c, and it explains why Arm 1 receives more power in the example illustrated. The power splitting between the two arms varies with the structure length, and this has been verified with a series of PIC simulations on structures with different numbers of longitudinal periods.

4.3.4 Conclusions

To conclude the design work in this section, the idea of the reversed metamaterial waveguide was proposed and simulated. Based on the Stage I experiment discoveries, reversing the symmetry would help with generation of high microwave power in the Cherenkov-cyclotron type of interaction. The CST PIC simulation supports the idea, and shows the new feature of the Stage II experiment design. The simulation also predicts multi-MW microwave power generation at 2.4 GHz. With these theoretical results, the MTM-R structure was built and tested at MIT, as will be presented in Chapter 5.

Chapter 5

Experiment of Metamaterial Structures for High Power Microwave Generation

In Chapter 4, I introduced theoretical studies of metamaterial structures for high power microwave applications. A design of the reversed metamaterial (MTM-R) structure was finalized in Section 4.3.

Based on the design work, the MTM-R structure at 2.4 GHz was built and tested at MIT as the Stage II experiment. The Stage I experiment is reviewed in Section 4.1. Multi-MW microwave power pulses were measured, but only with a short pulse length of 100 ns to 400 ns. The Stage II experiment is focused to solve this problem.

In this chapter, I will present the experimental facilities of the MIT Stage II metamaterial experiment in Section 5.1. Then the experimental results will be introduced in Section 5.2. Finally conclusions on the metamaterial high power microwave source experiment will be given in Section 5.3.

5.1 Experimental Facilities

The experimental facilities for the metamaterial-based high power microwave source include a 490 kV, 84 A thermionic electron gun with the high voltage modulator system, the magnet system for beam confinement, the diagnostic system, and the interaction metamaterial structure itself inside a vacuum chamber.

In this chapter, I will first give an overview of the test facilities in Section 5.1.1, and then move on to introduce individual components in the experimental setup. Section 5.1.2 will describe the electron gun and the high voltage system. Section 5.1.3 will describe the magnet system. Section 5.1.4 will present the experimental diagnostics for the microwaves and the electron beam. Section 5.1.5 will show the built MTM-R structure and how it was assembled into the system.

5.1.1 Overview of Test Facilities at MIT

The overall CAD drawing of the experimental setup is shown in Fig. 5-1. As a reference, the metamaterial structure, as the copper plates in Fig. 5-1, is 37 cm long.

A lab photo is shown in Fig. 5-2. The high voltage modulator is in an oil tank, part of which is shown on the right of the photo. Then from the right to the left there is the electron gun, the solenoid magnet with the MTM-R structure in the magnet bore, the collector and output waveguides. The controls and the diagnostics are wired to a control room. A photo of the control room is shown in Fig. 5-3.

The electron beam is emitted from a thermionic electron gun (not shown in Fig. 5-1). The electron gun with a thermionic cathode is pulsed by 1 μs high voltage pulses up to 490 kV, and the emitted beam current at 490 kV is 84 A.

The electron beam is then confined by two magnets powered by external DC power supplies. The one closer to the gun is referred to as the magnetic lens, and the one farther away from the gun and overlapping the metamaterial circuit region is referred to as the solenoid magnet.

After the beam passes through the interaction region, it is dumped into the collector, and the microwaves generated in the metamaterial structure are guided through two waveguide bends. We call the two waveguide bends Arm 1 and Arm 2. The waveguide bends are WR284 rectangular waveguides, which remain single-moded (TE_{10} mode) in the frequency range from 2.078 GHz to 4.156 GHz.

On both Arm 1 and Arm 2, we have installed Bethe hole directional couplers to measure the microwave power. The couplers pick up a small amount of power in the waveguide with a coupling coefficient of -64 dB for Arm 1 and -61 dB for Arm 2 at

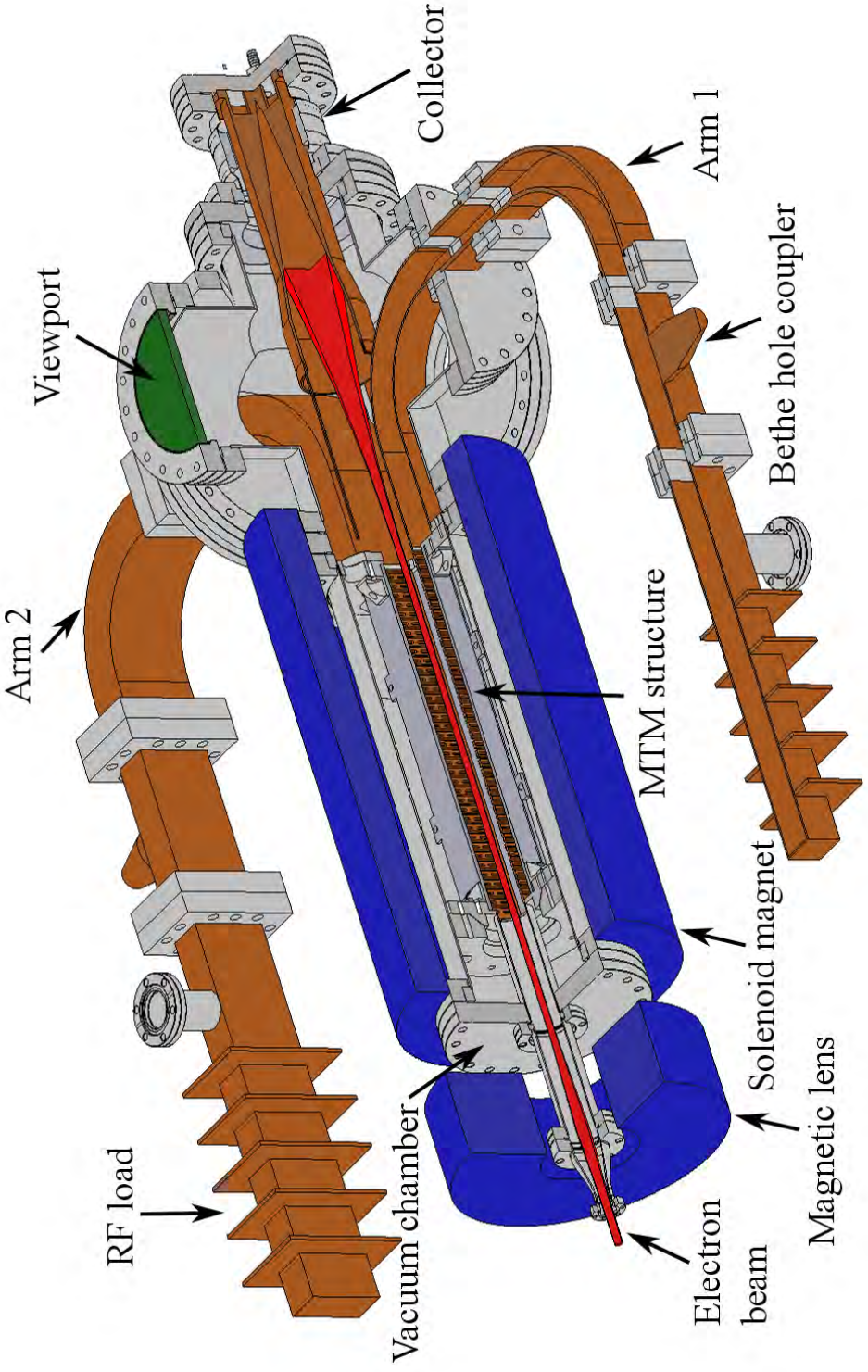

Figure 5-1: Experimental Facilities at MIT.

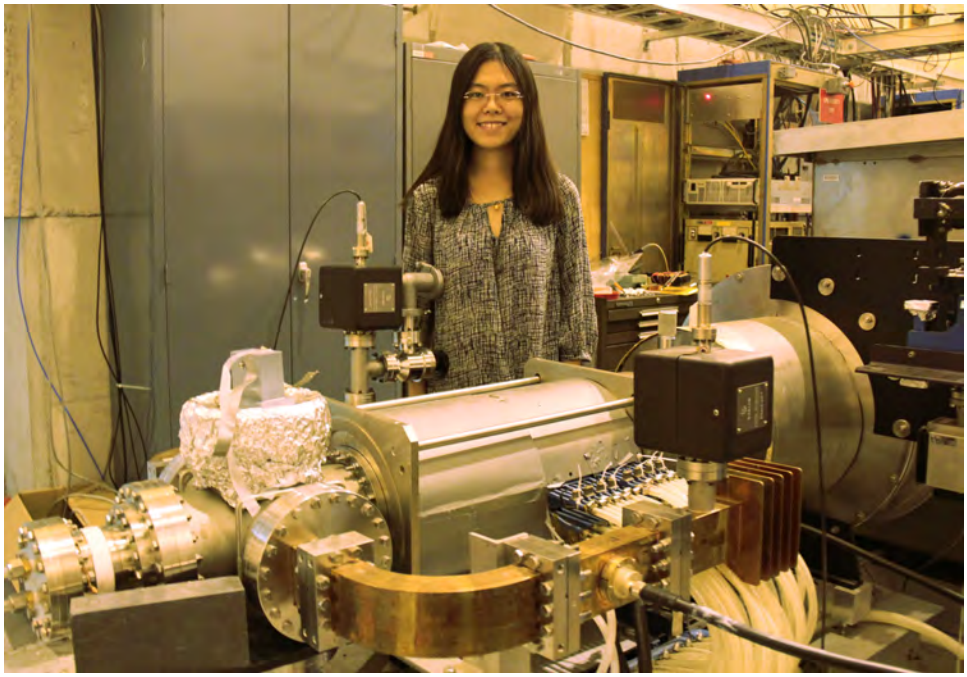

Figure 5-2: Lab photo of the MTM-R experiment. The electron gun, the solenoid, the collector and one of the two output arms with the Bethe hole coupler can be seen in the photo. On the right is part of the oil tank holding the high voltage modulator.

2.4 GHz. The coupling coefficients were determined using a vector network analyzer (VNA). After the power measurement, the microwaves are guided into the RF loads for absorption.

We have maintained a good vacuum condition throughout the experiment. The pressure can reach 10^{-9} Torr as the base pressure. Four ion pumps are constantly pumping, a 150 L/s pump at the electron gun location, a 75 L/s ion pump at the beam collector location, and two 20 L/s pumps at the two output arms. They help keep the ultra high vacuum for the experiment. The vacuum environment in the electron gun is isolated from the rest of the vacuum system by a gate valve when the electron gun is not pulsed to protect the gun cathode.

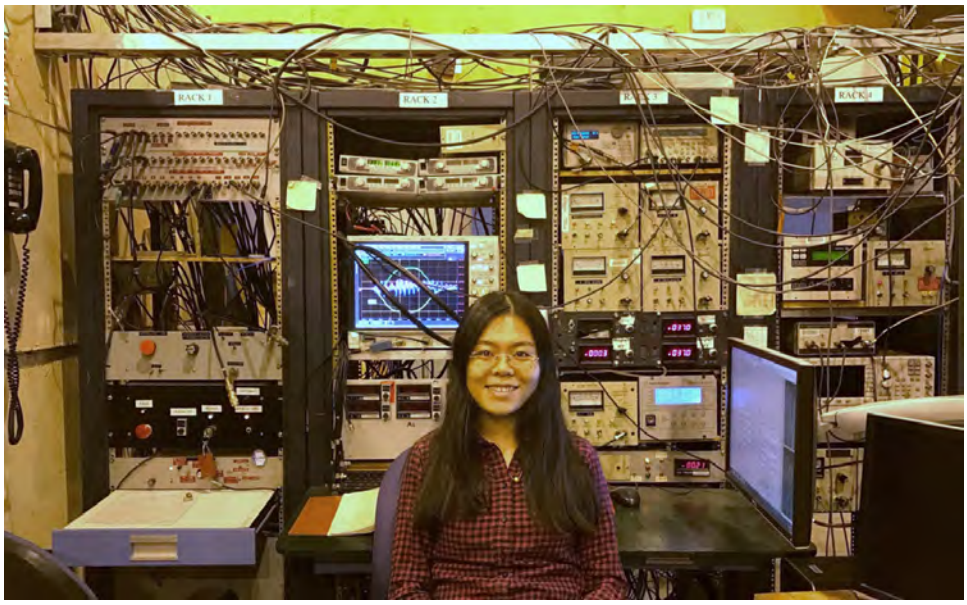

Figure 5-3: Photo of the control room. Soon after the photo was taken, the control room was moved and rearranged.

5.1.2 Electron Gun and High Voltage System

The electron gun was built by Haimson Research Corporation (HRC) and installed at MIT. It is a Pierce electron gun with a thermionic cathode.

Figure 5-4 shows the interior of the electron gun. The cathode is pulsed by high voltage signals of up to 490 kV with 1 μs flattop generated by the modulator, and the anode is grounded. Figure 5-5 shows the high voltage modulator, which sits in a tank filled with oil. The heater is connected to the HRC electron gun.

The cathode is heated by a Tungsten heater, so when a high voltage pulse is applied, an electron beam with a pulse length of 1 μs is emitted. The shape of the cathode is designed so that a laminar electron beam is generated and then focused down to a beam waist. The beam waist is where the electron beam has the smallest transverse size, and the transverse velocity is zero at the waist position. The beam waist for the 490 kV beam is 7.5 mm in diameter.

For a Pierce gun, the current I scales with the voltage V as $I \propto V^{3/2}$ [54, 112] by the Child-Langmuir law [113,114]. The relativistic correction to the law is insignificant

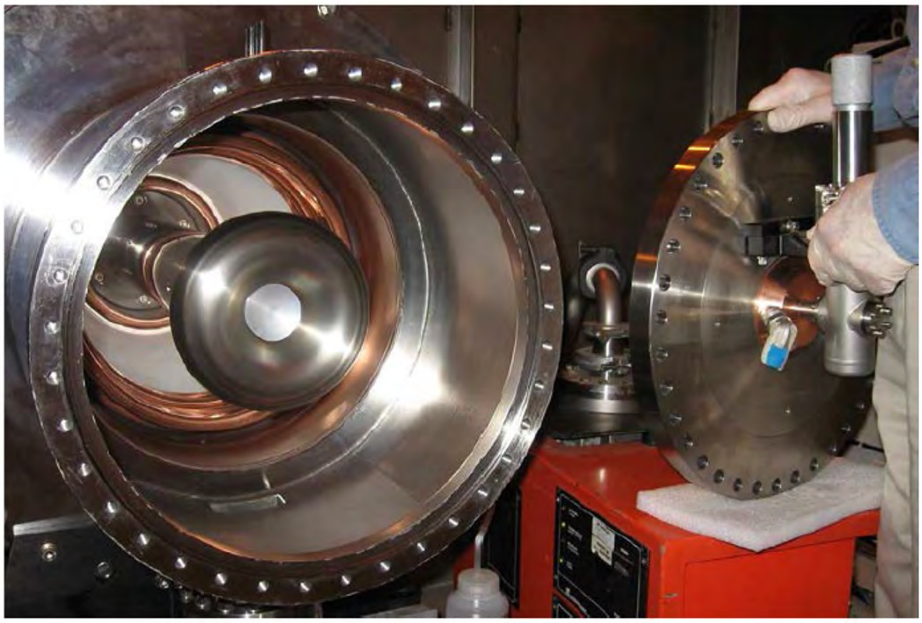

Figure 5-4: Interior structure of the Pierce type electron gun. The gun cathode is opened up for installation. The anode is attached to the flange on the right. Photo credit: Jason Hummelt [19].

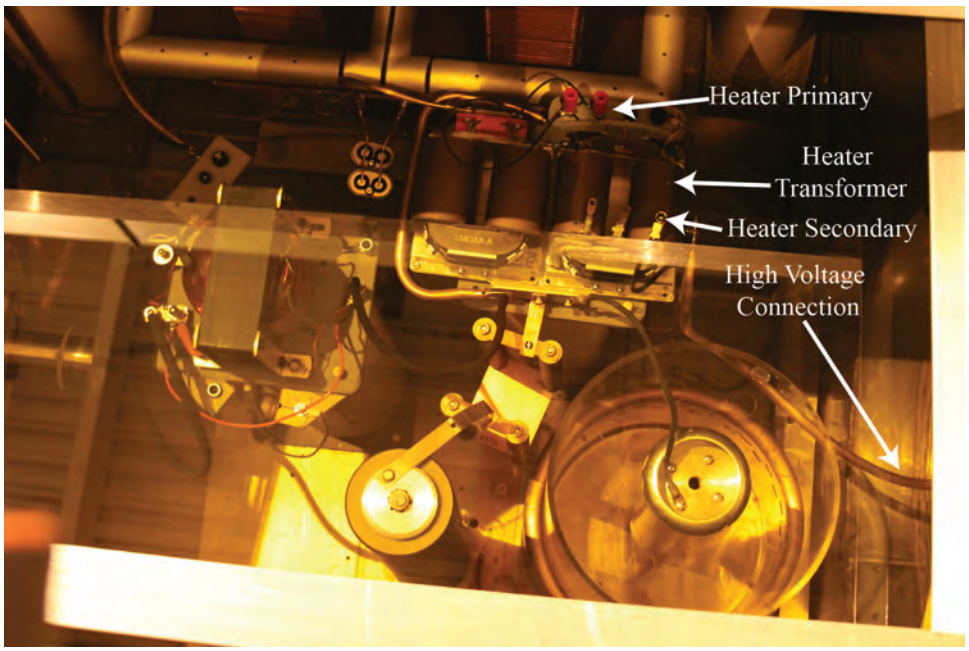

Figure 5-5: High voltage modulator inside an oil tank. Photo credit: Jason Hummelt [19].

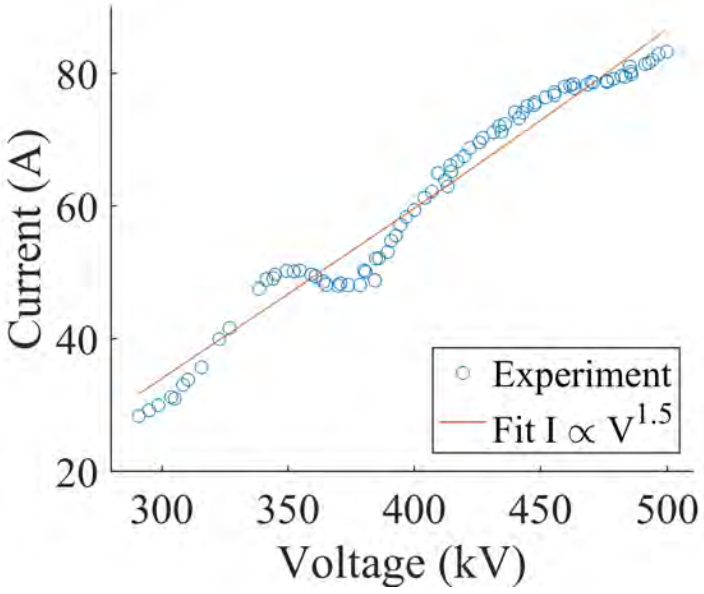

Figure 5-6: Voltage and current curve for the HRC electron gun at the MIT facility. High magnetic field was applied in these measurements for the best beam confinement.

at the operating beam voltage. For a given geometry, the ratio $I/V^{3/2}$ is a constant, defined as the electron gun perveance. The I-V curve was measured for the HRC gun in the lab, and the result is shown in Fig. 5-6. The electron gun perveance is about 0.23 μperv from the fitting.

The current was measured from the beam collector by a Faraday cup. Note that the current measurement happens after the electron beam travels through the interaction metamaterial circuit. So if a beam collision happens with the interaction circuit, we will see a decrease in the collector current. Later in Section 5.2, I will present the current traces when high power microwaves are generated from the Cherenkov-cyclotron instability with a gyrating electron beam colliding into the structure. The measured collector current drops in this case.

From Fig. 5-6, we can see that there is some deviation from the theoretical line of $I \propto V^{3/2}$ by the Child-Langmuir Law, and this is due to the slightly different collector current trace shapes at different voltages. Some examples of the current and voltage traces at different operation conditions are shown in Fig. 5-7. In Fig. 5-6, the current

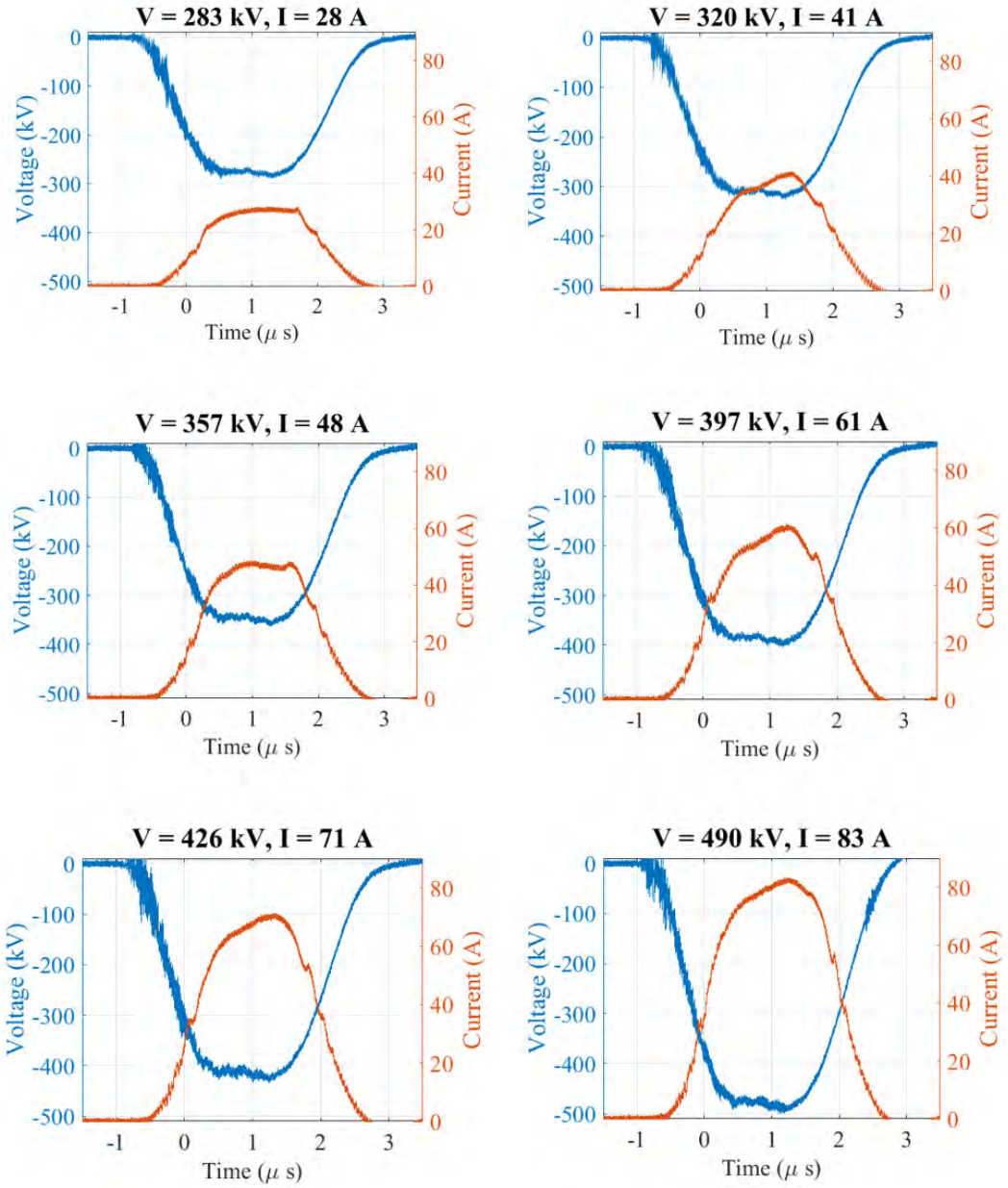

Figure 5-7: Voltage and collector current traces of the electron gun at different operating voltages. High magnetic field was applied in these measurements for the best beam confinement.

in the vertical axis is recorded as the peak current from the current traces in Fig. 5-7. This leads to the slight deviation of the measured V-I curve from the theoretical line in Fig. 5-6.

5.1.3 Magnet System for Beam Transport

Two water-cooled magnets are installed to confine the electron beam. They were also built by the Haimson Research Corporation. The focusing magnetic field is in the same direction as the beam propagation direction, and we call this the longitudinal direction. The direction perpendicular to the beam direction is called the transverse direction.

The lens magnet is closer to the electron gun, located between the gun and the metamaterial structure. The solenoid magnet overlaps with the metamaterial structure, and the structure is placed in the center of the solenoid magnet bore. Figure 5-1 shows the locations of both the lens and the solenoid magnets.

The field of both the lens magnet and the solenoid magnet can be adjusted independently and continuously from zero to their maximum values of 900 G for the lens and 1500 G for the solenoid. An example of the magnetic field distribution along the beam axis is presented in Fig. 5-8. The magnetic field peak around the position of 160 mm from the beam waist is the lens field, and the broader flattop in the region between about 400 mm and about 700 mm is the solenoid field.

5.1.4 Diagnostics for Microwave Power

Since the experiment is expected to generate a few megawatts of power, we need to pick up a small amount of the power to measure the power level. Bethe hole couplers can serve the purpose [115]. The couplers were designed and built by the CML Engineering Inc.

The principle of a Bethe hole coupler is that a small hole or a few small holes are cut on the broad wall of the S-band waveguide, so that the fundamental TE_{10} mode of the waveguide can be coupled into the hole by scattering. Then a stripline detector

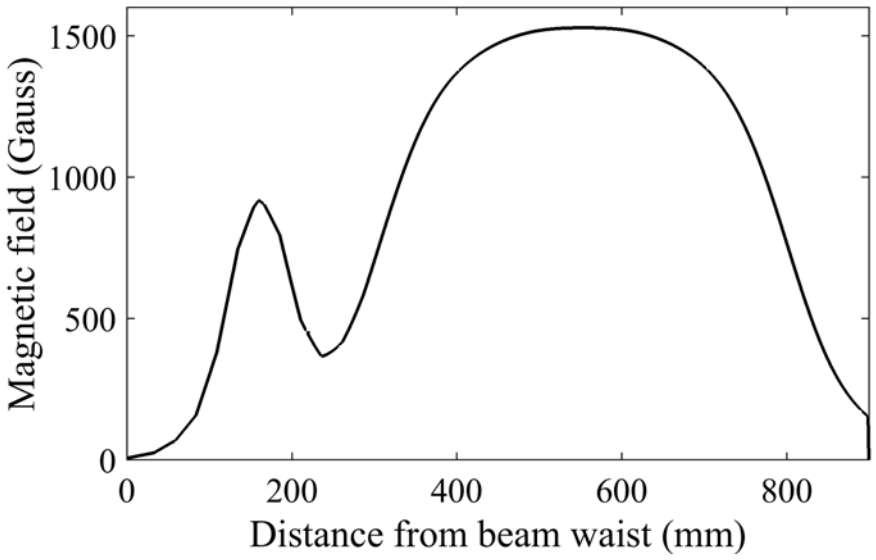

Figure 5-8: Longitudinal magnetic field profile with both the lens and the solenoid magnets at the maximum field values. Lens field: 900 G, solenoid field: 1.5 kG.

can pick up the signal with directivity. The power received by the stripline is then coupled to a coax connector and measured by a power meter.

The Bethe hole couplers used in this experiment are directional couplers. They can only measure the power flowing in the forward direction of the waveguide, but the reflected power in the backward direction cannot be coupled into the hole and thus is not measured. The Bethe hole couplers can be rotated to change the directivity.

In the experiment, we have one Bethe hole directional coupler on each of the output waveguides, Coupler A on Arm 1 and Coupler B on Arm 2. They have the same coupler design, but we rotated Coupler B a little bit to make a different coupling value for verification of the measured power. When the coupler was rotated, the stripline direction was changed, so the coupling coefficient was different.

The coupling coefficients for both couplers were measured with a VNA, and the calibration result is presented in Fig. 5-9. At 2.4 GHz, Coupler A on Arm 1 has a coupling coefficient of -64 dB, and Coupler B on Arm 2 has -61 dB.

Simulation results of the Bethe hole coupler are also presented in Fig. 5-9. The simulation is done in CST Microwave Studio on a guessed model of the Bethe hole

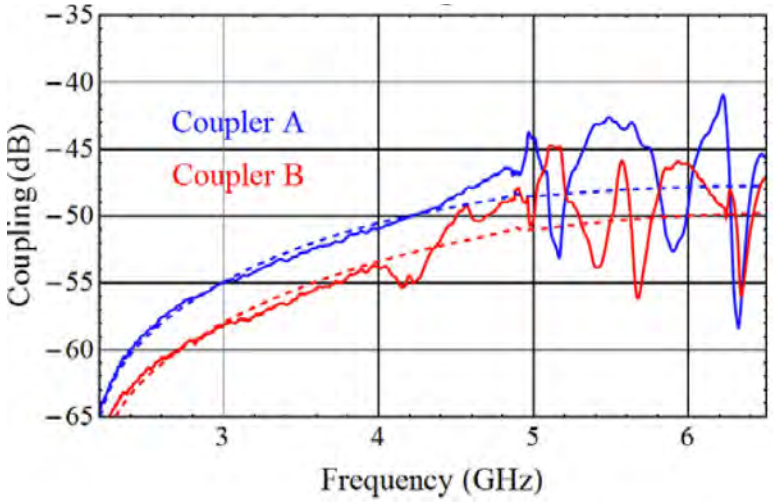

Figure 5-9: Coupling coefficients of the Bethe hole coupler A on Arm 1 and the coupler B on Arm 2. Solid lines: VNA measurement. Dashed lines: CST Microwave simulations of the guessed model.

coupler, since we do not know the interior geometry of the commercial Bethe hole couplers.

Figure 5-10 shows the guessed model of the waveguide, the hole and the stripline. In Fig. 5-10a, the vacuum part and the stripline are shown, while the metal part of the waveguide is hidden in the view. Figure 5-10b shows a detailed illustration of the coupler in the cross section view. There is a vacuum window between the stripline sitting in air and the waveguide in vacuum. The coupling is calculated as the power picked up by the stripline over the power coming in through a waveguide port.

In the model, the waveguide wall thickness is 5 mm, and the hole diameter is 9.1 mm. The model geometry is guessed by fitting the simulation and the cold test results. They agree well in the single-moded regime for the WR284 waveguide below 4.156 GHz. This also means that the Bethe hole coupler cannot measure the TE_{10} mode of the waveguide beyond 4.156 GHz.

With the Bethe hole couplers, the power and frequency of the microwave pulses were measured respectively with a power meter and a fast oscilloscope up to 6 GHz. Care was taken to assure that the power measurement with the Bethe hole coupler only measured the power in the operating mode at 2.4 GHz. Small amounts of power

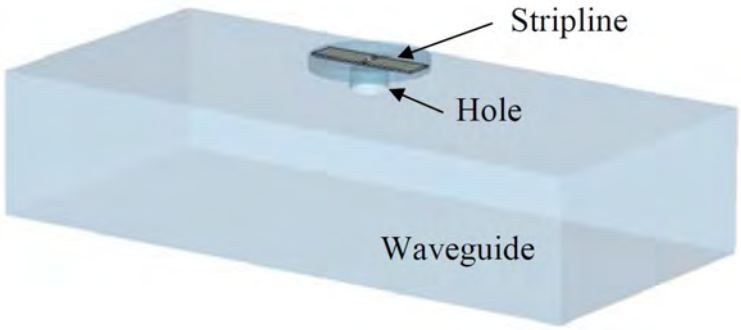

(a)

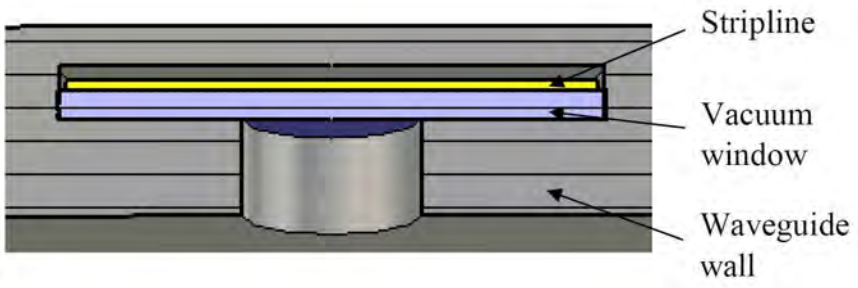

(b)

Figure 5-10: Model of the Bethe hole coupler. The model geometry is decided from fitting the CST simulation results with the VNA measurement.

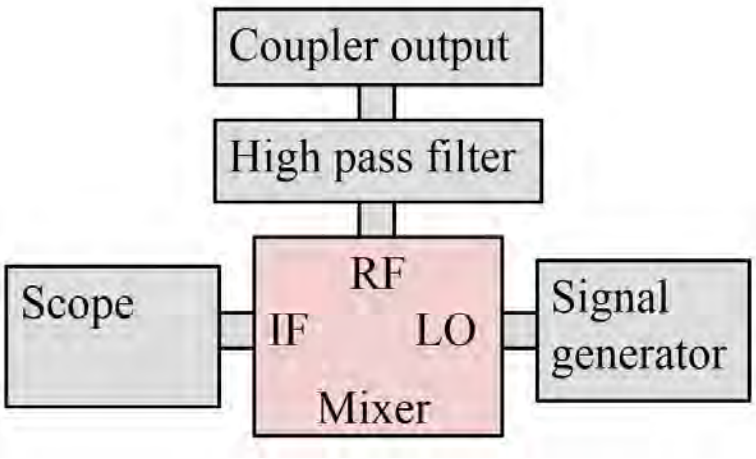

Figure 5-11: Diagram of the mixer measurement for frequencies of the higher harmonics. The mixer transforms the RF signal (output microwave power at the Bethe hole coupler) to an intermediate frequency (IF) signal (to be measured on the oscilloscope) with the help of a local oscillator (LO) signal.

at higher frequency mainly at higher harmonics also can couple into the hole coupler but was carefully filtered out using low pass and bandpass filters.

A mixer was also used to extend the measurable higher harmonics frequency to 15 GHz using a signal generator as a local oscillator. The diagram for the mixer measurement is shown in Fig. 5-11. The mixer transforms the RF signal (output microwave power at the Bethe hole coupler) to an intermediate frequency (IF) signal (to be measured on the oscilloscope) with the help of a local oscillator (LO) signal. The local oscillator is a signal generator.

With a proper LO frequency f_{LO}, we can transform the RF signal with a frequency of f_{RF} to the IF signal within the measurable range of the oscilloscope (up to 6 GHz). The IF frequency f_{IF} as the output of the mixer is

$$f_{\mathrm{IF}} = f_{\mathrm{RF}} \pm f_{\mathrm{LO}}. \tag{5.1}$$

Since there are two solutions for f_{RF} given a measured f_{IF} on the oscilloscope, we need to vary the frequency of the LO signal to determine the RF frequency. We measured the frequency spectrum with a frequency step of 0.5 GHz in the LO

frequency from 5 GHz to 14 GHz. From this measurement, we observed up to the 6^{th} order harmonics of the fundamental mode, while later, in measuring the power at 2.4 GHz, all these higher harmonics were filtered out correctly with the low pass filters.

5.1.5 MTM-R Structure Fabrication and Assembly

The MTM-R structure was built at the MIT Central Machine Shop. Photos of the MTM-R structure are shown in Fig. 5-12.

The stainless steel waveguides are welded together, with the cross section dimension of 63 mm $\times$ 43 mm. Two slots are cut for the insertion of the copper metamaterial plates.

The copper plates with CSRRs are brazed to the stainless steel waveguides. The distance between the two parallel plates is 33 mm. The two plates are arranged in the reverse symmetry, with the C-shaped cuts in the CSRR design pointing to opposite directions in the waveguide.

The structure is 37 cm long. It is held by two customized flanges on the two ends, as can be seen in Fig. 5-12a. The complete assembly sits in a vacuum pipe which holds the vacuum. Then the vacuum pipe is inserted into the bore of the solenoid magnet. The structure was cleaned in a sonicator and baked at 150°C before being assembled in the vacuum system.

5.2 Experimental Results

In this section, I will present the experimental results of the Stage II MTM-R experiment. The major achievements include that we measured full 1 μs long microwave pulses up to 2.9 MW, and that we identified the beam-wave interaction to be the Cherenkov-cyclotron type.

Section 5.2.1 will explore the operation space in the search for multi-MW output microwave power of the device. Section 5.2.2 will show sample output power traces from different experimental conditions. Section 5.2.3 will present the experimental evidence that the high power is generated by the Cherenkov-cyclotron interaction.

(a)

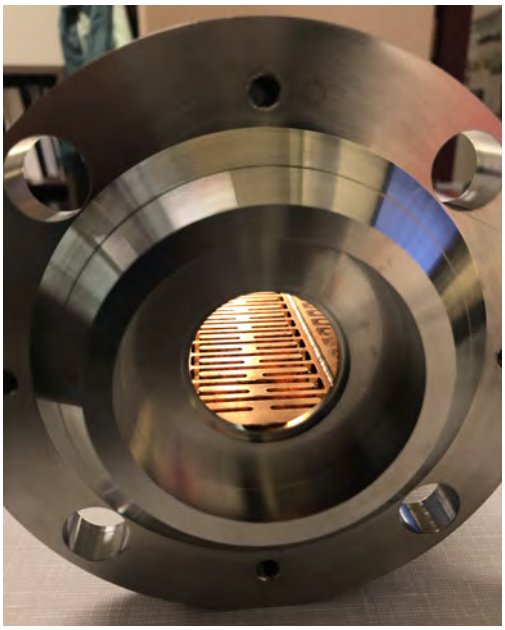

(b)

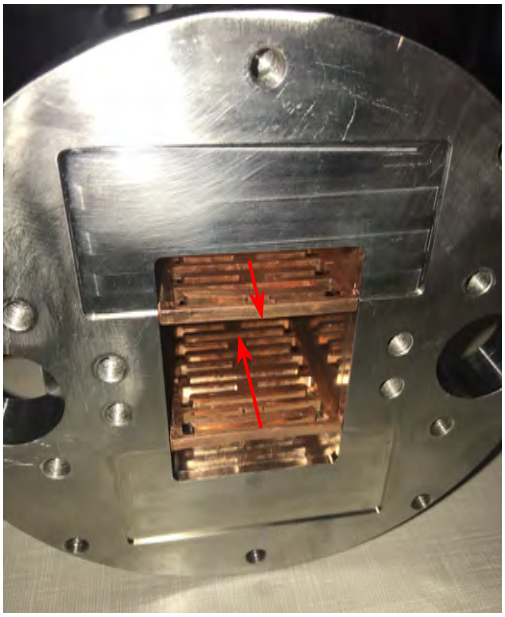

(c)

Figure 5-12: Photos of the MTM-R structure. The waveguide itself is 37 cm long. Two customized flanges are bolted on the two ends of the waveguide. (a) Full MTM-R structure with two flanges on the ends. (b) MTM-R structure looking from the gun side flange. (c) MTM-R structure looking from the collector side flange. Red arrows denote the opposite directions of the C-shaped cuts, as the CSRR design arranged with reverse symmetry.

Section 5.2.4 will discuss an improvement of the experimental results by adding a pair of steering coils.

5.2.1 Tunable Operation Space for High Power Microwave Generation

The power and frequency measurements of the device were done in a large 3D parameter space, with the three parameters being the beam voltage, the lens field and the solenoid field. For the Pierce type gun, the beam current scales with the beam voltage, so it is not an independent parameter.

In the 3D parameter space of voltage-lens field-solenoid field, we observed in some regions full-length, one microsecond microwave pulses with a few megawatts of power. The high power region in the lens-solenoid 2D space with a fixed beam voltage is shown in Figure 5-13a. In the half-bounded region between the two boundary lines, marked 'high power' in the figure, the output power is higher than 1 MW. However, the power drops abruptly to the level of 1 kW outside of the high power region.

The boundary contour denotes the critical condition for the megawatt level power to start. The contour shrinks with a lower beam voltage. In the high power region, the operating voltage (490 kV, 460 kV, or 420 kV) is higher than the critical voltage; while outside of the bounded region, the operating voltage is below the critical voltage. So the shrinking high power region indicates that the critical voltage varies with both the lens and the solenoid field. Figure 5-13b then shows measurement of the critical voltage at some lens field values. The trend is in agreement with the information in Figure 5-13a that with a lower operating voltage, the high power operation space shrinks.

The occurrence of regions of megawatt level power as shown in Figure 5-13 has several reasons.

The first reason is that the generated high power is from the Cherenkov-cyclotron instability. This instability arises only when the solenoid field is below a certain threshold so that the cyclotron motion wins over the longitudinal bunching.

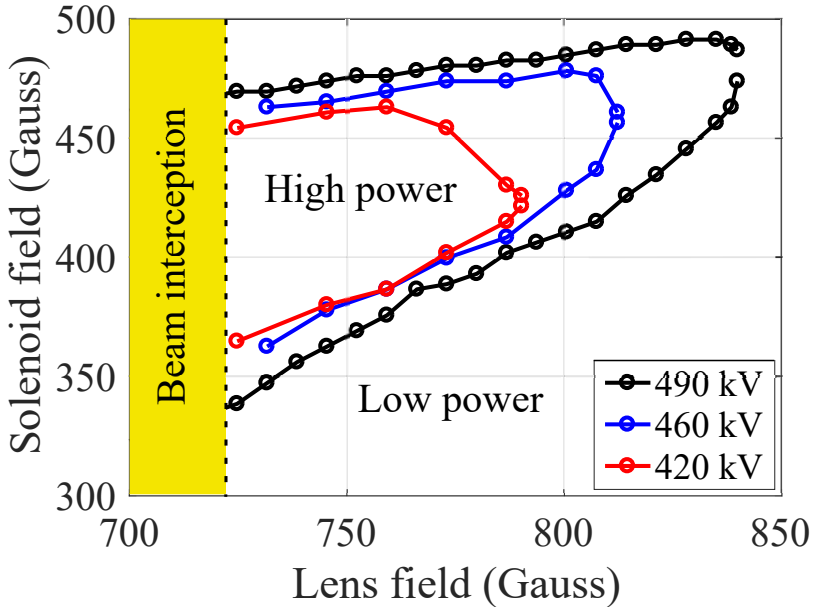

(a)

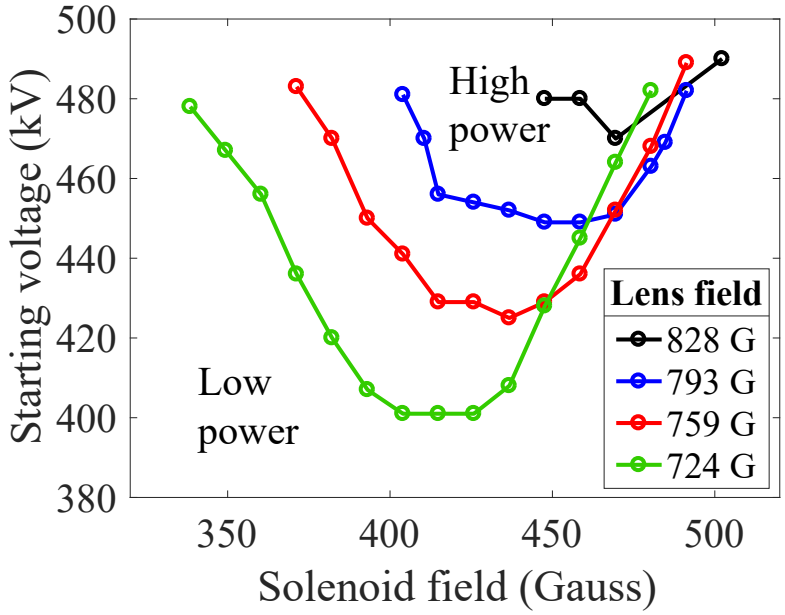

(b)

Figure 5-13: High power operation space. (a) High power region in the solenoid-lens field 2D parameter space with a fixed beam voltage of 490 kV, 460 kV and 420 kV. The half-bounded region between the two boundary lines is the megawatt power operation space, and outside is the low power region. The shaded area in yellow is where beam interception happens. (b) Variation of the critical voltage with the solenoid field for multiple lens field values.

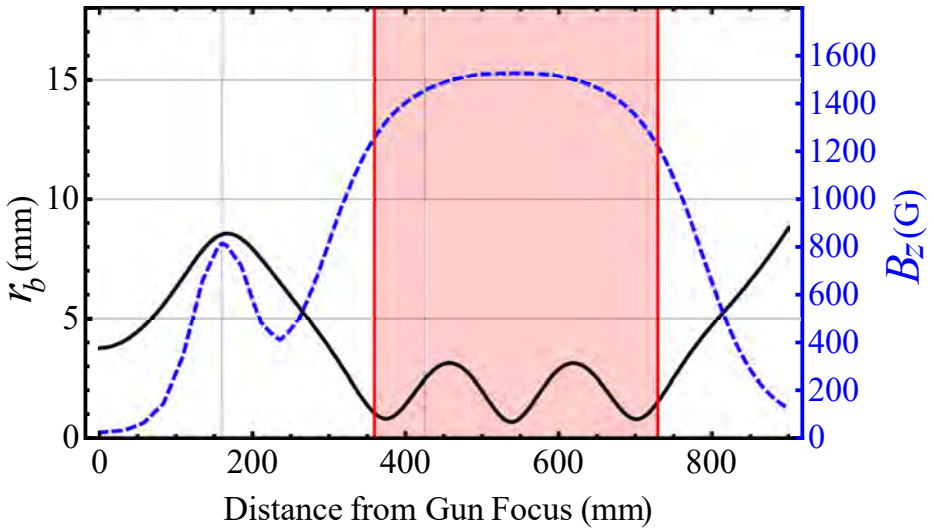

(a)

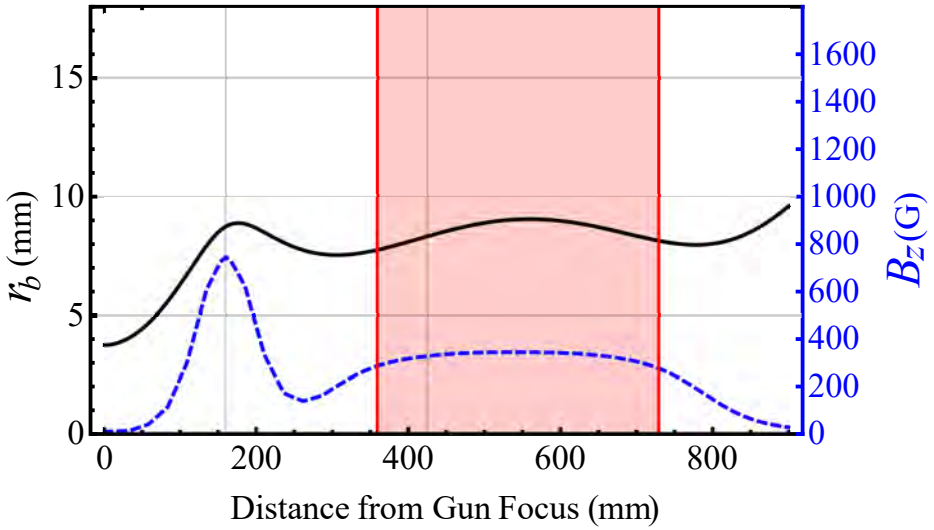

(b)

Figure 5-14: Magnetic field profiles and beam envelopes radii r_b of the 490 kV electron beam. The shaded area in pink marks the region of the metamaterial waveguide. Half of the distance between the two metamaterial plates is 16.3 mm as a reference. The black solid curves are the radii of the beam envelopes, and the blue dashed curves represent the longitudinal magnetic field. The peak lens field for both plots is 724 G, and the solenoid flat-top field is 1511 G for (a), and 341 G for (b). In the experiment, high power was measured in case (b), but not in case (a).

The second reason is that the beam quality is varied at different conditions. The lens field, together with the solenoid field, decides the beam radius and scalloping through the space charge effect. The spatial locations of the electron gun, the lens and the solenoid were not varied during the experiment so that at constant beam voltage, the electron beam matching and scalloping depended only on the magnitude of the magnetic field in the two magnets. Two examples of the beam profiles are presented in Figure 5-14. In the experiment, high power was measured with the condition of Figure 5-14b, but not Figure 5-14a. With the same lens field, a higher solenoid field in Figure 5-14a leads to a mismatched beam with a smaller initial radius at the structure entrance and heavier scalloping compared to the low solenoid field in Figure 5-14b.

The beam radius and scalloping are the two aspects that make the difference between high power and low power in the two cases.

On the one side, the beam radius should be reasonably large to fill the space between the two metamaterial plates. The metamaterial plates support surface waves concentrated on the plates, so the electron beam under a lower magnetic field sees a stronger electric field near the plates resulting in a stronger interaction. But when the magnetic field is too low, beam interception happens before the microwave mode is excited so the effective beam current is reduced and high power cannot be generated.

On the other side, scalloping is not favorable to high power generation, and this has been illustrated in the CST PIC simulations. If the scalloping before the beam enters the metamaterial waveguide is neglected in the PIC simulation, the code predicts high power from longitudinal bunching with a high magnetic field of over 1 kG. However, when scalloping is taken into account, the saturation time of high power lengthens from below 300 ns to above 600 ns. With a finite high voltage pulse length on the electron gun, a longer saturation time makes it more difficult to excite high microwave power.

5.2.2 Sample Microwave Pulses

Among the megawatt and microsecond long pulses, three categories of pulses were observed. In the first category, the two output arms have the same microwave frequency; while in the second category, the measured frequencies in the two arms differ by about 30 MHz. In these two categories, each arm has a single frequency indicating coherent radiation from the electron beam. In the third category, multiple frequencies are measured in one or both arms.

Figure 5-15 is an example of the first category where both arms have the same frequency. Figure 5-15a shows the gun voltage trace and the collector current trace. The beam voltage is 490 kV, and the collector current goes up and then drops to zero quickly. The full current at the gun is 84 A, and the missing collector current is from beam interception on the structure. This is as expected since the design modes are hybrid with a transverse deflecting electric field. However, the MTM-R structure is comprised of copper plates of 3 mm thickness and there was no evidence of arcing or damage to the plates.

Figure 5-15b shows the power traces. The flat-top power is 1.5 MW, so the efficiency is 4%. The power rises from almost zero to the full value within a very short time, just 100 ns. The operating lens field is 725 G and the solenoid field is 339 G. Figure 5-15c shows the measured voltage spectra for the microwaves in Arm 1 and Arm 2. Both arms see the same single frequency of 2.37 GHz. The radiated waves are coherent with a bandwidth of only a few MHz. The signal in Arm 2 has a small side band at 2.39 GHz, but it is 12 dB down in power from the main peak at 2.37 GHz since the spectrum represents the relative voltage.

Figure 5-16 is an example of the second category where the two arms each have a single but different frequency. The peak voltage is 420 kV, and the full beam current at the gun is 65 A. The total output power is 2.5 MW with a full 1 μs pulse width; the efficiency is 9%. The lens field is 725 G and the solenoid field is 437 G.

The second category has the flattest output power traces and the highest energy efficiency. Observation of this category is always under the condition that the operat-

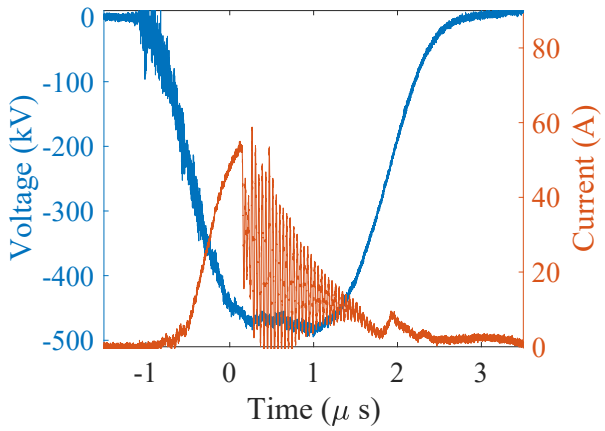

(a)

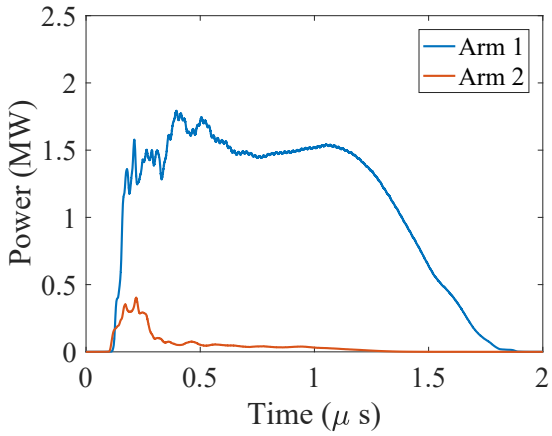

(b)

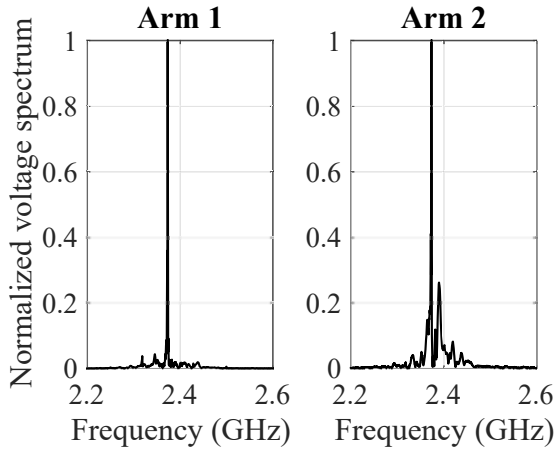

(c)

Figure 5-15: Sample pulse in the first category, with high power microwaves in both arms at the same coherent frequency of 2.37 GHz. The operating lens field is 725 G and the solenoid field is 339 G. (a) Voltage and collector current traces. (b) High power microwave traces. (c) Normalized voltage spectra of the microwaves in the two arms.

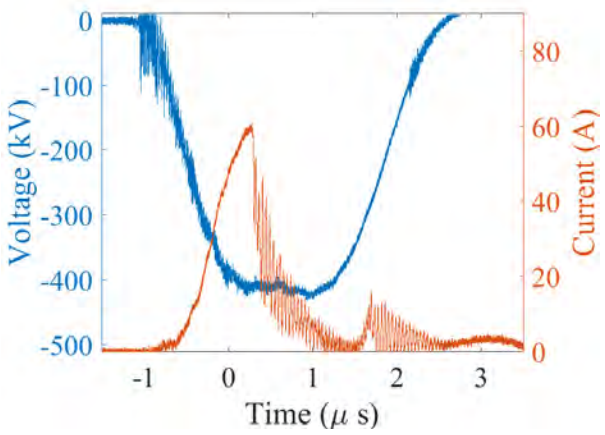

(a)

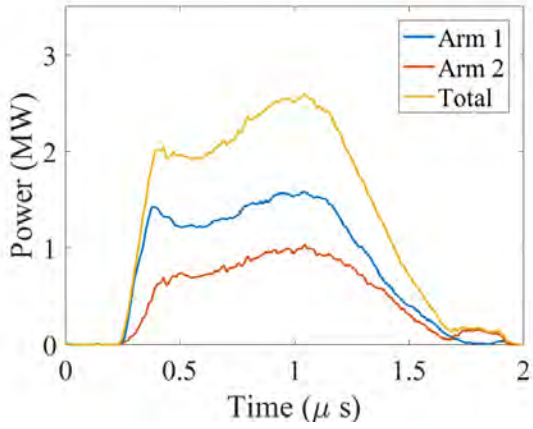

(b)

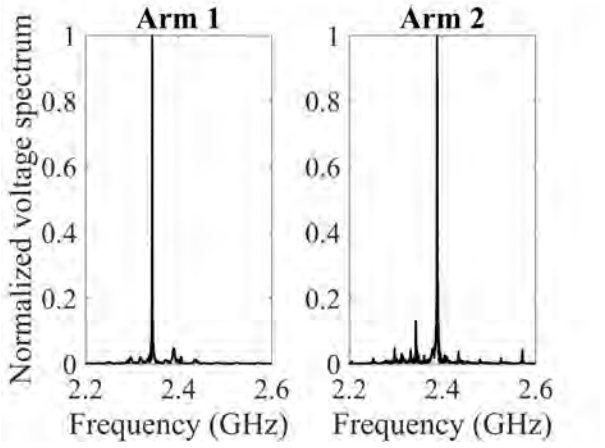

(c)

Figure 5-16: Sample pulse in the second category, with high power microwaves in both arms each at a single but different frequency. The operating lens field is 725 G and the solenoid field is 437 G. (a) Voltage and collector current traces. (b) High power microwave traces. (c) Normalized voltage spectra of the microwaves in the two arms.

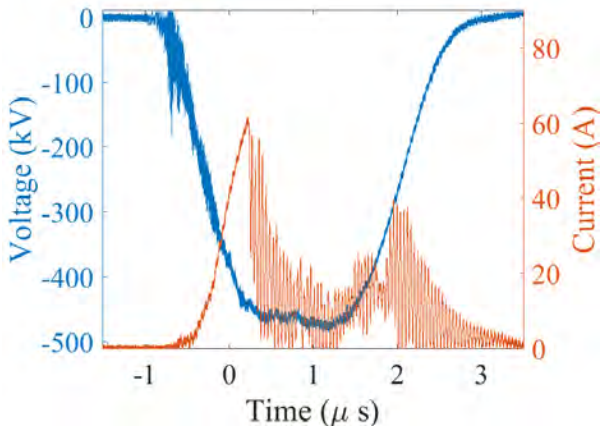

(a)

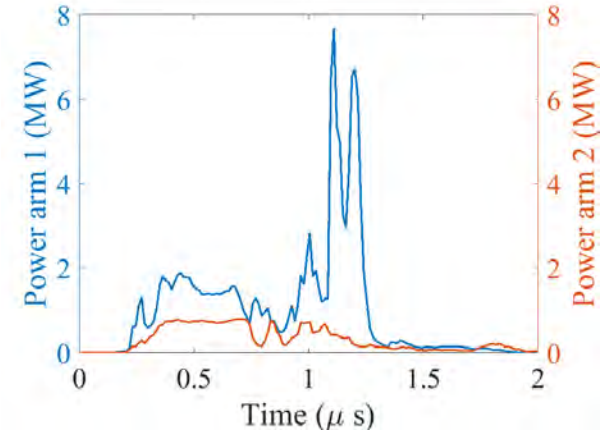

(b)

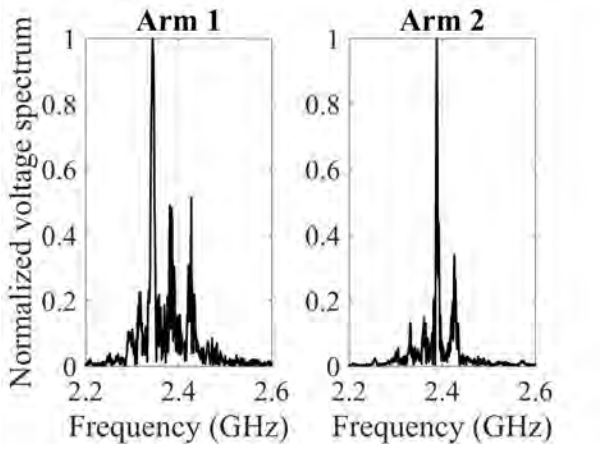

(c)

Figure 5-17: Sample pulse in the third category, with high power microwaves at multiple frequencies. The operating lens field is 739 G and the solenoid field is 450 G. (a) Voltage and collector current traces. (b) High power microwave traces. (c) Normalized voltage spectra of the microwaves.

ing voltage is above but very close to (within 20 kV) the critical voltage. The reason is that there are several modes with different interaction types possibly happening in the structure. These modes all have various critical voltages, so when the operating voltage is just above the lowest threshold, only one type of interaction leads to high power microwaves, and the pulse shape is flat. As the voltage goes higher, mode competition occurs, so the third category of pulses is observed, with multiple frequencies and a messy pulse shape.

In the third category, multiple frequencies are generated in the microwave pulses. A sample pulse in this category with a high peak microwave power is shown in Fig. 5-17. The beam voltage is 475 kV, and the peak collector current before beam interception happens is 60 A. The peak power is 8 MW though it happens in a short burst. Mode competition exists in this category, when the operating voltage is far away from the critical voltage of high power in any mode.

5.2.3 Verification of the Cherenkov-Cyclotron Instability by Frequency Tuning Measurement

By analyzing the frequency tuning with the beam voltage and the magnetic field, we can determine the type of beam wave interaction, since the frequency dependence varies for different modes and interaction types.

Figure 5-18 shows the frequency dependence on the beam voltage under different magnetic field combinations. For both Figure 5-18a and Figure 5-18b, the lens value is 729 G, but the solenoid field is 648 G and 1511 G, respectively. We can see that the frequency tuning with voltage fits the Cherenkov-cyclotron type and the Cherenkov type of interaction, respectively. The fitted Cherenkov-cyclotron theory line in Figure 5-18a has a larger slope than the Cherenkov theory line in Figure 5-18b, since in the Cherenkov-cyclotron dispersion $\omega = k_z v_z - \Omega_c/\gamma$, both terms on the right-hand side increase with a higher beam energy.

Figure 5-19 shows the frequency dependence vs. solenoid field. The Cherenkov frequency is not affected by the magnetic field, while the Cherenkov-cyclotron fre-

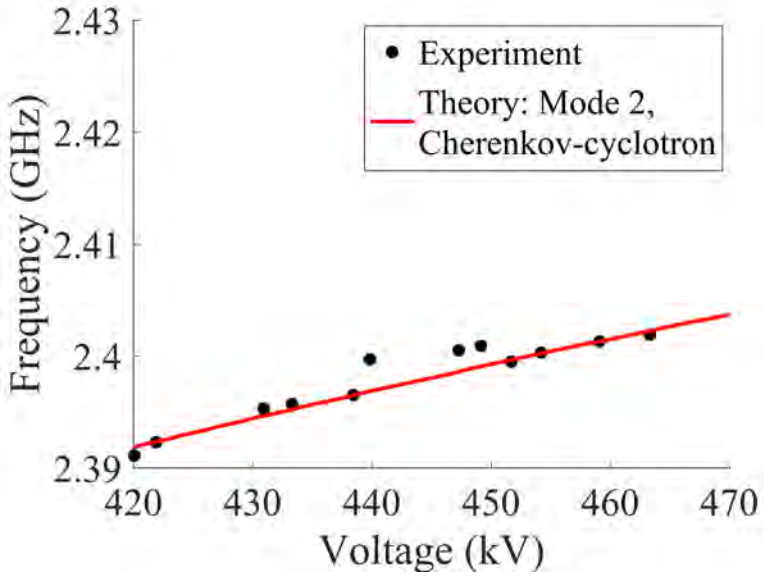

(a)

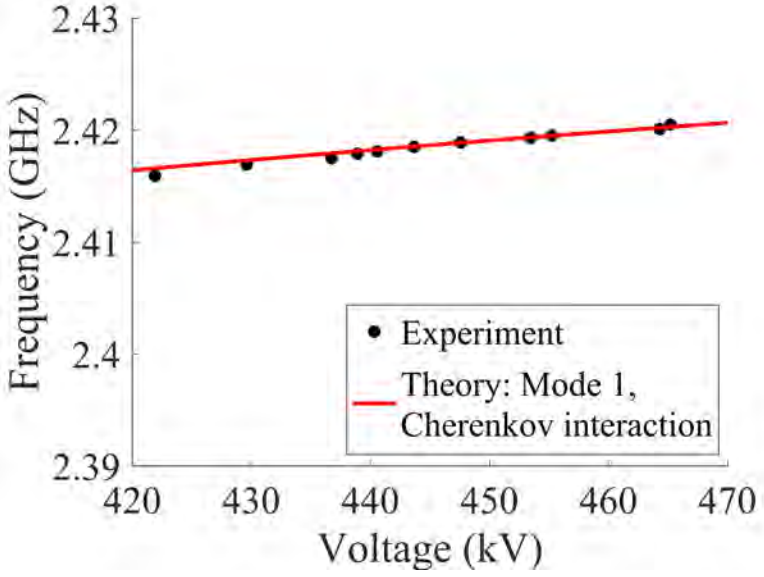

(b)

Figure 5-18: Tuning of the output microwave frequency with the beam voltage. Data were taken at a solenoid field of (a) 648 G, (b) 1511 G. The theory line in (a) is for the Cherenkov-cyclotron mode, upshifted by 25 MHz, and in (b) is for the Cherenkov mode, downshifted by 5 MHz.

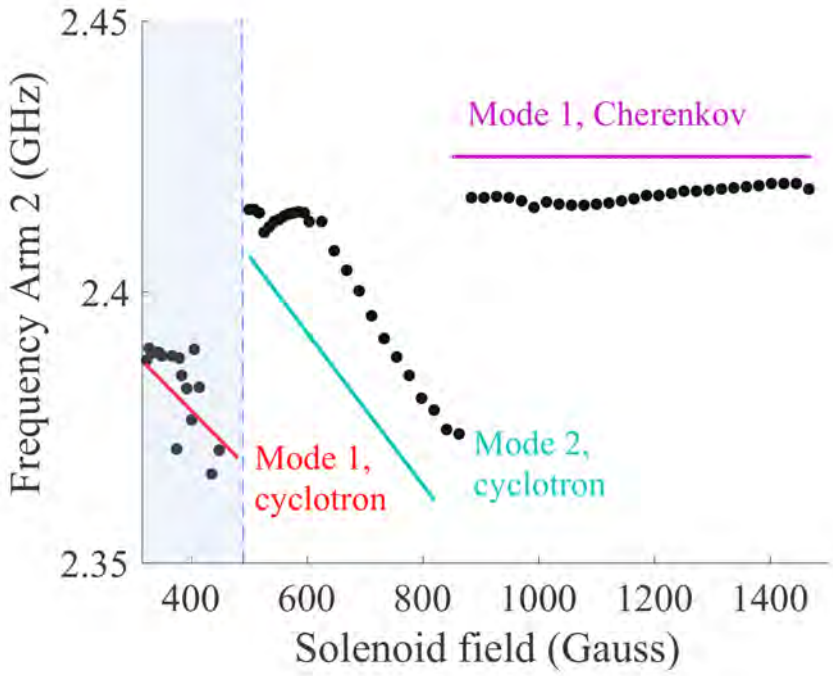

Figure 5-19: Frequency tuning of the output microwave pulse with the solenoid field. All the data in the plot were taken with a fixed lens field of 725 G and a fixed beam voltage of 460 kV. Different interaction types, both the Cherenkov type and the Cherenkov-cyclotron type of interaction were observed.

quency decreases with a higher field. Both types are observed in the experiment. The high power is always in the Cherenkov-cyclotron type of interaction below 475 G. In the low power region, the Cherenkov-cyclotron mode is observed below 830 G and the Cherenkov interaction is observed above 830 G. This feature also agrees with the mode selection based on the measurement in Figure 5-18.

5.2.4 Improvement by Steering Coils

The idea of applying steering coils comes from the fact that high power is always observed in the deflecting field mode with the cyclotron motion involved. We added a transverse steering magnetic field to give the beam a modest transverse kick with the hope that it would initiate the higher-power Cherenkov-cyclotron instability. Also, pushing the beam closer to one of the plates can increase the field amplitude witnessed

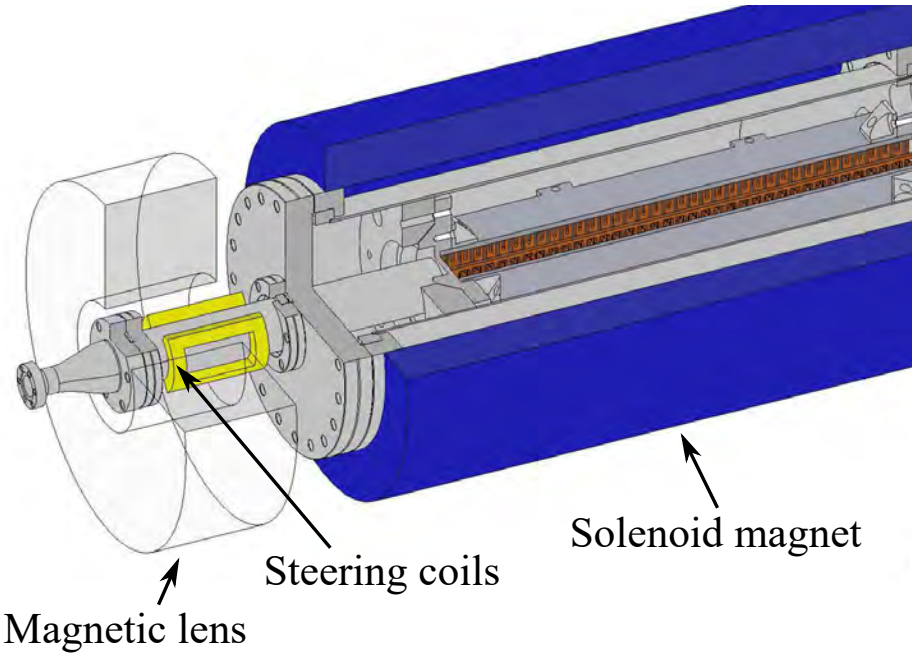

Figure 5-20: Illustration of the position of the steering coils. One pair of steering coils is mounted on the beam pipe overlapping with the lens. The coils were rotated to a position that makes the transverse magnetic field perpendicular to the metamaterial plates.

by the beam, thus improving the beam-wave interaction.

The steering coils, built by the Haimson Research Corporation, are shown in Figure 5-20. The coils consist of two pieces facing together providing a transverse magnetic field. With the combined effect of the transverse magnetic field from the steering coils and the longitudinal focusing magnetic field from the lens, the electron beam starts a cyclotron motion. In the experiment, the coils are arranged almost parallel to the metamaterial plates, so they create a transverse magnetic field pointing perpendicular to the plates. With this kicking field, the electron beam with an initial longitudinal velocity gains an initial transverse velocity parallel to the plates, and then the cyclotron motion is initiated. The guiding center of the beam then moves closer to one of the plates.

An illustration from a CST simulation of the steered beam profile with 0.1 A of current applied in the steering coil is shown in Figure 5-21. The integral of the

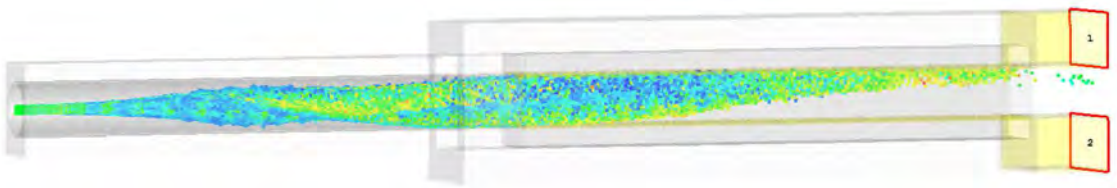

Figure 5-21: Steered beam profile with 0.1 A in the steering coil. The beam energy is 490 kV, the lens field is 725 G, and the solenoid field is 339 G.

transverse magnetic field of the pair of steering coils along the beam axis is 182 G-cm/A, and if they were placed in free space, a 490 kV beam would be deflected by 13 milliradians with 0.2 A of current applied in the coils.

Figure 5-22 shows a sample of the improved pulse with the steering coils applied. The power pulse now has a better flattop and a higher total power of 2.9 MW, at an efficiency of about 9%. This pulse falls into the second category where the two arms have a frequency difference of 30 MHz.

The steering coils have also changed the high power operating space. Figure 5-23a shows the variation of the high power region (the shaded area) with the applied steering coil current. The beam voltage and the lens field are both fixed. Positive steering current means that the beam is steered closer to Arm 2, and negative current pushes the beam closer to Arm 1. The plot shows the anisotropic feature of the MTM-R structure with reverse symmetry.

The critical voltage for achieving high power (> 1 MW) with different steering coil current values is measured and shown in Figure 5-23b. In agreement with Figure 5-23a, a coil current of 0.1 A raises the critical voltage, while a current of -0.2 A lowers the voltage. When the coil current goes up to 0.6 A, a second valley appears around 650 G.

The measurement with the steering coils on the one hand improves the pulse shape and raises the power, on the other hand, it shows the anisotropic effect of the reverse symmetry in the MTM-R design.

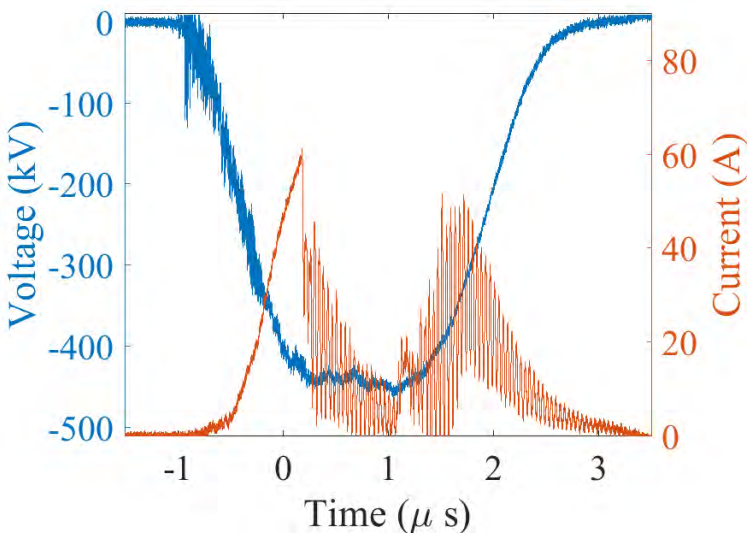

(a)

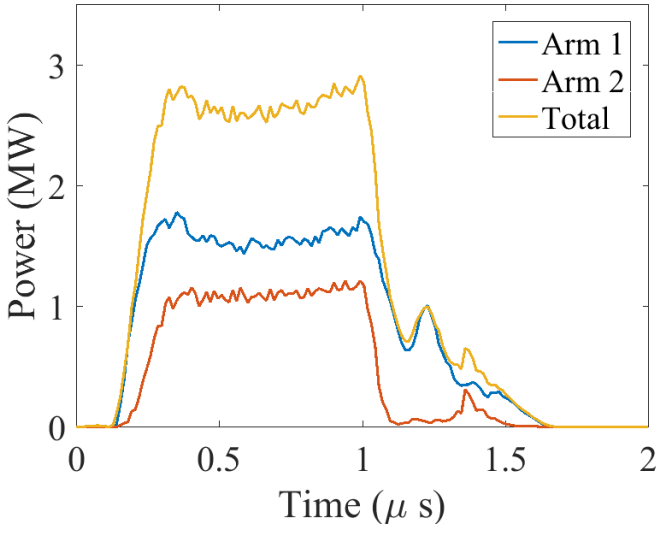

(b)

Figure 5-22: Sample pulse with 0.2 A of current applied in the steering coils. (a) Gun voltage and collector current vs. time. (b) Output microwave power vs. time. A peak power of 2.9 MW was reached.

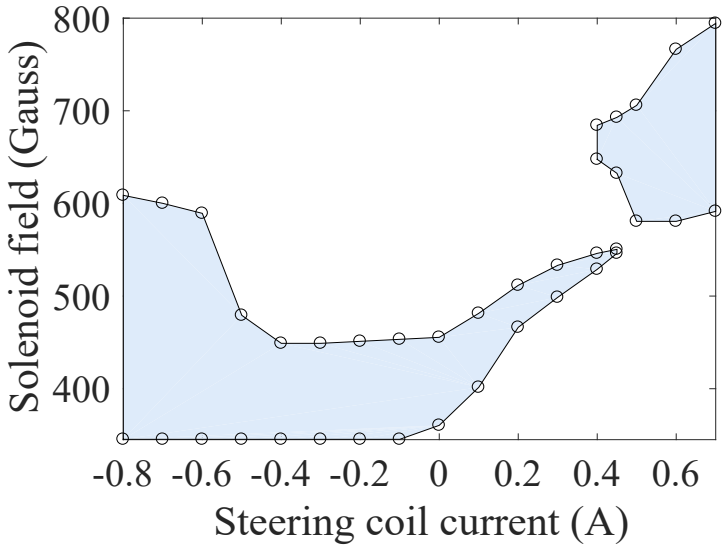

(a)

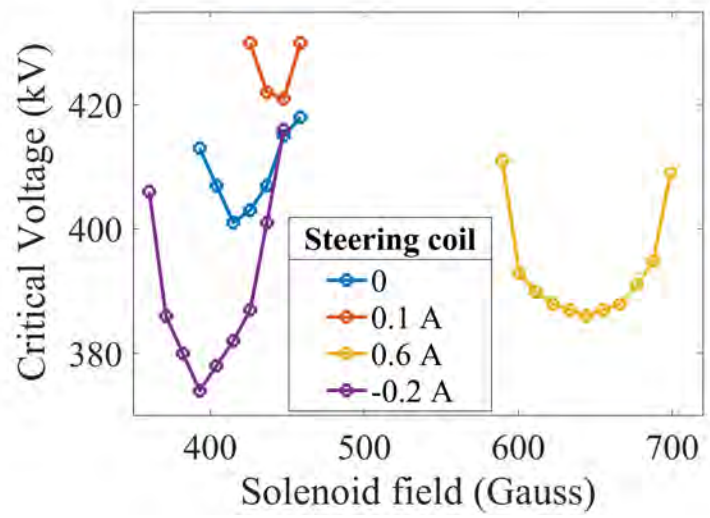

(b)

Figure 5-23: High power operation space with the steering coils applied. (a) High power region as the shaded area. (b) Measurements of the starting voltage with varied steering coil current applied. All the data were taken with a fixed beam voltage of 450 kV and a fixed lens field of 760 G.

5.3 Conclusions

In conclusion, the MTM-R structure has provided a rich environment to study different types of beam-wave interaction. Metamaterial plates arranged with reverse symmetry operate in a deflecting mode with a negative group velocity to generate high power.

PIC simulations show a helical beam trajectory, indicating the Cherenkov-cyclotron instability. In the experiment, megawatt level output power with a full 1 microsecond pulse length was observed with various combinations of the three major parameters: the beam voltage, the lens field and the solenoid field. Coherent radiation was generated at the Cherenkov-cyclotron frequency.

A typical total output power for the beam with a voltage of up to 490 kV and current of 84 A is 2 to 3 MW with an efficiency of up to 10%. Further investigation of the frequency tuning with the beam voltage and the solenoid field identifies different types of interaction at varied operating conditions. A pair of steering coils were put on to improve the output power traces, and they also reveal the anisotropic feature of the MTM-R structure.

Chapter 6

Conclusions and Future Plans

This section summarizes the achievements in this thesis and proposes directions for future research on the two topics: metamaterial structures for wakefield acceleration and metamaterial structures for high power microwave generation.

6.1 Conclusions of Metamaterial Structures for Wakefield Acceleration

6.1.1 Summary of Theoretical Studies

This thesis has presented the design of several metallic metamaterial structures for wakefield acceleration, as follows:

(1) The subwavelength deep corrugation structure has been investigated analytically and benchmarked with simulations. The structure has been proved to be a good candidate for collinear wakefield acceleration.

(2) The 3D volumetric metamaterial structure with a cubic unit cell has provided a good model to investigate the approach of using the homogeneity approximation with spatial dispersion to describe the dispersion characteristics. The phenomenon of the reversed Cherenkov radiation has been simulated in a stack of the cubic unit cells, and the generated wakefield can be applied to collinear wakefield acceleration.

(3) The wagon wheel structure has proved to be a good candidate for wakefield

acceleration for the applications of both collinear and two-beam acceleration. The fundamental mode in the structure is a TM mode with a negative group velocity, so the wakefield is generated by the reversed Cherenkov radiation. This phenomenon has been observed in CST particle-in-cell simulations. A 40-cell wagon wheel structure has been designed to work at X-band with the 65 MeV short electron bunches at the Argonne Wakefield Accelerator.

(4) The subwavelength elliptical structure has been proposed as a novel structure for two-beam acceleration. The drive beam and the witness beam can travel side by side in one elliptical structure instead of two separate structures, so the coupling system between the two separate structures is not needed in the elliptical structure design.

6.1.2 Summary of Experimental Studies

The experiment of high power microwave generation with the X-band wagon wheel metamaterial structure was completed successfully at the Argonne Wakefield Accelerator Facilities with the 65 MeV electron beam.

The reversed Cherenkov radiation from a short and relativistic electron bunch in a metamaterial structure has been directly verified experimentally for the first time. The wagon wheel structure, as a rugged and simple structure, has been demonstrated to generate high power microwaves for the application of wakefield acceleration. A single bunch with a charge of 45 nC and a length of $\sigma_z = 1.2$ mm going through the wagon wheel structure excited 25 MW of microwave power at 11.4 GHz in its wakefield, and the microwave pulse length was short (below 2 ns), which helped to eliminate RF breakdowns and multipactor events. The experimental results agree very well with the analytical calculation and CST simulations.

The highest microwave power was generated by a train of two bunches with a total charge of 85 nC, and the peak RF power reached 80 MW. The highest decelerating gradient was 50 MV/m, and the available gradient for a witness bunch was 75 MV/m. The wagon wheel structure can be applied to both collinear wakefield acceleration and two-beam acceleration.

6.2 Conclusions of Metamaterial Structures for High Power Microwave Generation

6.2.1 Summary of Theoretical Studies

On the analytical side, this thesis has presented an analytical theory to model the Cherenkov-cyclotron instability when an electron beam interacts with the antisymmetric mode in a metamaterial-loaded waveguide. From the device starting current calculation, the Cherenkov-cyclotron instability is found to start only at low magnetic field, and the starting current from the analytical calculation agrees with the observations in the previous Stage I metamaterial experiment at MIT.

On the simulation side, the metamaterial structure with reverse symmetry (MTM-R) has been proposed and simulated. The idea of the reverse symmetry stems from the Stage I metamaterial experiment, where high microwave power was only observed in the antisymmetric mode rather than the symmetric mode. Reversing the symmetry was proved in CST particle-in-cell simulations to be helpful to the Cherenkov-cyclotron type of interaction. The simulations show a helical beam trajectory, indicating the Cherenkov-cyclotron instability. Multi-MW microwave power generation at 2.4 GHz has been observed in simulations with an electron beam at a beam voltage of 490 kV and a current of 84 A.

6.2.2 Summary of Experimental Studies

A high power microwave device at S-band with a metamaterial-loaded waveguide with reverse symmetry exhibiting negative group velocity has been built and tested at MIT.

Output microwave pulses of 2.5 MW, 1 μs long at 2.4 GHz were generated from an electron beam up to 490 kV, 84A. The MTM-R structure has provided a rich environment to study different types of beam-wave interaction. Both the Cherenkov type of interaction and the Cherenkov-cyclotron type have been observed in experiment, but the megawatt power was generated only from the Cherenkov-cyclotron instability

at a low magnetic field, as verified by measuring the tuning of the output frequency with both the magnetic field and the beam voltage. A pair of steering coils were installed to further improve the performance of the device, by increasing the output power to 2.9 MW.

6.3 Future Plans

6.3.1 Future Plans for Wakefield Acceleration

Based on our first successful wakefield experiment on the X-band wagon wheel metamaterial structure, we have planned the next experiment at AWA with a longer metamaterial structure, and the goal is to achieve one gigawatt of microwave power in the wakefield from the reversed Cherenkov radiation.

Previously, we have demonstrated very precise control of the spacing between bunches in two-bunch trains with laser splitters, and the maximum charge we managed to transmit in two bunches was 85 nC. Depending on the exact spacing between bunches, the wakefield radiation from each bunch can either add or cancel. When the wakefield from N bunches adds up coherently, the power scales as N^2. So the bunch-train operation is beneficial for achieving high RF power for high-gradient wakefield acceleration.

Figure 6-1 shows the CAD drawing of the next experiment, where the length of the metamaterial structure has been increased from 8 cm in the first experiment to 22 cm. The longer structure can generate a longer RF pulse from each bunch, so the wakefield from more bunches can overlap with each other to push up the peak power by the N^2 scaling. When 8 bunches with the charge of 40 nC/bunch in phase with each other travel through, the structure can generate 1.2 GW of peak power with a pulse length of 11 ns. The output power trace from the CST PIC simulation is shown in Fig. 6-2. The decelerating electric field on the 8th bunch reaches 200 MV/m, and the available accelerating gradient for a witness bunch after the bunch train would be about 300 MeV/m, making a strong candidate for structure-based

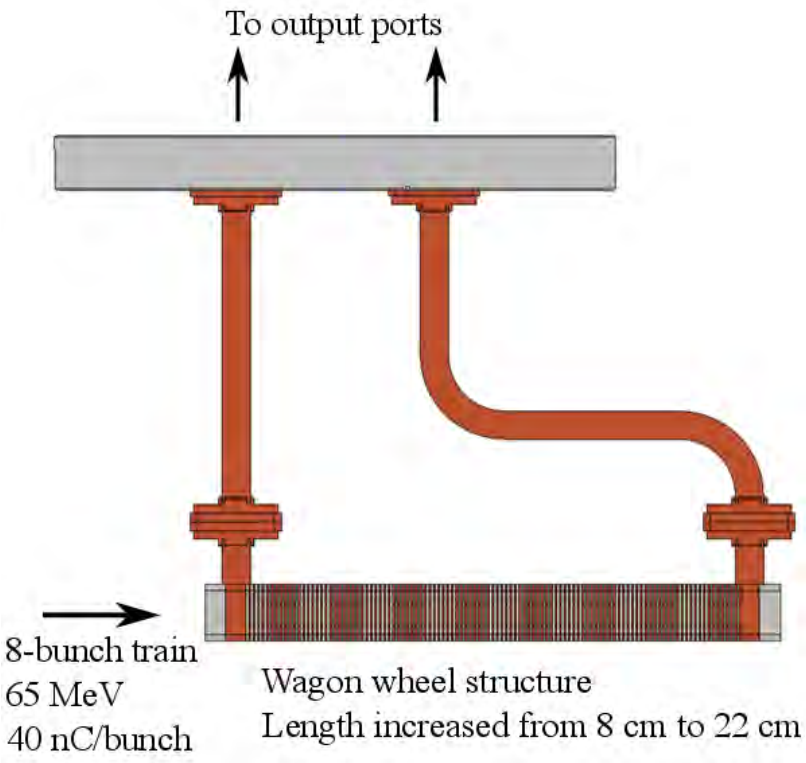

Figure 6-1: CAD drawing of the 22 cm wagon wheel structure designed for a future experiment at AWA

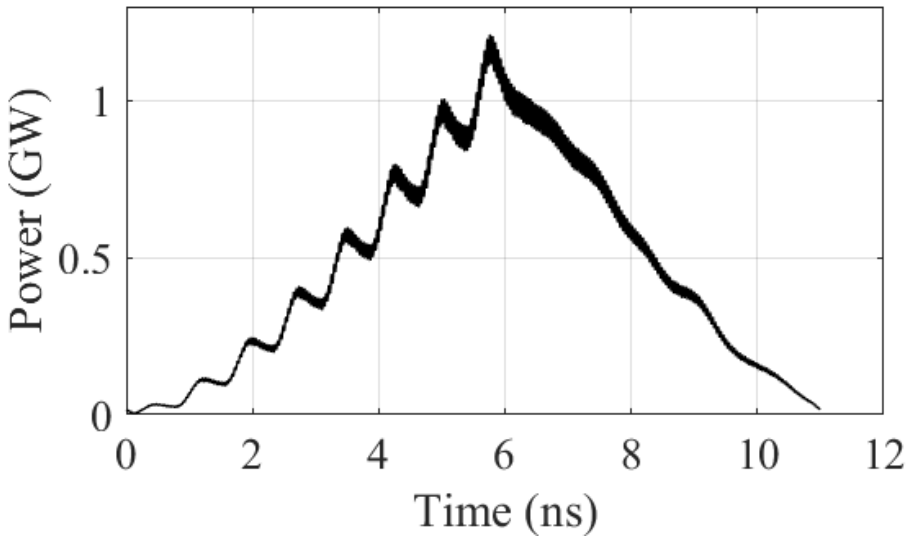

Figure 6-2: CST particle-in-cell simulation of the output power at the backward port when the 22 cm structure is excited by a train of 8 bunches with 40 nC/bunch.

wakefield acceleration.

This future experiment on the one hand can achieve the goal of high power, high gradient wakefield generation, and on the other hand can provide a possible platform to study the RF breakdown phenomenon at the high-field (a few hundred MV/m) and short-pulse (10 ns) operation regime.

After this first future experiment, several other experiments on the wagon wheel structure are also available and promising to try at the AWA facility, including: (1) scaling the structure to a much higher frequency f, investigating whether the output power follows the f^2 scaling; (2) accelerating a trailing electron bunch in the collinear regime; (3) accelerating a witness electron bunch in the two-beam acceleration regime, where the drive beam and the witness beam travel in two separate wagon wheel structures with different design strategies. For all these tasks, the metamaterial design allows great flexibility and creates a huge parameter space for various optimization goals.

6.3.2 Future Plans for High Power Microwave Generation

The discovery of the Cherenkov-cyclotron interaction for high power microwave generation can inspire new vacuum electron devices. Theoretically, more work would be interesting to investigate the onset of the Cherenkov-cyclotron interaction in different structures and its competition with other modes. Experimentally, various metamaterial circuits can be explored and optimized to generate high power microwaves from the Cherenkov-cyclotron instability. Some ideas to increase the device efficiency include tapering the phase velocity and shaping the longitudinal magnetic field.

Bibliography

[1] V. G. Veselago, "The electrodynamics of substances with simultaneously negative values of and μ", *Sov. Phys. Usp.*, vol. 10, no. 4, p. 509, 1968.

[2] D. R. Smith, W. J. Padilla, D. C. Vier, S. C. Nemat-Nasser, and S. Schultz, "Composite medium with simultaneously negative permeability and permittivity", *Phys. Rev. Lett.*, vol. 84, pp. 4184–4187, 2000.

[3] R. S. Kshetrimayum, A brief intro to metamaterials, *IEEE Potentials*, vol. 23, pp. 44–46, 2005.

[4] R. Marqués, F. Martín, and M. Sorolla, *Metamaterials with Negative Parameters: Theory, Design and Microwave Applications.* John Wiley & Sons, 2011.

[5] S. A. Ramakrishna and T. M. Grzegorczyk, *Physics and applications of negative refractive index materials.* CRC press, 2008.

[6] D. Schurig, J. J. Mock, B. J. Justice, S. A. Cummer, J. B. Pendry, A. F. Starr, and D. R. Smith, "Metamaterial electromagnetic cloak at microwave frequencies", *Science*, vol. 314, no. 5801, pp. 977–980, 2006.

[7] J. B. Pendry, "Negative refraction makes a perfect lens", *Phys. Rev. Lett.*, vol. 85, pp. 3966–3969, 2000.

[8] A. K. Iyer and G. V. Eleftheriades, "Mechanisms of subdiffraction free-space imaging using a transmission-line metamaterial superlens: An experimental verification", *Appl. Phys. Lett.*, vol. 92, p. 131105, 2008.

[9] S. Enoch, G. Tayeb, P. Sabouroux, N. Guérin, and P. Vincent, "A metamaterial for directive emission", *Phys. Rev. Lett.*, vol. 89, p. 213902, 2002.

[10] S. Antipov, L. Spentzouris, W. Gai, M. Conde, F. Franchini, R. Konecny, W. Liu, J. G. Power, Z. Yusof, C. Jing, "Observation of wakefield generation in left-handed band of metamaterial-loaded waveguide", *J. Appl. Phys.*, vol. 104, p. 014901, 2008.

[11] X. Lu, M. A. Shapiro, and R. J. Temkin, "Modeling of the interaction of a volumetric metallic metamaterial structure with a relativistic electron beam", *Phys. Rev. ST Accel. Beams*, vol. 18, p. 081303, 2015.

[12] X. Lu, M. A. Shapiro, and R. J. Temkin, "Interaction of a volumetric metamaterial structure with an electron beam", in *Proc. 6th Int. Particle Accelerator Conf. (IPAC'15), Richmond, VA, May 2015*, pp. 2640–2642, 2015.

[13] X. Lu, M. A. Shapiro, and R. J. Temkin, "Novel metallic structures for wakefield acceleration", in *Proc. North American Particle Accelerator Conf. (NAPAC'16), Chicago, IL, Oct 2016*, pp. 762–764, 2017.

[14] X. Lu, M. Conde, C. Jing, I. Mastovsky, J. G. Power, J. Shao, M. A. Shapiro, R. J. Temkin, and E. E. Wisniewski, "A metamaterial wagon wheel structure for wakefield acceleration by reversed Cherenkov radiation", in *Proc. 9th Int. Particle Accelerator Conf. (IPAC'18), Vancouver, BC, Canada, May 2018*, pp. 1–3, 2018.

[15] Z. Duan, X. Tang, Z. Wang, Y. Zhang, X. Chen, M. Chen, and Y. Gong, "Observation of the reversed cherenkov radiation", *Nat. Commun.*, vol. 8, p. 14901, 2017.

[16] S. Xi, H. Chen, T. Jiang, L. Ran, J. Huangfu, B.-I. Wu, J. A. Kong, and M. Chen, "Experimental verification of reversed Cherenkov radiation in left-handed metamaterial", *Phys. Rev. Lett.*, vol. 103, p. 194801, 2009.

[17] H. Chen and M. Chen, "Flipping photons backward: reversed Cherenkov radiation", *Materials Today*, vol. 14, no. 1, pp. 34 – 41, 2011.

[18] H. Wiedemann, *Particle accelerator physics*. Springer, 2015.

[19] J. S. Hummelt, *High power microwave generation using an active metamaterial powered by an electron beam*. PhD thesis, Massachusetts Institute of Technology, 2016.

[20] J. S. Hummelt, X. Lu, H. Xu, I. Mastovsky, M. A. Shapiro, and R. J. Temkin, "Coherent Cherenkov-cyclotron radiation excited by an electron beam in a metamaterial waveguide", *Phys. Rev. Lett.*, vol. 117, p. 237701, 2016.

[21] M. D. Forno, V. Dolgashev, G. Bowden, C. Clarke, M. Hogan, D. McCormick, A. Novokhatski, B. O'Shea, B. Spataro, S. Weathersby, and S. G. Tantawi, "High gradient tests of metallic mm-wave accelerating structures", *Nucl. Instrum. Methods Phys. Res. A*, vol. 864, pp. 12 – 28, 2017.

[22] G. Gatti, A. Marcelli, B. Spataro, V. Dolgashev, J. Lewandowski, S. Tantawi, A. Yeremian, Y. Higashi, J. Rosenzweig, S. Sarti, C. Caliendo, G. Castorina, G. Cibin, L. Carfora, O. Leonardi, V. Rigato, and M. Campostrini, "X-band accelerator structures: On going R&D at the INFN", *Nucl. Instrum. Methods Phys. Res. A*, vol. 829, pp. 206 – 212, 2016.

[23] T. P. Wangler, *RF Linear Accelerators*. John Wiley & Sons, 2 ed., 2008.

[24] V. Dolgashev, "Recent studies of RF breakdown physics in normal conducting cavities", *AIP Conference Proceedings*, vol. 1299, pp. 274–279, 2010.

[25] B. Cros and P. Muggli, "Towards a Proposal for an Advanced Linear Collider", *Report on the Advanced and Novel Accelerators for High Energy Physics Roadmap Workshop, CERN, Geneva*, 2017.

[26] E. R. Colby and L. K. Len, *Roadmap to the Future*. Singapore: World Scientific Publishing Co., 2016.

[27] W. Leemans, A. Gonsalves, H.-S. Mao, K. Nakamura, C. Benedetti, C. Schroeder, C. Tóth, J. Daniels, D. Mittelberger, S. Bulanov, *et al.*, "Multi-gev electron beams from capillary-discharge-guided subpetawatt laser pulses in the self-trapping regime", *Phys. Rev. Lett.*, vol. 113, p. 245002, 2014.

[28] R. J. England, R. J. Noble, K. Bane, D. H. Dowell, C.-K. Ng, J. E. Spencer, S. Tantawi, Z. Wu, R. L. Byer, *et al.*, "Dielectric laser accelerators", *Rev. Mod. Phys.*, vol. 86, pp. 1337–1389, 2014.

[29] K. P. Wootton, Z. Wu, B. M. Cowan, A. Hanuka, I. V. Makasyuk, E. A. Peralta, K. Soong, R. L. Byer, and R. J. England, "Demonstration of acceleration of relativistic electrons at a dielectric microstructure using femtosecond laser pulses", *Opt. Lett.*, vol. 41, pp. 2696–2699, 2016.

[30] W. Gai, P. Schoessow, B. Cole, R. Konecny, J. Norem, J. Rosenzweig, and J. Simpson, "Experimental Demonstration of Wake-Field Effects in Dielectric Structures", *Phys. Rev. Lett.*, vol. 61, p. 2756, 1988.

[31] F. Gao, M. E. Conde, W. Gai, C. Jing, R. Konecny, W. Liu, J. G. Power, T. Wong, and Z. Yusof, "Design and testing of a 7.8 GHz power extractor using a cylindrical dielectric-loaded waveguide", *Phys. Rev. ST Accel. Beams*, vol. 11, p. 041301, 2008.

[32] M. J. Hogan, C. D. Barnes, C. E. Clayton, F. J. Decker, S. Deng, P. Emma, C. Huang, R. H. Iverson, D. K. Johnson, *et al.*, "Multi-gev energy gain in a plasma-wakefield accelerator", *Phys. Rev. Lett.*, vol. 95, p. 054802, 2005.

[33] B. D. O Shea, G. Andonian, S. K. Barber, K. L. Fitzmorris, S. Hakimi, J. Harrison, P. D. Hoang, M. J. Hogan, B. Naranjo, O. B. Williams, V. Yakimenko, and J. B. Rosenzweig, "Observation of acceleration and deceleration in gigaelectron-volt-per-metre gradient dielectric wakefield accelerators", *Nat. Commun.*, vol. 7, p. 12763, 2016.

[34] Q. Gao, G. Ha, C. Jing, S. P. Antipov, J. G. Power, M. Conde, W. Gai, H. Chen, J. Shi, E. E. Wisniewski, D. S. Doran, W. Liu, C. E. Whiteford, A. Zholents, P. Piot, and S. S. Baturin, "Observation of high transformer ratio

of shaped bunch generated by an emittance-exchange beam line", *Phys. Rev. Lett.*, vol. 120, p. 114801, 2018.

[35] A. M. Cook, R. Tikhoplav, S. Y. Tochitsky, G. Travish, O. B. Williams, and J. B. Rosenzweig, "Observation of narrow-band terahertz coherent Cherenkov radiation from a cylindrical dielectric-lined waveguide", *Phys. Rev. Lett.*, vol. 103, p. 095003, 2009.

[36] C. Jing, S. Antipov, M. Conde, W. Gai, G. Ha, W. Liu, N. Neveu, J. Power, J. Qiu, J. Shi, D. Wang, and E. Wisniewski, "Electron acceleration through two successive electron beam driven wakefield acceleration stages", *Nucl. Instrum. Methods Phys. Res. A*, vol. 898, pp. 72 – 76, 2018.

[37] P. D. Hoang, G. Andonian, I. Gadjev, B. Naranjo, Y. Sakai, N. Sudar, O. Williams, M. Fedurin, K. Kusche, C. Swinson, P. Zhang, and J. B. Rosenzweig, "Experimental characterization of electron-beam-driven wakefield modes in a dielectric-woodpile cartesian symmetric structure", *Phys. Rev. Lett.*, vol. 120, p. 164801, 2018.

[38] E. I. Simakov, S. A. Arsenyev, C. E. Buechler, R. L. Edwards, W. P. Romero, M. Conde, G. Ha, J. G. Power, E. E. Wisniewski, and C. Jing, "Observation of wakefield suppression in a photonic-band-gap accelerator structure", *Phys. Rev. Lett.*, vol. 116, p. 064801, 2016.

[39] D. Wang, S. Antipov, C. Jing, J. G. Power, M. Conde, E. Wisniewski, W. Liu, J. Qiu, G. Ha, V. Dolgashev, C. Tang, and W. Gai, "Interaction of an ultrarelativistic electron bunch train with a w-band accelerating structure: High power and high gradient", *Phys. Rev. Lett.*, vol. 116, p. 054801, 2016.

[40] S. Gessner, E. Adli, J. M. Allen, W. An, C. I. Clarke, C. E. Clayton, S. Corde, J. Delahaye, J. Frederico, S. Z. Green, *et al.*, "Demonstration of a positron beam-driven hollow channel plasma wakefield accelerator", *Nat. Commun.*, vol. 7, p. 11785, 2016.

[41] A. Caldwell, E. Adli, L. Amorim, R. Apsimon, T. Argyropoulos, R. Assmann, A.-M. Bachmann, F. Batsch, J. Bauche, V. B. Olsen, *et al.*, "Path to AWAKE: Evolution of the concept", *Nucl. Instrum. Methods Phys. Res. A*, vol. 829, pp. 3 – 16, 2016.

[42] J. Rosenzweig, N. Barov, A. Murokh, E. Colby, and P. Colestock, "Towards a plasma wake-field acceleration-based linear collider", *Nucl. Instrum. Methods Phys. Res. A*, vol. 410, no. 3, pp. 532 – 543, 1998.

[43] A. Seryi, M. Hogan, S. Pei, T. Raubenheimer, P. Tenenbaum, T. Katsouleas, C. Huang, C. Joshi, W. Mori, and P. Muggli, "A Concept of Plasma Wake Field Acceleration Linear Collider (PWFA-LC)", in *Proceedings of 23rd Conference (PAC'09): Vancouver, Canada, May 4-8, 2009.*

[44] J.-P. Delahaye, E. Adli, W. An, S. Gessner, M. Hogan, C. Joshi, W. Mori, and T. Raubenheimer, "A beam driven plasma-wakefield linear collider from higgs factory to multi-TeV", in *5th Int. Particle Accelerator Conf.(IPAC'14), Dresden, Germany, June 15-20, 2014*.

[45] C. Jing, A. Kanareykin, P. Schoessow, M. Conde, W. Gai, J. Power, and S. Antipov, "Argonne flexible linear collider", in *Proceedings of 4th Int. Particle Accelerator Conf.(IPAC'13): Shanghai, China, May 12-17, 2013*.

[46] L. Linssen, A. Miyamoto, M. Stanitzki, and H. Weerts, "Physics and detectors at CLIC: CLIC conceptual design report", arXiv:1202.5940, 2012.

[47] A. Zholents, W. Gai, R. Lindberg, J. Power, Y. Sun, C. Jing, A. Kanareykin, C. Li, C. Tang, D. Shchegolkov, *et al.*, "A collinear wakefield accelerator for a high repetition rate multi-beamline soft X-ray FEL facility", Tech. Rep., Los Alamos National Laboratory, 2017.

[48] W. Leemans, "Report of workshop on laser technology for k-bella and beyond", Tech. Rep., Lawrence Berkeley National Laboratory, Berkeley, CA, 2017.

[49] T. Tajima and J. M. Dawson, "Laser electron accelerator", *Phys. Rev. Lett.*, vol. 43, pp. 267–270, 1979.

[50] M. Litos, E. Adli, W. An, C. Clarke, C. Clayton, S. Corde, J. Delahaye, R. England, A. Fisher, J. Frederico, *et al.*, "High-efficiency acceleration of an electron beam in a plasma wakefield accelerator", *Nature*, vol. 515, no. 7525, p. 92, 2014.

[51] A. Grudiev, S. Calatroni, and W. Wuensch, "New local field quantity describing the high gradient limit of accelerating structures", *Phys. Rev. ST Accel. Beams*, vol. 12, p. 102001, 2009.

[52] "Argonne wakefield accelerator facility." https://www.anl.gov/awa.

[53] W. Gai, J. G. Power, and C. Jing, "Short-pulse dielectric two-beam acceleration", *J. Plasma Phys.*, vol. 78, no. 4, pp. 339–345, 2012.

[54] S. E. Tsimring, *Electron beams and microwave vacuum electronics*, vol. 191. John Wiley & Sons, 2006.

[55] J. E. Walsh, "Stimulated čerenkov radiation", vol. 58, pp. 271–310, 1982.

[56] Computer Simulation Technology (CST) website, *www.cst.com*.

[57] S. Antipov, L. Spentzouris, W. Liu, W. Gai, and J. G. Power, "Wakefield generation in metamaterial-loaded waveguides", *J Appl. Phys.*, vol. 102, p. 034906, 2007.

[58] X. Lu, J. C. Stephens, I. Mastovsky, M. A. Shapiro, and R. J. Temkin, "High power long pulse microwave generation from a metamaterial structure with reverse symmetry", *Phys. of Plasmas*, vol. 25, p. 023102, 2018.

[59] R. Marqués, F. Martín, and M. Sorolla, *Metamaterials with negative parameters: theory, design, and microwave applications.* John Wiley & Sons, Hoboken, NJ, 2008.

[60] F. Falcone, T. Lopetegi, M. Laso, J. Baena, J. Bonache, M. Beruete, R. Marqués, F. Martín, and M. Sorolla, "Babinet principle applied to the design of metasurfaces and metamaterials", *Phys. Rev. Lett.*, vol. 93, p. 197401, 2004.

[61] J. H. Shao, S. P. Antipov, M. E. Conde, W. Gai, Q. Gao, G. Ha, W. Liu, N. R. Neveu, J. G. Power, Y. R. Wang, E. E. Wisniewski, L. M. Zheng, *et al.*, "Recent two-beam acceleration activities at Argonne Wakefield Accelerator Facility", in *Proc. 8th Int. Particle Accelerator Conf. (IPAC'17), Copenhagen, Denmark, May 2017*, pp. 3305–3307, 2017.

[62] M. A. Shapiro, S. Trendafilov, Y. Urzhumov, A. Alù, R. J. Temkin, and G.Shvets, "Active negative-index metamaterial powered by an electron beam", *Phys. Rev. B*, vol. 86, p. 085132, 2012.

[63] D. R. Smith, D. C. Vier, T. Koschny, and C. M. Soukoulis, "Electromagnetic parameter retrieval from inhomogeneous metamaterials", *Phys. Rev. E*, vol. 71, p. 036617, 2005.

[64] S. Arslanagić, T. V. Hansen, N. A. Mortensen, A. H. Gregersen, O. Sigmund, R. W. Ziolkowski, and O. Breinbjerg, "A review of the scattering-parameter extraction method with clarification of ambiguity issues in relation to metamaterial homogenization", *IEEE Antennas and Propagation Magazine*, vol. 55, pp. 91–106, 2013.

[65] X. Chen, T. M. Grzegorczyk, B.-I. Wu, J. Pacheco, and J. A. Kong, "Robust method to retrieve the constitutive effective parameters of metamaterials", *Phys. Rev. E*, vol. 70, p. 016608, 2004.

[66] Z. Duan, J. S. Hummelt, M. A. Shapiro, and R. J. Temkin, "Sub-wavelength waveguide loaded by a complementary electric metamaterial for vacuum electron devices", *Phys. Plasmas*, vol. 21, p. 103301, 2014.

[67] L. D. Landau and E. M. Lifshits, *Electrodynamics of Continuous Media.* Butterworth-Heinemann Co., 1984.

[68] V. M. Agranovič and V. L. Ginzburg, *Crystal Optics with Spatial Dispersion, and Excitons.* Springer, 1984.

[69] A. Demetriadou and J. B. Pendry, "Taming spatial dispersion in wire metamaterial", *Journal of Physics: Condensed Matter*, vol. 20, p. 295222, 2008.

[70] M. A. Shapiro, G. Shvets, J. R. Sirigiri, and R. J. Temkin, "Spatial dispersion in metamaterials with negative dielectric permittivity and its effect on surface waves", *Opt. Lett.*, vol. 31, pp. 2051–2053, 2006.

[71] V. M. Agranovich and Y. N. Gartstein, "Spatial dispersion and negative refraction of light", *Physics-Uspekhi*, vol. 49, p. 1029, 2006.

[72] W. C. Haxton, "The Nuclear Response of Water Cherenkov Detectors to Supernova and Solar Neutrinos", *Phys. Rev. D*, vol. 36, p. 2283, 1987.

[73] A. Grbic and G. V. Eleftheriades, "Experimental verification of backward-wave radiation from a negative refractive index metamaterial", *J. Appl. Phys.*, vol. 92, pp. 5930–5935, 2002.

[74] J. Lu, T. M. Grzegorczyk, Y. Zhang, J. P. Jr, B.-I. Wu, J. A. Kong, and M. Chen, "Cherenkov radiation in materials with negative permittivity and permeability", *Opt. Express*, vol. 11, pp. 723–734, 2003.

[75] Z. Duan, B.-I. Wu, J. Lu, J. A. Kong, and M. Chen, "Cherenkov radiation in anisotropic double-negative metamaterials", *Opt. Express*, vol. 16, pp. 18479–18484, 2008.

[76] B.-I. Wu, J. Lu, J. A. Kong, and M. Chen, "Left-handed metamaterial design for Čerenkov radiation", *J. Appl. Phys.*, vol. 102, p. 114907, 2007.

[77] S. Xi, H. Chen, T. Jiang, L. Ran, J. Huangfu, B.-I. Wu, J. A. Kong, and M. Chen, "Experimental verification of reversed cherenkov radiation in left-handed metamaterial", *Phys. Rev. Lett.*, vol. 103, p. 194801, 2009.

[78] V. V. Vorobev and A. V. Tyukhtin, "Nondivergent cherenkov radiation in a wire metamaterial", *Phys. Rev. Lett.*, vol. 108, p. 184801, 2012.

[79] ANSYS HFSS (High Frequency Structure Simulator) website, *https://www.ansys.com/products/electronics/ansys-hfss*

[80] A. F. Aleksandrov, L. S. Bogdankevich, and A. A. Rukhadze, *Principles of plasma electrodynamics*. Springer, 1984.

[81] W. Gai, P. Schoessow, J. Norem, J. Rosenzweig, and J. Simpson, "Experimental Demonstration of Walce-Field Effects in Dielectric Structures", *Phys. Rev. Lett.*, vol. 61, p. 2756, 1988.

[82] T.-B. Zhang, J. Hirshfield, T. Marshall, and B. Hafizi, "Stimulated dielectric wake-field accelerator", *Phys. Rev. E*, vol. 56, p. 4647, 1997.

[83] A. Cook, R. Tikhoplav, S. Tochitsky, G. Travish, O. Williams, and J. Rosenzweig, "Observation of narrow-nand terahertz coherent Cherenkov radiation from a cylindrical dielectric-lined waveguide", *Phys. Rev. Lett.*, vol. 103, p. 095003, 2009.

[84] G. Andonian, D. Stratakis, M. Babzien, S. Barber, M. Fedurin, E. Hemsing, K. Kusche, P. Muggli, B. O'Shea, X. Wei, O. Williams, V. Yakimenko, and J. B. Rosenzweig, "Dielectric wakefield acceleration of a relativistic electron beam in a

slab-symmetric dielectric lined waveguide", *Phys. Rev. Lett.*, vol. 108, p. 244801, 2012.

[85] F. Gao, M. E. Conde, W. Gai, C. Jing, R. Konecny, W. Liu, J. G. Power, T. Wong, and Z. Yusof, "Design and testing of a 7.8 ghz power extractor using a cylindrical dielectric-loaded waveguide", *Phys. Rev. ST Accel. Beams*, vol. 11, p. 041301, 2008.

[86] W. Gai, "Two Beam Wakefield Acceleration at Argonne Wakefield Accelerator Facility", in *Proceedings of 7th Int. Particle Accelerator Conf. (IPAC'16): Busan, Korea, May 2016*.

[87] C. Jing, A. Kanareykin, J. G. Power, M. Conde, Z. Yusof, P. Schoessow, and W. Gai, "Observation of enhanced transformer ratio in collinear wakefield acceleration", *Phys. Rev. Lett.*, vol. 98, p. 144801, 2007.

[88] H. Zha, C. Jing, J. Qiu, E. E. Wisniewski, M. Conde, J. G. Power, D. S. Doran, W. Liu, J. Shi, C. Li, W. Gai, and H. Chen, "Beam-induced wakefield observation in X-band choke-mode cavities", *Phys. Rev. Accel. Beams*, vol. 19, p. 081001, 2016.

[89] C. W. Steele, "A nonresonant perturbation theory", *IEEE Trans. on Microwave theory and Techniques*, vol. 14, no. 2, pp. 70–74, 1966.

[90] C. Li, W. Gai, C. Jing, J. G. Power, C. X. Tang, and A. Zholents, "High gradient limits due to single bunch beam breakup in a collinear dielectric wakefield accelerator", *Phys. Rev. ST Accel. Beams*, vol. 17, p. 091302, 2014.

[91] J. S. Hummelt, S. M. Lewis, M. A. Shapiro, and R. J. Temkin, "Design of a metamaterial-based backward-wave oscillator", *IEEE Trans. on Plasma Science*, vol. 42, pp. 930–936, 2014.

[92] J. Hummelt, X. Lu, H. Xu, M. Shapiro, and R. Temkin, "High power microwave generation from a metamaterial waveguide", in *Vacuum Electronics Conference (IVEC), 2016 IEEE International*, pp. 1–3, IEEE, 2016.

[93] X. Lu, J. S. Hummelt, M. A. Shapiro, and R. J. Temkin, "Long pulse operation of a high power microwave source with a metamaterial loaded waveguide", in *Vacuum Electronics Conference (IVEC), 2017 IEEE International*, pp. 1–2, IEEE, 2017.

[94] X. Lu, J. C. Stephens, I. Mastovsky, M. A. Shapiro, and R. J. Temkin, "High power microwave generation by Cherenkov-cyclotron instability in a metamaterial structure with negative group velocity", in *Vacuum Electronics Conference (IVEC), 2018 IEEE International*, pp. 27–28, IEEE, 2018.

[95] D. Shiffler, J. Luginsland, D. M. French, and J. Watrous, "A Cerenkov-like maser based on a metamaterial structure", *IEEE Trans. on Plasma Sci.*, vol. 38, pp. 1462–1465, 2010.

[96] S. C. Yurt, M. I. Fuks, S. Prasad, and E. Schamiloglu, "Design of a metamaterial slow wave structure for an O-type high power microwave generator", *Phys. Plasmas*, vol. 23, p. 123115, 2016.

[97] U. Chipengo, N. K. Nahar, and J. L. Volakis, "Cold test validation of novel slow wave structure for high-power backward-wave oscillators", *IEEE Trans. Plasma Sci.*, vol. 44, p. 911, 2016.

[98] U. Chipengo, N. K. Nahar, and J. L. Volakis, "Backward-wave oscillator operating in low magnetic fields using a hybrid-TE_{11} mode", *IEEE Trans. Electron Devices*, vol. 64, p. 3863, 2017.

[99] M. A. K. Othman, M. Veysi, A. Figotin, and F. Capolino, "Giant amplification in degenerate band edge slow-wave structures interacting with an electron beam", *Phys. Plasmas*, vol. 23, p. 033112, 2016.

[100] M. A. K. Othman, X. Pan, G. Atmatzakis, C. G. Christodoulou, and F. Capolino, "Experimental demonstration of degenerate band edge in metallic periodically loaded circular waveguide", *IEEE Trans. Microwave Theory Tech.*, vol. 65, p. 4037, 2017.

[101] S. Prasad, S. Yurt, K. Shipman, D. Andreev, D. Reass, M. Fuks, and E. Schamiloglu, "A compact high-power microwave metamaterial slow-wave structure: From computational design to hot test validation", in *2017 Computing and Electromagnetics International Workshop (CEM)*, pp. 61–62, 2017.

[102] A. Phipps, A. Maclachlan, C. Robertson, L. Zhang, I. Konoplev, A. Cross, and A. Phelps, "Electron beam excitation of coherent sub-terahertz radiation in periodic structures manufactured by 3D printing", *Nucl. Instrum. Methods Phys. Res. Sect. B*, vol. 402, p. 202, 2017.

[103] T. Rowe, N. Behdad, and J. Booske, "Metamaterial-enhanced resistive wall amplifier design using periodically spaced inductive meandered lines", *IEEE Trans. Plasma Sci.*, vol. 44, p. 2476, 2016.

[104] G. Shvets, "Photonic approach to making a material with a negative index of refraction", *Phys. Rev. B*, vol. 67, p. 035109, 2003.

[105] G. S. Nusinovich, *Introduction to the Physics of Gyrotrons*, 1st ed. JHU Press, 2004.

[106] G. S. Nusinovich, M. Walter, and J. Zhao, "Excitation of backward waves in forward wave amplifiers", *Phys. Rev. E*, vol. 58, p. 6594, 1998.

[107] G. S. Nusinovich, M. Korol, and E. Jerby, "Theory of the anomalous Doppler cyclotron-resonance-maser amplifier with tapered parameters", *Phys. Rev. E*, vol. 59, p. 2311, 1999.

[108] N. A. Estep, A. N. Askarpour, and A. Alù, "Experimental demonstration of negative-index propagation in a rectangular waveguide loaded with complementary split-ring resonators", *IEEE Antennas and Wireless Propagation Lett.*, vol. 14, pp. 119–122, 2015.

[109] N. Ginzburg, "Nonlinear theory of the amplification and generation of electromagnetic waves by the anomalous doppler effect", *Radiofizika*, vol. 22, pp. 470–479, 1979.

[110] L.-B. Kong, P.-K. Liu, and L. Xiao, "Nonlinear analysis of electron cyclotron maser based on anomalous doppler effect", *Phys. Plasmas*, vol. 14, p. 053108, 2007.

[111] N. F. Kovalev, "Cyclotron suppression of generation in a relativistic backward-wave oscillator of cherenkov type", *Radiophysics and Quantum Electronics*, vol. 49, pp. 93–107, 2006.

[112] A. Gilmour, *Klystrons, traveling wave tubes, magnetrons, crossed-field amplifiers, and gyrotrons.* Artech House, 2011.

[113] C. Child, "Discharge from hot CaO", *Phys. Rev. (Series I)*, vol. 32, p. 492, 1911.

[114] I. Langmuir and K. B. Blodgett, "Currents limited by space charge between concentric spheres", *Phys. Rev.*, vol. 24, p. 49, 1924.

[115] R. Levy, "Analysis and synthesis of waveguide multiaperture directional couplers", *IEEE Trans. on Microwave Theory and Techniques*, vol. 16, pp. 995–1006, 1968.